

Archive ouverte UNIGE

https://archive-ouverte.unige.ch

Thèse 2021

Open Access

This version of the publication is provided by the author(s) and made available in accordance with the copyright holder(s).

Solution-Based Self-Assembly of Au25(SR)18 Nanocluster Building Blocks: Towards Functional Nanomaterials

Banach, Ewa Marta

How to cite

BANACH, Ewa Marta. Solution-Based Self-Assembly of Au25(SR)18 Nanocluster Building Blocks: Towards Functional Nanomaterials. Doctoral Thesis, 2021. doi: 10.13097/archive-ouverte/unige:157446

This publication URL: https://archive-ouverte.unige.ch/unige:157446

Publication DOI: <u>10.13097/archive-ouverte/unige:157446</u>

© This document is protected by copyright. Please refer to copyright holder(s) for terms of use.

Professeur T. Bürgi

Solution-Based Self-Assembly of Au₂₅(SR)₁₈ Nanocluster Building Blocks: Towards Functional Nanomaterials

THÈSE

présentée à la Faculté des sciences de l'Université de Genève pour obtenir le grade de Docteur ès sciences, mention chimie

par

Ewa Marta BANACH

de

Zakopane (Pologne)

Thèse Nº 5591

GENÈVE
Atelier ReproMail
2021



DOCTORAT ÈS SCIENCES, MENTION CHIMIE

Thèse de Madame Ewa Marta BANACH

intitulée :

«Solution-Based Self-Assembly of Au₂₅(SR)₁₈ Nanocluster Building Blocks: Towards Functional Nanomaterials»

La Faculté des sciences, sur le préavis de Monsieur T. BÜRGI, professeur ordinaire et directeur de thèse (Département de chimie physique), Monsieur T. ADACHI, professeur assistant (Département de chimie physique), Madame J. OLESIAK-BANSKA, professeure (Advanced Materials Engineering and Modelling Group, Wroclaw University of Technology, Wroclaw, Poland), autorise l'impression de la présente thèse, sans exprimer d'opinion sur les propositions qui y sont énoncées.

Genève, le 17 septembre 2021

Thèse - 5591 -

Le Doven

Acknowledgements

It is with great pleasure that I can take an opportunity to thank all the people whose assistance was indispensable for the completion of this project. I would like to pay special regards to my thesis supervisor, Prof. Thomas Bürgi, for welcoming me to his group and giving me the opportunity to carry out research in his laboratory. I am very grateful for his inspiring ideas, his patience, and the confidence he entrusted in me throughout my PhD study. A special thanks also must go to the members of my thesis committee: Prof. Joanna Olesiak-Bańska and Prof. Takuji Adachi for accepting to evaluate the work presented in this dissertation. I would also like to acknowledge the financial support of the Swiss National Science Foundation and their MHV funding scheme, which made my PhD study possible. My sincere gratitude goes to Dr Arnulf Rosspeintner for all his support and patience in explaining and guiding me through the meanders of photophysics. The accomplishment of the photoligand project could not have been possible without his help. I would also like to express my gratitude to all the collaborators that helped to make the photoligand project a success: Dr Lay-Thang Lee from the Laboratoire Léon Brillouin CEA-Saclay, France for the SAXS analyses, Dr Mohammad M. Dadras from CSEM Centre Suisse d'Electronique et de Microtechnique for carrying out the HRTEM imaging, Dr Céline Besnard from Laboratory of crystallography (UniGE) for the crystal structure determination, Dr Latevi Max Lawson Daku from the Departement of physical chemistry (UniGE) for the DFT calculations and Marion Pupier for the NMR analyses. I am very grateful to the team from the Mass Spectrometry Core Facility: Dr Emmanuel Varesio, Harry Théraulaz, Julien Meyer, and Eliane Sandmeier for countless analyses and support in operating the MALDI mass spectrometer. I would like to thank Prof. Nicolas Winssinger for providing access to MALDI-TOF mass spectrometer. I acknowledge the team from the Photonic Bioimaging Centre of the University of Geneva: Dr Christoph Bauer and Michal Parkan for their assistance and training on the transmission electron microscope. I wish to acknowledge the technical support of Patrick Barman, Eric Studemann and Laurent Devenoge for the construction of the custom photoirradiation setup, and for all their help on various technical issues during my stay at the University of Geneva. I would like to acknowledge Catherine Ludy and Sophie Jacquemet for their help with all administrative matters. I would like to extend my sincere thanks to my colleagues from the organic chemistry department at the University of Geneva Dr Kévin Martin, Dr Johann Bosson, Dr Ramakrishna Kota, and Stéphane Grass, as well as Dr Daniele Fiorito for their help and guidance on the organic synthesis. I am grateful to Raymond Azoulay and Louna Armand for help synthesizing the dithiol

photoligand. I wish to acknowledge the current and past members of Prof. Claude Piguet's group: Dr Homayoun Nozary for NMR training, as well as Benjamin, Juan, Mohsen, Bahman, Neel, Inès, Soroush, Maxime for their scientific advice and providing a great atmosphere that made working in the labs of the 'rez-de-chaussée' truly enjoyable. I also thank current and former members of the Bürgi group: Ani, Rossella, Rania, Michal, Ugo, Igor, Naoko, Martin, Patric, Yuming, Krishnadas, Yanan, Huayan, Xianwei, Ariel, Abi, Jiangtao, Sarita, Khadi, Jasmina, Belen, Giovanni, Annelies and Bei for a memorable time we spent together in the lab and in social settings. I would like to thank Florian for helping me with the French translation of the abstract. I am deeply indebted to Prof. Reinhard Neier for his mentorship. I would not be where I am right now if it were not for his encouragement and persistent support. I would like to express my gratitude to my close friends and family. They were always by my side and this work would not have been accomplished without their support and encouragement. Finally, I wish to thank Kevin, who encouraged me to do the right thing even when the road got tough.

Abstract

Ligand-protected gold nanoclusters (Au NCs) are a unique class of nanomaterials at the interface between molecular complexes and noble metal nanoparticles. Au NCs possess a core-shell structure in which the metal kernel is capped with a monolayer of ligands that ensure their stability. Like for the other nanomaterials, the properties of gold nanoclusters are size- and structure-dependent. However, the uniqueness of Au NCs lies in the fact that their physicochemical properties can change significantly with only minor modifications to their atomic composition (e.g., metal- or ligand-exchange). For these reasons, Au NCs are attractive for fundamental investigations and as building blocks for functional nanomaterials.

Self-assembly has emerged as a powerful tool for the fabrication of a new generation of nanosystems. The possibility to control functionalization of the ligand shell of Au NCs is utilized in this work to investigate different strategies to realize self-assembled Au NC-based architectures. For this purpose, the benchmark ultrasmall (< 2 nm) atomically precise thiolate (SR)-protected [Au₂₅(SR)₁₈]⁰ nanoclusters were employed.

First, an investigation into deploying metalloporphyrins as potential molecular anchors for Au₂₅ nanoclusters containing coordinating pyridine functionalities in the ligand shell was performed. The binding of the Au₂₅ clusters to the porphyrin macrocycles coordinated with two different transition metals, ZnTPP and CoTPP (TPP = tetraphenylporphyrine), was followed spectroscopically during supramolecular titration experiments by monitoring UV-vis absorption and fluorescence. The conducted study led to the conclusion that the employed metalloporphyrins and Au₂₅ nanoclusters formed coordination complexes in a 1:1 binding stoichiometry. No evidence for substantial biaxial binding was found for both CoTPP and ZnTPP compounds, making them unsuitable candidates for anchors in prospective metalloporphyrin–Au NC assembled systems. However, the 1:1 binding between the metalloporphyrins and Au₂₅ nanoclusters led to interesting assembled units with several porphyrins rings coordinated to the functionalized Au₂₅ nanocluster surface.

The second strategy employed the already-demonstrated concept of utilizing dithiolate ligands, where the strong Au–S bonds are formed, to achieve covalently linked Au₂₅ clusters. Importantly, in this study an additional light-switching functionality was introduced to the bridging molecule to control the extent of the electronic conjugation between the paramagnetic Au₂₅ cluster units. This strategy was motivated

by the possible application of the Au NCs in molecular electronic devices. The formation of discrete Au_{25} assemblies connected with the synthesized dithiol linker containing a photoactive dithienylethene (DTE) moiety was shown. Furthermore, the reversible photoswitching of the Au_{25} assemblies having different sizes was demonstrated. Photoirradiation was shown to induce structural rearrangements of the Au_{25} assemblies. Extensive investigations into evolution of the photophysical properties coupled with the observed structural transformation indicated a photoinduced cross-linking of the formed Au_{25} assemblies. Overall, the work in this thesis makes important steps toward the use of Au NCs in tailor-made and self-assembled molecular electronic devices.

Résumé

Les "nanoclusters" d'or protégés par des ligands (Au NCs) constituent une classe unique de nanomatériaux à l'interface de la recherche sur les complexes moléculaires et celle sur les nanoparticules de métaux nobles. Les "nanoclusters" d'or possèdent une structure noyau-enveloppe dans laquelle le noyau métallique est recouvert d'une monocouche de ligands qui assure leur stabilité. Comme pour les autres nanomatériaux, les propriétés des "nanoclusters" d'or dépendent de leur taille et de leur structure. Cependant, le caractère unique des "nanoclusters" d'or réside dans le fait que leurs propriétés physicochimiques peuvent changer drastiquement, en modifiant légèrement leur composition atomique (par exemple, échange de métaux ou de ligands). Pour ces raisons, les NC d'Au sont captivantes, non seulement pour la recherche fondamentale, mais elles offrent de larges possibilités en tant que blocs de construction de nanomatériaux fonctionnels.

L'auto-assemblage est devenu récemment un outil puissant pour la fabrication d'une nouvelle génération de nanosystèmes. La fonctionnalisation contrôlée des Au NCs par différentes enveloppes ligands est utilisée dans ce travail pour étudier diverses stratégies pour réaliser des architectures auto-assemblées à base des Au NCs. Pour atteindre cet objectif, des "nanoclusters" de référence ultrascopiques (< 2 nm) protégés par un thiolate (-SR) et d'une précision atomique [$Au_{25}(SR)_{18}$] 0 ont été utilisés.

Premièrement, le déploiement des métalloporphyrines comme ancres moléculaires potentielles pour les "nanoclusters" Au₂₅ contenant des fonctionnalités pyridine de coordination dans l'enveloppe du ligand a été explorée. La liaison chimique des clusters Au₂₅ aux macrocycles de porphyrine coordonnés avec deux métaux de transition différents, ZnTPP et CoTPP (TPP = tétraphénylporphyrine), a été controlée spectroscopiquement, à travers des expériences de titrage supramoléculaire, en mesurant l'absorption UV-vis et la fluorescence. Cette étude a révélé que les métalloporphyrines employées et les nanoclusters Au₂₅ formaient des complexes de coordination avec une stœchiométrie de liaison 1:1. Les résultats indiquent que la formation de liaison biaxiale pour les composés n'est pas prédominante pour les composés CoTPP et ZnTPP, ce qui en fait des candidats inadaptés pour les ancrages dans les systèmes assemblés métalloporphyrine-Au NC. Cependant, la découverte de liaison 1:1 entre les métalloporphyrines et les nanoclusters Au₂₅ a entrainé la synthèse d'unités assemblées intéressantes avec plusieurs macrocycles de porphyrines coordonnés à la surface du nanocluster Au₂₅ fonctionnalisé.

La deuxième stratégie exploitée dans ce projet explore le concept établi de l'utilisation de ligands dithiolates, où les fortes liaisons Au–S sont formées, pour obtenir des clusters Au₂₅ liés de manière covalente. Il est important de noter que dans cette étude, une fonctionnalité supplémentaire de commutation de la lumière a été introduite dans la molécule de pontage pour contrôler l'étendue de la conjugaison électronique entre les unités paramagnétiques des clusters Au₂₅. Cette stratégie a été motivée par l'application possible des NCs d'Au dans des dispositifs électroniques moléculaires. La formation d'assemblages Au₂₅ discrets connectés avec des connecteurs dithiols synthétiques contenant une partie photoactive de dithiényléthène (DTE) a été démontrée. En outre, cette étude a révélé une commutation optique réversible des assemblages Au₂₅ de différentes tailles. Il a été démontré que l'irradiation lumineuse induit le réarrangement structurel des assemblages Au₂₅. Des recherches approfondies sur l'évolution des propriétés photophysiques, couplées à la transformation structurelle observée, ont soutenu l'hypothèse d'une réticulation photoinduite des assemblages Au₂₅ ainsi formés. Dans l'ensemble, le travail de cette thèse constitue une étape importante, favorisant l'utilisation de NCs d'Au dans des dispositifs électroniques moléculaires auto-assemblés et conçu sur-mesure.

Table of contents

Acknowledgements	i
Abstract	ii
Résumé	v
Abbreviations	1
General Introduction	5
Chapter 1 Introduction: Au ₂₅ (SR) ₁₈ -a benchmark gold nanocluster	7
1.1 Thiolate-protected gold nanoclusters	7
1.1 Au ₂₅ (SR) ₁₈ nanoclusters	10
1.2 Thiolate-protected gold nanoclusters—highly versatile species amenable to tailoring	14
1.3 References	16
Chapter 2 Metal nanoclusters as versatile building blocks for hierarchical structures	21
2.1 Introduction	21
2.2 Discrete multimers of metal nanoclusters	21
2.2.1 Covalently linked nanoclusters	22
2.3 One-dimensional (1D) metal nanocluster assemblies	29
2.3.1 Metal–metal interactions (aurophilic interactions)	29
2.3.2 Connection via heteroatom (direct metal–metal bond)	33
2.3.3 Counterion-induced metal NC assemblies	36
2.4 Two-dimensional (2D) metal nanocluster assemblies	37
2.4.1 Intraligand interactions	37
2.4.2 Template-directed assembly of metal NCs	41
2.4.3 Amphiphilicity	42
2.5 Three-dimensional (3D) metal nanocluster assemblies	42
2.5.1 Ion—ion interactions	43
2.5.2 Ag–O, Ag–S and Ag–Cl bond formation	45
2.5.3 Control of counterions	46
2.5.4 Molecular linkers	47
2.5.5 Intraligand interactions	50

2.6 Conclusions	52
2.7 References	53
Research aims and objectives	57
References	59
Chapter 3 Materials and experimental methods	61
3.1 Materials	61
3.2 Characterization methods	61
3.2.1 Steady-state electronic absorption spectroscopy	61
3.2.2 Matrix-assisted laser desorption-ionization/time of flight mass spectrometry (MALDI-TOF-I	MS) 62
3.2.3 Steady-state photoluminescence spectroscopy	62
3.2.4 Time-resolved photoluminescence	63
3.2.5 Nuclear magnetic resonance (NMR) spectroscopy	63
3.2.6 Transmission electron microscopy (TEM)	63
3.2.7 Small angle X-ray scattering (SAXS) analysis	63
3.3 Photoirradiation setup	65
3.4 Mathematical analyses and fitting	66
3.5 Synthesis of Au ₂₅ (SR) ₁₈ nanoclusters	67
3.5.1 Synthesis of [Au ₂₅ (SC ₂ H ₄ Ph) ₁₈] ⁰	67
3.5.2 Synthesis of $[Au_{25}(SC_4H_9)_{18}]^0$	68
3.6 References	68
Chapter 4 Towards metalloporphyrin–Au ₂₅ nanoassemblies: solution-state binding study	71
4.1 Introduction	71
4.2 Functionalized Au ₂₅ (SR) ₁₈ nanoclusters–synthesis and characterization	73
4.2.1 Synthesis of [Au ₂₅ (SBu) ₁₈] ⁰	73
4.2.2 Ligand-exchange reaction of [Au ₂₅ (SBu) ₁₈] ⁰ with 4-pyridylethanemercaptan	73
4.2.3 Characterization of the mixed ligand shell Au ₂₅ (SBu) _{18-x} (4PEM) _x nanoclusters spectrophotometric titration	
4.3 Metalloporphyrin selection	78
4.4 Spectrophotometric titrations: principle and data fitting	79
4.4.1 Calculation of binding constants from the UV-vis titration data	79
4.4.2 Calculation of binding constants from the fluorescence titration data	81

4.4.3 Solution-state UV-vis/fluorescence titration experiments	82
4.5 Interactions of ZnTPP with functionalized Au ₂₅ nanoclusters probed with spectrophotometr	ic titrations. 83
4.5.1 UV-vis titration of ZnTPP with pyridine and $Au_{25}(SBu)_{18-x}(4PEM)_x$ nanoclusters	83
4.5.2 Fluorescence titration of ZnTPP with pyridine and Au ₂₅ (SBu) _{18-x} (4PEM) _x nanoclusters	87
4.6 Interactions of CoTPP with functionalized Au ₂₅ nanoclusters probed with spectrophotometr	ic titrations 91
4.6.1 UV-vis titration of CoTPP with pyridine and Au ₂₅ (SBu) _{18-x} (4PEM) _x nanoclusters	92
4.6.2 Fluorescence titration of CoTPP with pyridine and $Au_{25}(SBu)_{18-x}(4PEM)_x$ nanoclusters	94
4.7 Conclusions	97
4.8 References	99
Chapter 5 Synthesis of Au ₂₅ (2PET) ₁₈ -based assemblies covalently bound with pho	otoswitchable
linker	103
5.1 Introduction	103
5.2 Synthesis of dithiol photoligand	107
5.3 The photoswitching reaction of dithienylethene (DTE) compounds	109
5.4 Characterization of the photoswitching properties of DTE ligands	110
5.4.1 Reversible photoswitching of the DTE photoligands	110
5.4.2 Quantum yield of the photocyclization (Φ_C) and photocycloreversion (Φ_O) reaction	of DTE ligands
	112
5.4.3 Photofatigue of DTE ligands	116
5.5 Synthesis of photoswitchable Au ₂₅ assemblies	119
5.6 Characterization of the formed Au ₂₅ assemblies linked with a DTE photoligand	120
5.6.1 Steady-state UV-vis-NIR spectroscopy in solution	120
5.6.2 Identification of the separated fractions with MALDI-TOF mass spectrometry	121
5.6.3 Small angle X-ray scattering (SAXS) analysis of the formed Au ₂₅ assemblies	124
5.7 Conclusions	130
5.8 Acknowledgements	130
5.9 References	131
Chapter 6 Photoresponsive Au ₂₅ nanoassemblies:structural and spectroscopic invest	igations 135
6.1 Introduction	135
6.2 Reversible photoswitching of DTE-linked Au ₂₅ assemblies	137
6.2.1 Principle of photoswitching reaction	137

6.2.2 Reversible photoswitching of the DTE-linked Au ₂₅ assemblies–qualitative inspection using the U	V-vis-
NIR spectroscopy	. 137
6.2.3 MALDI-TOF-MS analysis of photoirradiated Au ₂₅ assemblies	. 140
6.2.4 Photoluminescence behaviour of photoirradiated Au ₂₅ assemblies	. 142
6.3 Investigation of the light-induced structural changes within the Au ₂₅ assemblies using small angle scattering	-
6.3.1 Steady-state absorption spectroscopy of the Au ₂₅ assemblies connected with o-DTE and c photoligand isomers	
6.3.2 SAXS investigation into photoinduced structural changes of Au ₂₅ assemblies	. 146
6.4 Photoinduced self-assembly of Au ₂₅ dimers: insight into structure and photophysical properties	. 150
6.4.1 Photoswitching of Au ₂₅ dimers and mixed ligand shell Au ₂₅ monomers	. 151
6.4.2 Photoluminescent properties of the Au ₂₅ assemblies linked with DTE ligand	. 153
6.4.3 Characterization of the photoinduced structural changes in small Au ₂₅ assemblies	. 159
6.5 Conclusions	. 165
6.6 References	. 166
General conclusions and outlook	.169
Appendix A	.173
Appendix B	.213

Abbreviations

(FE)SEM (field emission) scanning electron microscopy

(HR)TEM (high resolution) transmission electron microscopy

(M)TPP (metal)tetraphenylporphine 1D/2D/3D one/ two/ three dimensional

2-phenylethanethiolate
4PEM 4-pyridylethylmercaptan
A-Adm 1-ethynyladamantane

Au NC atomically precise gold nanocluster

Au NP gold nanoparticle

BCC body-centred cubic

BDT benzene-1,4-dithiol

BE dibenzylether

BPDT biphenyl-4,4'-dithiol

bpy 4,4'-bipyridine

Bu butyl

C₃-AMT azobenzene-alkyl monothiol

CCS collision cross-section

c-DTE closed-ring dithienylethene isomer
CPL circularly polarized luminescence
CTAB cetyltrimethylammonium bromide

DAE diarylethene

DCM dichloromethane

DCTB *trans*-2-[3-(4-tert-butylphenyl)-2-methyl-2-propenylidene]malononitrile

DFT density functional theory

DMBT 2,4-dimethylbenzenethiolate

DMF N,N'-dimethylformamide

DMSO dimethyl sulfoxide
DOS density of states

DOSY diffusion-ordered spectroscopy

DT 1-dodecanethiolate
DTE dithienylethene

DZVP double-zeta valence polarized

EDC 1-ethyl-3-(3-dimethylaminopropyl)carbodiimide

EELS STEM electron energy-loss spectroscopy

ESI-MS electrospray-ionization mass spectrometry

Et ethyl

FCC face-centred cubic
FET field-effect transistor
FFT fast Fourier transform

FRET Förster resonance energy transfer

FWHM fullwidth at half maximum
HAADF high-angle annular dark-field

HCP hexagonal close packed

HOMO highest occupied molecular orbital

HPLC high-performance liquid chromatography

HS high-spin

IFE inner-filter effect

IM-MS ion mobility mass spectrometry

iPrS 2-propanethiolateLE ligand-exchangeLED light-emitting diode

LEISST ligand-exchange-induced size/structure transformation

LMMCT ligand-to-metal-metal charge transfer

LP liquid paraffin
LS low-spin

LUMO lowest unoccupied molecular orbital

MALDI matrix-assisted laser desorption—ionization mdppz 2-(3-methylpyrazinyl)diphenylphosphine

Me methyl methanol

MHA 6-mercaptohexanoic acid
MOF metal-organic framework
MTBE tert-butyl methyl ether

NC nanocluster
NIR near infrared

NMP N-methyl-2pyrrolidone

NMR nuclear magnetic resonance

o-DTE open-ring dithienylethene isomer

OEP 2,3,7,8,12,13,17,18-octaethylporphinato

ORR oxygen reduction reaction

PAGE polyacrylamide gel electrophoresis

PBE Perdew-Burke-Ernzerhof

PCP bis(diphenylphosphinomethane)

PL photoluminescence

PLE photoluminescence excitation

p-MBA para-mercaptobenzoic acid

p-MBT para-methylbenzenethiolate

PMT photomultiplier tube PSS photostationary state

py pyridine

rGO reduced graphene oxide

ROKS restricted open-shell Kohn-Sham

RS- organic thiolate
RT room temperature

SAc thioacetate

S-Adm 1-adamantanethiolate
SAM self-assembled monolayer
SAXS small angle X-ray scattering

SBu 1-butanethiolate

SCIF superatom complex inorganic framework

SC-XRD single-crystal X-ray diffraction SEC size-exclusion chromatography

SERS surface-enhanced Raman spectroscopy

SG glutathione

SSR 1,3-benzene dithiol

STEM scanning transmission electron microscopy

SWNT single-walled carbon nanotube

TBT 4,4-thiodibenzenethiol

t-Bu *tert*-butyl

TCSPC time-correlated single photon counting

THF tetrahydrofuran

TLC thin layer chromatography

TMS tetramethylsulfone

TOABr tetraoctylammonium bromide

UKS unrestricted Kohn-Sham

UV ultraviolet vdW van der Waals

vis visible

VOC volatile organic compound

General Introduction

Self-assembly has emerged as a powerful tool for the fabrication of a new generation of multifunctional nanomaterials with applications in magnetism, sensing, molecular recognition, bioimaging or catalysis. Employing atomically precise gold nanoclusters (Au NCs), rather than gold nanoparticles (Au NPs), as structural units can afford novel hierarchical solids with new (or enhanced) collective properties arising from the periodic order and perfect monodispersity of NCs. Indeed, the rich universe of ligand-protected Au NCs provides a broad library of building blocks with atomically precise anatomies and wellunderstood structure-property relationships. Moreover, a great advantage of ligand-protected Au NCs, over Au NPs or nanocrystals, is their enhanced stability paired with their customizable size, molecular composition, structure, and surface chemistry. The structural tuneability of Au NCs is therefore expected to overcome the drawbacks of aggregation, polydispersity and directionality presented by Au NPs assemblies. Overall, utilizing Au NCs as building units can pave the way for understanding the physicochemical properties of the NC assemblies at the nanometer level. Additionally, an improved design of higher order structures and control over their performance becomes accessible. However, despite the promise of self-assembled Au NCs, much work is needed to develop tools to control the selfassembly and functionality of these superstructures. It is known that the organization of Au NCs into discrete multimers, 1D, 2D, and 3D architectures occurs via self-assembly driven by various types of intercluster interactions: covalent bonding, hydrogen bonding, van der Waals, electrostatic, $\pi \cdots \pi$, and $C-H\cdots\pi$ interactions, metallophillic forces, or physical/chemical adsorption. This thesis endeavours to leverage some of these self-assembly approaches to demonstrate novel assembly strategies and novel functionality.

This dissertation is laid out in the following way: Chapter 1 briefly introduces the field of atomically precise Au NCs, their structure and properties using archetypical $Au_{25}(SR)_{18}$ cluster as an example. An extensive literature review on the self-assembly of Au (and Ag) NCs into 1D, 2D and 3D structures is presented in Chapter 2 followed by the specific Aims and Objectives of this dissertation. Chapter 3 entails the methods used in this thesis. Chapters 4-6 contain the experimental part concerning the different approaches towards achieving $Au_{25}(SR)_{18}$ -assemblies. Lastly, the General Conclusions and Outlook are presented. The Appendices A–B, contain the supporting information to the experimental study.

Chapter 1

Introduction:

Au₂₅(SR)₁₈—a benchmark gold nanocluster

1.1 Thiolate-protected gold nanoclusters

Ligand-protected atomically precise metal nanoclusters belong to an important class of nanomaterials that exhibit great potential for applications in the field of catalysis, optoelectronics, chemical sensors, and biomedicine.^{1, 2} With diameters between 1–3 nm they span across the size continuum between molecular compounds/complexes and metal nanoparticles (**Figure 1.1**).

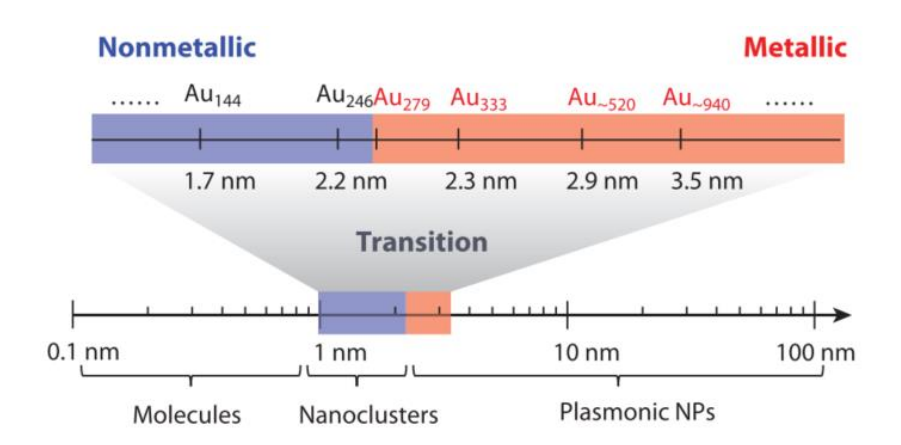


Figure 1.1 Size of gold nanoclusters in relation to molecules and gold nanoparticles. Transition from the nonmetallic (blue colour) to the metallic (orange colour) state in Au NCs. Reproduced with permission from Reference [3]. Copyright 2021 Annual Reviews.

The synthesis of Au NCs was developed in the late 1990s by modifying a protocol used for a preparation of gold nanoparticles capped with thiolate ligands established by Brust and Schiffrin.⁴ Briefly, the synthesis was carried out in an organic phase by reacting a gold^{III} salt with tetraoctylammonium bromide (TOABr). The obtained tetraoctylammonium salt of gold, [TOA]⁺[AuCl₄]⁻, was then reduced in the presence of thiols with sodium tetraborate, NaBH₄, to afford a mixture of clusters.⁵ Later it was shown that the polydisperse nanoclusters could be separated using high-performance liquid chromatography (HPLC)⁶ or size-exclusion chromatography (SEC, on a semi-preparative scale) techniques and organic solvents as eluents.⁷ The accurate determination of the chemical composition of Au_n(SR)_m clusters with mass spectrometry,⁸ which soon after was followed with the total structure determination by single-crystal X-ray diffraction (SC-XRD),⁹ brought a breakthrough to the field. In particular, it opened the possibility to identify new clusters not only in terms of their varying molecular compositions but also with respect to their structural diversity in a relatively fast and accessible manner. Since then, there has been a tremendous progress in the total structure determination (i.e., core and ligands) of Au NCs with X-ray crystallography, which has expanded the library of ligand-protected nanoclusters.¹⁰⁻¹³

Structure. Broadly speaking, Au NCs display a core–shell structure where the zerovalent Au core is protected by a monolayer of ligands (**Figure 1.2**).

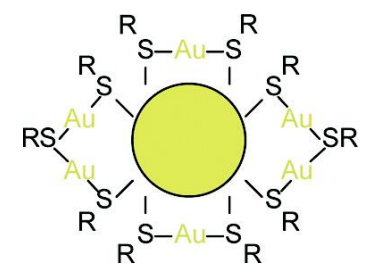


Figure 1.2 Schematic illustration of the core—shell structure of Au NCs where metallic gold core is surrounded by the $Au(SR)_2$ and $Au_2(SR)_3$ staple motifs. Reproduced with permission from Reference [14]. Copyright 2010 American Chemical Society.

The shell consists of Au^I –SR motifs called staples that are a characteristic structural pattern in ligand protected nanoclusters. Consequently, such a core–shell structure exhibits a Au^0 core (or kernel) with a high packing symmetry and an ordered arrangement of ligands on the surface. Jadzinsky et al., in their report on the X-ray crystal structure of a gold nanocluster, $Au_{102}(p\text{-MBA})_{44}$ (p-MBA = para-mercaptobenzoic acid), revealed the existence of staple motifs for the first time. Identical Au–S binding patterns were later found in other Au NCs. In principle, staples can be defined as $[RS-(AuSR)_x]$ (x=1,2,...) oligomeric units that bind to two Au atoms of the outermost layer of a Au kernel via the terminal (RS–) groups in the units. In II, II,

Stability. The exceptional thermodynamic stability of certain clusters can be explained by their 'magic composition/size'. This concept relates the valence electron count to the unusual stability of the species.¹⁹

For ligand-protected metal nanoclusters the number of valence electrons, N_e , in the nanocluster is obtained from the following expression (**Equation 1.1**):

$$N_e = n - m - q \tag{1.1}$$

where n is the number of metal atoms in the cluster, m corresponds to the number of protective ligands having one localized electron and q is the net charge of the cluster. If the obtained value of N_e fulfils the shell closing of superatom orbitals $| 1S^2 | 1P^6 | 1D^{10} 2S^2 | 1F^{14} 2P^6 |$ (just like in the case of noble atoms) then the stability of the nanoclusters can be explained using an electronic argument. It needs to be said however that the superatom concept, which is based on the jellium model, is only valid for species with (nearly) spherical cores. Nevertheless, while the stability of some nanoclusters could be attributed to their full electronic shell, having a closed shell is not a prerequisite for stability, hence it cannot be used as universal descriptor of thermodynamic stability of metal nanoclusters. In fact, many clusters have been reported that cannot be considered as 'magic', nevertheless their stability is exceptional. ^{20,21} An example is $Au_{38}(SR)_{24}$. Here, the geometric structure of the cluster has been considered preponderant for the stability of these species. Indeed, another important factor contributing to the nanocluster stability is the geometric arrangement of the metal atoms in the core (geometric argument). The protective ligands, specifically their structure and electronic properties, also play a key role in stabilizing clusters. Ligands not only prevent aggregation of metal atoms, but also dictate the cluster size, physicochemical properties, or self-assembly behaviour. ²²⁻²⁶

The presence of staples was anticipated by Häkkinen and co-workers in the 'divide-and-protect' model describing the general core-shell morphology of ligand-protected Au NCs. Specifically, it served to rationalize the observed structural characteristics of Au NCs, by employing computational modelling based on first-principles.²⁷ This theory put forward the dual chemical nature of Au atoms in the nanoclusters: a metallic form of the innermost Au atoms constituting of a closed packed kernel, and the external Au atoms, bearing the formal oxidation state of +1, bound to the organic ligands and forming a protective layer surrounding the gold core.

A significant advance of the 'divide-and-protect' concept was made recently by Taylor and Mpourmakis. They proposed a DFT-based theory that introduced quantitative descriptors to relate the thermodynamic stability of thiolate-protected Au NCs in solution to their specific structural characteristics. The calculated values of the shell-to-core binding energies and the cohesive energies of the metal core for the experimentally defined $Au_n(SR)_m$ clusters were shown to be nearly identical. As can be seen in **Figure 1.3**, the clusters for which the binding and cohesive energies are very similar in value can be found near or on the diagonal line which indicates where the stable clusters can be found. Hence, this theory states that stability of nanoclusters arises from a fine energy balance between the strength of adsorption of the ligand shell to the metal core and the cohesive energy of the core.

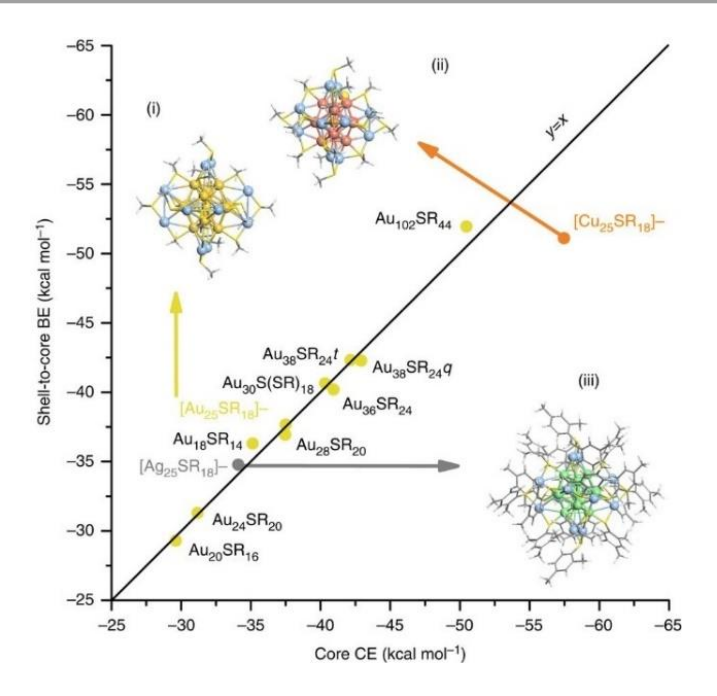


Figure 1.3 Parity between the core cohesive energy (CE) and the shell-to-core binding energy obtained from the first-principle calculations of the experimentally produced $Au_n(SR)_m$ nanoclusters. Reproduced form Reference [28]. Published by Springer Nature.

The unique structure of Au NCs lead to their physicochemical characteristics to be distinct from those of the bulk metal, coordination complexes, and gold nanoparticles. Similar to the latter, the properties of Au NCs are also size-dependent. However, in contrast to their plasmonic counterparts, nanoclusters do not follow a straightforward linear relationship between size and properties. For example, the $Au_{36}(SR)_{24}$ cluster has a larger HOMO–LUMO gap than $[Au_{25}(SR)_{18}]^-$ (1.7 vs. 1.3 eV, respectively) despite its larger size. ^{29,30} Nevertheless, the structure determination that was achieved for many clusters using X-ray crystallography has made it possible to correlate the anatomy of Au NCs with their properties. One of the consequences of the ultrasmall size of Au NC is that their electronic structure is reminiscent to that of molecular systems with their discrete energy levels. Indeed, it is evident that, for very small clusters, a distinct HOMO–LUMO gap can be described.

1.1 Au₂₅(SR)₁₈ nanoclusters

As one of the prototypical nanoclusters, $Au_{25}(SR)_{18}$ species lend themselves as ideal candidates for introducing various functionalities in a controlled manner, thanks to their known structure and well-studied properties.³¹⁻³⁴ Indeed, the commonly studied $Au_{25}(2PET)_{18}$ (2PET = 2-phenylethanethiolate) was amongst the first synthesized thiolate-protected Au NCs. Since this thesis will extensively employ $Au_{25}(SR)_{18}$ species, a detailed characterization of their formation and structure is given below.

The careful investigation into the growth mechanism of $[Au_{25}(SR)_{18}]^-$ nanoclusters revealed a two-stage bottom-up process.³⁵ In the first stage, a fast reduction–growth led to the formation of a narrow

distribution of nanoclusters from the Au^I complex precursors: cyclic Au_n(SR)_m, and linear [Au_n(SR)_{n+1}]⁻, and [Au_n(SR)_{n-p}Cl_{p+1}]⁻. These reactive species formed thiolated Au NCs in a sequential 2 e⁻ reduction—growth reaction yielding Au NCs with a progressively larger and even number of valence electrons, N_e . In the second stage, during the relatively slow thermodynamically controlled size-focusing reaction, the intermediate NCs were transformed into the final, thermodynamically-stable [Au₂₅(SR)₁₈]⁻ nanoclusters. It needs to be said that this size-focusing method differs from the conventional one, where a mixture of larger-size clusters is etched into smaller and more stable species.^{36, 37} Here, the opposite process is taking place and it has been postulated to occur via (at least) three pathways, depicted in **Scheme 1.1**: isoelectronic addition (1), disproportionation (2), and comproportionation (3).

Scheme 1.1 Isoelectronic addition (1), disproportionation (2) and comproportionation (3) reactions occurring during the size-focusing process of the $[Au_{25}(SR)_{18}]^-$ clusters. Number of valence electrons, N_e , for each nanocluster species is denoted in grey. Reproduced with permission form Reference [35]. Copyright 2014 American Chemical Society.

The chemical composition of $Au_{25}(SR)_{18}$ was confirmed by electrospray-ionization mass spectrometry (ESI-MS) in 2005 by the Tsukuda group⁸ followed by the resolution of the crystal structure of the anionic form of the cluster, $[Au_{25}(2PET)_{18}]^-$, in 2008 by two groups independently.^{38, 39} Soon after the crystal structure of the charge-neutral $[Au_{25}(2PET)_{18}]^0$ species was reported.¹⁶

As depicted in **Figure 1.4**, [Au₂₅(2PET)₁₈]⁰ structure is built of a centred Au₁₃ icosahedral core composed of metallic Au atoms (i.e., kernel), and a protective thiolate ligand shell. At the core—shell interface, six dimeric staple units, [RS–Au–(R)S–Au–SR] are positioned symmetrically around the core (**Figure 1.4**-b). A total of eighteen thiolate ligands are distributed between two types of symmetry non-equivalent positions called inner and outer sites (**Figure 1.4**-c). Six ligands are connected to the two Au atoms of the staple that are denoted as outer positions. The remaining twelve ligands occupy the inner positions where they serve as bridges for two chemically different Au atoms: one from the surface of the icosahedral core and the second from the staple. The two ligand positions exhibit different reactivity in ligand-exchange reactions.^{40,41}

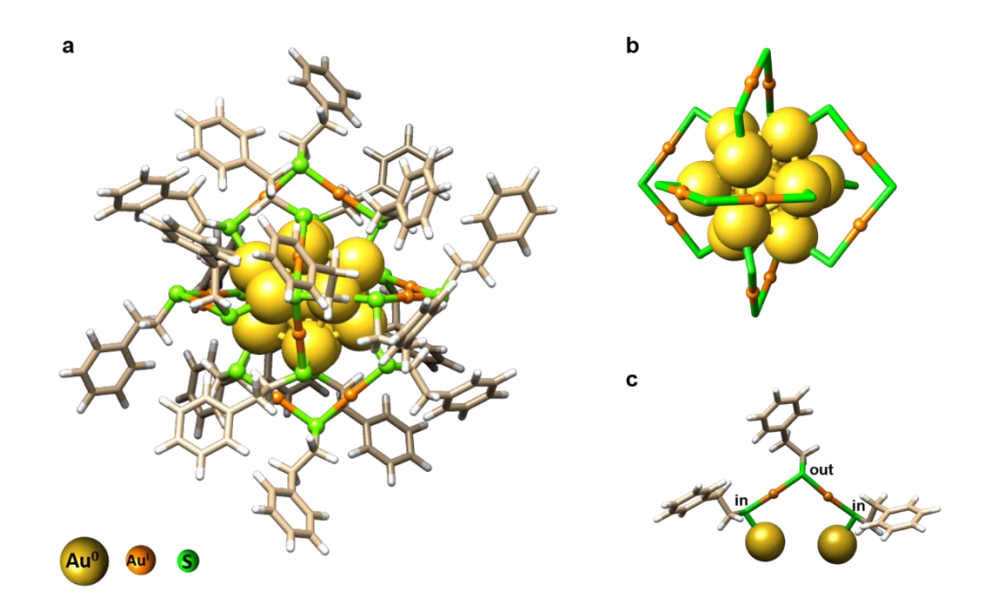


Figure 1.4 (a) The crystal structure of $[Au_{25}(2PET)_{18}]^0$. (b) Icosahedral Au_{13} core surrounded by six dimeric staple motifs. (c) Structure of the dimeric staple motif depicting two symmetry non-equivalent thiolate binding sites. Structure prepared using the crystal data published in Reference [16].

In general Au₂₅(SR)₁₈ clusters can exist in three stable oxidation states, $[Au_{25}(SR)_{18}]^q$, for which q = -1, 0 or +1. Their crystal structures display identical connectivity between the atoms, i.e., an icosahedral core composed of 13 gold atoms, enveloped with 6 dimeric staple units (**Figure 1.5**). The relation between their oxidation states, structure and magnetism were ascribed to first-order Jahn-Teller distortions.⁴²

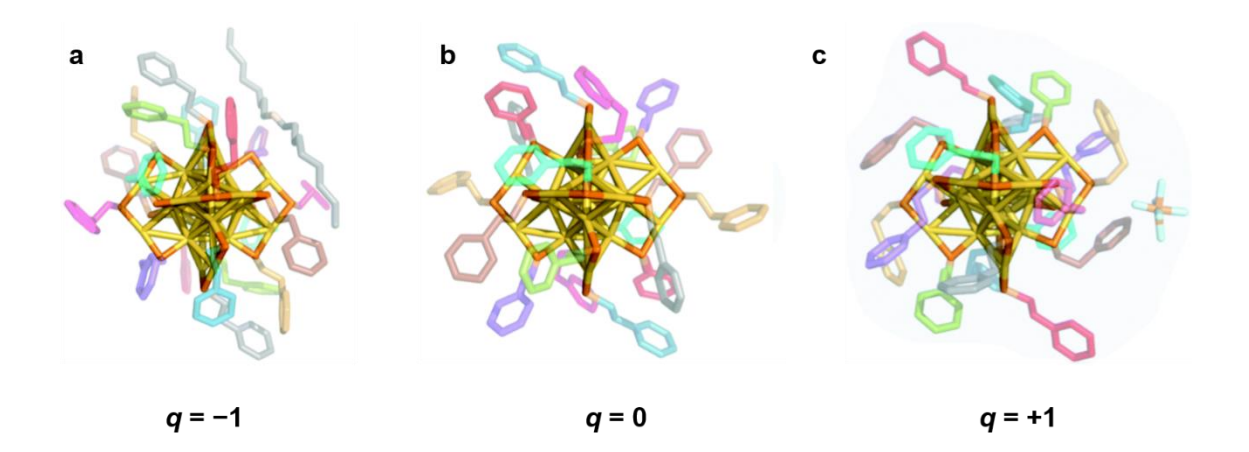


Figure 1.5 The crystal structures of $[Au_{25}(2PET)_{18}]^q$ in 3 different oxidation states: (a) -1; (b) 0; (c) +1. Colour code: Au-yellow, S-orange. Crystallographically independent 2PET ligands bear unique colours. Figure adapted from Reference [42]. Published by The Royal Society of Chemistry.

The $[Au_{25}(SR)_{18}]^{-1}$ cluster exhibits a closed-shell electron configuration $(1S^21P^6)$ and diamagnetism. The $[Au_{25}(SR)_{18}]^0$ species, having an $1S^21P^5$ superatom electron configuration, is paramagnetic with one unpaired electron in the 1P orbital. Because the 1P orbital is not-completely filled, it becomes

nondegenerate, which manifests as a more oblate cluster structure relative to its anionic counterpart. The $[Au_{25}(SR)_{18}]^{+1}$ cation, with an $1S^21P^4$ configuration shows even larger structural distortions than the anionic and charge neutral analogues. This cluster is also diamagnetic.

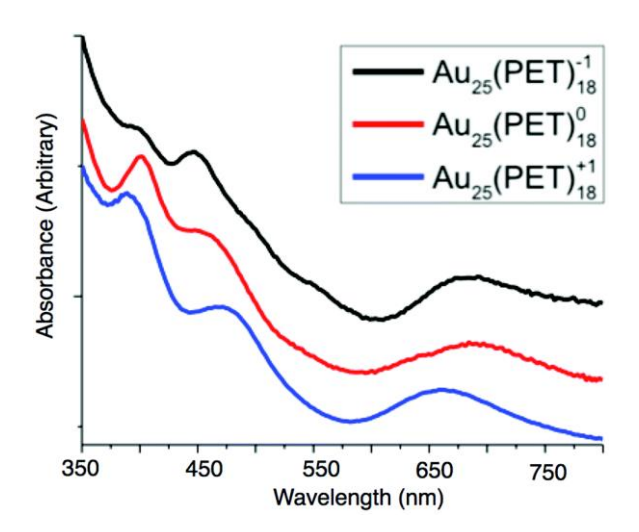


Figure 1.6 Electronic absorption spectra of $[Au_{25}(SR)_{18}]^q$ in three oxidation states: anionic (black), charge neutral (red) and cationic (blue). Figure reproduced from Reference [42]. Published by The Royal Society of Chemistry.

The electronic absorption spectra of $[Au_{25}(SR)_{18}]^q$ in three oxidation states (**Figure 1.6**) depict differences in their electronic structure.

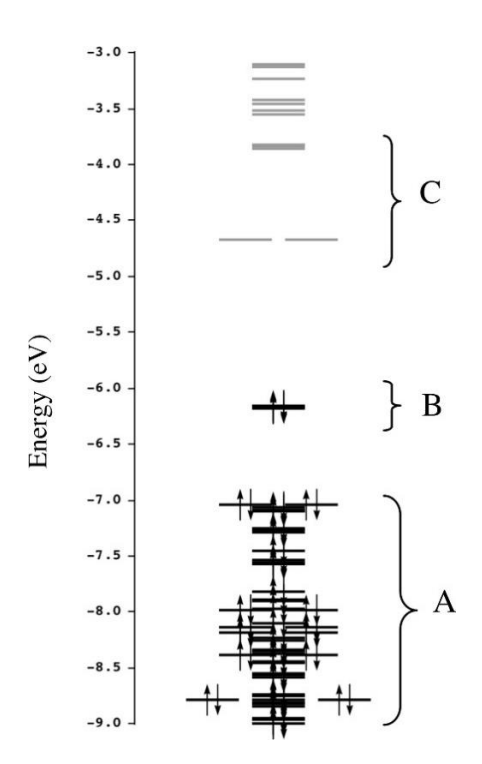


Figure 1.7 Orbital energy diagram for $[Au_2s(SH)_{18}]^-$. A: ligand band; occupied orbitals below the HOMO arising from $[Au_2(SH)_3]^-$ units. B: delocalized (superatom P) HOMO orbitals from the Au_{13}^{5+} core. C: delocalized unoccupied orbitals (superatom D) primarily from the Au_{13}^{5+} core with some mixing from $[Au_2(SH)_3]^-$ units. Reproduced with permission from Reference [14]. Copyright 2010 American Chemical Society.

Three absorption peaks are evident: the peak around 680 nm corresponds to a $1P \rightarrow 1D$ (HOMO \rightarrow LUMO) transition, the band between 450–470 nm to a $1P \rightarrow 1D$ (HOMO \rightarrow LUMO +1) transition. The higher energy transition (380–400 nm) is ascribed to a ligand \rightarrow D transition (see orbital energy diagram in **Figure 1.7**). The HOMO–LUMO energy gap was found to decrease with increasing oxidation of $[Au_{25}(SR)_{18}]^q$ cluster.

1.2 Thiolate-protected gold nanoclusters—highly versatile species amenable to tailoring

The modification of the structure and properties of Au NCs can be realized using various strategies that take advantage of their core—shell structure, which affords distinct active sites for interactions with a variety of different species: ligands, ions, other nanoclusters.⁴³ **Figure 1.8** schematically shows three distinct active site types on Au NCs that can be exploited for functionalisation and property tuning: core, interface and ligand.

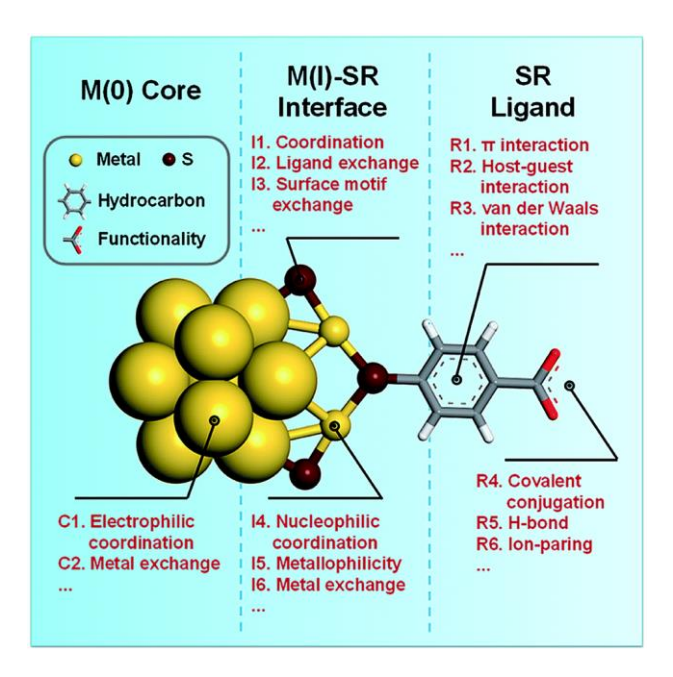


Figure 1.8 Schematic depiction of the metal nanoclusters active sites for their interactions with ions, molecules, or other nanoclusters. Reproduced from Reference [44]. Published by The Royal Society of Chemistry.

Core. The metallic kernel of Au NCs can exhibit various packing modes: icosahedral, ³⁹ decahedral, ^{9, 45} face-centred cubic (FCC), ^{46, 47} body-centred cubic (BCC), ^{48, 49} or hexagonal close packed (HCP). ⁵⁰ These structures affect the electronic properties of Au NCs but also offer varying types of coordination sites (of unsaturated Au⁰) that are accessible for chemical or physical adsorption. Usually, the Au core is electron-rich, due to the delocalization of the valence electrons, and hence exhibits an affinity towards species with high electronegativity. Additionally, the Au atoms in the core can be substituted with metal

heteroatoms, which has been shown to increase nanocluster stability and reactivity (new active sites for adsorption).⁵¹

Interface. The Au^I–SR staples in the Au–SR interface have two sites: Au^I atoms and S atoms of the thiolate ligands. The Au^I atoms are electron-deficient due to the electron withdrawing properties of the thiolate ligands. Therefore, these sites exhibit an affinity towards electropositive molecules. Evidently, these sites are also more accessible than the core Au⁰ atoms. As such, these positions have been shown as active sites for metallophillic Au^I···Au^I interactions⁵² and also metal-exchange reactions.^{34,53} Interestingly, the S atoms of the thiolate ligands are also known to be coordination sites for the molecules in catalytic reactions.⁵⁴ Overall, the interface provides the main reactive sites for ligand exchange reactions, which represent the primary method to modify the structure, size, surface chemistry and properties of Au NCs. 22, 43, 55, 56 Given the variety of structures and arrangement patterns of the staple motifs within the nanocluster interface, the sulfur atom active sites can differ in their chemical environment, which affects the preferential sites for the ligand exchange reaction. 41,57 For example, a study by the Ackerson group established that exchanging the initial ligands for the HS-Ph-p-Br in Au₁₀₂(p-MBA)₄₄ and [Au₂₅(2PET)₁₈] clusters was occurring on the solvent accessible inner positions (where one of the two Au atoms to which the S atom of the thiolate ligand connects is the core Au⁰ atom). In addition, specifically for the case of ligand exchange with $[Au_{25}(2PET)_{18}]^{-}$, the stabilizing $\pi - \pi$ interactions between the 2PET ligands and the incoming ligand led to preferential exchange of the inner position. In another example, a study by Pengo et al. revealed that the preferential exchange sites for ligands within the staple (inner vs outer positions) of $Au_{25}(2PET)_{18}$ clusters was highly dependent on the electronic structure of the incoming thiols.⁵⁸ Particularly, lower selectivity for the inner staple sites were demonstrated for aromatic thiols with an electron-donating substituent in the para-position. Furthermore, the relative affinity of the incoming thiols for binding to the Au surface in combination with the stability of the free thiols in solution were found to be key factors in the ligand exchange reactions as demonstrated by Salassa et al.⁵⁹

Overall ligand-exchange reactions have been established as widely used methods for tailoring the surface ligands of metal nanoclusters.^{56,57} The ligand-exchange process can either lead to (i) a partial or total substitution of the ligands in the shell with no induced alteration of the chemical formula of the parent nanocluster⁴¹ or (ii) a transformation of both structure and chemical formula in a process termed ligand-exchange-induced size/structure transformation (LEISST).²²

Next to a simple substitution of the ligands in the nanocluster, the exchange of all of the surface motifs can also occur with or without affecting the original structure of the nanocluster.⁶⁰⁻⁶²

Thiolate ligands. Given their position on the nanocluster extremity, the thiolate ligands play a major role in the surface and recognition chemistry of Au NCs. The rich diversity of the thiolate ligand carbon

tails in terms of their size, structure and function lend themselves to an array of tuneable covalent and noncovalent interactions.

Covalent bonds are exploited to introduce extra functionality into the Au NCs. A common strategy involves an amination reaction between the water soluble Au NCs (with ligands containing carboxylic groups) and 1-ethyl-3-(3-dimethylaminopropyl)carbodiimide (EDC).^{63, 64}

Thiolate-ligand-based noncovalent interactions can also be utilized for surface modification and self-assembly processes. The carboxyl (–COOH), amine (–NH₂) and hydroxyl (–OH) groups present within the structure of thiolate ligands were shown to influence the solvation, crystallization and self-assembly behaviours of water-soluble Au NCs via the formation of H–bonding. Deprotonated carboxyl groups (–COO $^-$) become available for electrostatic interactions, like e.g., ion-pairing with cationic surfactants CTA $^+$ (CTA = cetyltrimethylammonium). For Au NCs soluble in the organic phase, it is the π interactions (i.e., π – π and CH– π interactions) and van der Waals forces that dictate their surface chemistry and self-assembly into hierarchical structures.

Host–guest interactions belong to an important class of supramolecular interactions and are essential in fields of molecular recognition and self-assembly. These types of interactions can also be instituted on the nanocluster surface. This strategy has allowed larger structures like cyclodextrins, fullerenes or MOFs to be anchored to the Au NCs. ⁶⁷⁻⁶⁹

1.3 References

- 1. Du, Y.; Sheng, H.; Astruc, D.; Zhu, M., Atomically Precise Noble Metal Nanoclusters as Efficient Catalysts: A Bridge between Structure and Properties. *Chemical Reviews* **2020**, *120* (2), 526-622.
- 2. Jin, R.; Zeng, C.; Zhou, M.; Chen, Y., Atomically Precise Colloidal Metal Nanoclusters and Nanoparticles: Fundamentals and Opportunities. *Chemical Reviews* **2016**, *116* (18), 10346-10413.
- 3. Zhou, M.; Jin, R., Optical Properties and Excited-State Dynamics of Atomically Precise Gold Nanoclusters. *Annual Review of Physical Chemistry* **2021**, *72* (1), 121-142.
- 4. Brust, M.; Walker, M.; Bethell, D.; Schiffrin, D. J.; Whyman, R., Synthesis of Thiol-Derivatised Gold Nanoparticles in a Two-Phase Liquid-Liquid System. *Journal of the Chemical Society, Chemical Communications* **1994**, (7), 801-802.
- Terrill, R. H.; Postlethwaite, T. A.; Chen, C.-h.; Poon, C.-D.; Terzis, A.; Chen, A.; Hutchison, J. E.; Clark, M. R.; Wignall, G., Monolayers in Three Dimensions: NMR, SAXS, Thermal, and Electron Hopping Studies of Alkanethiol Stabilized Gold Clusters. *Journal of the American Chemical Society* 1995, 117 (50), 12537-12548.
- 6. Jimenez, V. L.; Leopold, M. C.; Mazzitelli, C.; Jorgenson, J. W.; Murray, R. W., HPLC of Monolayer-Protected Gold Nanoclusters. *Analytical Chemistry* **2003**, *75* (2), 199-206.
- 7. Knoppe, S.; Boudon, J.; Dolamic, I.; Dass, A.; Bürgi, T., Size Exclusion Chromatography for Semipreparative Scale Separation of Au₃₈(SR)₂₄ and Au₄₀(SR)₂₄ and Larger Clusters. *Analytical Chemistry* **2011**, *83* (13), 5056-5061.

- 8. Negishi, Y.; Nobusada, K.; Tsukuda, T., Glutathione-Protected Gold Clusters Revisited: Bridging the Gap between Gold(I)—Thiolate Complexes and Thiolate-Protected Gold Nanocrystals. *Journal of the American Chemical Society* **2005**, *127* (14), 5261-5270.
- 9. Jadzinsky, P. D.; Calero, G.; Ackerson, C. J.; Bushnell, D. A.; Kornberg, R. D., Structure of a Thiol Monolayer-Protected Gold Nanoparticle at 1.1 Å Resolution. *Science* **2007**, *318* (5849), 430-433.
- 10. Liao, L.; Wang, C.; Zhuang, S.; Yan, N.; Zhao, Y.; Yang, Y.; Li, J.; Deng, H.; Wu, Z., An Unprecedented Kernel Growth Mode and Layer-Number-Odevity-Dependent Properties in Gold Nanoclusters. *Angewandte Chemie International Edition* **2020**, *59* (2), 731-734.
- 11. Dong, H.; Liao, L.; Wu, Z., Two-Way Transformation Between fcc- and Non fcc-Structured Gold Nanoclusters. *The Journal of Physical Chemistry Letters* **2017**, 8 (21), 5338-5343.
- 12. Yan, N.; Xia, N.; Liao, L.; Zhu, M.; Jin, F.; Jin, R.; Wu, Z., Unraveling the Long-Pursued Au₁₄₄ Structure by X-ray Crystallography. *Science Advances* **2018**, *4* (10), eaat7259.
- 13. Zhuang, S.; Liao, L.; Yuan, J.; Wang, C.; Zhao, Y.; Xia, N.; Gan, Z.; Gu, W.; Li, J.; Deng, H.; Yang, J.; Wu, Z., Kernel Homology in Gold Nanoclusters. *Angewandte Chemie International Edition* **2018**, *57* (47), 15450-15454.
- 14. Aikens, C. M., Electronic Structure of Ligand-Passivated Gold and Silver Nanoclusters. *The Journal of Physical Chemistry Letters* **2011**, 2 (2), 99-104.
- 15. Tian, S.; Li, Y.-Z.; Li, M.-B.; Yuan, J.; Yang, J.; Wu, Z.; Jin, R., Structural Isomerism in Gold Nanoparticles Revealed by X-ray Crystallography. *Nature Communications* **2015**, *6* (1), 8667.
- 16. Zhu, M. Z.; Eckenhoff, W. T.; Pintauer, T.; Jin, R., Conversion of Anionic [Au₂₅(SCH₂CH₂Ph)₁₈]⁻ Cluster to Charge Neutral Cluster via Air Oxidation. *The Journal of Physical Chemistry C* **2008**, *112* (37), 14221-14224.
- 17. Grönbeck, H.; Häkkinen, H., Polymerization at the Alkylthiolate–Au(111) Interface. *The Journal of Physical Chemistry B* **2007**, *111* (13), 3325-3327.
- 18. Li, Y.; Higaki, T.; Du, X.; Jin, R., Chirality and Surface Bonding Correlation in Atomically Precise Metal Nanoclusters. *Advanced Materials* **2020**, 1905488.
- 19. Walter, M.; Akola, J.; Lopez-Acevedo, O.; Jadzinsky, P. D.; Calero, G.; Ackerson, C. J.; Whetten, R. L.; Grönbeck, H.; Häkkinen, H., A Unified View of Ligand-Protected Gold Clusters as Superatom Complexes. *Proceedings of the National Academy of Sciences* **2008**, *105* (27), 9157-9162.
- 20. Zeng, C.; Liu, C.; Chen, Y.; Rosi, N. L.; Jin, R., Gold–Thiolate Ring as a Protecting Motif in the Au₂₀(SR)₁₆ Nanocluster and Implications. *Journal of the American Chemical Society* **2014**, *136* (34), 11922-11925.
- 21. Das, A.; Liu, C.; Zeng, C.; Li, G.; Li, T.; Rosi, N. L.; Jin, R., Cyclopentanethiolato-Protected Au₃₆(SC₅H₉)₂₄ Nanocluster: Crystal Structure and Implications for the Steric and Electronic Effects of Ligand. *The Journal of Physical Chemistry A* **2014**, *118* (37), 8264-8269.
- 22. Zeng, C.; Chen, Y.; Das, A.; Jin, R., Transformation Chemistry of Gold Nanoclusters: From One Stable Size to Another. *The Journal of Physical Chemistry Letters* **2015**, *6* (15), 2976-2986.
- Gan, Z.; Chen, J.; Wang, J.; Wang, C.; Li, M.-B.; Yao, C.; Zhuang, S.; Xu, A.; Li, L.; Wu, Z., The Fourth Crystallographic Closest Packing Unveiled in The Gold Nanocluster Crystal. *Nature Communications* 2017, 8 (1), 14739.
- 24. Nieto-Ortega, B.; Bürgi, T., Vibrational Properties of Thiolate-Protected Gold Nanoclusters. *Accounts of Chemical Research* **2018**, *51* (11), 2811-2819.

- Yoon, B.; Luedtke, W. D.; Barnett, R. N.; Gao, J.; Desireddy, A.; Conn, B. E.; Bigioni, T.; Landman, U., Hydrogen-Bonded Structure and Mechanical Chiral Response of a Silver Nanoparticle Superlattice. *Nature Materials* 2014, 13 (8), 807-811.
- 26. Chevrier, D. M.; Raich, L.; Rovira, C.; Das, A.; Luo, Z.; Yao, Q.; Chatt, A.; Xie, J.; Jin, R.; Akola, J.; Zhang, P., Molecular-Scale Ligand Effects in Small Gold–Thiolate Nanoclusters. *Journal of the American Chemical Society* **2018**, *140* (45), 15430-15436.
- 27. Häkkinen, H.; Walter, M.; Grönbeck, H., Divide and Protect: Capping Gold Nanoclusters with Molecular Gold–Thiolate Rings. *The Journal of Physical Chemistry B* **2006**, *110* (20), 9927-9931.
- 28. Taylor, M. G.; Mpourmpakis, G., Thermodynamic Stability of Ligand-Protected Metal Nanoclusters. *Nature Communications* **2017**, *8*, 15988.
- 29. Zeng, Ch.; Qian, H.; Li, T.; Li, G.; Rosi, N. L.; Yoon, B.; Barnett, R. N.; Whetten, R. L.; Landman, U.; Jin, R., New Insight into the Electronic Shell of Au₃₈(SR)₂₄: a Superatomic Molecule. *Nanoscale* **2013**, *5* (4), 1475-1478.
- 30. Song, Y.; Zhong, J.; Yang, S.; Wang, S.; Cao, T.; Zhang, J.; Li, P.; Hu, D.; Pei, Y.; Zhu, M., Crystal Structure of Au₂₅(SePh)₁₈ Nanoclusters and Insights into Their Electronic, Optical and Catalytic Properties. *Nanoscale* **2014**, *6* (22), 13977-13985.
- 31. Parker, J. F.; Fields-Zinna, C. A.; Murray, R. W., The Story of a Monodisperse Gold Nanoparticle: Au₂₅L₁₈. *Accounts of Chemical Research* **2010**, *43* (9), 1289-1296.
- 32. Kang, X.; Chong, H.; Zhu, M., Au₂₅(SR)₁₈: the Captain of the Great Nanocluster Ship. *Nanoscale* **2018**, *10* (23), 10758-10834.
- 33. Antonello, S.; Dainese, T.; Maran, F., Exploring Collective Substituent Effects: Dependence of the Lifetime of Charged States of Au₂₅(SC_nH_{2n+1})₁₈ Nanoclusters on the Length of the Thiolate Ligands. *Electroanalysis* **2016**, 28 (11), 2771-2776.
- 34. Fei, W.; Antonello, S.; Dainese, T.; Dolmella, A.; Lahtinen, M.; Rissanen, K.; Venzo, A.; Maran, F., Metal Doping of Au₂₅(SR)₁₈⁻ Clusters: Insights and Hindsights. *Journal of the American Chemical Society* **2019**, *141* (40), 16033-16045.
- 35. Luo, Z.; Nachammai, V.; Zhang, B.; Yan, N.; Leong, D. T.; Jiang, D.-e.; Xie, J., Toward Understanding the Growth Mechanism: Tracing All Stable Intermediate Species from Reduction of Au(I)–Thiolate Complexes to Evolution of Au₂₅ Nanoclusters. *Journal of the American Chemical Society* **2014**, *136* (30), 10577-10580.
- 36. Qian, H.; Zhu, Y.; Jin, R., Size-Focusing Synthesis, Optical and Electrochemical Properties of Monodisperse Au₃₈(SC₂H₄Ph)₂₄ Nanoclusters. *ACS Nano* **2009**, *3* (11), 3795-3803.
- 37. Nimmala, P. R.; Jupally, V. R.; Dass, A., Core Size Conversion: Route for Exclusive Synthesis of Au₃₈ or Au₄₀ Nanomolecules. *Langmuir* **2014**, *30* (9), 2490-2497.
- 38. Heaven, M. W.; Dass, A.; White, P. S.; Holt, K. M.; Murray, R. W., Crystal Structure of the Gold Nanoparticle [N(C₈H₁₇)₄][Au₂₅(SCH₂CH₂Ph)₁₈]. *Journal of the American Chemical Society* **2008**, *130* (12), 3754-3755.
- 39. Zhu, M.; Aikens, C. M.; Hollander, F. J.; Schatz, G. C.; Jin, R., Correlating the Crystal Structure of a Thiol-Protected Au₂₅ Cluster and Optical Properties. *Journal of the American Chemical Society* **2008**, *130* (18), 5883-5885.
- 40. Wu, Z.; Jin, R., Stability of the Two Au–S Binding Modes in Au₂₅(SG)₁₈ Nanoclusters Probed by NMR and Optical Spectroscopy. *ACS Nano* **2009**, *3* (7), 2036-2042.
- 41. Ni, T. W.; Tofanelli, M. A.; Phillips, B. D.; Ackerson, C. J., Structural Basis for Ligand Exchange on Au₂₅(SR)₁₈. *Inorganic Chemistry* **2014**, *53* (13), 6500-6502.

- 42. Tofanelli, M. A.; Salorinne, K.; Ni, T. W.; Malola, S.; Newell, B.; Phillips, B.; Häkkinen, H.; Ackerson, C. J., Jahn–Teller Effects in Au₂₅(SR)₁₈. *Chemical Science* **2016**, *7* (3), 1882-1890.
- 43. Yao, Q.; Yuan, X.; Chen, T.; Leong, D. T.; Xie, J., Engineering Functional Metal Materials at the Atomic Level. *Advanced Materials* **2018**, *30* (47), 1802751.
- 44. Yao, Q.; Wu, Z.; Liu, Z.; Lin, Y.; Yuan, X.; Xie, J., Molecular Reactivity of Thiolate-Protected Noble Metal Nanoclusters: Synthesis, Self-Assembly, and Applications. *Chemical Science* **2021**, *12* (1), 99-127.
- 45. Zeng, C.; Chen, Y.; Kirschbaum, K.; Lambright, K. J.; Jin, R., Emergence of Hierarchical Structural Complexities in Nanoparticles and Their Assembly. *Science* **2016**, *354* (6319), 1580.
- 46. Omoda, T.; Takano, S.; Yamazoe, S.; Koyasu, K.; Negishi, Y.; Tsukuda, T., An Au₂₅(SR)₁₈ Cluster with a Face-Centered Cubic Core. *The Journal of Physical Chemistry C* **2018**, *122* (24), 13199-13204.
- 47. Zhuang, S.; Liao, L.; Li, M.-B.; Yao, C.; Zhao, Y.; Dong, H.; Li, J.; Deng, H.; Li, L.; Wu, Z., The fcc structure isomerization in gold nanoclusters. *Nanoscale* **2017**, *9* (39), 14809-14813.
- 48. Higaki, T.; Zeng, C.; Chen, Y.; Hussain, E.; Jin, R., Controlling the Crystalline Phases (FCC, HCP and BCC) of Thiolate-Protected Gold Nanoclusters by Ligand-Based Strategies. *CrystEngComm* **2016**, *18* (37), 6979-6986.
- 49. Yang, R.; Morris, D. J. Higaki, T.; Ward, M. J.; Jin, R.; Zhang, P., New Insights on the Bonding Properties of BCC-like Au₃₈S₂(SR)₂₀ Nanoclusters from X-ray Absorption Spectroscopy. *The Journal of Physical Chemistry C* **2018**, *122* (39), 22776-22782.
- 50. Morris, D. J.; Yang, R.; Higaki, T.; Ward, M. J.; Jin, R.; Zhang, P., Core Geometry Effect on the Bonding Properties of Gold–Thiolate Nanoclusters: The Case of Hexagonal-Close-Packed Au₃₀(SR)₁₈. *The Journal of Physical Chemistry C* **2018**, *122* (41), 23414-23419.
- 51. Bootharaju, M. S.; Sinatra, L.; Bakr, O. M., Distinct Metal-Exchange Pathways of Doped Ag₂₅ Nanoclusters. *Nanoscale* **2016**, *8* (39), 17333-17339.
- 52. De Nardi, M.; Antonello, S.; Jiang, D.-e.; Pan, F.; Rissanen, K.; Ruzzi, M.; Venzo, A.; Zoleo, A.; Maran, F., Gold Nanowired: A Linear (Au₂₅)_n Polymer from Au₂₅ Molecular Clusters. *ACS Nano* **2014**, *8* (8), 8505-8512.
- 53. Liao, L.; Zhou, S.; Dai, Y.;Liu, L.; Yao, C.; Fu, C.; Yang, J.; Wu, Z., Mono-Mercury Doping of Au₂₅ and the HOMO/LUMO Energies Evaluation Employing Differential Pulse Voltammetry. *Journal of the American Chemical Society* **2015**, *137* (30), 9511-9514.
- 54. Kauffman, D. R.; Alfonso, D.; Matranga, C.; Ohodnicki, P.; Deng, X.; Siva, R. C.; Zeng, C.; Jin, R., Probing Active Site Chemistry with Differently Charged Au₂₅^q Nanoclusters (q = -1, 0, +1). *Chemical Science* **2014**, 5 (8), 3151-3157.
- 55. Krishnadas, K. R.; Natarajan, G.; Baksi, A.; Ghosh, A.; Khatun, E.; Pradeep, T., Metal–Ligand Interface in the Chemical Reactions of Ligand-Protected Noble Metal Clusters. *Langmuir* **2019**, *35* (35), 11243-11254.
- 56. Wang, Y.; Bürgi, T., Ligand Exchange Reactions on Thiolate-Protected Gold Nanoclusters. *Nanoscale Advances* **2021**, *3* (10), 2710-2727.
- 57. Heinecke, C. L.; Ni, T. W.; Malola, S.; Mäkinen, V.; Wong, O. A.; Häkkinen, H.; Ackerson, C. J., Structural and Theoretical Basis for Ligand Exchange on Thiolate Monolayer Protected Gold Nanoclusters. *Journal of the American Chemical Society* **2012**, *134* (32), 13316-13322.
- 58. Pengo, P.; Bazzo, C.; Boccalon, M.; Pasquato, L., Differential Reactivity of the Inner and Outer Positions of Au₂₅(SCH₂CH₂Ph)₁₈ Dimeric Staples Under Place Exchange Conditions. *Chemical Communications* **2015**, 51 (15), 3204-3207.

- 59. Salassa, G.; Sels, A.; Mancin, F.; Bürgi, T., Dynamic Nature of Thiolate Monolayer in Au₂₅(SR)₁₈ Nanoclusters. *ACS Nano* **2017**, *11* (12), 12609-12614.
- 60. Song, Y.; Huang, T.; Murray, R. W., Heterophase Ligand Exchange and Metal Transfer between Monolayer Protected Clusters. *Journal of the American Chemical Society* **2003**, *125* (38), 11694-11701.
- 61. Yao, Q.; Feng, Y.; Fung, V.; Yu, Y.; Jiang, D.-e.; Yang, J.; Xie, J., Precise Control of Alloying Sites of Bimetallic Nanoclusters via Surface Motif Exchange Reaction. *Nature Communications* **2017**, *8* (1), 1555.
- 62. Yao, Q.; Fung, V.; Sun, C.; Huang, S.; Chen, T.; Jiang, D.-e.; Lee, J. Y.; Xie, J., Revealing Isoelectronic Size Conversion Dynamics of Metal Nanoclusters by a Noncrystallization Approach. *Nature Communications* **2018**, *9* (1), 1979.
- 63. Pyo, K.; Thanthirige, V. D.; Kwak, K.; Pandurangan, P.; Ramakrishna, G.; Lee, D., Ultrabright Luminescence from Gold Nanoclusters: Rigidifying the Au(I)–Thiolate Shell. *Journal of the American Chemical Society* **2015**, *137* (25), 8244-8250.
- 64. Lin, C. A. J.; Yang, T. Y.; Lee, C. H.; Huang, S. H.; Sperling, R. A.; Zanella, M.; Li, J. K.; Shen, J. L.; Wang, H. H.; Yeh, H. I.; Parak, W. J.; Chang, W. H., Synthesis, Characterization, and Bioconjugation of Fluorescent Gold Nanoclusters Toward Biological Labeling Applications. *ACS Nano* **2009**, *3* (2), 395-401.
- 65. Nonappa; Ikkala, O., Hydrogen Bonding Directed Colloidal Self-Assembly of Nanoparticles into 2D Crystals, Capsids, and Supracolloidal Assemblies. *Advanced Functional Materials* **2018**, 28 (27), 1704328.
- 66. Yao, Q.; Yuan, X.; Yu, Y.; Yu, Y.; Xie, J.; Lee, J. Y., Introducing Amphiphilicity to Noble Metal Nanoclusters via Phase-Transfer Driven Ion-Pairing Reaction. *Journal of the American Chemical Society* **2015**, *137* (5), 2128-2136.
- 67. Mathew, A.; Natarajan, G.; Lehtovaara, L.; Häkkinen, H.; Kumar, R. M.; Subramanian, V.; Jaleel, A.; Pradeep, T., Supramolecular Functionalization and Concomitant Enhancement in Properties of Au₂₅ Clusters. *ACS Nano* **2014**, *8* (1), 139-152.
- 68. Chakraborty, P.; Nag, A.; Mondal, B.; Khatun, E.; Paramasivam, G.; Pradeep, T., Fullerene-Mediated Aggregation of M₂₅(SR)₁₈⁻ (M = Ag, Au) Nanoclusters. *The Journal of Physical Chemistry C* **2020**, *124* (27), 14891-14900.
- 69. Zhao, Y.; Zhuang, S.; Liao, L.; Wang, C.; Xia, N.; Gan, Z.; Gu, W.; Li, J.; Deng, H.; Wu, Z., A Dual Purpose Strategy to Endow Gold Nanoclusters With Both Catalysis Activity and Water Solubility. *Journal of the American Chemical Society* **2020**, *142* (2), 973-977.

Chapter 2

Metal nanoclusters as versatile building blocks for hierarchical structures

2.1 Introduction

In this Chapter, different approaches to realize the NCs assemblies and the underlying forces that drive the assembly are discussed. Changes in the physicochemical properties as well as the emergence of new functions upon superstructure formation are also described.

2.2 Discrete multimers of metal nanoclusters

The step toward obtaining the highly ordered superstructures based on nanocluster units is the formation of discrete oligomers (dimers, trimers, etc.). It is expected that coupling of nanoclusters into stable dimers via organic linkers will induce significant changes in both optical and electronic properties. These properties depend greatly on the bridging organic linker that is used. The idea to employ Au NCs to form extended systems was first explored by Akola et al. using DFT methods. Their study focused on modelling of discrete dimeric species constructed with anionic Au₂₅(SR)₁₈ nanoclusters covalently linked by a benzene-1,4-dithiol (BDT) molecule. (**Figure 2.1**). The optimized structure of the Au₂₅–BDT–Au₂₅ dimer showed an overall linear geometry. Furthermore, the analysis has found that Au₂₅ units in the dimer preserve their individual electron shell structures after linking with the dithiol ligand, even when the clusters were doped with magnetic (Mn) or nonmagnetic (Pd) metal atoms. The calculations of HOMO–LUMO gaps for Au₂₅(SMe)₁₈ and Au₂₅–BDT–Au₂₅ species in the gas-phase were almost identical (1.24 and 1.25 eV, respectively). Additionally, the density of states was higher for the

dimers, as a result of individual contributions of two Au_{25} units. The study by Akola unearthed the potential of using Au NCs as building blocks for functional materials given that suitable methods for their linking can be found.

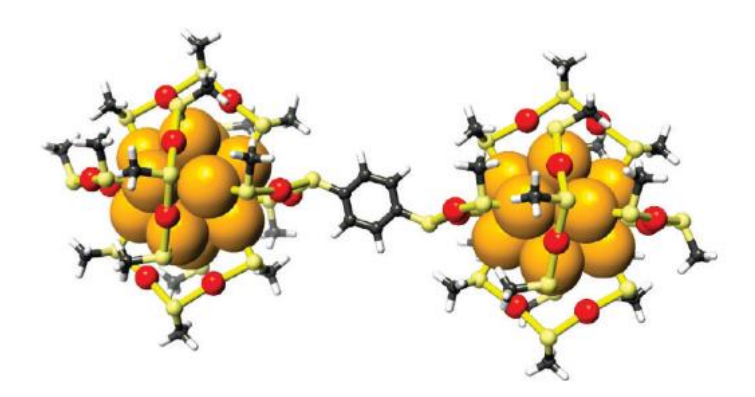


Figure 2.1 Structure of the relaxed $[Au_{25}(SCH_3)_{17}-BDT-(SCH_3)_{17}Au_{25}]^{2-}$ dimer. Colour code: Au^0 -orange, Au^I -yellow, S-red, C-black, H-white. Reproduced with permission from Reference [1]. Copyright 2010 American Chemical Society.

Creating the superstructures from metal NCs whilst still preserving the structure of individual building blocks poses a great challenge. In this regard, ligand exchange reaction utilizing appropriate dithiol linking molecules, which favour intercluster binding, is one of the most successful strategies yielding the desired assembly. Furthermore, using organic linker gives a possibility to introduce an extra functionality. Hitherto, Au₂₅(SR)₁₈, Ag₂₅(SR)₁₈, Au₁₀₂(SR)₄₄ and Au_{~250}(SR)_{~80} clusters were employed as assembly units for larger oligomeric structures.

2.2.1 Covalently linked nanoclusters

In this Section the synthetic chemistry approaches allowing the selective functionalization and formation of covalently linked NC multimers will be presented.

The first experimental demonstration of formation of dimeric (and higher order) Au NC-species linked with dithiol molecules was reported by Lahtinen et al.² In their study large clusters, i.e., Au₁₀₂(SR)₄₄ and Au₋₂₅₀(SR)₋₈₀ (SR = *para*-mercaptobenzoic acid, *p*-MBA) were bound with biphenyl-4,4'-dithiol (BPDT) molecules during the ligand-exchange reaction. Transmission electron microscopy (TEM) analysis coupled with the molecular dynamics (MD) simulations, showed that the cluster linking occurred via disulfide bridges formed between two BPDT bridging molecules (**Figure 2.2**A-E). Given that the Au NC ligand shells contained partially deprotonated *p*-MBA ligands, the electrostatic repulsion between the adjacent clusters (more pronounced in larger Au₂₅₀ clusters) favoured linking through longer bridging molecules. This finding was later corroborated by electron energy-loss spectroscopy in a scanning transmission electron microscopy (EELS-STEM).³ The obtained dimeric assemblies of Au₁₀₂ displayed no optical coupling, however the larger multimers of Au₂₅₀ exhibited hybridized plasmon

modes with red shifts of absorption maxima (ascribed to electron tunnelling through the molecular states of the disulfide bridges) (**Figure 2.2**F-G).

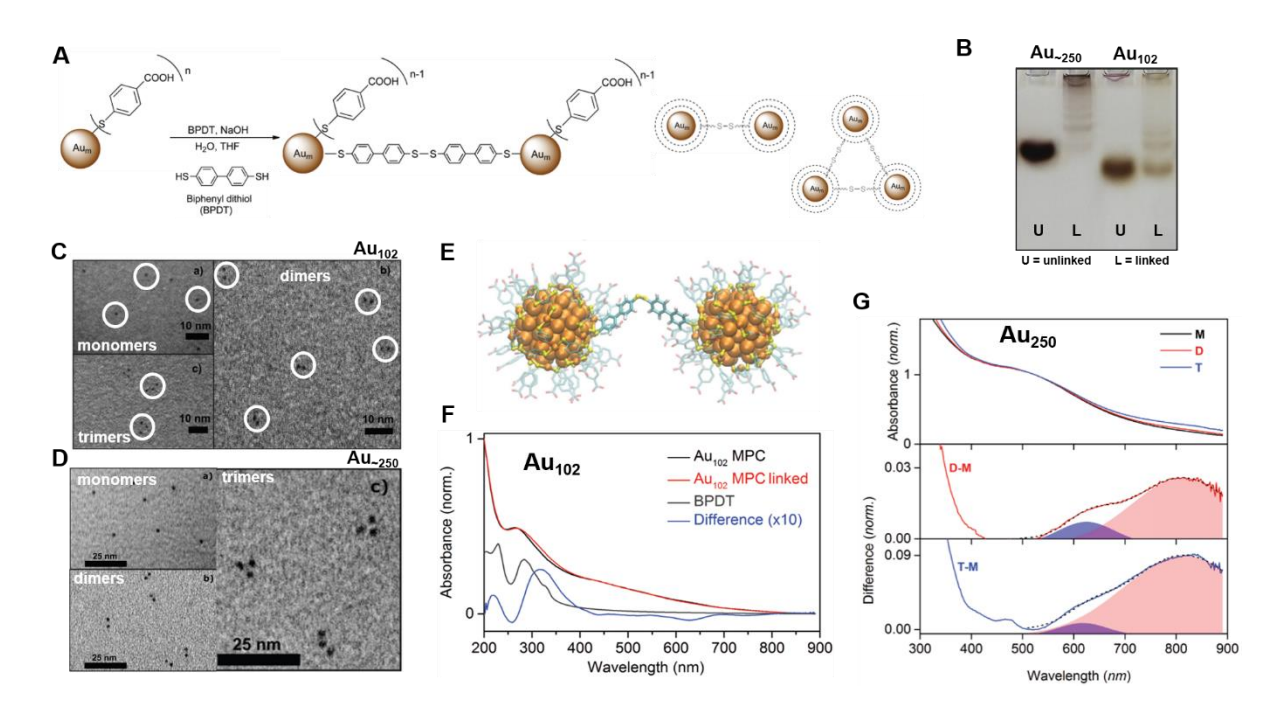


Figure 2.2 (A) Schematic representation of the multimer formation in the ligand-exchange reaction; (B) PAGE separation bands of linked Au-250 and Au₁₀₂ clusters compared with unlinked clusters; TEM images of PAGE isolated monomers, dimers and trimers of (C) Au₁₀₂ and (D) Au-250 clusters; (E) MD simulated structure of fully-deprotonated Au₁₀₂–(BPDT)₂–Au₁₀₂ in H₂O; Normalized UV-vis spectra of (F) unlinked Au₁₀₂ (black trace), BDPT-linked Au₁₀₂ (crude mix, red trace) in H₂O are juxtaposed with the arbitrarily scaled spectrum of the free BDPT linker (grey) and the difference spectrum (scaled by factor of 10) of unlinked and linked Au₁₀₂ spectra (blue trace); (G) PAGE isolated monomers (M, black trace), dimers (D, red trace) and trimers (T, blue trace). The lower panels depict the difference spectra of dimers and monomers, and trimers and monomers. The shaded areas are the Gaussian components of the deconvoluted data. Figure adapted with permission from Reference [2]. Copyright 2016 The Royal Society of Chemistry.

In their report, Sels et al.⁴ described the formation of multimeric Au₂₅ species covalently bound with three linear dithiol molecules (**Figure 2.3**A). The effectiveness of the multimer formation was affected by both the length of the dithiol linker and the type of ligands in the protective shell. Specifically, the short benzene-1,4-dithiol (**1**) was shown to interconnect the Au₂₅(SBu)₁₈ (SBu = 1-butanethiolate) but not the Au₂₅(PET)₁₈ (PET = 2-phenylethanethiolate) clusters due to the steric hindrance imposed by the 2-phenylethanethiolate ligand shell. The resulted mixture of multimers was separated on a size-exclusion chromatography (SEC) column. The isolated fractions were subjected to small angle X-ray scattering (SAXS) analysis and found to contain dimers and trimers as well as large assemblies of 10–20 Au NCs (**Figure 2.3**B-C). The electronic absorption spectra of the formed assemblies revealed that small multimers (dimers and trimers) largely retain the spectral characteristics of monomeric Au₂₅ clusters (red and blue trace in **Figure 2.3**D). On the contrary, for the large aggregates these features disappeared and instead a new band in the near-IR region (840 nm) developed, which was assigned to electronic coupling between Au₂₅ NC via the dithiol bridge. The emergence of this band was observed only for the larger aggregates when connected via conjugated linkers (benzene-1,4-dithiol (1) and *p*-terphenyl-4,4"-dithiol

(2); **Figure 2.3**E). Moreover, upon addition of free thiols to the solution containing large aggregates, the 840 nm band started to blue-shift and the characteristic spectral features of Au₂₅ started to reappear (**Figure 2.3**F). This behaviour was ascribed to the "unlinking" reaction during which the degree of interconnection between the clusters was reduced. Therefore, not only the type of the ligand but also its concentration was shown to play a crucial role in forming covalent Au₂₅ assemblies and greatly affected their size and optical properties.

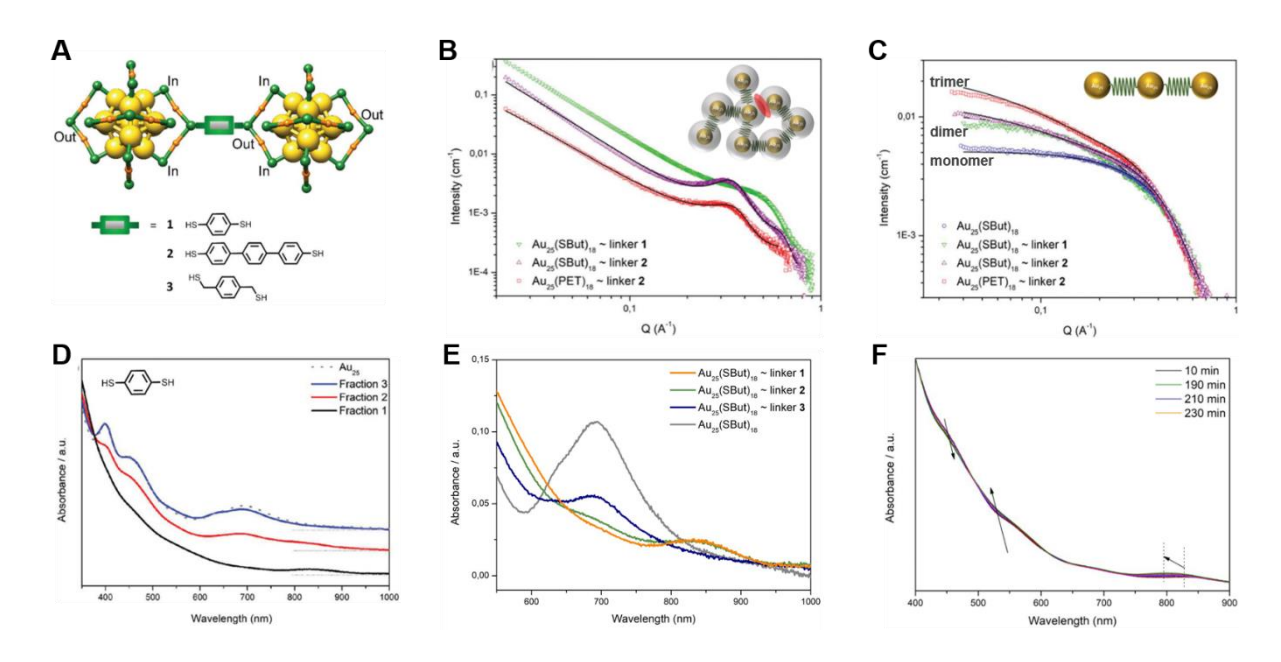


Figure 2.3 (A) Schematic representation of $Au_{25}(SR)_{18}$ dimers linked by various dithiol ligands 1-3. Protective monothiolate ligands omitted for clarity, colour code: Au^0 -yellow, Au^l -orange, S-green; SAXS spectra of (B) large-size SEC isolated species obtained for different Au_{25} clusters linked with conjugated dithiols 1 and 2, and (C) small-size SEC fractions containing monomers, dimers and trimers. Electronic absorption spectra of (D) SEC isolated large aggregates (black trace), dimers and trimers (red trace) and unreacted Au_{25} clusters (blue trace); (E) large multimers obtained by using various linkers 1-3; (F) UV-vis monitoring of the unlinking reaction of the dimers-trimers mixture upon introduction of free Bu-SH ligand. Figure adapted with permission from Reference [4]. Copyright 2017 The Royal Society of Chemistry.

In their work, Ho-Wu et al. investigated the influence a bridging linker can have on linear and non-linear optical properties of Au NC oligomers. Water-soluble anionic $[Au_{25}(SG)_{18}]^-(SG = glutathione)$ clusters were covalently linked with 4,4-thiodibenzenethiol (TBT) in the ligand-exchange reaction to produce a mixture of oligomers which were then separated using gel electrophoresis (PAGE) technique (**Figure 2.4**A-B). The systematic spectroscopic investigation of the formed multimers showed significant changes in their linear and non-linear properties when compared to the single $[Au_{25}(SG)_{18}]^-$ clusters. Importantly, the spectrum of dimeric species displayed the characteristic features attributed to Au_{25}^- clusters. For trimers and higher species, the spectral bands were less defined. The further analysis of optical spectra of Au_{25}^- TBT- Au_{25} dimers (blue trace in **Figure 2.4**C) shows widening of the ~450 nm absorption band which was ascribed to the higher density of states (DOS) than in monomeric Au_{25}^- clusters. The disappearance of a distinctive 670 nm peak was explained by the broadening and bathochromic shift of the 553 nm peak. Further, almost featureless absorption spectra of trimers and

multimers (pink and yellow traces in **Figure 2.4**C) were reasoned with even higher DOS exhibited in these species.

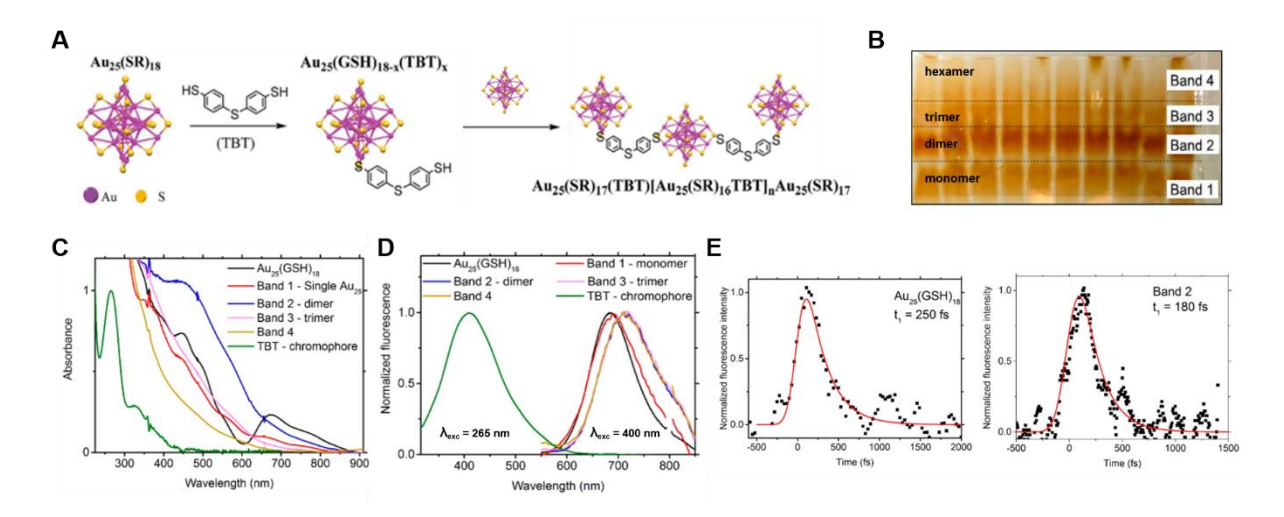


Figure 2.4 (A) Schematic representation of the formation of Au₂₅ oligomers linked with a chromophore TBT linker during the ligand-exchange reaction; (B) PAGE separation of TBT-Au₂₅ oligomers; (C) Steady-state absorption of isolated TBT-Au₂₅ oligomers; (D) Steady-state emission of TBT-Au₂₅ oligomers excited at 400 nm compared to the emission of free TBT excited at 265 nm; (E) Time-resolved fluorescence at 500 nm of the unlinked Au₂₅ (left panel) and Au₂₅ dimers. Figure adapted with permission from Reference [5]. Copyright 2018 American Chemical Society.

Moreover, the dimers existed in a non-collinear arrangement, dictated by the bent geometry of the TBT linker with electronegative central sulfur atom, which explained their larger net dipole moment. This demonstrated that larger oscillator strengths and polarizability can be obtained when both the geometry of the linked assemblies and their size can be controlled. Additional experimental arguments highlighting the importance of the linker molecule were provided by photoluminescence (PL), transient absorption and time-resolved PL measurements. The near-IR photoluminescence emission behaviour of the linked Au₂₅ oligomers (spectra shown in **Figure 2.4D**) was ascribed to the collective response of each of its constitutive Au₂₅ units, under the assumption that the PL emission occurs from the core-tosurface energy transfer.^{6,7} Furthermore, the covalent linking of nonpolar TBT contributed to the redshift of the emission wavelength by ca. 27 nm (0.07 eV) between single Au₂₅ and Au₂₅ oligomers, as it was shown for other Au₂₅ NCs protected with nonpolar ligands. More insights were provided when the PL of the dimeric species was probed with different excitation wavelengths: 265 nm and 400 nm. Overall, the energy transfer from the Au₂₅ core states to the surface states as well as from the TBT linker to the NC surface states was postulated to be at the origin of the enhanced NIR emission in multimers. Moreover, the longer excited-state lifetime (250 fs) observed for dimers (180 fs for single Au₂₅ clusters, Figure 2.4E) was attributed to a collective emission of each of the Au₂₅ units, further suggesting that enhanced NIR emission is expected for the linked clusters. However, the PL quantum yield (Φ_{PL}) of dimers was very close to that of single Au_{25}^-NCs (2.2 × 10⁻³ vs 1.8 × 10⁻³, respectively) indicating that the PL quenching was occurring. This behaviour was explained by the energy transfer between the NCs

(interactions of dipoles on the surface of Au_{25} NCs which were positioned within the FRET (Förster resonance energy transfer) distance and spectral overlap between the emission and 670 nm absorption). Therefore, the possibility of tuning the photoluminescence can arise from controlling the intercluster distance through both the length and geometry of the linker.

In their work Pradeep and co-workers used a multidentate metal complex as a linker to covalently bind Ag NCs.⁹ More specifically, they showed the formation of $[Ag_{25}(DMBT)_{18}]^-$ (DMBT = 2,4-dimethylbenzenethiolate) dimers when reacting the discrete Ag_{25} clusters with ruthenium^{II} bipyridyl-4,4'-dithiol ($[Ru(bpy)_2bpy(CH_2SH)_2]^{2+}$) (**Figure 2.5**A-B).

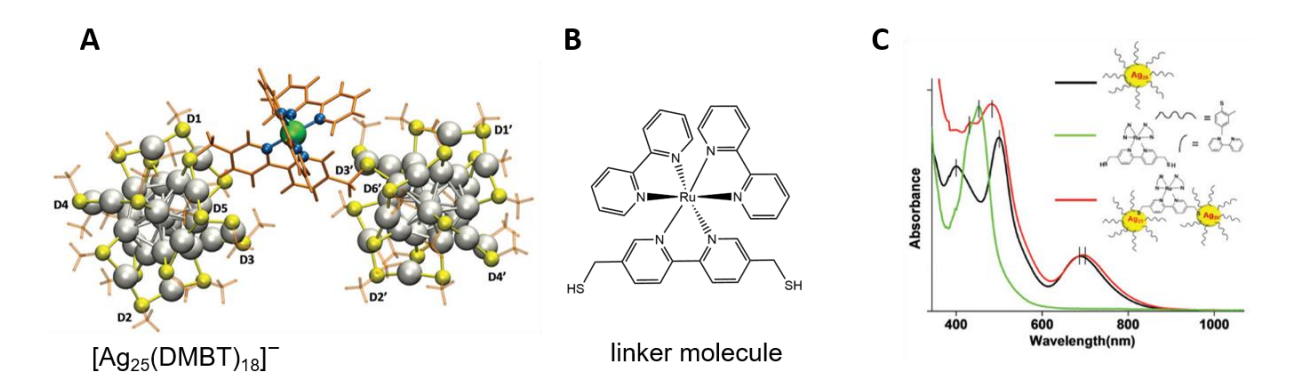


Figure 2.5 (A) DFT optimized structure of the most stable isomer of $[Ag_{25}(DMBT)_{18}^{-}]$ dimer. (B) Ruthenium^{II} bipyridyl-4,4'-dithiol linker. (C) Comparison of the optical absorption spectra of a single Ag_{25} NC (black trace), ($[Ru(bpy)_2bpy(CH_2SH)_2]^{2+}$ linker (green trace), and Ag_{25} dimers (red trace). Figure adapted with permission from Reference [9]. Copyright 2019 The Royal Society of Chemistry.

The obtained product characterized by the optical spectroscopy showed minimal changes with respect to the parent Ag_{25} cluster, suggesting that the core of the cluster remained largely unmodified. Slight red-shift of a 600 nm absorption band and changes around 400 nm were assigned to optical coupling between the Ru^{II} -based linker and Ag NCs (**Figure 2.5**C). Moreover, the DFT calculations have demonstrated that for the overall stability of the dimeric structure a smaller number of DMBT ligands in the vicinity of the exchanged sites on both clusters is preferred. This minimized steric hindrance was argued to contribute toward the higher conformational freedom of the linker and, which then translated into shorter intercluster distance. In addition to covalent linking, contribution from non-covalent interactions such as intercluster ligand—ligand van der Waals interactions or $\pi \cdots \pi$ interactions between the pyridyl rings in the linker complex and phenyl units in DMBT were stabilizing the dimeric structure.

An alternative strategy for connecting $[Au_{25}(S-C_2H_4Ph)_{18}]^-$ nanoclusters to form stable dimers was recently reported by Liu et al. Rather than using the organic bridging molecule, the two Au_{25} NCs were linked with two silver ions in a so-called "hand-in-hand" mode. As a result, stable $Ag_2Au_{50}(PET)_{36}$ dimers were obtained (**Figure 2.6**A). Their optical and catalytic properties were significantly altered with respect to discrete Au_{25} clusters. Interestingly, the preferential formation of the dimeric species was

reasoned by a relatively weak affinity between Au^+ and $\mathrm{NO_3}^-$ anions which prevented the doping of $\mathrm{Au_{25}}$. Moreover, the formation of higher assemblies, such as trimers and tetramers, was inhibited by the steric hindrance effect of the surface 2-phenylethanethiolate ligands, which were preventing the successive binding of an additional $\mathrm{Au_{25}}^-$ unit to the $\mathrm{Ag_2Au_{50}(PET)_{36}}$ dimer.

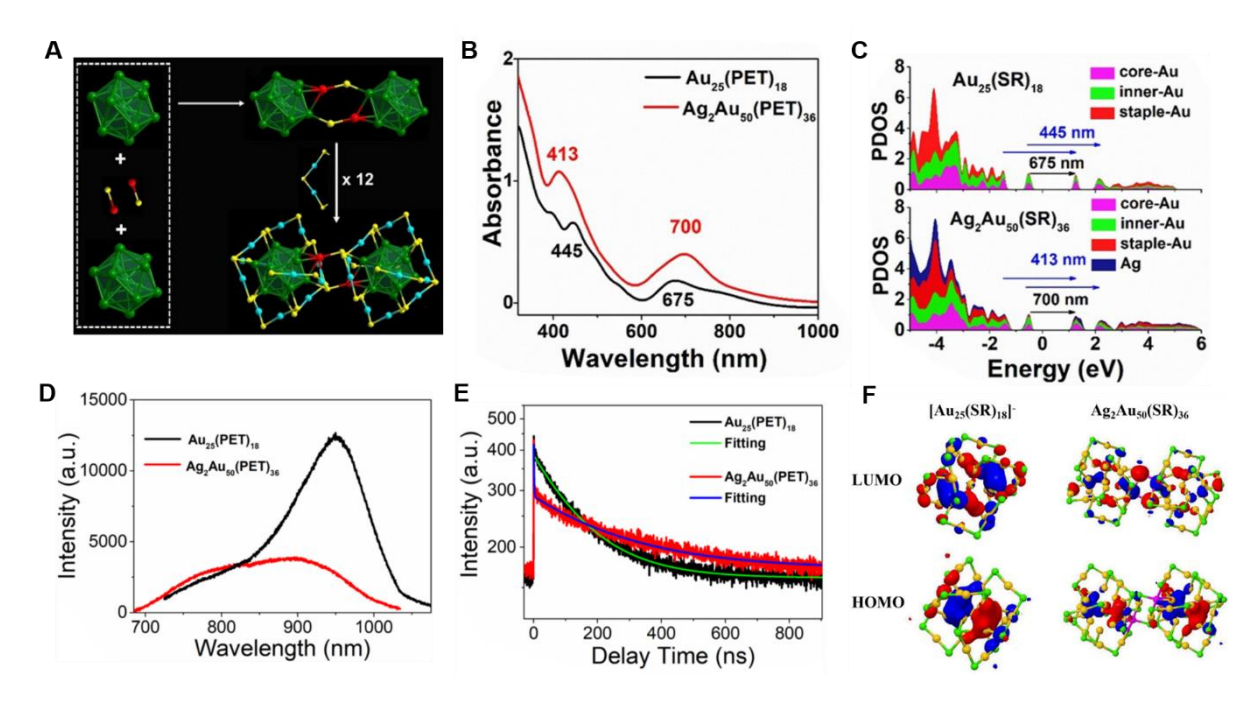


Figure 2.6 (A) Structure of the Ag2Au50(PET)36 dimer depicting two Au13 icosahedra coordinated by Ag atoms in a "hand-in-hand" pattern. Two S atoms binding to Ag originate from the Au2(SR)3 staple motifs. Colour code: Au^0 –green, Au^1 –blue, Ag-red, S-yellow, C and H atoms omitted for clarity; (B) Electronic absorption spectra of $[Au25(S-C2H4Ph)18]^-$ (black trace) and Ag2Au50(PET)36 dimer (red trace); (C) Predicted partial DOS and UV-vis spectra assignments for monomeric Au25 and Ag2Au50(PET)36 dimer at the DFT level; (D) Steady-state PL spectra of Au25 (black trace) and Ag2Au50(PET)36 dimer (red trace); (E) Time-resolved PL spectra measured at 940 nm for Au25 (black trace) and 840 nm for Ag2Au50(PET)36 (red trace), $\lambda_{exc} = 405$ nm; (F) Isodensity plots for the HOMO and LUMO for Au25 and Ag2Au50(PET)36 dimer at the DFT level. Colour code: Au-yellow, Ag-pink, S-green. Figure adapted with permission from Reference [10]. Copyright 2020 Wiley-VCH.

Significant change in the electronic absorption was observed for the dimers, with two prominent bands at 413 and 700 nm (**Figure 2.6**B). The DOS analysis revealed the significant role of Ag^+ on the electronic structure, causing the band broadening due to Ag–Au interactions. This band broadening causes the reduction of the HOMO–LUMO gap from 1.70 eV (for a single Au_{25}^- NC) to 1.64 eV. While it was expected that the linking of two Au_{25}^- NC with two Ag bridge atoms would significantly reduce the intramolecular rotation and vibration, which favours the PL emission, an opposite behaviour was observed. In fact, the PL emission intensity decreased upon dimerization of Au_{25}^- NCs (**Figure 2.6**D) and it was accompanied by the blue-shift and broadening of the emission peak. The explanation was provided by the DFT study that revealed a significant reduction of the charge transfer from the ligand to the Au kernel. In addition, a nearly two times slower PL decay for the Ag_2Au_{50} (**Figure 2.6**E) was explained by the Ag induced spatial separation of the HOMO and LUMO (**Figure 2.6**F).

The above examples describe the formation of discrete multimers that occurs in the solution during the ligand exchange reaction upon introduction of a linking agent. However, the formation of small Au_{25} multimers in the gas phase has also been observed using ion mobility mass spectrometry technique (IM-MS).¹¹ In fact, the assembly of $[Au_{25}(SC_2H_4Ph)_{18}]^0$ dimers and trimers took place within the instrumental setup. The obtained species were subsequently separated based on the differences in their ion mobility (**Figure 2.7**) and identified as dimers and trimers. The experimentally calculated values of collision cross-sections (CCS) for dimers and trimers were slightly lower than expected. Therefore, the structure of the dimer was proposed, in which the intercluster bonding occurs via two Au_2S_3 staples (inset in **Figure 2.7**C).

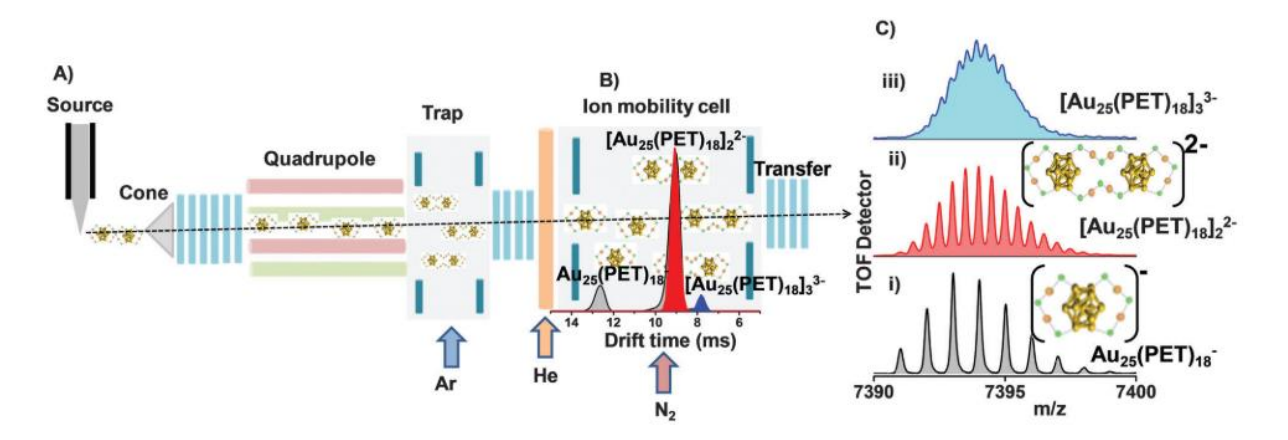


Figure 2.7 (A) Schematic representation of the instrumental setup where $Au_{25}(SC_2H_4Ph)_{18}$ cluster multimers are created and (B) subsequently separated by IM-MS. (C) Expansion of each of the peaks obtained from ion mobility corresponding to $[Au_{25}(SC_2H_4Ph)_{18}]^-$ (grey profile), $[Au_{25}(SC_2H_4Ph)_{18}]_2^{-2-}$ (red profile), and $[Au_{25}(SC_2H_4Ph)_{18}]_3^{-3-}$ (blue profile) with representative structures shown as insets. Figure reproduced with permission from Reference [11]. Copyright 2016 The Royal Society of Chemistry.

2.2.2 van der Waals interactions

Formation of assemblies constructed with negatively charged $M_{25}(SR)_{18}^-$ (M = Ag, Au) NCs linked with fullerenes (either C_{60} or C_{70}) was reported by Chakraborty et al.¹² The supramolecular interaction between the NCs and fullerenes produced dimers, trimers, tetramers and higher assemblies (**Figure 2.8**A), for both the Ag and Au NCs. These aggregates were obtained as a mixture in solution (see the ESI-MS spectrum in **Figure 2.8**B) hence selective formation of a particular adduct could not be controlled. Importantly, the structural aspects, such as inherent cluster geometry, type of metal atoms and nature of ligands in the monolayer, were found to affect the complexation between the building units resulting in a size distribution of cluster–fullerene adducts.

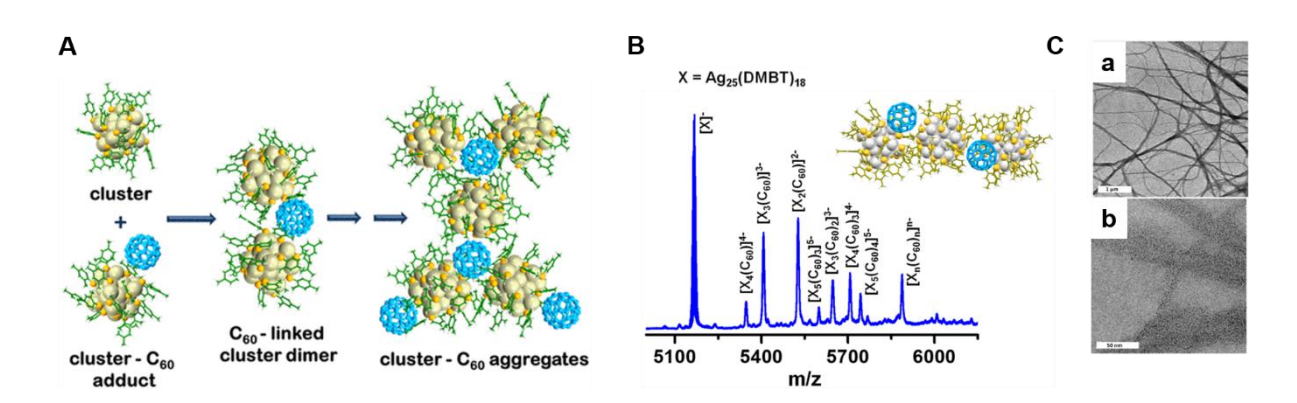


Figure 2.8 (A) Schematic representation of the (Ag, Au)₂₅-fullerene adduct formation; (B) ESI-MS depicting the adducts of Ag_{25}^- and C_{60} ; (C) TEM images of $[(Ag_{25}_n-C_{60}]^n$ assemblies forming wires, scale bar: (C-a) 1 μ m, (C-b) 50 nm. Figure adapted with permission from Reference [12]. Copyright 2020 American Chemical Society.

The DFT investigation identified the "ligand pockets" on the surface of the cluster as the adsorption sites for fullerenes. Additionally, two types of interactions were stabilizing this complex: (i) the van der Waals (vDW) interactions and $C-H\cdots\pi$ occurring between the protons of $-CH_3$ groups of 2,4-DMBT ligands and the fullerene π system, and (ii) ion-induced dipole interactions between the $M_{25}(SR)_{18}^-$ and fullerenes. Dimers $[(Ag_{25})_2-C_{60}]^{2^-}$ and trimers $[(Ag_{25})_3-C_{60}]^{3^-}$ bound by a single fullerene molecule were found to be less stable, specifically in the trimer case (binding energies of -9.80 and -3.86 kcal/mol, respectively), due to the steric hindrance and increase in electrostatic repulsion between negatively charged Ag_{25} cluster units. As a result, the stabilizing $C-H\cdots\pi$ interactions were weakened. The TEM imaging of the Ag_{25} – C_{60} adducts in the solid state showed the wire-like structures that formed (**Figure 2.8C**).

2.3 One-dimensional (1D) metal nanocluster assemblies

The synthesis of metal NC 1D assemblies are of importance for establishing the reliable methods for fabrication of nanodevices by bottom-up methods. The construction of such superstructures relies on different strategies: bond formation (metal-metal, metal-X (X = O, S, Cl)), control of counterions, introduction of linker molecules, and use of interligand interactions, which will be discussed in this section. To ensure the assembly of 1D structures and concurrently prevent formation of branched aggregates the ability to manipulate the nanocluster monolayer is of utmost importance.

2.3.1 Metal-metal interactions (aurophilic interactions)

Aurophilic interactions (Au^I···Au^I) belong to the class of attractive metallophilic interactions that play important role in arrangement and stabilization of oligonuclear metal ion complexes.¹³ These interactions show both structure-directing and property-enhancing (e.g., stronger luminescence) capabilities.

Au^I...Au^I interactions were found to be a driving force for aligning Au NCs into 1D nanowires. ¹⁴ Investigation into the role of various short chain n-alkylthiolate ligands on the properties of paramagnetic Au₂₅ NCs lead to the unexpected discovery of formation of linear polymers composed by $[Au_{25}(SBu)_{18}]^0$ (SBu = 1-butanethiolate) units upon crystallization. The single-crystal X-ray analysis revealed that the 1D cluster chains were stabilized by the aurophilic interactions. Importantly, the critical factor in the formation of these 1D structures was the length of the protective thiolate ligands. It was found that the C₄- and C₅-thiols facilitated the Au₂₅ cluster polymerization in the solid state. On the contrary, the very short ligands (i.e., C₂- and C₃-thiolates) and bulkier PhC₂H₄-S⁻ ligand did not afford the 1D chains in the crystal. Given the flexibility of the longer n-alkyl chains (exhibiting more degrees of freedom) some of the C₄- or C₅-groups were disordered within the staple motifs. In other words, these groups presented different conformation with respect to the staple plane which manifested itself in the specific orientation of these ligands on the surface of Au₂₅ NC.

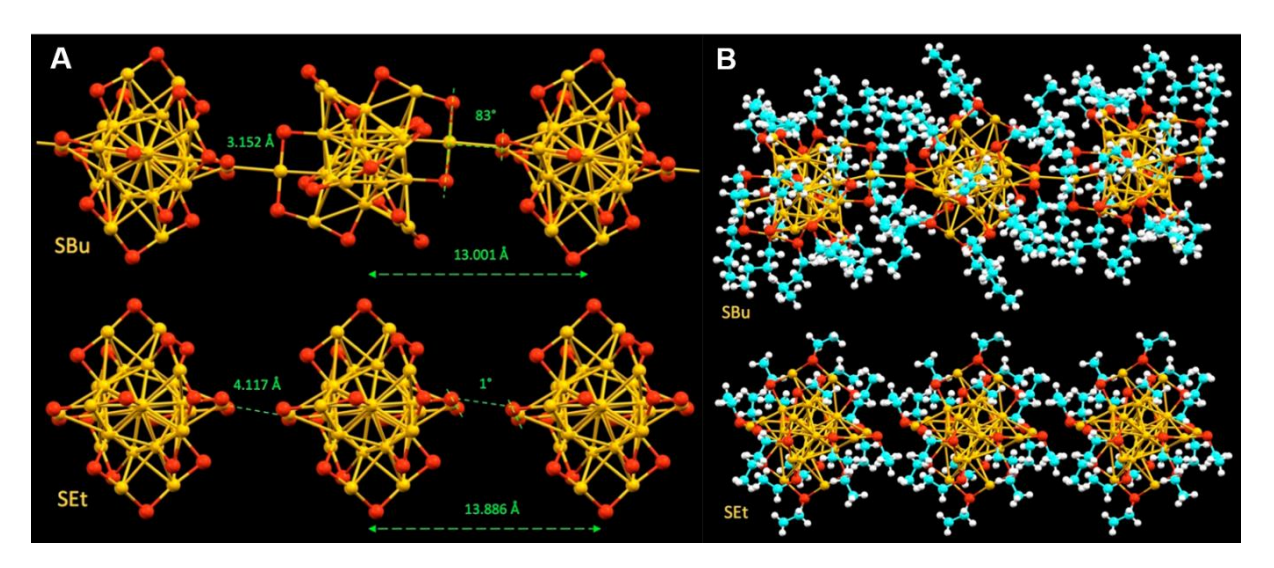


Figure 2.9 (A) Comparison between the $Au_{25}S_{18}$ skeletons of $Au_{25}(SBu)_{18}$ and the $Au_{25}(SEt)_{18}$ crystals, with relevant distances and torsional angles; (B) View of the two Au_{25} sequences to highlight the interdigitation of ligands in $Au_{25}(SBu)_{18}$, or its absence, in $Au_{25}(SEt)_{18}$. Colour code: Au-yellow, S-red, C-light blue, H-white. Reproduced with permission from Reference [14]. Copyright 2014 American Chemical Society.

Careful investigation revealed that the "twist-and-lock" mechanism was responsible for the formation of the polymeric assemblies. This mechanism is based on the 90° twist of every other Au_{25} cluster in a polymer chain resulting in the interdigitation (i.e., "lock") of the ligands having a suitable alkyl chain length (**Figure 2.9**).

In contrast, ligands with either not sufficiently long carbon chain ("no lock") or very long ligands exhibited a steric hindrance that precluded short intercluster Au–Au distance. Hence, these types of ligands were not suitable for stabilizing the 1D polymers. In addition, the theoretical investigations further corroborated that the van der Waals interactions between the alkyl chains in the C₄ ligands of adjacent clusters made the lock mechanism possible. These 1D Au₂₅ nanowire assemblies were shown

to be antiferromagnetic at low temperatures, in contrast to the paramagnetic behaviour exhibited by the Au_{25} units. The loss of magnetic properties was explained by the formation of a connected structure. More specifically, the high proximity of neighbouring clusters connected via aurophilic interactions made possible for the two unpaired electrons located on individual units of Au_{25} to form electron pairs. As a result, the conduction band of the 1D-structure was filled and the valence band was unoccupied, imparting the assembled structures with semiconducting properties. Similarly, the monodoped diamagnetic $Au_{24}M(SBu)_{18}$ (M = Cd, Hg) NCs formed the same type of nanowires demonstrating that the magnetic state of the cluster posed no challenge to the formation of 1D assembly. On the other hand, $Au_{24}Pt(SBu)_{18}$ did not form assemblies indicating that, in addition the ligand structure, also electronic factors could play an important role in enabling superstructures. ¹⁵

More in-depth study focusing on the importance of intracluster ligand interactions in the formation of the 1D nanocluster assembly was conducted by Negishi and coworkers.¹⁶

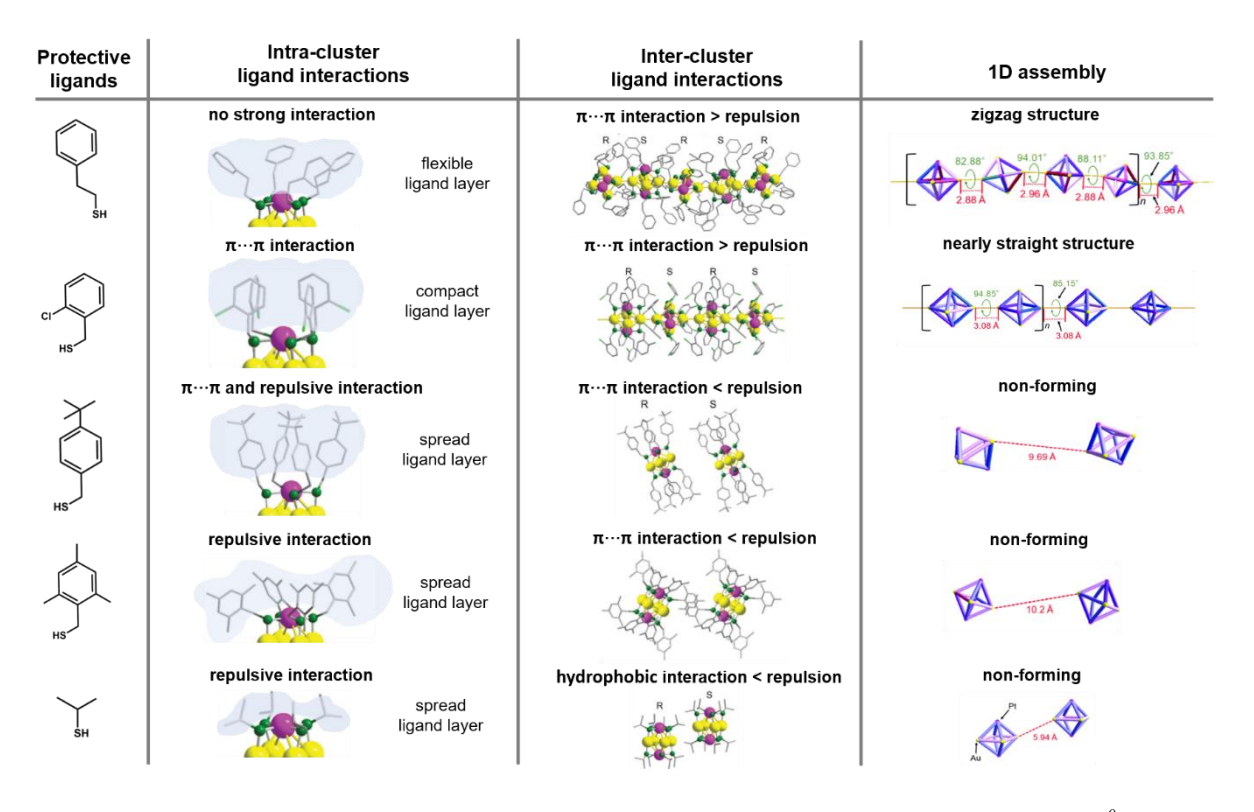


Figure 2.10 Structures of protective thiolate ligands, geometrical structures of individual [Au₄Pt₂(SR)₈]⁰ NCs and 1D assemblies. Relationship between intra-cluster ligand interactions which is related to the distribution of the ligands within each cluster, inter-cluster ligand interactions and 1D assembly patterns in the crystal. Figure adapted from Reference [16]. Published by The Royal Society of Chemistry.

By analysing small heterometallic [Au₄Pt₂(SR)₈]⁰ NCs capped with a series of thiolate ligands, they expanded on Maran's findings which, as discussed previously, revealed that the control over the ligand interactions between the neighbouring clusters (intercluster ligand interaction) is crucial for achieving extended 1D structures.

Negishi's contribution showed that for the appropriate intercluster ligand interactions to arise, the intracluster ligand interactions must be primarily controlled. They demonstrated that the ligand structure not only governs the 1D assembly but also affects the linkage pattern within the assembly. Bulky ligands were shown to distribute isotropically (steric hindrance) whereas phenylthiolates with non-bulky substituents formed a compact structure within the ligand shell ($\pi \cdots \pi$ interactions). The right balance of attractive forces and steric repulsion between the ligands was proven to induce the appropriate intracluster interactions that facilitated the 1D assemblies (**Figure 2.10**).

The optical absorption spectra of $[Au_4Pt_2(SR)_8]^0$ clusters were measured in solution, dry amorphous state, and crystalline state. The spectra of crystalline samples showed the onset of optical absorption at longer wavelength than for amorphous powders or dissolved samples. Given that the observed changes in the electronic structure were accompanying crystallization, they were attributed to the formation of 1D assemblies. Theoretical studies further confirmed the change in the electronic structure of cluster assemblies with respect to the individual monomeric clusters. At large, the 1D structures were shown to maintain the electronic structure of individual monomeric components however the HOMO–LUMO gap of the assemblies was narrower (2.17 eV) than that of individual clusters (2.93 eV for $[Au_4Pt_2(2PET)_8]^0$).

Formation of ultralong nanoribbons with well-defined width (10–50 nm) and thickness (up to several μ m) assembled from $[Au_{25}(p\text{-MBA})_{18}]^-$ in aqueous phase was recently reported by Xie and co-workers.¹⁷

This colloidal self-assembly was also directed by the aurophilic interactions and was initiated by a pH-triggered reconstruction of the surface staple motifs where short dimeric motifs were transformed into longer ones at the expense of the Au₁₃ kernel modification. As a result, the newly formed smaller Au NCs adopted an elongated structure, similar to that of the Au₂₂(SR)₁₆ (ref. 18) or Au₂₄(SR)₂₀ (ref. 19) cluster. As confirmed by the XPS study, the ratio of Au¹ in the NC surface shell increased, giving rise to strong and anisotropic aurophilic interactions between neighbouring NC units and therefore leading to the formation of 1D nanowires (**Figure 2.11**A). Subsequently, the secondary self-assembly of nanowires into nanoribbons was driven by interligand interactions ($\pi \cdots \pi$ stacking and dispersive interactions) between individual nanowires owing to intense interdigitation of the *p*-MBA ligands. The formation of supramolecular structures led to the emergence of photoluminescence in nanoribbons. Specifically, an appearance of two independent emission bands (483 and 620 nm) at low temperature (77 K), ascribed to two independent emission states, was observed (**Figure 2.11**B).

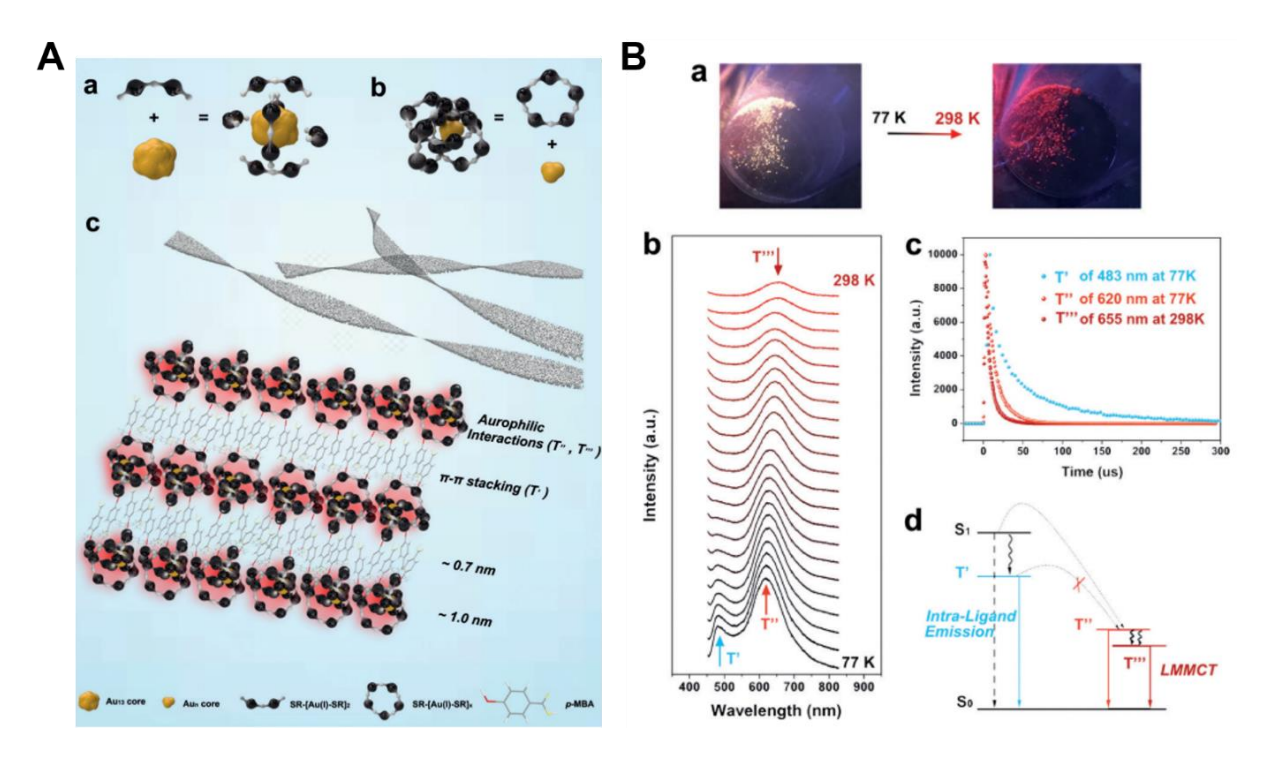


Figure 2.11 (A) Schematic illustration of the evolution of self-assembly from (A-a) the single [Au₂₅(p-MBA)₁₈] ¬NCs; (A-b) pH-triggered reconstruction of the surface motifs; (A-c) Self-assembly of transformed Au NCs units into nanowires and nanoribbons. The hydrocarbon tails are omitted for clarity. (B) Emission behaviour of nanoribbons upon excitation at 365 nm at low temperature and room temperature (B-a) Digital optical photograph of the as-assembled nanoribbons powder (B-b) Changes in the emission spectra as a function of temperature, (B-c) PL lifetime profiles of T', T" and T"' state; (B-d) Schematic diagram of the excited state relaxation dynamics of the nanoribbons. S₀, S₁, and T (T', T" and T"') represent ground, excited singlet, and triplet states, respectively, where T' is related to the intraligand relaxation process while both T" and T"' are responsible for LMMCT relaxation dynamics. Reproduced with permission from Reference [17]. Copyright 2019 Wiley-VCH.

The higher-energy emission state (T') has been hypothesized to originate from the well-organized interwire packing (governed by $\pi \cdots \pi$ stacking), whereas the lower-energy T" emission, that red-shifts to 655 nm at room temperature to yield T" state, was ascribed to the triplet state LMMCT occurring in the 1D nanowire. Moreover, the T" emission at room temperature exhibited significant increase in Φ_{PL} (6.2 % vs 0.01 % for parent [Au₂₅(p-MBA)₁₈] cluster).

2.3.2 Connection via heteroatom (direct metal-metal bond)

Differently to the above-discussed strategies that utilize aurophilic interactions as means to construct 1D NC assemblies, simple silver atoms were also shown to successfully serve as linkers to connect the NC units.

 L-Ag) along the c-crystallographic axis (**Figure 2.12**A-C). To realize 1D polymers, a structural transformation of the linker hinge, from the original bent geometry in the monomeric nanocluster to the linear geometry, is required. As a result of this transformation, one silver atom is "inserted" into the vicinity of the adjacent cluster and the chain propagation reaction is initiated. The single crystal X-ray analysis shows the packing of the cluster polymer chains in the monoclinic unit cell along the c-axis of the single crystal whereas, the bulky adamantane alkyl ligands form an insulating layer between the polymeric NC chains. Contrary to the $[Au_{25}(p\text{-MBA})_{18}]^-$ assembly, this superstructure formation was spontaneous yet controlled. Depending on the solvent used in the process, either monomeric species or 1D assemblies were be obtained. Increase in a number of single Ag—Au bonds from two in a monomer to three in polymeric structure was found to be a driving force behind the monomer to polymer transformation.

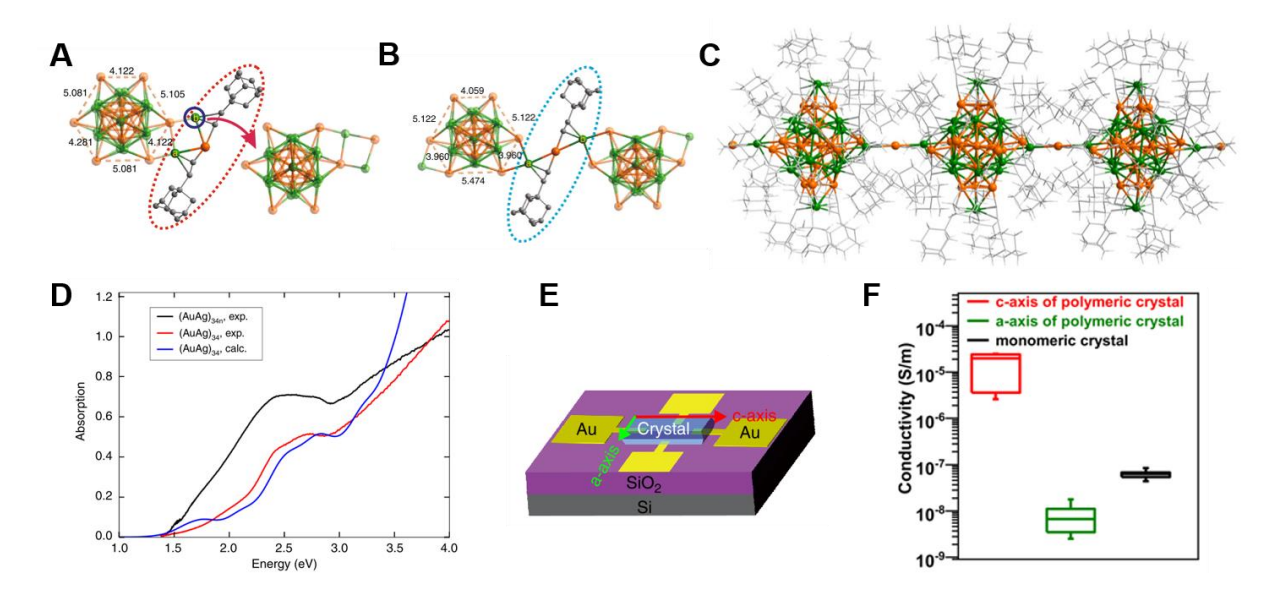


Figure 2.12 (A) Linker hinge "Ag-L-Au-L-Ag" unit of monomeric (AuAg)₃₄ NC and (B) polymeric (AuAg)_{34n} structure. Colours: Au-orange; Ag-green; C-grey. All hydrogens are omitted for clarity. (C) Atomic structure of the cluster polymer viewed orthogonal to the c-axis. (D) The solid-state optical diffuse reflectance spectra of monomeric (red trace) and polymeric crystals (black trace) juxtaposed with the computed spectrum of one of the isolated modelled clusters (blue trace). (E) The structure of the polymer crystal FET. (F) Box-and-whisker plot for the conductivity of the monomeric crystal (black) and polymeric crystal (red and green). Depicted are median, 25 and 75 % quartiles, and a full range. Figure adapted from Reference [20]. Copyright 2020 Springer-Nature.

This material, when in crystal state, showed anisotropic semiconducting properties. The DFT method was used to get insights into the electronic structure of the 1D assemblies. The magnitude of the computed HOMO–LUMO energy gap of about 1.3 eV, indicated that the NC polymer should behave as a semiconductor-type material. Furthermore, the calculations revealed that appreciable electron state density overlap between the adjacent clusters in the polymer exists only in the direction of polymer axis, implying the anisotropy of the electronic conductivity in the crystal. The field-effect transistor (FET) devices made with a single-crystal nanocluster FET chip (**Figure 2.12**E) allowed to measure the electrical conductivity along the orthogonal *c*- and *a*-crystallographic axes. The electrical conductivity,

measured at RT and 56 % relative humidity, along the a-axis $(6.27 \times 10^{-8} \text{ S m}^{-1})$ was comparable with the electrical conductivity of the monomeric species. However, the electrical conductivity probed along c-crystallographic axis was 1800 times higher $(1.49 \times 10^{-5} \text{ S m}^{-1}, \text{ Figure 2.12F})$. The effect was shown to be a p-type field effect with a hole conduction mechanism. This study demonstrated that direct linking of the nanocluster lead to improved carrier transport.

One more example of 1D NC assemblies linked by simple Ag atoms was reported by Wen et al.²¹ Interestingly, the synthesis of bimetallic NC linear polymer, (structure in **Figure 2.13**A), $[Au_7Ag_9(dppf)_3(CF_3CO_2)_7BF_4]_n$ (dppf = 1,1'-bis(diphenylphosphino)ferrocene) was obtained in a one-pot reaction without the pre-formation of the cluster monomer. The single crystal X-ray analysis of the formed 1D structure showed that the cluster units, $Au_7Ag_8(dppf)_3(CF_3CO_2)_7$, were connected via the covalent Ag–O bonds.

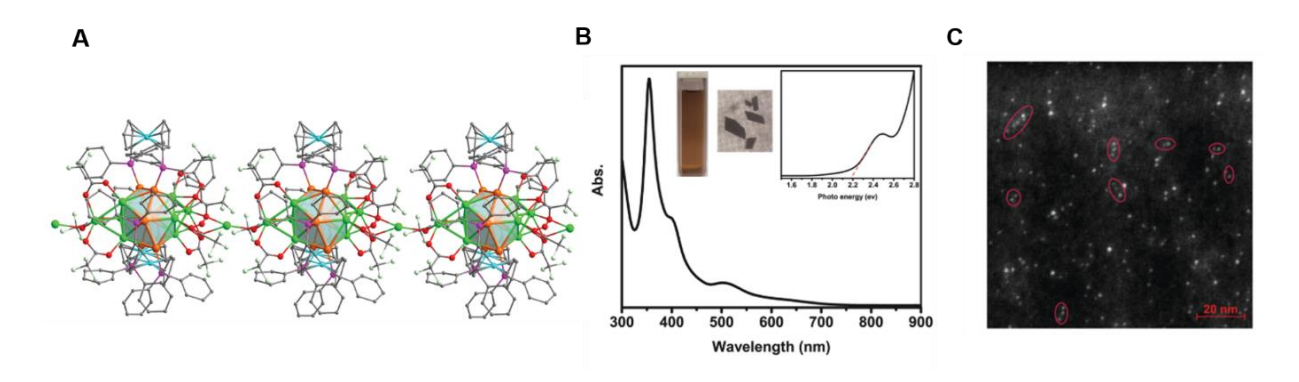


Figure 2.13 (A) 1D [Au7Ag9(dppf)3(CF3CO2)7BF4]n polymeric assembly (anions and H atoms omitted for clarity). Colour code: Ag-green, Au-orange, O-red, P-purple, C-grey, Fe-blue; (B) Optical absorption spectrum of 1D Au7Ag8 assemblies in CH2Cl2 solution. Inset: the spectrum on the energy (eV) scale and digital photographs of assembly in solution and crystalline state; (C) TEM image of assembly in MeOH solution. The red circles indicate dimers, trimer and multimeric forms obtained upon breakdown of the polymer. Figure adapted with permission from Reference [21]. Copyright 2019 The Royal Society of Chemistry.

It has been postulated that the excess free Ag^I ions in the reaction mixture was binding to the CF₃COO⁻ ligands of the already formed NC units during the synthesis. Given the versatile coordination ability of the trifluoroacetate ligands towards the Ag ions (four different modes) the formation of 1D polymer could be realized. The optical spectrum of [Au₇Ag₉(dppf)₃(CF₃CO₂)₇BF₄]_n polymer depicted a sharp band at 355 nm with two additional bands at 400 and 507 nm (**Figure 2.13**B). The optical energy gap was determined to be 2.18 eV. Interestingly, the polymer was found to be unstable when kept in solution, leading to its breakdown into monomeric, dimeric, trimeric or multimeric forms, as depicted in the TEM image (**Figure 2.13**C).

2.3.3 Counterion-induced metal NC assemblies

A hierarchical fibrous (1D to 3D) assembly of Au₂₁ clusters exhibiting electrical conductivity was reported by Li et al.²² Unusually, the obtained assembly could be modulated with atomic precision via site-specific tailoring of the atypical surface motif (comprising four ligands and a counteranion). The atomic structure as well as the forces driving the assembly were unveiled with single-crystal X-ray analysis. Two Au₂₁ NCs that differ in the counteranion were used to form the assemblies, namely $[Au_{21}(S-C_6H_{11})_{12}(PCP)_2]^+[AgCl_2]^-$ and $[Au_{21}(S-C_6H_{11})_{12}(PCP)_2]^+[Cl]^-$ (S-C₆H₁₁ = cyclohexylthiolate, PCP = bis(diphenylphosphinomethane). The assembly of Au₂₁ NCs into 1D nanofibrils was driven by the $\pi \cdots \pi$, anion π , and ary C-H···Cl interactions of the counteranions and phenyl rings of the PCP ligands. The counteranions, [AgCl₂] and [Cl] residing between the two sets of phenyls rings on the PCP ligands from the adjacent clusters formed a specific surface motifs called "surface hooks". The orientation of the Au₂₁ NCs in the 1D assembly was influenced by the counteranion structure (Figure 2.14). The subsequent assembly into 3D μm-sized crystals was dictated by the solvent effects, but also the counteranions were shown to strongly affect the packing modes. This led to distinctive electrical transport properties exhibited by the assembled solids. Namely, $[Au_{21}(S-C_6H_{11})_{12}(PCP)_2]^+[C1]^$ superstructure showed two orders of magnitude better charge transport properties compared to $[Au_{21}(S-C_6H_{11})_{12}(PCP)_2]^+[AgCl_2]^-$ due to the parallel-displaced π -stacking arrangement of the phenyl ligands and a smaller interparticle spacing.

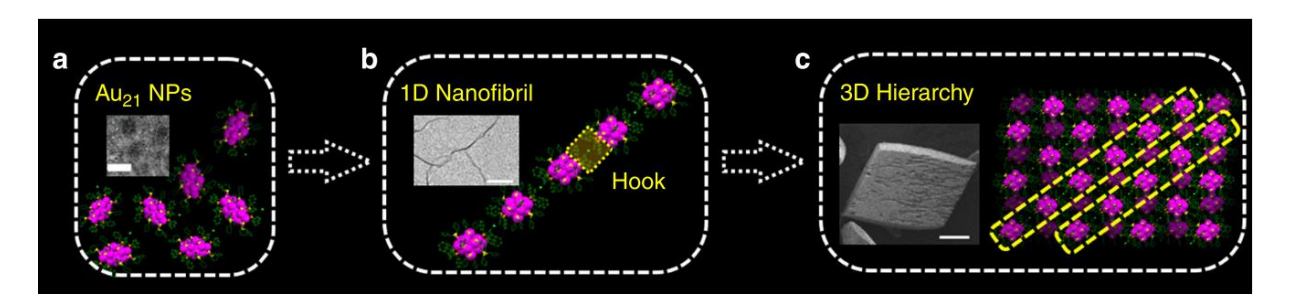


Figure 2.14 Schematic representation of the hierarchical fibrous (1D to 3D) assembly of Au₂₁ NCs. Insets are the TEM images of (a) individual Au₂₁ NCs (scale bar: 2 nm); (b) 1D nanofibril assembled from Au₂₁ NCs (scale bar: 50 nm); (c) SEM image of 3D crystals assembled from Au₂₁ NCs (scale bar: 50 µm). Colour codes: Au-magenta, S-yellow, Cl-light green, P-orange, C-green, H atoms omitted for clarity. The yellow rectangles indicate in (b) the surface hook and in (c) the 1D motifs (fibrils) in the 3D crystals. Figure reproduced from Reference [22]. Published by Springer Nature.

Ion-cluster interactions were also found to induce the assembly of $Ag_{29}(SSR)_{12}(PPh_3)$ (SSR = 1,3-benzene dithiol; PPh_3 = triphenylphosphine) NCs into higher order structures.²³ The Cs^+ cations were shown to strip the PPh_3 ligands from the surface of the parent Ag_{29} NC leading to the formation of $Cs_3Ag_{29}(SSR)_{12}(DMF)_x$ -based linear assembly in the solid state. The structural analysis revealed that the capture of the Cs^+ on the surface of Ag NC was facilitated by a Cs-S bond and $Cs\cdots\pi$ forces. Moreover, the $Cs^+\cdots DMF\cdots Ag_{29}$ interactions were driving the assembly into 1D linear chains. Interestingly, replacing the DMF with a different oxygen-carrying solvent, led to the formation

of Ag_{29} -2D grid network (*N*-methyl-2pyrrolidone solvent, NMP) or Ag_{29} -3D superstructure (tetramethylsulfone solvent, TMS, **Figure 2.15**A). Different crystalline packing modes and surface structures exhibited by these materials strongly affected their optical properties (**Figure 2.15**B).

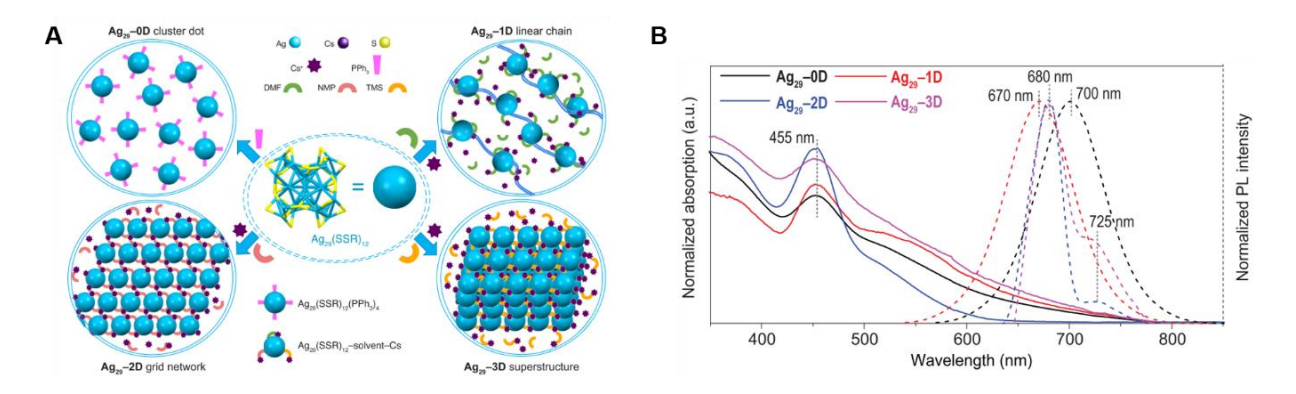


Figure 2.15 (A) Schematic representation of the 1D–3D assemblies of Ag₂₉(SSR)₁₂ building blocks depicting Ag₂₉(SSR)₁₂(PPh₃)–0D cluster, Ag₂₉–1D linear chains, Ag₂₉–2D grid networks, and Ag₂₉–3D superstructures; (**B**) Comparison of optical absorptions and emissions of assemblies in a crystalline form: Ag₂₉–0D (black traces), Ag₂₉–1D (red traces), Ag₂₉–2D (blue traces), and Ag₂₉–3D (purple traces). Figure adapted from Reference [23]. Published by Oxford University Press.

2.4 Two-dimensional (2D) metal nanocluster assemblies

Extensive study on 2D assemblies of nanomaterials uncovered that the main force holding the layers together are van der Waals (vdW) interactions, in contrast to the building units that are comprised within the layer as those are held by much stronger interactions (e.g. covalent or ionic). ²⁴ Given that vdW forces are isotropic, the anisotropy that is required to obtain 2D nanostructures, can be generated either via formation of the lamellar mesophase templates or 2D-directed self-assembly of building blocks (nanoparticles, polymers, protein). In contrast to the numerous reports on 2D self-assembly of nanoparticles composed of hundreds of atoms, the limited success has been achieved for small metal NCs. Given that energy of the intercluster interactions is comparable to thermal fluctuation of the surroundings²⁴, breaking of the assembled NC structures and restriction of the formation of ordered architectures is very likely.

2.4.1 Intraligand interactions

In this section surface ligands-induced assembly will be discussed with the focus on the role of various nanoscale surface forces (dipolar, van der Waals, electrostatic interactions, hydrogen bonding) on the self-assembly of metal NCs.

2.4.1.1 Dipolar interactions and van der Waals interactions

Wu et al.²⁵ reported the 2D self-assembly of $Au_{15}(DT)_{15}$ (DT = 1-dodecanethiolate) into mono-, few-, and multilayered sheets in a colloidal solution. This assembly was initiated by the organization of Au_{15} clusters into dense 1D structures, which was driven by the intercluster dipole–dipole attractions. The theoretical calculations showed that $Au_{15}DT_{15}$ exhibited a permanent dipole moment (μ) of up to 13.27 D and originated from both the specific arrangement of Au atoms and ligand distribution within the ligand shell.

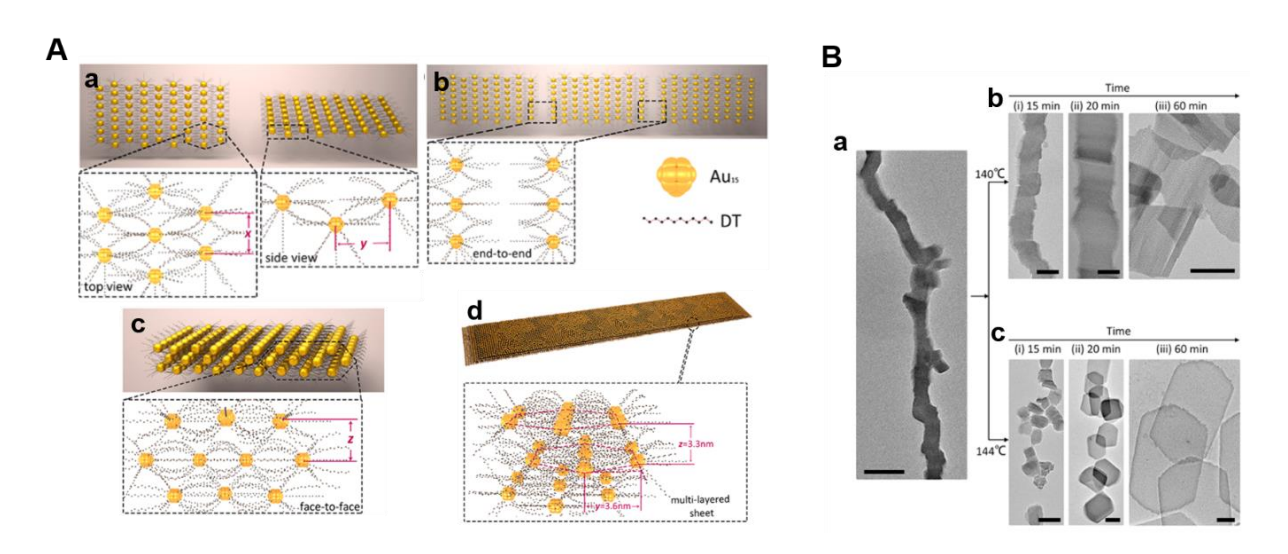


Figure 2.16 (A) Schematic representation of secondary assembly of small isolated 2D assemblies into long multilayered architectures, which involved the distribution of DT alkyls over (A-a) elongated architectures, (A-b) the end-to-end, (A-c) the face-to-face self-assembly, and (A-d) the spatial arrangement of Au₁₅ NCs within the multilayered architectures. (B) Time-dependent morphology evolution of Au₁₅ self-assembly architectures annealed at (B-b) 140 and (B-c) 144 °C for 60 min. Figure adapted with permission from Reference [25]. Copyright 2015 American Chemical Society.

Upon 1D assembly, the long DT protective ligands redistributed on the surface of Au₁₅ NCs which gave origin to asymmetric van der Waals attractions. In turn, vDW forces governed the assembly into small isolated 2D architectures (**Figure 2.16**A). Further heating treatment afforded stable multilayered 2D assemblies (**Figure 2.16**B). The 2D morphologies could be controlled by carefully tuning the length, aspect ratio and thickness of the final architectures.

2.4.1.2 Electrostatic and hydrogen-bonding interactions

Ikkala and co-workers reported on the dynamic self-assembly of $Au_{102}(p\text{-MBA})_{44}$ (p-MBA = para-mercaptobenzoic acid) clusters into colloidal superstructures. ²⁶ The carboxylic groups of p-MBA ligands have driven the dissolution of the Au_{102} NCs, depending on the extent of their protonation. Explicitly, when all carboxylic groups were protonated, the cluster was soluble in polar solvents but insoluble in water. Deprotonation of more than 22 carboxylic groups in the ligand shell

could reverse the trend. Importantly, the distribution of the p-MBA ligands within the Au₁₀₂ shell was found not to be spherical (**Figure 2.17**A), i.e., the patchiness that resulted from protonated and deprotonated carboxylate groups gave rise to the surface charge distribution.²⁷

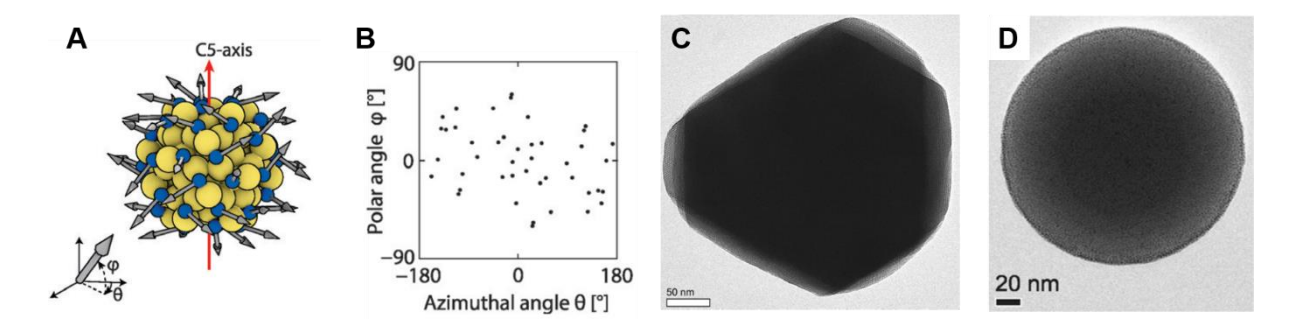


Figure 2.17 (A) Resolved ligand directions illustrated with arrows, elucidating the possible hydrogen bonding directions. (B) A polar coordinate system (polar angle φ and azimuthal angle Θ) for $Au_{102}(p\text{-MBA})_{44}$ clusters can be identified where the ligand directions are predominantly in the equatorial plane. A TEM image of (C) 2D nanosheet with faceted edges (three sheets with monocluster thickness are stacked); and (D) spherical capsoid of $Au_{102}(p\text{-MBA})_{44}$ (2D projection). Figure adapted with permission from Reference [26]. Copyright 2016 Wiley-VCH.

Controlling the kinetic of crystallization by dialyzing the aqueous solution of partially deprotonated Au_{102} against MeOH, accomplished the colloidal crystallization of Au_{102} into 2D nanosheets with one nanocluster thickness (**Figure 2.17**C). It was corroborated that the hydrogen bonding interactions were driving the self-assembly. The protonated *p*-MBA ligands directed themselves towards "equatorial plane" of the Au_{102} NC in a preferential manner leading to local concentration of hydrogen bonds around the equator belt of the NC (**Figure 2.17**A-B). Furthermore, such an arrangement and composition of ligands on the Au_{102} surface gave these clusters amphiphilic character. Notably, direct addition of the Au_{102} dispersion into MeOH solution resulted in the formation of spherical superstructures with monolayer thickness, called capsids (**Figure 2.17**D).

2.4.2 Template-directed assembly of metal NCs

Templates could also play an important role in the formation of organized NC assemblies. Templates could be regarded as substrates with multitude of active sites to which NCs could bind selectively. The formation of such hybrid structures depends to great extent on both the stability of metal NCs and the template—NC interactions. Recently, diverse synthetic strategies and various templates were probed to realize the NC assemblies. This section will discuss some of them.

2.4.2.1 Soft templates

Liquid-liquid assembly techniques were proven to be the promising platform to assemble colloidal particles in a well-defined manner. This method was used to direct the self-assembly of Au NCs at the oil/water interface to produce the large area nanosheets. In this process, the Au^I –DT (DT = 1-dodecanethiolate) complexes were first dissolved in octadecene and then the aqueous solution of formaldehyde (reducing agent) was added. The resulting two-phase reaction environment forced the Au^I –DT to behave like natural surfactants orienting their polar Au^I heads toward the aqueous phase and aligning their long hydrophobic DT tails in the organic phase. The reduction of Au^I to Au^0 occurred at the liquid-liquid interface producing the Au NCs in-situ which subsequently assembled at the oil/water interface. The obtained assemblies had the nano-ribbon structure with the 50–100 nm width and the length of up to 20–30 μ m. Higher reaction temperature (120 °C) caused the nanoribbons to curl into nanotubes. The formed nanoribbons showed strong red photoluminescence emission along the whole fibres upon 360 nm light excitation.

The idea to extend the colloidal synthesis of crystalline nanosheets to obtain the 2D self-assembled architectures based on metal NCs was investigated by Wu et al.²⁹ In the first step, the Au₁₅ NCs $(Au^0_{11}Au^I_4(DT)_{15})$ were prepared in dibenzylether (BE) using 1-dodecanethiol (DT) as both the reducing and capping agent. The self-assembly was induced by adding liquid paraffin (LP) to the BE solution with Au₁₅ NCs and annealing at 140 °C.

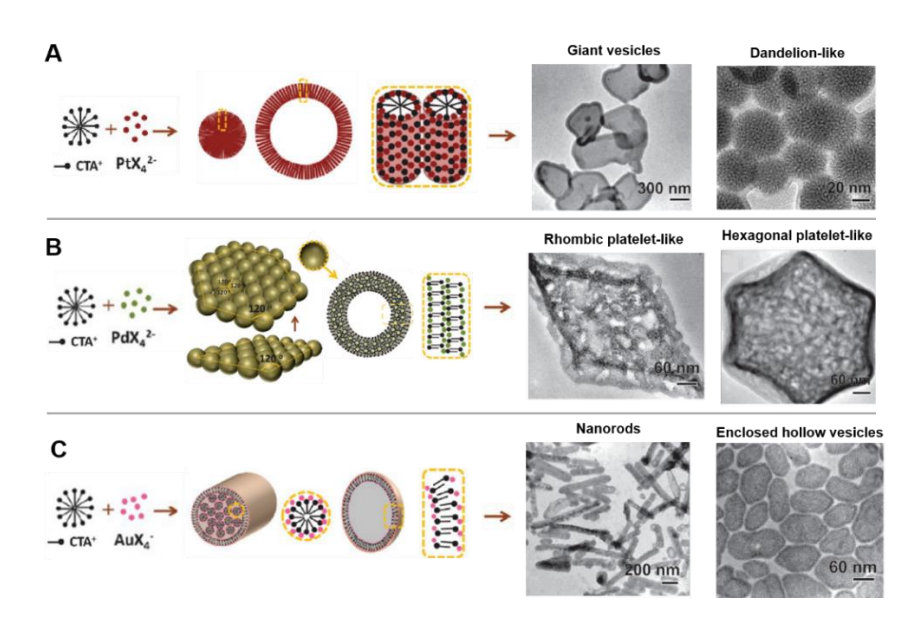


Figure 2.18 Schematic representation of soft template structures with their respective TEM/HRTEM images (A) dandelion-like assemblage and hollow vesicle formed from $PtX_4^2-CTA^+$ complex; (B) various platelet assemblages formed from $PtX_4^2-CTA^+$ complex; (C) rod-shaped and spherical vesicles formed from $AuX_4^2-CTA^+$ complex. Various morphologies resulted from varying CTAB concentration, temperature and stirring rate. Figure adapted with permission from Reference [30]. Copyright 2014 American Chemical Society.

As a result, nanosheets having a single cluster thickness were formed at the BE/LP interface. This liquid-liquid interface acted as a micro-soft template and directed the 2D self-assembly. The structural evolution of the self-assembled architectures into isolated nanosheets with uniform size and shape was tuned by controlling the evaporation rate of the solvents.

The *in-situ* formation of mesoscale hierarchical assemblies of Au, Pt, and Pd NCs characterized by the well-defined boundaries was achieved using variable micellar templates.³⁰ These giant variable micelles were prepared in water by reacting metal halides with cetyltrimethylammonium bromide (CTAB) and thiourea leading to formation of CTA⁺–MX₄²⁻ complexes.

The control over geometric shape, hierarchical organization, and packing density of the assemblies could be realized by varying the metal precursor and CTAB concentration. These assemblies "inherited" pristine shapes from their respective micelle templates. Accordingly, rod-like, dandelion-clock-like, and rhombic/hexagonal platelet assemblies were obtained from Au, Pt, and Pd NCs, respectively (**Figure 2.18**).

2.4.2.2 Hard templates

Hard templates provide less control over the periodicity of the formed assemblies. The choice of the right template is dictated by its morphology and functionality.

Reduced graphene oxide (rGO) proved to be an excellent platform for the growth of anchoring functional nanomaterials, given its strong absorption and moderate reduction towards metal ions in solution. rGO sheets were employed as a template for growth of Au NCs to produce hybrid materials with enhanced electrocatalytic performance in oxygen reduction reaction (ORR).³¹ This novel strategy allowed to grow Au (and other metals such as Pd or Pt) clusters on the rGO in absence of protective thiol ligands or reducing agent. However, to generate metal NC/rGO hybrids selective adsorption combined with the restricted deposition of metal ions was essential. Therefore, only the rGO sheets with moderate number of heteronuclear nucleation sites gave rise to the desired hybrid materials, as it not only provided the nucleation sites for the growth of Au NCs but at the same time restricted their expansion.

2.4.3 Amphiphilicity

A wide range of nanostructures (micelles, vesicles, bilayers) can be produced when the amphiphilic molecular level surfactants or block-copolymers undergo a self-assembly. The challenging task of imparting the amphiphilicity to metal NCs could be achieved by functionalizing the surface ligands to yield a particular arrangement of both hydrophobic and hydrophilic ligands, therefore creating the NC analogues of molecular amphiphiles. Implementing the "surfactant-mimicking" strategy to drive the

self-assembly of Au_{25} NCs into regularly stacked 2D layers was reported by Yao et al.³² Amphiphilic Au_{25} NCs were prepared by modifying the hydrophilic ligand shell of $Au_{25}(MHA)_{18}$ (MHA = 6-mercaptohexanoic acid) NCs with hydrophobic cetyltrimethylammonium cations (CTA⁺) in a phase-transfer driven ion-pairing reaction (**Figure 2.19**A). The electrostatic interaction of COO⁻ groups of MHA ligands and CTA⁺ cations led to the formation of amphiphilic $[Au_{25}(MHA)_{18}@xCTA]$ (x = 6-9) NCs. The coexistence of flexible hydrophilic MHA and hydrophobic MHA····CTA ligands within the monolayer at almost equimolar ratio enabled the dissolution of Au_{25} NCs in solvents with distinctly different polarities and allowed the Au_{25} NCs to form bilayers at the air–liquid interface. Further degree of self-organization, the stacked bilayers with regular interlayer packing, was obtained by slow solvent evaporation that caused the micelles and/or vesicles in the bulk solvent to rearrange to adapt to the changing polarity (**Figure 2.19**B).

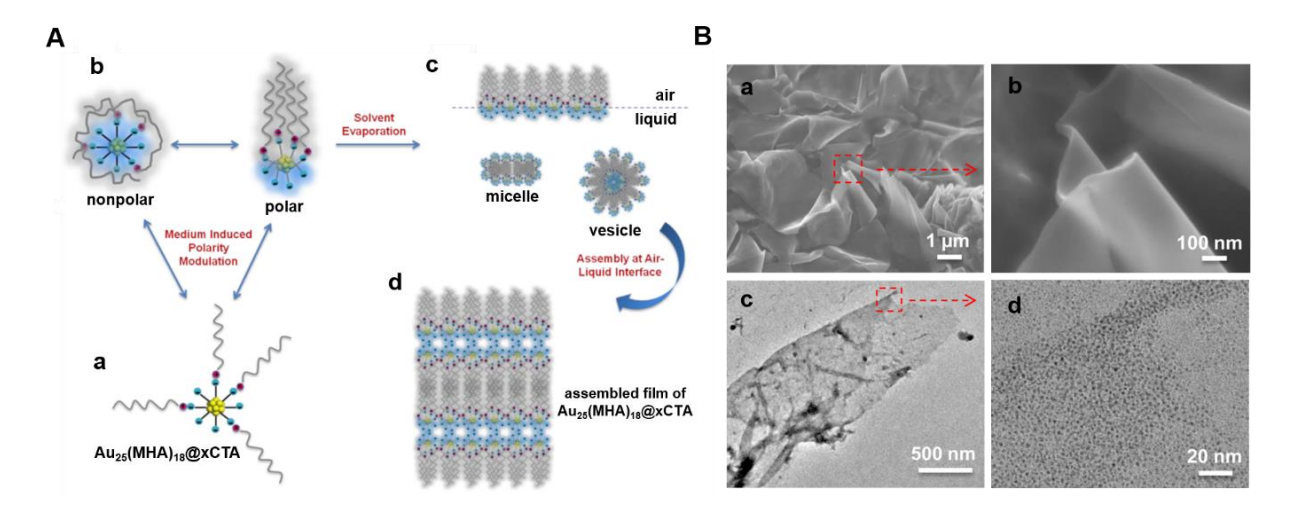


Figure 2.19 (A) Schematic illustration of the self-assembly process of $Au_{25}(MHA)_{18}@xCTA$ (x = 6-9) NCs; (B) Electron microscopy images of the $Au_{25}(MHA)_{18}@xCTA$ (x = 6-9) NCs assembled at the air-liquid interface. (B-a, b) FESEM images depicting a deformable (presence of creases) flexible sheet-like structure (thickness ~15 nm); (B-c) TEM images of a single-NC-thick sheet folded in several places; (B-d) HRTEM depicting small Au_{25} NCs (< 2 nm). Figure adapted with permission form Reference [32]. Copyright 2015 American Chemical Society.

2.5 Three-dimensional (3D) metal nanocluster assemblies

The principles of NC assembly governing the realization of 3D structures are similar to these in 1D and 2D formation, although different ligands are employed to connect the metal NC units. Generally, the 3D assemblies possess stronger framework than 2D structures, making the 3D assembly an effective strategy to enhance the NC stability.

2.5.1 Ion-ion interactions

Metal NCs can form assemblies directed via ion-ion interactions. Indeed, Yao et al. demonstrated for the first time the successful formation of metal NCs assemblies in aqueous solution.³³ Their method exploited the electrostatic interactions between hydrophilic ligands protecting the Au NCs (more specifically the dissociated carboxyl groups of glutathione) and divalent countercations (Zn²⁺ and Cd²⁺) introduced to the solution. Interestingly, the Au NCs protected with hydrophilic thiolate ligands acted as 3D nano-ions owing to their high charge density, ultrasmall size, and structural uniformity. In fact, these clusters displayed ion-like behaviour as the assembly proceeded in a step-like fashion to ultimately occur after the divalent metal cation-to-thiolate-ligand ratio ($R_{\text{M}2+\text{V}\text{I}-\text{SR}}$) exceeded specific threshold values. The intercluster electrostatic linking (-COO-···M²⁺···-OOC-) led to the formation of uniformly dispersed, fractal-like spherical assemblies (Figure 2.20A). Importantly, these assemblies differed distinctly from the random colloidal nanoparticle aggregates held by counterions suggesting that the assembled NC structures possessed higher order of regularity, bearing resemblance to the ionic crystals that form in the solution. The divalent cations influenced the self-assembly in two-ways: (i) by reducing the negative charge on the Au NC through formation of intracluster electrostatic interactions (screening effect), and formation of intercluster electrostatic linkages that acted as bridges, hence propagating the growth of the assemblies.

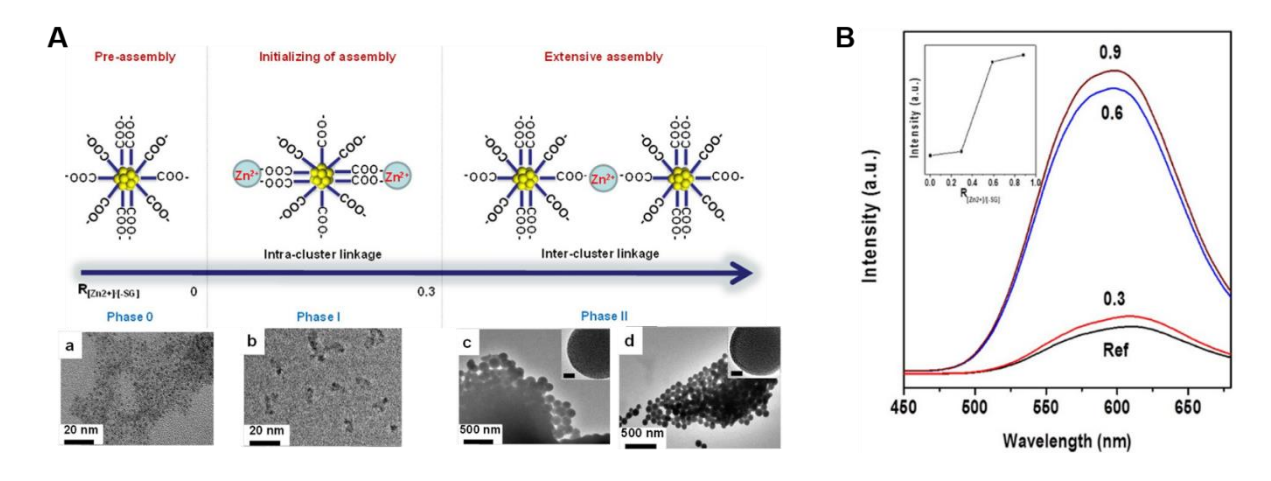


Figure 2.20 (A) Top panel: Proposed mechanism for Zn^{2+} -induced assembly of Au NCs. Bottom panel: TEM images of Au NCs assembled at different Zn^{2+} concentrations: $R_{[M2+]/[-SR]} = (a)$ 0; (b) 0.3; (c) 0.6; (d) 0.9. Insets in (c) and (d) show the corresponding HRTEM images (scale bar: 20 nm); (B) PL emission spectra (excited at 365 nm) of Au NCs assembled under different $R_{[M2+]/[-SR]}$ values: 0 (black trace); 0.3 (red trace); 0.6 (blue trace), and 0.9 (brown trace). The inset shows the emission intensity maximum as a function of $R_{[M2+]/[-SR]}$. Figure reproduced from Reference [33]. Published by Springer-Nature.

Moreover, the photoluminescence properties of the assemblies were enhanced with respect to discrete Au NCs, implying strong synergistic effects between closely packed NC units within the formed assemblies (**Figure 2.20**B).

Quite recently, the cation-induced micellization of Ag_{29} NCs was reported by Kang et al.³⁴ This strategy rendered the negatively charged hydrophobic $[Ag_{29}(SSR)_{12}(PPh_3)_4]^{3-}$ NCs $(Ag_{29}-Na_0)$ water-soluble by exploiting the cation-cluster interactions. It involved the formation of two distinct complex countercations composed of Na⁺ ions conjoined with oxygen-containing solvent molecules, $[Na(NMP)_5]^+$ $(NMP = N-methyl-2-pyrrolidine; Na_1)$ and $[Na_3(DMF)_{12}]^{3+}$ $(DMF = N,N'-dimethyl-formamide; Na_3)$. These "solvent-conjoined Na⁺" complex cations acted both as countercations to anionic Ag_{29} clusters (yielding the $Ag_{29}-Na_1$ and $Ag_{29}-Na_3$ structures, **Figure 2.21**A) and surface cosolvent of the formed 3D Ag_{29} -based micelles in the aqueous phase (HAADF-STEM images of micellization process depicted in **Figure 2.21**C).

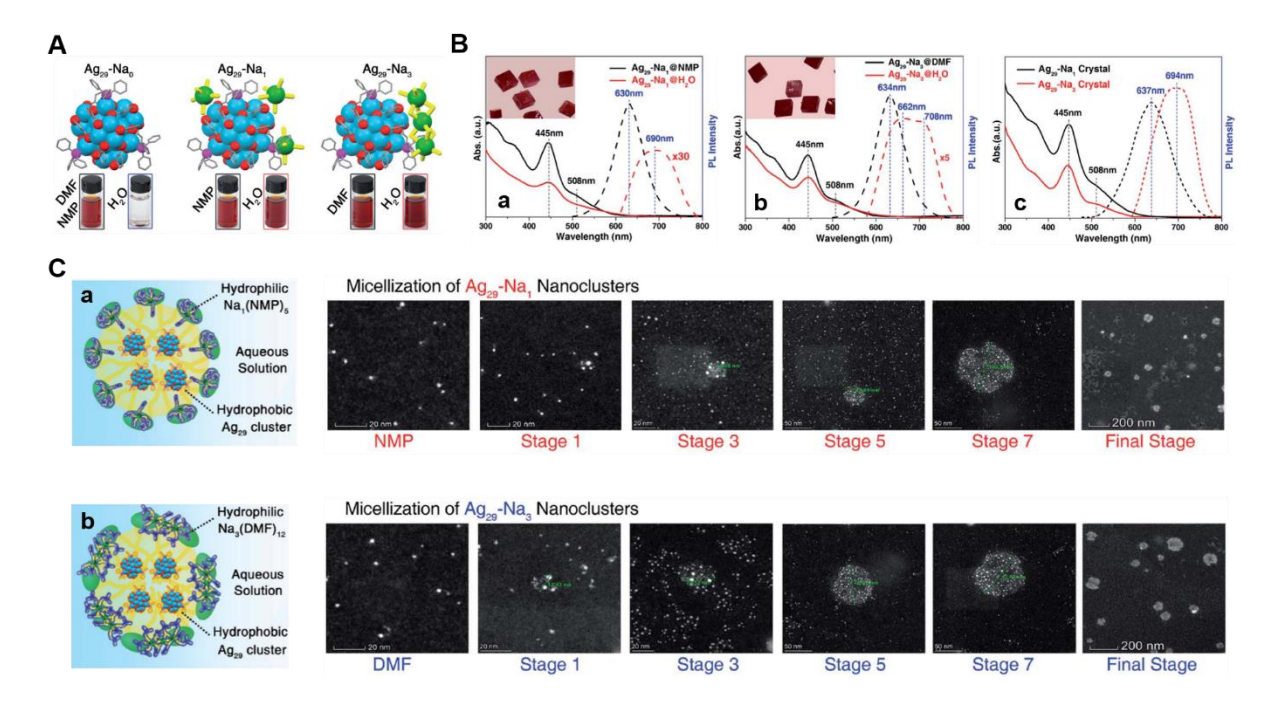


Figure 2.21 (A) Structure of Ag29-Na₀, Ag29-Na₁, and Ag29-Na₃ and their respective solutions in DMF, NMP, and H₂O; (B) Optical absorptions and emissions of (B-a) Ag29-Na₁ in NMP (black trace) and H₂O (red trace). Inset: digital photograph of Ag29-Na₁ crystals; (B-b) Ag29-Na₃ in DMF (black trace) and H₂O (red trace). Inset: digital photograph of Ag29-Na₃ crystals; (B-c) Ag29-Na₁ (black trace) and Ag29-Na₃ (red trace) in the crystalline state; (C) Micellization of (C-a) Ag29-Na₁ (C-b) Ag29-Na₃ nanoclusters. Left panels: the schematic illustration of the micelle formation; right panels: the aberration-corrected HAADF STEM images of Ag29-Na_x micelles. Figure reproduced from Reference [34]. Published by The Royal Society of Chemistry.

The cation-induced micellization of nanoclusters was shown to work for other hydrophobic negatively-charged clusters: $[Au_{25}(SR_I)_{18}]^-$, $[Ag_{25}(SR_2)_{18}]^-$, $[Pt_1Ag_{24}(SR_2)_{18}]^2^-$, $[Ag_{44}(SR_3)_{30}]^4^-$, $[Au_{12}Ag_{32}(SR_3)_{30}]^4^-$, and $[Ag_{28}Cu_{12}(SR_4)_{24}]^4^-$ ($R_I = C_2H_4Ph$; $R_2 = SPhMe_2$; $R_3 = SPhF_2$; $R_4 = SPhCl_2$).

2.5.2 Ag-O, Ag-S and Ag-Cl bond formation

Ag NCs are excellent building blocks for constructing the superstructures because they offer the advantage of good connectivity with many ligands/linkers thus enabling the versatile structures.

Mak and co-workers reported the formation of a covalent 3D metal-organic framework, $[Ag_3\{Ag_{14}(S-iPr)_6(CF_3COO)_{11}(H_2O)_3(CH_3OH)]\cdot (H_2O)_{2.5}]_n$ utilizing the ellipsoidal $Ag_{14}(S-iPr)_6$ NCs as building blocks. The adjacent $Ag_{14}(S-iPr)_6$ NC units were connected through Ag–O–Ag bonds created between the trifluoroacetate anions and isolated Ag^I ions (**Figure 2.22**A). Each $Ag_{14}(S-iPr)_6$ cluster was linked with six identical neighbouring NCs in a distorted octahedral manner (**Figure 2.22**B). This led to formation of a convoluted 3D net with single hexaconnected node (**Figure 2.22**C).

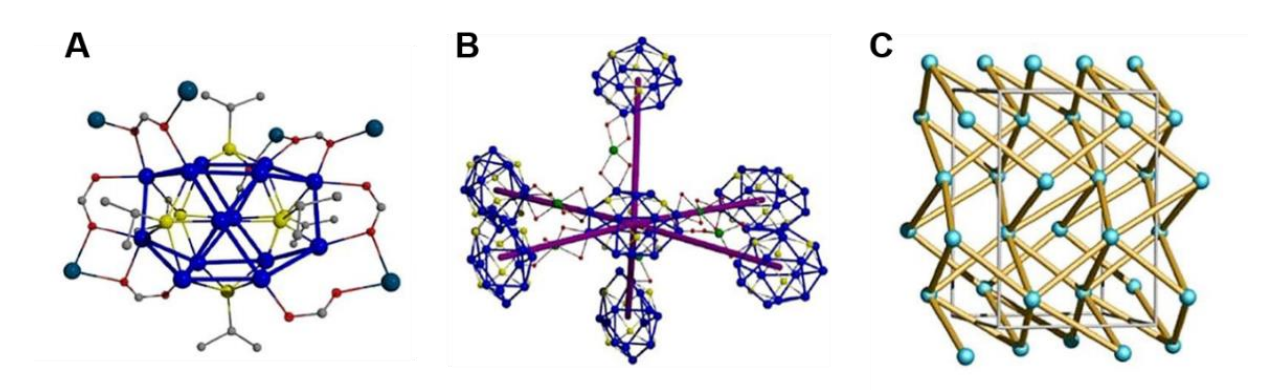


Figure 2.22 (A) Molecular cluster-based building block Ag14(S-iPr)6 with its six Ag¹ binding sites (in cyan); (B) Ball-and-stick diagram depicting the spatial arrangement of a centre Ag14(S-iPr)6 surrounded by six adjacent clusters in an octahedral geometry; (C) 3D unimodal hexaconnected network of Ag14(S-iPr)6NCs (each cluster represented by a light blue node). Colour codes: Ag-blue, cyan, light blue; S-yellow; O-red; C-grey. Reproduced with permission from Reference [35]. Copyright 2017 Wiley-VCH.

Gao et al. employed a multi-sulfur ligand to construct a new Ag-NC based 3D structure.³⁶ The advantage of multi-sulfur linker resides not only in the ability to stabilize Ag^I cluster building units via the Ag···S bonds but also in its flexible coordination mode that can afford 3D arrangement of adjacent clusters.

The Ag^I NC-based porous network was obtained in a two-step process that involved primarily the synthesis of discrete Ag NCs building units, $Ag_{11}S(C_5NS_2H_{10})_9$ ($C_5NS_2H_{10} = diethylthiocarbamate$), which were subsequently converted to { $[Ag_{17}(C_5NS_2H_{10})_{14}]_n \cdot 7n$ (CH₃)₂CO}, (UJN-1) in a solvothermal process (**Figure 2.23**A). Additionally, the chemical treatment of UJN-1 with NaBH₄ afforded reduced UJN-1 heterostructure containing both Ag^I and Ag^0 . Owing to the generation of Ag^0 "hot spots" within the reduced UJN-1, this material was found to exhibit highly sensitive SERS reactivity towards *p*-MBA molecules (**Figure 2.23**B).

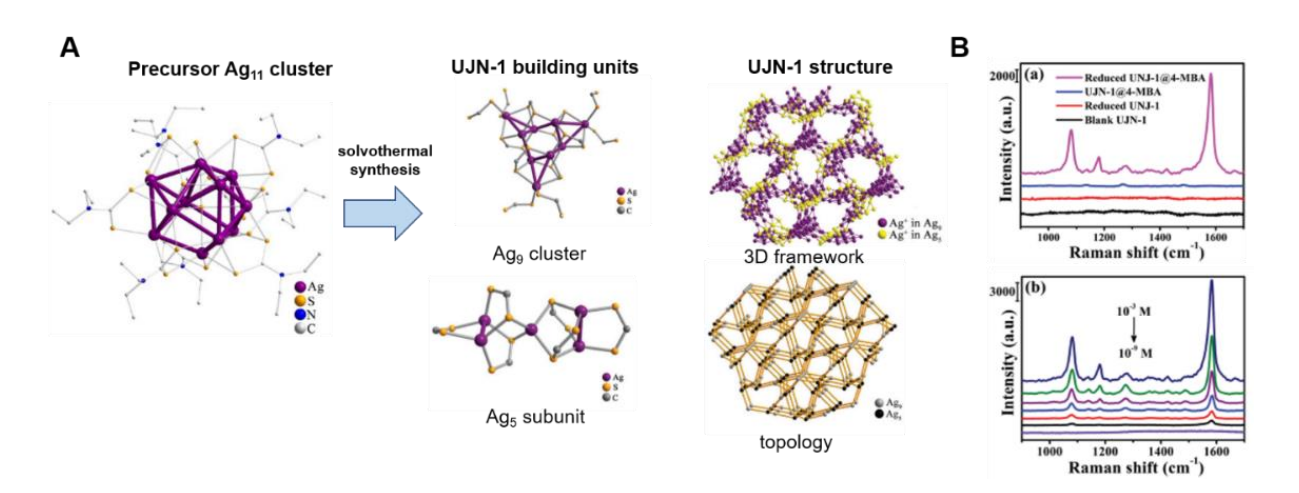


Figure 2.23 (A) Crystal structure of $Ag_{11}S(C_5NS_2H_{10})_9$ NC serving as a precursor to UJN-1 Ag_9 and Ag_5 building blocks assembled in 3D hexagonal system. (B) SERS spectra of (B-a) UJN-1 and the reduced UJN-1 substrates with or without adsorption of 10^{-3} M ethanolic solution of p-MBA, (B-b) p-MBA with different concentrations on the reduced UJN-1 substrate. Figure adapted with permission form Reference [36]. Copyright 2019 The Royal Society of Chemistry.

2.5.3 Control of counterions

It has been demonstrated that the self-assembly between the metal nanoclusters and small inorganic ions can lead to formation of 3D superstructures.³⁷ The recent report from Zhu's group shows the formation of two novel types of open-framework 3D structures which were named "superatom complex inorganic frameworks (SCIFs)".³⁸ The framework building units consisted of chiral cationic heterometal cluster, $[Au_1Ag_{22}(S-Adm)_{12}]^{3+}$, (S-Adm = 1-adamantanethiolate) and inorganic hexafluoroantimonate (SbF₆⁻) ion.

The SbF₆⁻ ions served not only as counterions for the charged Au₁Ag₂₂ clusters but were also protecting the silver atoms on the surface as ligands and linkers. The formation of intermolecular Ag–F bonds resulted in two types of chiral 3D open frameworks with different pore sizes that could be obtained by tuning the amount of counterion.

The chiral arrangement in the first structure, SCIF-1, results from the two enantiomers of Au₁Ag₂₂ to create interpenetrated homomultimers in a diamond topology leading to an overall racemic superstructure (**Figure 2.24**A). In the SCIF-2 structure, however, the left- and right-handed Au₁Ag₂₂ enantiomers were packed in separate (enantiomerically-pure) crystals (**Figure 2.24**B) leading to formation of a framework with larger channels displaying unique circularly polarized luminescence (CPL) properties (**Figure 2.25**A). Additionally, both SCIF materials exhibited a photoluminescence (PL) "switching behaviour" in an aggregated (solid) state: the PL was "off' under vacuum with no solvents, and "on" with strong red PL in the presence of protic solvents, making the SCIF materials potential sensors for polar solvents.

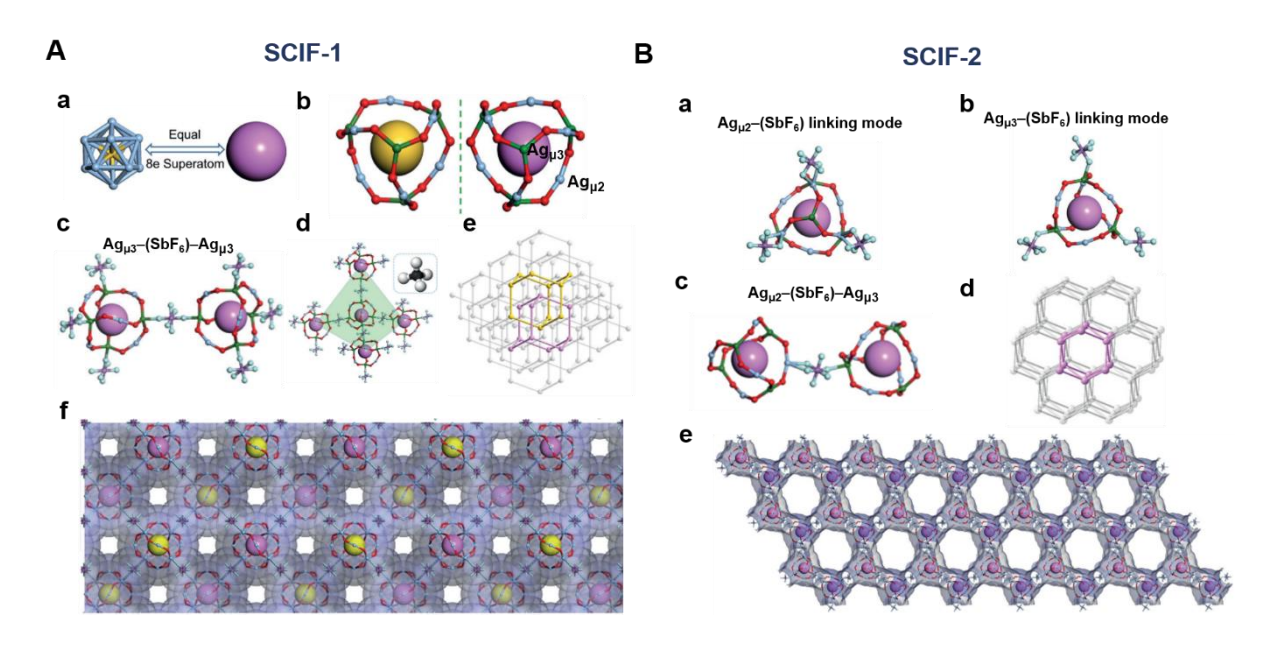


Figure 2.24 (A) Crystal and channel structure of SCIF-1 network. (A-a) Icosahedral Au₁Ag₁₂ core; (A-b) A pair of Au₁Ag₂₂ isomers; (A-c) Two NCs connected with SbF₆⁻ linker; (A-d) Tetrahedral arrangement of Au₁Ag₂₂ NCs; (A-e) Diamond topology structure adopted by the Au₁Ag₂₂ NCs in the solid state; (A-f) Interconnected channels of Au₁Ag₂₂ along the z-axis. (B) Crystal and channel structure of SCIF-2 network. Linking mode of SbF₆⁻ linker with (B-a) Ag_{µ2} atoms and (B-b) Ag_{µ3} atoms in the Au₁Ag₂₂ NC; (B-c) Two Au₁Ag₂₂ NCs connected with SbF₆⁻ linker; (B-d) Hexagonal network structure adopted by Au₁Ag₂₂ in SCIF-2; (B-e) Hexagonal channel structure in SCIF-2. Colour codes: Ag_{µ2}-pale blue, Ag_{µ3}-green, S-red, F-light turquoise, Sb-purple. C and H atoms omitted for clarity. Figure adapted with permission from Reference [38]. Copyright 2020 Wiley-VCH.

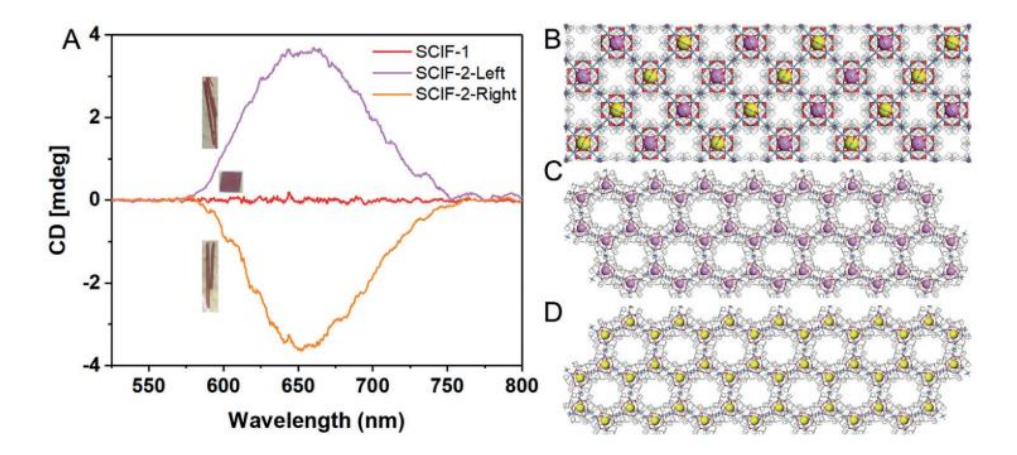


Figure 2.25 (A) CPL spectrum of racemic SCIF-1 resulted from (B) interpenetrating structure of left- and right-handed networks in its structure and chiral SCIF-2 network that was obtained by Au₁Ag₂₂ enantiomers packed in two crystal arrays: (C) left-handed SCIF-2 and (D) right-handed SCIF-2. Figure reproduced with permission form Reference [38]. Copyright 2020 Wiley-VCH.

2.5.4 Molecular linkers

This strategy is employed to produce the metal-organic frameworks (MOFs) based on NC building units. NC-MOF assembly is driven by coordinative interactions between metal ions and NCs functionalized with suitable binding units. The 3D architecture composed of metal NCs not only yields the metal NCs

more stable but affords the porous structures capable of adsorbing gas molecules within their cages. Because of their narrow pores, such structures have the potential to act as highly selective catalysts, in a similar fashion to conventional MOF materials. More importantly, since metal NCs serve as nodes more variety for coordination direction with respect to simple metal ions exists, giving the possibility to create novel framework structures.

Interestingly, before the metal NCs started to be exploited as nodes to construct the 3D framework materials, they were used as linkers. The cluster-linker approach was used by Lei et al. to prepare porous highly emissive framework by linking Ag ions with luminescent Au^I clusters, $[(C)-(Au-mdppz)_6](BF_4)_2]$ (mdppz = 2-(3-methylpyrazinyl)diphenylphosphine), containing hypercoordinated carbon in the centre of hexagold^I octahedral core.³⁹ The Au^I cluster-linker with its six coordination points, provided by the outward N donors of mdppz ligands, was capable of binding metal ions (**Figure 2.26**A). Consequently, a 3D structure consisting of two interpenetrating frameworks with NbO topology was formed. The 1D hexagonal channels of ~1.1 nm featuring along the *c*-axis (**Figure 2.26**B) were capable of accommodating solvent molecules.

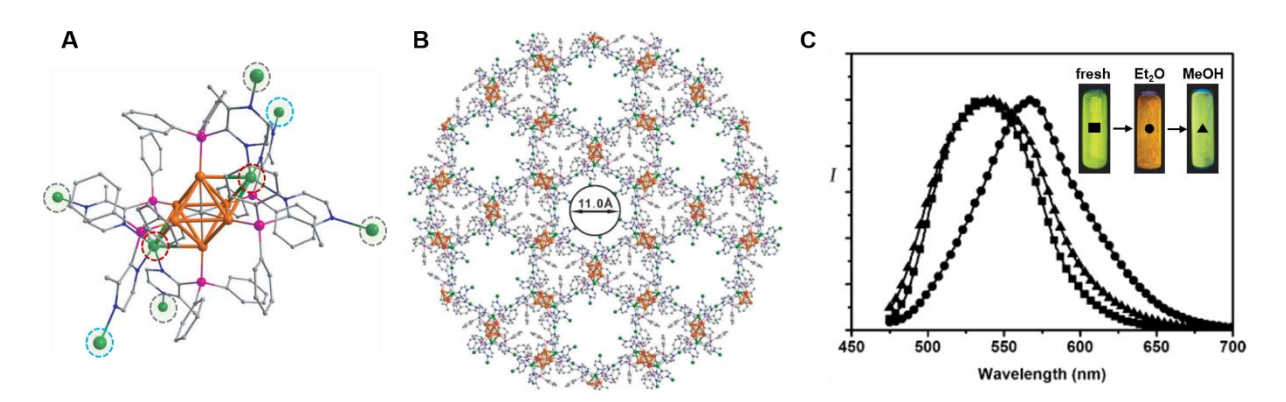


Figure 2.26 (A) Structure of the building unit of 3D $[(C)-(Au-mdppz)_6](BF4)_2]$ assembly depicting three crystallographically different Ag atoms: coordinating to outward N donor of mdppz and involved in structural extension (circled in grey), coordinating to outward N donor of mdppz but not involved in structural extension (circled in blue), coordinating to inward N donors in mdppz (circled in red); (B) 3D crystal structure of NC-MOF along the c-axis. Colour code: Au-orange, Ag-green, P-purple, N-blue, C-grey, H atoms omitted for clarity; (C) Emission spectra of (\blacksquare) freshly prepared MOF, (\bullet) MOF soaked with Et₂O, and (\blacktriangle) MOF soaked with Et₂O, then with MeOH. Inset shows the digital photographs of samples. Figure adapted with permission from Reference [39]. Copyright 2014 Wiley-VCH.

The assembled cluster-based MOF was found to be highly emissive in the solid state. Green emission was centred at 539 nm under UV excitation, the emission lifetime of $4.67 \pm 0.28 \,\mu s$ was $1.6 \,times$ higher than in the single Au^I NC. Moreover, the significant increase in PL quantum yield (Φ_{PL}) of the 3D structure from $1.5 \,\%$ for Au^I NC to $25.6 \,\%$ for the 3D network was observed. The large Stokes shift and the PL lifetime (in the order of microseconds) strongly suggested that this material was phosphorescent. Further investigation revealed the influence of silver atoms on the PL behaviour of the assembled species. The ligation of Ag to the inwards N donors of the mdppz linker contributed to the red-shift of the solid state emission form single Au^I NC to 3D network, while the coordination of other

Ag atoms outward N donors to yield the rigid porous superstructure gives rise to higher Φ_{PL} . Interestingly, the assembled NC-based MOF showed the solvatochromic behaviour. The solvent molecules were coordinating to the Ag ions accessible within the channels of the superstructure, which was accompanied with the luminescence responses (**Figure 2.26C**).

Mak and co-workers have been extensively studying the formation of 3D MOF materials using various types of Ag NCs as nodes. In 2017 they reported the first synthesis of a cluster-based metal organic framework. An Dodecanuclear silver clusters, $[Ag_{12}(S'Bu)_6(CF_3COO)_6(CH_3CN)_6] \cdot CH_3CN$, were bridged with the bidentate linear 4,4'-bipyridine (bpy) to form a rigid Ag_{12} -based MOF with a bilayer structure (Figure 2.27A). Markedly enhanced stability (from 30 minutes to one year) under ambient conditions combined with ca. 60-fold increase in the RT photoluminescence quantum yield (Φ_{PL} from 0.2 to 12.1%) were observed from a single Ag_{12} NC to Ag_{12} bpy MOF. Moreover, owing to its tuneable electronic properties (responsible for emission) and rigid open channels the Ag_{12} bpy MOF showed ultrafast dual-function photoluminescence switching, with the "OFF" function activated by molecular O_2 (Figure 2.27B) and multicolour "ON" switching by the volatile organic compounds (VOC, Figure 2.27C).

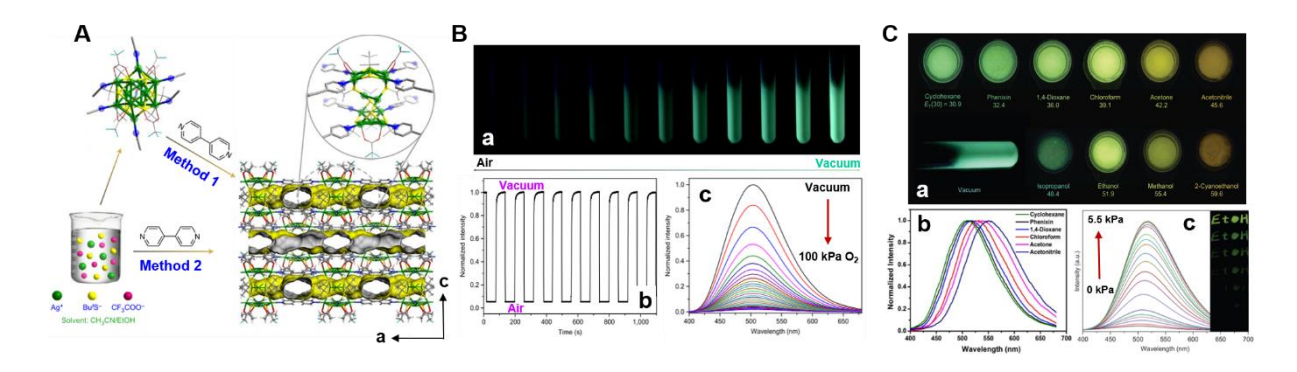


Figure 2.27 (A) Schematic representation of the ligand-exchange strategy employed to produce Ag12bpy crystals (Method 1, giving low yield) and one-pot synthesis (Method 2, gram-quantity sample) under identical conditions. Interconnected channels of Ag12bpy viewed along the **a** and **b** axes, yellow surface represents the pore surface. Colour code: Ag-green, C-grey, O-red, S-yellow, F-turquoise; (B) Luminescent quenching response to O2. (B-a) Digital photographs of Ag12bpy excited at 365 nm in a glass tube from vacuum to air (right to left); (B-b) Reversible luminescence on-off cycles under alternating exposure to air/vacuum for Ag12bpy; (B-c) Emission spectra at different O2 pressures (excited at 365 nm) form vacuum to 100 kPa O2; (C) Vapochromic responses of Ag12bpy. (C-a) Digital photographs of luminescence responses of Ag12bpy ·VOC under an UV lamp (365 nm); (C-b) Emission spectra of Ag12bpy ·VOCs (VOCs (trace colour) = cyclohexane (green), Phenixin (black), 1,4-dioxane (blue), chloroform (red), acetone (magenta), and acetonitrile (dark blue) (C-c) Emission spectra of Ag12bpy at different EtOH partial pressure (excitation at 365 nm) in the air mixture. Reproduced with permission from Reference [40]. Copyright 2017 Springer-Nature.

In the following years, many reports emerged describing the formation of 3D assemblies using small Ag NC as nodes and various organic, usually *N*-containing, linkers. For example, Wang et al. employed $Ag_{14}(C_2B_{10}H_{10}S_2)_6$ ($C_2B_{10}H_{10}S_2 = 1,2$ -dithiolate-*o*-carborane) NCs linked with bpy to yield a 3D FCC structure. However, the structure was unstable upon solvent evaporation. Employing

1,4-bis(4-pyridyl)benzene linkers instead resulted in a stable structure with stronger framework due to smaller pore size.⁴¹

A flexible luminescent Ag NC-based MOF was constructed with $Ag_{10}(S-Bu)_6(CF_3COO)_2(PhPO_3H)_2$ linked via bpy forming 2D layers connected with each other with hydrogen bond $(O-H\cdots O)$ and $C-H\cdots O$ interactions, to form the 3D connected $Ag_{10}(bpy)$ assemblies (**Figure 2.28**A).

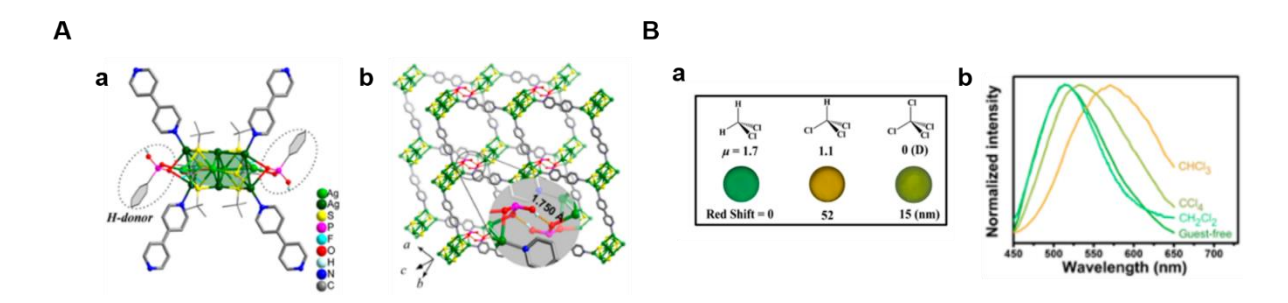


Figure 2.28 (A) Structure of $Ag_{10}(S^{-1}Bu)_6(CF_3COO)_2(PhPO_3H)_2$ -based MOF. (A-a) Perspective view of the $Ag_{10}(S^{-1}Bu)_6$ core; (A-b) two-layer stack of the flexible Ag MOF depicting the hydrogen bonding between the interlayer $-PO_2OH$ moieties. (B) Luminescence responsive upon 365 nm excitation (B-a) images of $Ag_{10}(bpy)$ MOF upon adsorption of different chloromethanes; (B-b) normalized PL spectra guest-free MOF and $Ag_{10}(bpy)$ MOF upon exposure to chloromethane vapours. Figure adapted with permission from Reference [42]. Copyright 2018 American Chemical Society.

These weak interactions allowed the framework breathing phenomenon to occur upon adsorption of VOC, which was accompanied by significant luminescence change. Specifically, the chloromethanes (CH₂Cl₂, CHCl₃, CCl₄) could be clearly distinguished given their distinctly different luminescence responses (**Figure 2.28**B).

2.5.5 Intraligand interactions

2.5.5.1 Electrostatic and hydrogen-bonding interactions

Mastering a delicate balance between the hydrogen-bond and electrostatic interaction can afford the self-assembly of metal NCs into superstructures with distinct symmetries and morphologies. The formation of superlattice composed of $[Na_4Ag_{44}(p-MBA)_{30}]$ (p-MBA = para-mercaptobenzoic acid) was reported by Yoon et al.⁴³ This superlattice was held together by intricate network of hydrogen bonds that acted as structure directing "synthons" leading to rhombus-shaped supracrystals (**Figure 2.29**A). The single crystal X-ray analysis revealed that the fully protonated carboxylic groups of p-MBA ligands were involved in an intralayer bonding of Ag_{44} NCs via dimeric bundles and interlayer bonding between neighbouring Ag_{44} NCs through triple-bundles (**Figure 2.29**B). Such anisotropic distribution of hydrogen bonds across the crystal facilitated the chiral rotation of Ag_{44} NCs in the superlattice upon exposure to hydrostatic compression (**Figure 2.29**C).

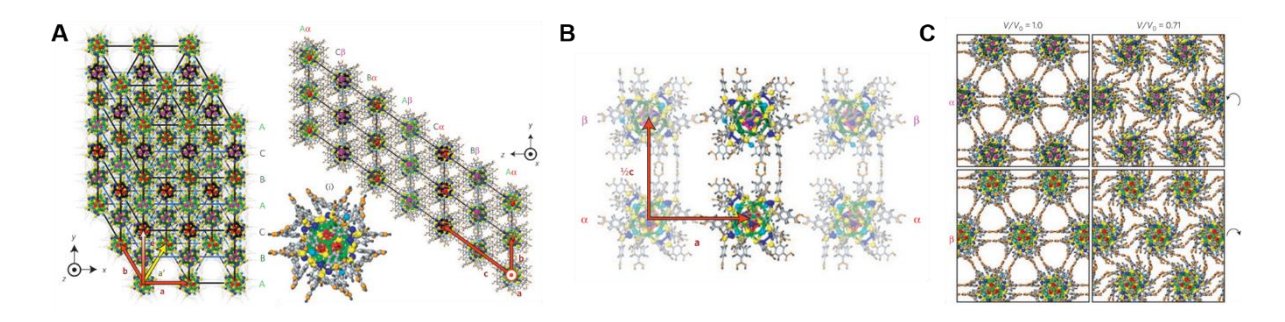


Figure 2.29 (A) 3D view of the superlattice structure with the triclinic unit-cell vectors. The unit cell contains two Ag44 NCs denoted with red and purple colour of their Ag12 cores. A view of a single Ag44 depicted in the inset. The Ag44 are organized in layers, each of them containing the identical NCs. The neighbouring layers were denoted by α and β . (B) The view illustrating the interlayer $(\alpha-\beta)$ hydrogen bonding occurring through twofold bundled ligands, and intralayer $(\alpha-\alpha$ and $\beta-\beta)$ hydrogen bonding involving triply bundled ligands; (C) Superlattice compression and rotational structural transition. Arrangement of the Ag44 NCs in two neighbouring layers $(\alpha$ and $\beta)$ viewed in the ab plane. The configurations on the left correspond to P=0 equilibrium state (the compression parameter $(V/V_0)=1$, where V_0 is the initial, equilibrium volume of the unit cell). The configurations on the right correspond to final state of the volume compression process, $(V/V_0)=0.71$. All Ag44 in the same layer $(\alpha$ or $\beta)$ rotate in unison, but the NCs' rotations in the two layers are in opposite senses—anticlockwise in the α layer and clockwise in the β layer. Colour codes: Ag-red, purple, green, blue; S-yellow; C-grey; O-orange, H-light blue. Figure adapted with permission from Reference [43]. Copyright 2014 Macmillan Publishers Limited.

Elimination of any directional hydrogen bonding by complete deprotonation of p-MBA ligands and subsequent introduction of Cs⁺ counterions to a dual-solvent crystallization system (DMSO/H₂O) resulted in octahedrally-shaped supracrystals of Ag₄₄(p-MBA)₃₀⁴⁻ NCs.⁴⁵ Remarkably, by further tuning the solvent polarity and ionic strength the crystallization kinetics could be modified via electrostatic interactions and as a result the shape of supracrystals could be altered to a concave octahedron.

2.5.5.2 van der Waals interactions ($\pi \cdots \pi$ interactions, CH $\cdots \pi$ interactions)

These types of interactions are mostly implicated in crystallization of metal NCs and were shown to be quite effective in inducing aesthetic and hierarchical molecular packing patterns at both the intra- and intercluster levels. In this way maximizing the binding between the clusters within the supercrystals can be ensured.

The single crystal X-ray study of large $Au_{246}(p\text{-MBT})_{80}$ (p-MBT = para-methylbenzenethiolate) NCs performed by Zeng et al. allowed to obtain a precise structural information regarding the assembly at the different levels: atomic (packing of Au atoms), molecular (packing of surface ligands) and nanoscale (packing of NCs). Feeting the p-MBT ligands were found to self-organize into two highly ordered patterns with different symmetry and packing density, i.e. α -rotational and β -parallel packing (**Figure 2.30**A).

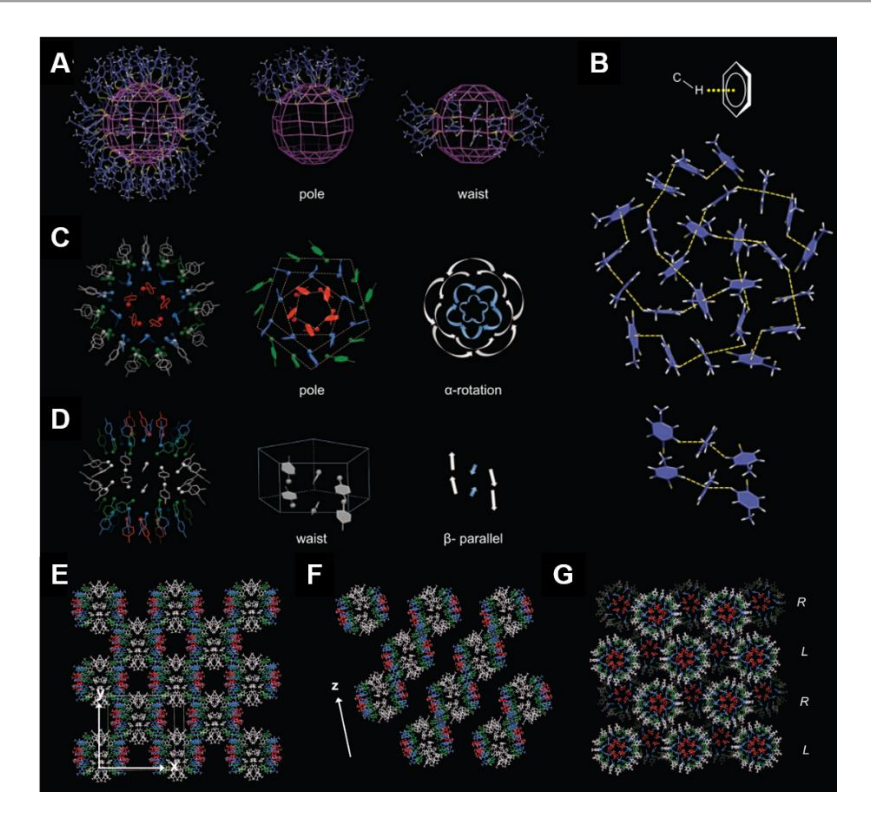


Figure 2.30 Self-assembled surface patterns of the p-MBT ligands on the Au₂₄₆ NC. (A) Overall structure of the ligands on the surface of NCs; (B) The $C-H\cdots\pi$ interactions for stabilizing the large-scale rotational and parallel patterns; (C) Rotational packing of ligands at the pole site of the NC; (D) Parallel packing of ligands at the waist of the NC. Packing structure of Au₂₄₆ NC in single crystals. (E-G) Alignment of p-MBT ligands among the Au₂₄₆ NCs. Colour codes: Grey-ligands located at the waist of the NC; red, blue, and green-ligands located at the poles. Figure reproduced with permission from Reference [46]. Copyright 2016 The American Association for the Advancement of Science.

The rotational packing of the p-MBT ligands, formed at the pole sites of the Au₂₄₆ NCs, was found to be a more preferred p-MBT alignment, indicated by its higher packing density (~14 ligands·nm⁻²). The less dense β parallel pattern (~6 ligands·nm⁻²) assembled around the equatorial belt of the NC (**Figure 2.30**C-D). Such an arrangement of the p-MBT ligands into complex patterns on the Au₂₄₆ surface was shown to be stabilized by intermolecular C–H··· π interactions (**Figure 2.30**B). Moreover, the ligands affected not only the NCs shell but also the packing structure of NCs within the crystal. The authors showed that the nonuniform but symmetric distribution of p-MBT on the cluster surface gave rise to directional "sticky bonds" which have driven the self-assembly into lattices with orientational, rotational and translational order (**Figure 2.30**E-F).

2.6 Conclusions

Ligand protected metal NCs have been successfully applied as building blocks to realize hierarchical superstructures produced via self-assembly. Their self-assembly was found to be driven by various interactions inherent to the nanocluster surface (e.g., metallophilic, H-bonding, dipolar, van der Waals, electrostatic). Moreover, different methods to connect the metal NCs were explored: direct connection

via metal-metal bonds, connection via heteroatoms (Ag-O, Ag-S or Ag-Cl), counterions, linker molecules and interligand interactions. The prevailing number of the assembled structures was produced via the linker molecules and heteroatom connections. The design of both the connecting linker as well as the right choice of protecting ligand on the metal NCs is of utmost importance for creating assemblies via these methods. Thus far, mainly Au and Ag NCs were used to create the superstructures, owing to their stability and well-understood structures and properties. However, application of other metal NCs is expected to follow. Assembly of metal NCs into superstructures was found to influence their properties and gave rise to new collective phenomena such as electronic coupling, photoluminescence, and magnetic exchange coupling. Furthermore, the formation of NCs superstructures, largely improved the stability of the NC units, independently of the connecting mode. Quite often the formation of assemblies led to the narrowing of the HOMO-LUMO gap opening the possibility to use broader wavelength of light, which is of interest for exploring the visible-light-driven photocatalysis with NC assemblies. Photoluminescence emission intensity was found to increase, especially for the 2D and 3D assemblies connected via linkers. Notably, the luminescence could be switched by the VOC guest molecules adsorbed in the pores of 3D assemblies. As demonstrated, electrical conductivity was found to hugely rely on the distance between the metal NC units and the mode of connection between them, i.e., direct metal-metal connection is preferred over linking via the counterion.

Despite the recent progress in the formation of superstructure, still several limitations persist. For example, the self-assembly of water-soluble metal NCs poses a challenge. The lack of well-resolved crystal structures for these NCs limits our understanding of their structure-property relationship. Though covalent modification offers routes for NCs oligomers, controlled long-range assembly via oligomerization is a technique that remains underexplored and could potentially pave the way to achieve the metamaterials from atomically precise nanoclusters. For that, controlling the spatial separation and orientation between the metal NCs is needed. Furthermore, it is important to shed a light on how the controlled assembly of NCs into superstructures dictates the photoluminescence and conductivity properties of these materials.

2.7 References

- Akola, J.; Kacprzak, K. A.; Lopez-Acevedo, O.; Walter, M.; Grönbeck, H.; Häkkinen, H., Thiolate-Protected Au₂₅ Superatoms as Building Blocks: Dimers and Crystals. *The Journal of Physical Chemistry C* 2010, 114 (38), 15986-15994.
- Lahtinen, T.; Hulkko, E.; Sokołowska, K.; Tero, T.-R.; Saarnio, V.; Lindgren, J.; Pettersson, M.; Häkkinen, H.; Lehtovaara, L., Covalently Linked Multimers of Gold Nanoclusters Au₁₀₂(p-MBA)₄₄ and Au_{~250}(p-MBA)_n. Nanoscale 2016, 8 (44), 18665-18674.
- 3. Sokolowska, K.; Hulkko, E.; Lehtovaara, L.; Lahtinen, T., Dithiol-Induced Oligomerization of Thiol-Protected Gold Nanoclusters. *The Journal of Physical Chemistry C* **2018**, *122* (23), 12524-12533.

- 4. Sels, A.; Salassa, G.; Cousin, F.; Lee, L.-T.; Bürgi, T., Covalently Bonded Multimers of Au₂₅(SBut)₁₈ as a Conjugated System. *Nanoscale* **2018**, *10* (26), 12754-12762.
- 5. Ho-Wu, R.; Sun, K.; Goodson, T., Synthesis and Enhanced Linear and Nonlinear Optical Properties of Chromophore–Au Metal Cluster Oligomers. *The Journal of Physical Chemistry C* **2018**, *122* (4), 2315-2329.
- Link, S.; Beeby, A.; FitzGerald, S.; El-Sayed, M. A.; Schaaff, T. G.; Whetten, R. L., Visible to Infrared Luminescence from a 28-Atom Gold Cluster. *The Journal of Physical Chemistry B* 2002, 106 (13), 3410-3415.
- 7. Devadas, M. S.; Kim, J.; Sinn, E.; Lee, D.; Goodson, T.; Ramakrishna, G., Unique Ultrafast Visible Luminescence in Monolayer-Protected Au₂₅ Clusters. *J Phys Chem C* **2010**, *114* (51), 22417-22423.
- 8. Wu, Z.; Jin, R., On the Ligand's Role in the Fluorescence of Gold Nanoclusters. *Nano Lett* **2010**, *10* (7), 2568-2573.
- 9. Bodiuzzaman, M.; Nag, A.; Pradeep Narayanan, R.; Chakraborty, A.; Bag, R.; Paramasivam, G.; Natarajan, G.; Sekar, G.; Ghosh, S.; Pradeep, T., A Covalently Linked Dimer of [Ag₂₅(DMBT)₁₈]⁻. *Chemical Communications* **2019**, *55* (34), 5025-5028.
- 10. Liu, X.; Saranya, G.; Huang, X.; Cheng, X.; Wang, R.; Chen, M.; Zhang, C.; Li, T.; Zhu, Y., Ag₂Au₅₀(PET)₃₆ Nanocluster: Dimeric Assembly of Au₂₅(PET)₁₈ Enabled by Silver Atoms. *Angewandte Chemie International Edition* **2020**, *59* (33), 13941-13946.
- 11. Baksi, A.; Chakraborty, P.; Bhat, S.; Natarajan, G.; Pradeep, T., [Au₂₅(SR)₁₈]₂²⁻: a Noble Metal Cluster Dimer in the Gas Phase. *Chemical Communications* **2016**, *52* (54), 8397-8400.
- 12. Chakraborty, P.; Nag, A.; Mondal, B.; Khatun, E.; Paramasivam, G.; Pradeep, T., Fullerene-Mediated Aggregation of M₂₅(SR)₁₈⁻ (M = Ag, Au) Nanoclusters. *The Journal of Physical Chemistry C* **2020**, *124* (27), 14891-14900.
- 13. Andris, E.; Andrikopoulos, P. C.; Schulz, J.; Turek, J.; Růžička, A.; Roithová, J.; Rulíšek, L., Aurophilic Interactions in [(L)AuCl]...[(L')AuCl] Dimers: Calibration by Experiment and Theory. *Journal of the American Chemical Society* **2018**, *140* (6), 2316-2325.
- 14. De Nardi, M.; Antonello, S.; Jiang, D.-e.; Pan, F.; Rissanen, K.; Ruzzi, M.; Venzo, A.; Zoleo, A.; Maran, F., Gold Nanowired: A Linear (Au₂₅)_n Polymer from Au₂₅ Molecular Clusters. *ACS Nano* **2014**, 8 (8), 8505-8512.
- 15. Fei, W.; Antonello, S.; Dainese, T.; Dolmella, A.; Lahtinen, M.; Rissanen, K.; Venzo, A.; Maran, F., Metal Doping of Au₂₅(SR)₁₈⁻ Clusters: Insights and Hindsights. *Journal of the American Chemical Society* **2019**, *141* (40), 16033-16045.
- 16. Hossain, S.; Imai, Y.; Motohashi, Y.; Chen, Z.; Suzuki, D.; Suzuki, T.; Kataoka, Y.; Hirata, M.; Ono, T.; Kurashige, W.; Kawawaki, T.; Yamamoto, T.; Negishi, Y., Understanding and Designing One-Dimensional Assemblies of Ligand-Protected Metal Nanoclusters. *Materials Horizons* **2020**, *7* (3), 796-803.
- 17. Wu, Z.; Du, Y.; Liu, J.; Yao, Q.; Chen, T.; Cao, Y.; Zhang, H.; Xie, J., Aurophilic Interactions in the Self-Assembly of Gold Nanoclusters into Nanoribbons with Enhanced Luminescence. *Angewandte Chemie International Edition* **2019**, *58* (24), 8139-8144.
- 18. Yu, Y.; Luo, Z.; Chevrier, D. M.; Leong, D. T.; Zhang, P.; Jiang, D.-e.; Xie, J., Identification of a Highly Luminescent Au₂₂(SG)₁₈ Nanocluster. *Journal of the American Chemical Society* **2014**, *136* (4), 1246-1249.
- Gan, Z.; Lin, Y.; Luo, L.; Han, G.; Liu, W.; Liu, Z.; Yao, C.; Weng, L.; Liao, L.; Chen, J.; Liu, X.; Luo, Y.;
 Wang, C.; Wei, S.; Wu, Z., Fluorescent Gold Nanoclusters with Interlocked Staples and a Fully Thiolate-Bound Kernel. *Angewandte Chemie International Edition* 2016, 55 (38), 11567-11571.

- Yuan, P.; Zhang, R.; Selenius, E.; Ruan, P.; Yao, Y.; Zhou, Y.; Malola, S.; Häkkinen, H.; Teo, B. K.; Cao, Y.; Zheng, N., Solvent-Mediated Assembly of Atom-Precise Gold-Silver Nanoclusters to Semiconducting One-Dimensional Materials. *Nature Communications* 2020, 11 (1), 2229.
- 21. Wen, Z.-R.; Guan, Z.-J.; Zhang, Y.;Lin, Y.-M.; Wang, Q.-M., [Au₇Ag₉(dppf)₃(CF₃CO₂)₇BF₄]_n: a Linear Nanocluster Polymer from Molecular Au₇Ag₈ Clusters Covalently Linked by Silver Atoms. *Chemical Communications* **2019**, *55* (86), 12992-12995.
- 22. Li, Q.; Russell, J. C.; Luo, T.-Y.; Roy, X.; Rosi, N. L.; Zhu, Y.; Jin, R., Modulating the Hierarchical Fibrous Assembly of Au Nanoparticles with Atomic Precision. *Nature Communications* **2018**, *9* (1), 3871.
- 23. Wei, X.; Kang, X.; Zuo, Z.; Song, F.; Wang, S.; Zhu, M., Hierarchical Structural Complexity in Atomically Precise Nanocluster Frameworks. *National Science Review* **2020**, *8* (3), nwaa077
- 24. Bishop, K. J. M.; Wilmer, C. E.; Soh, S.; Grzybowski, B. A., Nanoscale Forces and Their Uses in Self-Assembly. *Small* **2009**, *5* (14), 1600-1630.
- 25. Wu, Z.; Liu, J.; Li, Y.; Cheng, Z.; Li, T.; Zhang, H.; Lu, Z.; Yang, B., Self-Assembly of Nanoclusters into Mono-, Few-, and Multilayered Sheets via Dipole-Induced Asymmetric van der Waals Attraction. *ACS Nano* **2015**, *9* (6), 6315-6323.
- Nonappa; Lahtinen, T.; Haataja, J. S.; Tero, T.-R.; Häkkinen, H.; Ikkala, O., Template-Free Supracolloidal Self-Assembly of Atomically Precise Gold Nanoclusters: From 2D Colloidal Crystals to Spherical Capsids. Angewandte Chemie International Edition 2016, 55 (52), 16035-16038.
- 27. Koivisto, J.; Chen, X.; Donnini, S.; Lahtinen, T.; Häkkinen, H.; Groenhof, G.; Pettersson, M., Acid–Base Properties and Surface Charge Distribution of the Water-Soluble Au₁₀₂(pMBA)₄₄ Nanocluster. *The Journal of Physical Chemistry C* **2016**, *120* (18), 10041-10050.
- 28. Wang, F.; Zhang, X.; Zhang, Z.; He, C., In Situ Formation and Ordered Assembly of Gold Nanoclusters to Nano-Ribbons at the Oil/Water Interface. *Journal of Materials Chemistry* **2011**, *21* (39), 15167-15170.
- 29. Wu, Z.; Dong, C.; Li, Y.; Hao, H.; Zhang, H.; Lu, Z.; Yang, B., Self-Assembly of Au₁₅ into Single-Cluster-Thick Sheets at the Interface of Two Miscible High-Boiling Solvents. *Angewandte Chemie International Edition* **2013**, *52* (38), 9952-9955.
- 30. Zhou, Y.; Zeng, H. C., Simultaneous Synthesis and Assembly of Noble Metal Nanoclusters with Variable Micellar Templates. *Journal of the American Chemical Society* **2014**, *136* (39), 13805-13817.
- 31. Yin, H.; Tang, H.; Wang, D.; Gao, Y.; Tang, Z., Facile Synthesis of Surfactant-Free Au Cluster/Graphene Hybrids for High-Performance Oxygen Reduction Reaction. *ACS Nano* **2012**, *6* (9), 8288-8297.
- 32. Yao, Q.; Yuan, X.; Yu, Y.; Yu, Y.; Xie, J.; Lee, J. Y., Introducing Amphiphilicity to Noble Metal Nanoclusters via Phase-Transfer Driven Ion-Pairing Reaction. *Journal of the American Chemical Society* **2015**, *137* (5), 2128-2136.
- 33. Yao, Q.; Luo, Z.; Yuan, X.; Yu, Y.; Zhang, C.; Xie, J.; Lee, J. Y., Assembly of Nanoions via Electrostatic Interactions: Ion-Like Behavior of Charged Noble Metal Nanoclusters. *Scientific Reports* **2014**, *4* (1), 3848.
- 34. Kang, X.; Wei, X.; Xiang, P.; Tian, X.; Zuo, Z.; Song, F.; Wang, S.; Zhu, M., Rendering Hydrophobic Nanoclusters Water-Soluble and Biocompatible. *Chemical Science* **2020**, *11* (18), 4808-4816.
- 35. Chen, Z.-Y.; Tam, D. Y. S.; Zhang, L. L.-M.; Mak, T. C. W., Silver Thiolate Nano-Sized Molecular Clusters and Their Supramolecular Covalent Frameworks: An Approach Toward Pre-templated Synthesis. *Chemistry An Asian Journal* **2017**, *12* (20), 2763-2769.
- 36. Wu, T.; Yin, D.; Hu, X.; Yang, B.; Liu, H.; Xie, Y.-P.; Liu, S.-X.; Ma, L.; Gao, G.-G., A Disulfur Ligand Stabilization Approach to Construct a Silver(I)-Cluster-Based Porous Framework as a Sensitive SERS Substrate. *Nanoscale* **2019**, *11* (35), 16293-16298.

- 37. Wang, Z.; Li, X.-Y.; Liu, L.-W.; Yu, S.-Q.; Feng, Z.-Y.; Tung, C.-H.; Sun, D., Beyond Clusters: Supramolecular Networks Self-Assembled from Nanosized Silver Clusters and Inorganic Anions. *Chemistry A European Journal* **2016**, *22* (20), 6830-6836.
- 38. Chen, S.; Du, W.; Qin, C.; Liu, D.; Tang, L.; Liu, Y.; Wang, S.; Zhu, M., Assembly of the Thiolated [Au₁Ag₂₂(S-Adm)₁₂]³⁺ Superatom Complex into a Framework Material through Direct Linkage by SbF₆⁻ Anions. *Angewandte Chemie International Edition* **2020**, *59* (19), 7542-7547.
- 39. Lei, Z.; Pei, X.-L.; Jiang, Z.-G.; Wang, Q.-M., Cluster Linker Approach: Preparation of a Luminescent Porous Framework with NbO Topology by Linking Silver Ions with Gold(I) Clusters. *Angewandte Chemie International Edition* **2014**, *53* (47), 12771-12775.
- 40. Huang, R.-W.; Wei, Y.-S.; Dong, X.-Y.; Wu, X.-H.; Du, C.-X.; Zang, S.-Q.; Mak, T. C. W., Hypersensitive Dual-Function Luminescence Switching of a Silver-Chalcogenolate Cluster-Based Metal-Organic Framework. *Nature Chemistry* **2017**, *9* (7), 689-697.
- 41. Wang, Z.-Y.; Wang, M.-Q.; Li, Y.-L.; Luo, P.; Jia, T.-T.; Huang, R.-W.; Zang, S.-Q.; Mak, T. C. W., Atomically Precise Site-Specific Tailoring and Directional Assembly of Superatomic Silver Nanoclusters. *Journal of the American Chemical Society* **2018**, *140* (3), 1069-1076.
- 42. Dong, X.-Y.; Huang, H.-L.; Wang, J.-Y.; Li, H.-Y.; Zang, S.-Q., A Flexible Fluorescent SCC-MOF for Switchable Molecule Identification and Temperature Display. *Chemistry of Materials* **2018**, *30* (6), 2160-2167.
- 43. Yoon, B.; Luedtke, W. D.; Barnett, R. N.; Gao, J.; Desireddy, A.; Conn, B. E.; Bigioni, T.; Landman, U., Hydrogen-Bonded Structure and Mechanical Chiral Response of a Silver Nanoparticle Superlattice. *Nature Materials* **2014**, *13* (8), 807-811.
- 44. Desiraju, G. R., Supramolecular Synthons in Crystal Engineering—A New Organic Synthesis. *Angewandte Chemie International Edition in English* **1995**, *34* (21), 2311-2327.
- 45. Yao, Q.; Yu, Y.; Yuan, X.; Yu, Y.; Zhao, D.; Xie, J.; Lee, J. Y., Counterion-Assisted Shaping of Nanocluster Supracrystals. *Angewandte Chemie International Edition* **2015**, *54* (1), 184-189.
- 46. Zeng, C.; Chen, Y.; Kirschbaum, K.; Lambright, K. J.; Jin, R., Emergence of Hierarchical Structural Complexities in Nanoparticles and Their Assembly. *Science* **2016**, *354* (6319), 1580.

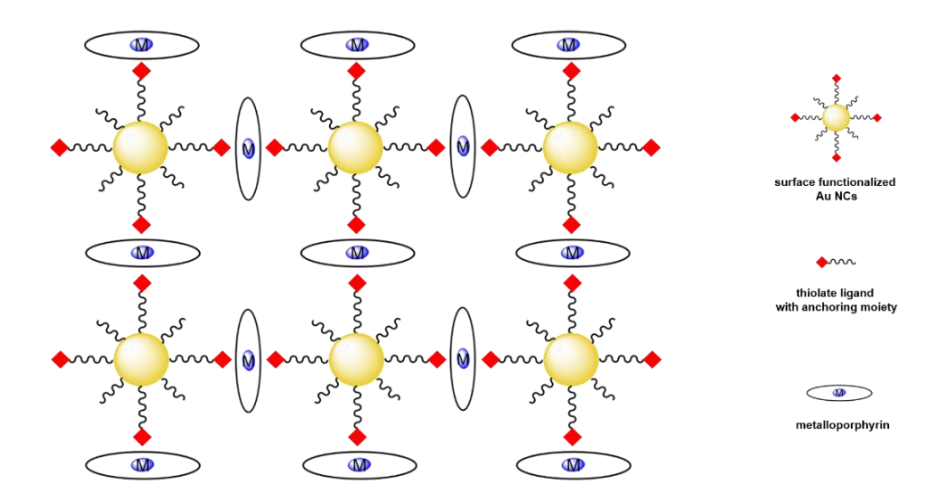
Research aims and objectives

Based on the state of the art in Au NCs self-assembly, it is clear that these nanoassemblies hold promise as tuneable systems in molecular electronics, however, the demonstration of more robust self-assembly strategies together with the incorporation of additional functionality (i.e., molecular switching capabilities) is still needed to advance the field.

This thesis aims to investigate two different approaches to advance the field by realizing novel self-assembled structures based on gold nanoclusters as building units.

Metalloporphyrins as anchoring points for gold nanocluster assemblies formed via supramolecular interactions.

Metalloporphyrins are coordination complexes of metal ions and nitrogen-based macrocycles. They have been shown to form supramolecular assemblies and been employed as building blocks in various self-assembled systems.^{1,2} Herein, the self-assembly between two building blocks: metalloporphyrins and gold nanoclusters is explored. The controlled preparation of superstructures that constitute of atomically precise and tuneable metal nanoclusters is desirable for creating novel nanomaterials that can find applications in the field of molecular electronics. If this strategy is proven successful, this would make extended nanocluster-based assemblies, an example of which is presented in **Scheme R.1**, more accessible.

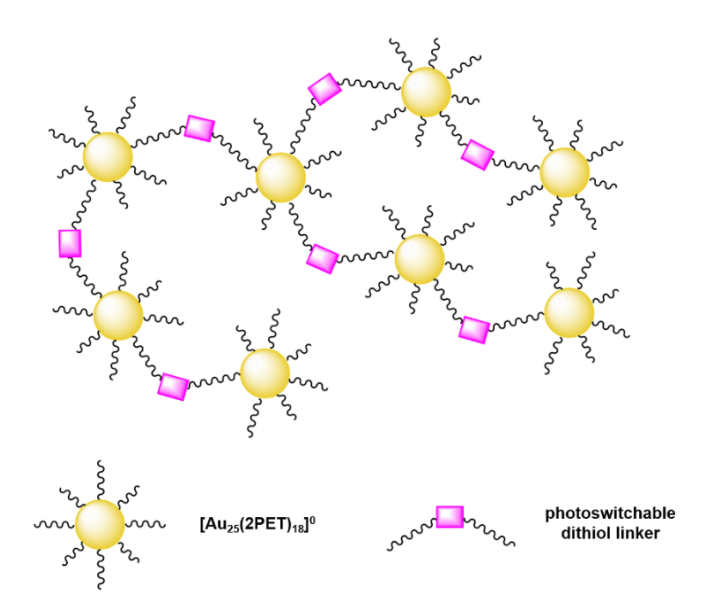


Scheme R.1 Schematic representation of the supramolecular self-assemblies composed of functionalized Au NCs and metalloporphyrins as anchor nodes.

The approach taken towards this goal will be to exploit the biaxial coordination mode of metalloporphyrins as anchoring nodes for the Au NCs. To realize the binding between the two building blocks, the protective shell of the employed $[Au_{25}(SBu)_{18}]^0$ (SBu = 1-butanethiolate) nanoclusters will be functionalized with pyridyl anchoring moieties. The number of introduced pyridyl ligands will be optimized. Further, a feasibility study for the coordination of Au NCs with the functionalized ligand to metalloporphyrins will be carried out with the Zn-based macrocycle. Once the successful binding is demonstrated, the investigation into possible biaxial coordination will be explored for both Zn and Co-based porphyrin using spectrophotometric titration techniques.

Photoswitchable dithiolate ligand as a potential linker for gold nanoclusters assemblies formed via covalent bonding.

Dithiol linkers have been shown to covalently bind Au NCs to obtain discrete nanocluster oligomers and large aggregates in both aqueous and organic phase.³⁻⁵ Interestingly, when aromatic conjugated dithiol linkers were used, the emergence of electronic communication between the nanoclusters was observed.⁵



Scheme R.2 Schematic representation of the Au NC assemblies covalently linked with a photoswitchable dithiol linker.

Herein, the extension of this work focuses on designing a linker molecule that would allow switching between two states of conjugation using external stimulus. The main objectives of this project are: (i) synthesis of a dithiol linker demonstrating light-controlled switching between the insulating and conductive states, (ii) the development of a controllable method for obtaining Au NC assemblies where Au NC building blocks are covalently linked with the novel photoligand (**Scheme R.2**), (iii) the characterization of the photophysical properties of discrete Au₂₅(SR)₁₈-based oligomers connected with the novel photoswitchable linker, and (iv) a demonstration of the photoswitchable properties of the formed assemblies. The preparation of Au NC assemblies equipped with a light-controlled switchable

functionality would pave the way towards utilizing atomically precise nanoclusters as nanomaterials for molecular electronic devices.

References

- 1. Abrahams, B. F.; Hoskins, B. F.; Michail, D. M.; Robson, R., Assembly of Porphyrin Building Blocks into Network Structures with Large Channels. *Nature* **1994**, 369 (6483), 727-729.
- 2. Wang, X.; Nurttila, S. S.; Dzik, W. I.; Becker, R.; Rodgers, J.; Reek, J. N. H., Tuning the Porphyrin Building Block in Self-Assembled Cages for Branched-Selective Hydroformylation of Propene. *Chemistry A European Journal* **2017**, 23 (59), 14769-14777.
- 3. Lahtinen, T.;Hulkko, E.; Sokołowska, K.; Tero, T.-R.;Saarnio, V.; Lindgren, J.; Pettersson, M.; Häkkinen, H.; Lehtovaara, L., Covalently Linked Multimers of Gold Nanoclusters Au₁₀₂(p-MBA)₄₄ and Au_{~250}(p-MBA)_n. *Nanoscale* **2016**, 8 (44), 18665-18674.
- 4. Sokolowska, K.; Hulkko, E.; Lehtovaara, L.; Lahtinen, T., Dithiol-Induced Oligomerization of Thiol-Protected Gold Nanoclusters. *The Journal of Physical Chemistry C* **2018**, 122 (23), 12524-12533.
- 5. Sels, A.; Salassa, G.; Cousin, F.; Lee, L.-T.; Bürgi, T., Covalently bonded multimers of Au₂₅(SBut)₁₈ as a conjugated system. *Nanoscale* **2018**, 10 (26), 12754-12762.

Chapter 3

Materials and experimental methods

3.1 Materials

Hydrogen tetrachloroaurate(III) trihydrate, HAuCl₄ · 3H₂O (49.99 % metal basis, Acros Organics); tetran-octylammonium bromide, TOABr (98 %, Fluorochem); sodium tetrahydroborate, NaBH₄ (99.9%, powder, ACROS Organics); 2-phenylethanethiol, PhC₂H₄SH (99 %, Apollo Chem); 1-butanethiol (≥98 %, Sigma Aldrich); 4-pyridylethanemercaptan, 4PEM (Aldrich^{CPR}); 5,10,15,20-tetraphenyl-21*H*,23*H*-porphine zinc, ZnTPP (low chlorin, Sigma-Aldrich); cobalt(II) *meso*-tetraphenylporphine (Strem Chemicals); tetrahydrofuran, THF (HPLC grade, Fisher Scientific); methanol, MeOH (puriss p.a., Fisher Scientific); toluene (puriss p.a., Fisher Scientific); water (ultrapure, 18.2 MΩ at 25 °C); BioBeads S-X1 (BioRad); *trans*-2-[3-(4-*tert*-butylphenyl)-2-methyl-2-propenylidene]malononitrile, DCTB (≥98.0 %, HPLC, Sigma-Aldrich); caesium triiodide, CsI₃ (≥99.9 %, Sigma-Aldrich). These chemicals were used as received.

3.2 Characterization methods

3.2.1 Steady-state electronic absorption spectroscopy

UV-vis-NIR spectra were recorded at 298 K on a Varian Cary 50 spectrophotometer using a quartz cuvette of 10 mm path length (unless otherwise specified) with 2 nm wavelength resolution. Absorption spectra were baseline corrected by subtracting the spectrum of the corresponding pure solvent. Many

absorption spectra were smoothed with an adjacent-averaging method using a weighted average with 6-12 points.

3.2.2 Matrix-assisted laser desorption-ionization/time of flight mass spectrometry (MALDI-TOF-MS)

MALDI-MS analysis was performed on Bruker AutoFlex spectrometer equipped with a 337 nm nitrogen laser. Mass spectra were acquired by summing spectra from 1000-3000 selected laser shots. The matrix solution of *trans*-2-[3-(4-*tert*-butylphenyl)-2-methyl-2-propenylidene]malononitrile (DCTB) was freshly prepared in toluene at a concentration of 140 µmol/mL. The matrix solution and a sample solution (also in toluene) were combined in an Eppendorf tube and vortexed to ensure proper mixing. One microlitre of the mixed solution was pipetted on a stainless steel MALDI target plate. CsI₃ was used for the mass calibration.

3.2.3 Steady-state photoluminescence spectroscopy

Photoluminescence measurements were performed at a controlled temperature of 293 K on a Horiba Scientific Fluorolog 3 spectrofluorometer equipped with a liquid nitrogen cooled NIR photomultiplier tube (PMT) with an extended detection capability in the visible region (R5509-73; Hamamatsu). The measurements were performed in a fluorescence quartz cell with a $10 \times 10 \text{ mm}^2$ path length. The PL emission spectra were corrected for the variation in the sensitivity of the detection system with emission wavelength and for the inner-filter effect (IFE). PL emission quantum yields (Φ_{PL}) were determined via the relative method^{1, 2} with Rhodamine 6G (R6G) in ethanol as a reference ($\lambda_{exc} = 440 \text{ nm}$, $\Phi_{R6G} = 0.95$ in ethanol at 293 K /298 K, $n_{tol} = 1.496$, $n_{EtOH} = 1.361$)³ using **Equation 3.1**:

$$\boldsymbol{\Phi}_{s} = \boldsymbol{\Phi}_{r} \frac{n_{s}^{2} \int I_{s}(\lambda) d\lambda}{n_{r}^{2} \int I_{r}(\lambda) d\lambda} \frac{A_{r} \cdot 10^{-0.548 \cdot A_{r}}}{A_{s} \cdot 10^{-0.548 \cdot A_{s}}}$$
3.1

where indices (s) and (r) denote sample and reference, respectively; $\Phi_{s/r}$ is the photoluminescence quantum yield, $I_{s/r}$ is the integrated photoluminescence intensity; $n_{s/r}$ denotes the refractive index, and $A_{s/r}$ is the absorbance value at the excitation wavelength (λ). The value of 0.548 corresponds to the optical pathlength.

3.2.4 Time-resolved photoluminescence

The photoluminescence lifetime measurements were done with the time-correlated single photon counting (TCSPC) technique. Excitation was performed at 637 nm with a pulsed laser diode (Picoquant model LDH-P-C-400B), two cut-off filters, 715 and 665 nm, were used. The width of the slit was 0.05 mm. Measurements were performed in a quartz cuvette with a 1 mm light path (Hellma Analytics) at ambient temperature. Samples were dissolved in toluene.

3.2.5 Nuclear magnetic resonance (NMR) spectroscopy

NMR spectra were recorded at 298 K on a Bruker Avance III HD, equipped with a 5mm CPP BBO probe. All measurements were carried out in deuterated solvents: dichloromethane- d_2 , chloroform- d_3 or toluene- d_8 . ¹H NMR chemical shifts are given in parts per million (ppm) relative to tetramethylsilane (TMS) as an internal reference. The measured coupling constants were calculated in Hertz (Hz). Spectra were analysed with MestReNova 12.0 software. The signals were quoted in the following manner: s = singlet, d = doublet, t = triplet, and m = multiplet.

DOSY NMR measurements were performed in a CH_2Cl_2 - d_2 solution at 293 K. Approximately 1.5 mg of a sample was subjected to the NMR analysis and 32 scans were acquired. The obtained data was processed with the T1/T2 module implemented in the Bruker Topspin 3.6 software yielding the diffusion coefficients for each analysed sample.

3.2.6 Transmission electron microscopy (TEM)

Samples for TEM imaging were prepared by drop-casting $2\,\mu\text{L}$ of toluene/DCM (80/20, vol/vol) solution onto AGS160 holey carbon film on 200 mesh copper grids (Plano GmbH, Germany). The solution was allowed to dry overnight. Samples were imaged with CM200 Philips transmission electron microscope operated at 200 kV.

3.2.7 Small angle X-ray scattering (SAXS) analysis

SAXS measurements were performed on a Xeuss 2.0 apparatus (Xenocs, France) using a microfocused Cu K-alpha source with a wavelength of 1.54 Å and a Pilatus3 detector (Dectris, Switzerland). The sample-to-detector distance was chosen to be 540 mm to achieve a Q range of 0.023 to 0.9 Å⁻¹ or at 2490 mm to reduce the Q range to about 0.01 Å⁻¹. The experiments were carried out with a collimated beam size of 0.5×0.6 mm and 0.8×0.8 mm was used at 540 and 2490 mm, respectively. Glass

capillaries (1.5 mm external diameter, wall thickness 0.01 mm) were used to contain sample solutions. Scattering from the solvent, empty capillary, and dark field were measured independently and subtracted using standard protocols.⁴ The data was normalized to absolute units.

Since SAXS is one of the key characterization tools employed in this study, some basic concepts of this technique are provided here.

SAXS is a powerful and effective technique that allows shape and size determination of particles at the nanoscale.⁵ A typical experiment involves irradiating the sample solution (placed in a quartz capillary) with a collimated monochromatic X-ray beam and the transmitted scattered X-rays are collected on a 2D area detector. The scattering pattern of the solvent is also acquired, which is subtracted from the scattering pattern of the sample resulting in the scattering pattern of the species of interest. In other words, SAXS is a contrast method where the scattering signal is derived from the electron density difference between the sample (ρ_{sample}) and the electron density of the solvent ($\rho_{solvent}$): ($\Delta \rho = \rho_{sample} - \rho_{solvent}$). SAXS provides complementary information to electron microscopy but in reciprocal rather than in real space. This implies that for spatial disparity of the electron density at the nanosize regime the X-ray beam will be scattered to low angles, whereas at the atomic scale it will be scattered to high angles.

The form, size and shape of the scattering species can be derived from their scattering intensity. Intensity function, I(Q), is related to the scattering vector amplitude, Q, by relation (**Equation 3.2**):

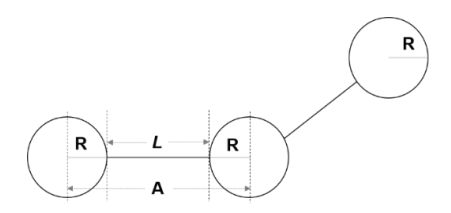
$$Q = 4\pi \left(\sin \theta \right) \times \lambda^{-1}$$
 3.2

where λ is the beam wavelength and 2θ is the a scattering angle. Q values are correlated to real-space distances, d, via the following relation (**Equation 3.3**):

$$d = 2\pi/Q \tag{3.3}$$

The scattering intensity of the sample is proportional to the concentration. Higher concentrations significantly improve the signal-to-noise ratio of the data after background solvent subtraction. Under the assumption that the inter-particle interference depends linearly on the concentration, it is possible to extrapolate the scattering pattern to infinite dilution.^{6,7}

The model employed to fit the acquired experimental data was a pearl-necklace model, which was designed for the colloidal spheres chained together with no preferential orientation. This model affords the form factor for a pearl necklace that consists of two components: N homogeneous spheres of radius R (spheres) interconnected by M rods, with the string segment length (or edge separation, L) expressed as: L = A - 2R, where A is the centre-to-centre pearl separation distance and is directly related to d in **Equation 3.3** (Scheme 3.1).

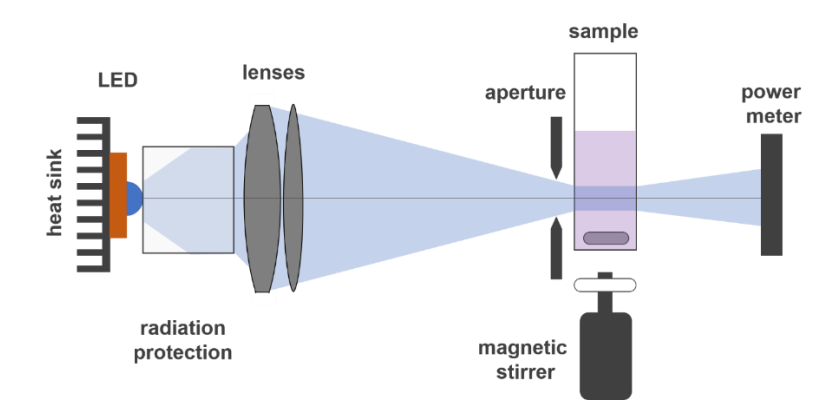


Scheme 3.1 Pearl-necklace schematic composed of two elements: N pearls with radius R freely jointed by M rods. L corresponds to the string segment length (or edge-separation) and A denotes the centre-to-centre pearl separation distance.

The log-normal distribution of both the sphere radius as well as the interparticle (edge-to-edge) distance was fitted/modelled for all samples. The analysis was performed in the Q region of $0.022 - 0.7 \text{ Å}^{-1}$ unless otherwise noted.

3.3 Photoirradiation setup

This work extensively utilizes the photoirradiation setup, which is described here in more detail. The photoswitching experiments in solution were performed using a custom-built irradiation setup based on the design of Riedle and co-workers. The setup, presented in the **Scheme 3.2**, uses two sources of light to perform the ON/OFF switching of samples investigated in this study. In particular, for the UV irradiation the dye of a UV-LED (Roithner, 340 nm, CUD4AF1B) was imaged onto the sample using a telescope (nominal magnification of 6) consisting of a pair of Best Form lenses (Halle Nachfl., fused silica, focal lengths of 25 and 150 mm). Irradiation at 532 nm was accomplished using a laser diode without the telescope. The emission spectrum of the UV-LED was measured using an Avantes fiber optic spectrometer (AvaSpec-2048) and is depicted in **Figure 3.1**.



Scheme 3.2 UV irradiation setup with a high-power light emitting diode as a light source. For visible light irradiation experiments coherent 532 nm laser diode is used making the collimation optics unnecessary. Scheme adapted from Reference [8].

The sample (inside a standard $10 \times 10 \text{ mm}^2$ fluorescence cuvette) was placed inside a custom-built holder, mounted inside the sample compartment of a Cary 50 photometer, with the LED irradiation being

perpendicular to the beam-path of the photometer. To avoid stray light hitting the sample, a 7×7 mm² mechanical aperture covered with an antireflection coating was placed in front of the cuvette (in the LED beam path). The photon flux was measured using a photodiode-based powermeter (Newport, 818-UV/DB) behind the cuvette position (without cuvette and with cuvette containing solvent) and monitored throughout the measurement picking up part of the light with a beam splitter mounted between the telescope and the sample. If necessary, the photon flux was attenuated using neutral density filters. The power arriving to the sample was in the range from tens of μ W up to 20 mW.

Sample solutions were stirred during the whole irradiation experiment, and sample volumes were kept low (≤ 1.5 mL), ensuring a quasi-equilibrium solution state.⁹

The scan speed for measuring the absorption spectra was set such that the recording of an entire spectrum was significantly shorter than the time between acquiring subsequent spectra (e.g., 6 s for a single scan with a 40 s recording interval) minimizing the spectral changes during the recording of a spectrum.

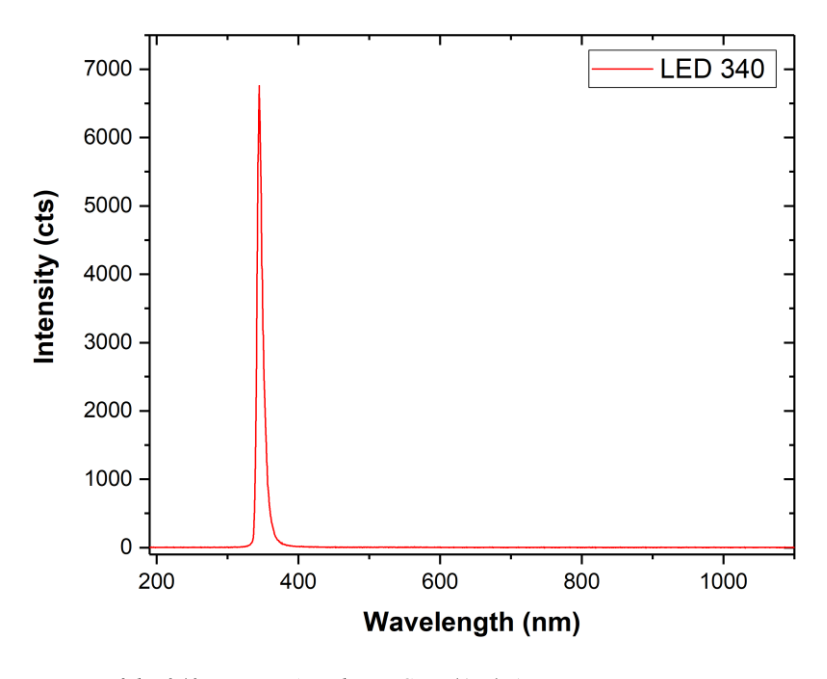


Figure 3.1 Emission spectrum of the 340 nm LED (Roithner, CUD4AF1B).

3.4 Mathematical analyses and fitting

Mathematical analyses and fitting were performed by using the Origin 2017 (originLab Corporation) software.¹⁰ The supramolecular titration data was fitted using the Bindfit v. 0.5 program.^{11,12} Modelling and fitting of the SAXS data was performed using the SasView 4.2.2 software¹³ applying the hard sphere¹⁴ and the pearl-necklace¹⁵ models. The ¹H, ¹³C and DOSY NMR spectra were analysed with the MestReNova v. 12.0.1 software and the Bruker Topspin 3.6 software.

3.5 Synthesis of Au₂₅(SR)₁₈ nanoclusters

3.5.1 Synthesis of [Au₂₅(SC₂H₄Ph)₁₈]⁰

The synthesis of the Au₂₅ nanocluster was done in two steps. First, the synthesis of [Au₂₅(SC₂H₄Ph)₁₈] [TOA]⁺ (TOA = tetraoctylammonium) was carried out via modified one-phase protocol reported by Lu et al. 16 Typically, HAuCl₄ · 3H₂O (1 g, 2.54 mmol, 1 equiv.) and TOABr (1.67 g, 3.05 mmol, 1.2 equiv.) were dissolved in 250 mL of THF and vigorously stirred for about 15 min (orange-red colour solution was obtained). Next, PhC₂H₄SH (1.7 mL, 12.68 mmol, 5 equiv.) was added dropwise to the stirring solution, during which the solution gradually changed colour from orange-red to yellow. The solution was left to stir for about 2 h until the solution became colourless. Then, 25 mL of a freshly prepared ice-cold aqueous solution of NaBH₄ (0.96 g, 25.37 mmol, 10 equiv.) was rapidly poured at once into the rapidly stirred reaction mixture. An immediate outgassing was observed, and the solution changed colour to brown-black. The reaction was left to stir for about 40 h. The reaction mixture was filtered on a filter paper to remove insoluble Au^I–SR complexes. The filtrate was concentrated under reduced pressure to yield a thick orange oil, and then was subsequently exposed to an extensive washing procedure that had for a goal the removal of unreacted thiol and other precursors. First, ~300 mL of MeOH was poured into the flask and was left to stand for a few hours until a brown precipitate formed. The supernatant was carefully decanted, and the precipitate was dissolved in toluene. Subsequently, the toluene was evaporated under reduced pressure. To the crude product a fresh portion of MeOH was added and the above procedure repeated several times until all free thiols were removed. The purification and isolation of the Au₂₅ clusters was done using size-exclusion chromatography (SEC) in toluene. The synthetic procedure and separation procedure produced both negatively charged and neutral Au₂₅ clusters. The second step involved the oxidation of the negatively charged Au₂₅ clusters on the silica column. Briefly, the separated sample of [Au₂₅(SC₂H₄Ph)₁₈] was dissolved in dichloromethane, loaded onto a silica column, and was subsequently oxidized by contact with the silica gel. The collected green solution was concentrated under reduced pressure and was stored in the freezer. The purity of the Au₂₅ clusters was tested with UV-vis-NIR, MALDI-MS and ¹H NMR spectroscopy (see **Appendix A**).

3.5.2 Synthesis of $[Au_{25}(SC_4H_9)_{18}]^0$

The $[Au_{25}(SC_4H_9)_{18}]^0$ nanoclusters, which will be denoted in the text as $[Au_{25}(SBu)_{18}]^0$, were synthesized according to the modified procedure reported by De Nardi et al.¹⁷

Typically, $HAuCl_4 \cdot 3H_2O$ (199 mg, 0.50 mmol, 1.0 equiv.) and TOABr (360 mg, 0.645 mmol, 1.3 equiv.) were dissolved in 50 mL of THF and vigorously stirred for about 15 min. Next, 1-butanethiol

(0.21 mL, 1.93 mmol, 3.8 equiv.) was added dropwise to the stirring solution at room temperature, during which the solution gradually changed colour from orange-red to yellow. The solution was left to stir for about 2 h until the solution became colourless. Then, the 10 mL of a freshly prepared ice-cold aqueous solution of NaBH₄ (197 mg, 5.15 mmol, 10.2 equiv.) was rapidly poured at once into the rapidly stirred reaction mixture. An immediate outgassing was observed, and the solution changed colour to brown-black. The reaction was left to stir for about 3 days at room temperature. After that, the reaction mixture was filtered over filter paper to remove insoluble Au^{I} –SR complexes. The filtrate was concentrated under reduced pressure to yield a mixture of a thick orange oil and an aqueous phase. The two-phase mixture was dissolved in toluene and extracted with ultrapure water (4 × 10 mL). The toluene was evaporated under reduced pressure and to the crude product MeOH was added (~75 % of the volume of the round-bottom flask) and was left to stand in the fume hood for ~2h or until a brownish-orange precipitate was formed. The supernatant was decanted over filter paper and the precipitated solids were extensively washed with cold MeOH. The MeOH-washed product was left to air dry for a few minutes and was subsequently dissolved in toluene. The toluene was removed under reduced pressure and the obtained brown product contained $[Au_{25}(SBu)_{18}]^{-}$ [TOA]⁺ as a main synthesized cluster.

The purification and isolation of the synthesized $[Au_{25}(SBu)_{18}]^-[TOA]^+$ clusters was done using size-exclusion chromatography (SEC) in toluene. During the synthetic reaction and later separation procedure both negatively charged and neutral Au_{25} clusters were formed. To transform the $[Au_{25}(SBu)_{18}]^-[TOA]^+$ into $[Au_{25}(SBu)_{18}]^0$ clusters, the former were dissolved in dichloromethane and passed over a silica gel column. The eluted green colour solution was concentrated under reduced pressure and was stored in the freezer. The purity of the Au_{25} clusters was tested with UV-vis-NIR, MALDI-MS and 1H NMR spectroscopy.

3.6 References

- 1. Brouwer, A. M., Standards for Photoluminescence Quantum Yield Measurements in Solution (IUPAC Technical Report). *Pure and Applied Chemistry* **2011**, *83* (12), 2213-2228.
- 2. Würth, C.; Grabolle, M.; Pauli, J.; Spieles, M.; Resch-Genger, U., Relative and Absolute Determination of Fluorescence Quantum Yields of Transparent Samples. *Nature Protocols* **2013**, *8* (8), 1535-1550.
- 3. Rurack, K.; Spieles, M., Fluorescence Quantum Yields of a Series of Red and Near-Infrared Dyes Emitting at 600–1000 nm. *Analytical Chemistry* **2011**, *83* (4), 1232-1242.
- 4. Brûlet, A.; Lairez, D.; Lapp, A.; Cotton, J.-P., Improvement of Data Treatment in Small-Angle Neutron Scattering. *Journal of Applied Crystallography* **2007**, *40* (1), 165-177.
- 5. Li, T.; Senesi, A. J.; Lee, B., Small Angle X-ray Scattering for Nanoparticle Research. *Chemical Reviews* **2016**, *116* (18), 11128-11180.
- 6. Kikhney, A. G.; Svergun, D. I., A Practical Guide to Small Angle X-Ray Scattering (SAXS) of Flexible and Intrinsically Disordered Proteins. *FEBS Letters* **2015**, *589* (19, Part A), 2570-2577.

- 7. Franke, D.; Kikhney, A. G.; Svergun, D. I., Automated Acquisition and Analysis of Small Angle X-Ray Scattering Data. *Nuclear Instruments and Methods in Physics Research Section A: Accelerators, Spectrometers, Detectors and Associated Equipment* **2012**, 689, 52-59.
- 8. Megerle, U.; Lechner, R.; König, B.; Riedle, E., Laboratory Apparatus for the Accurate, Facile and Rapid Determination of Visible Light Photoreaction Quantum Yields. *Photochemical & Photobiological Sciences* **2010**, *9* (10), 1400-1406.
- 9. This was tested by measuring the temporal response when placing a drop of concentrated Rhodamine 6G solution into 1.5 mL of pure solvent. The stationary absorption was reached within 5 s.
- 10. http://www.originlab.com
- 11. www.supramolecular.org
- 12. Thordarson, P., Determining Association Constants from Titration Experiments in Supramolecular Chemistry. *Chemical Society Reviews* **2011**, *40* (3), 1305-1323.
- 13. Doucet, M.; Cho, J. H.; Alina, G.; Bakker, J.; Bouwman, W.; Butler, P.; ...; Washington, A., SasView version 4.2.2. Zenodo. **2019**.
- 14. Guinier, A.; Fournet, G.; Walker, C. B.; Yudowitch, K. L., Small-Angle Scattering of X-rays. Wiley: 1955.
- 15. Schweins, R.; Huber, K., Particle Scattering Factor of Pearl Necklace Chains. *Macromolecular Symposia* **2004**, *211* (1), 25-42.
- 16. Lu, Y.; Jiang, Y.; Gao, X.; Chen, W., Charge State-Dependent Catalytic Activity of [Au₂₅(SC₁₂H₂₅)₁₈] Nanoclusters for the Two-Electron Reduction of Dioxygen to Hydrogen Peroxide. *Chemical Communications* **2014**, *50* (62), 8464-8467.
- 17. De Nardi, M.; Antonello, S.; Jiang, D.-e.; Pan, F.; Rissanen, K.; Ruzzi, M.; Venzo, A.; Zoleo, A.; Maran, F., Gold Nanowired: A Linear (Au₂₅)_n Polymer from Au₂₅ Molecular Clusters. *ACS Nano* **2014**, *8* (8), 8505-8512.

Chapter 4

Towards metalloporphyrin—Au₂₅ nanoassemblies: solution-state binding study

4.1 Introduction

Metalloporphyrins are complexes of metals and N_4 -macrocycles with conjugated π -electron systems. These versatile compounds are ubiquitously found in nature (e.g., chlorophyll, enzymes, vitamins). Thanks to their unique biological, photophysical and photochemical properties, synthetic metalloporphyrins have found application in photocatalysis, molecular photovoltaics, biological imaging, or theranostics. Metalloporphyrins are also capable of forming supramolecular assemblies and have been used as building blocks in various self-assembled systems. Typically, self-assemblies based on porphyrin units are formed via coordinative bonding of metalloporphyrins having free peripheral donor sites on the macrocycle. The situation where the central metal ion is capable of axial coordination, the donor site of one macrocycle can ligate to the metal centre of another porphyrin molecule forming a porphyrin dimer exhibiting two complementary coordination sites. Using this linking strategy, both discrete and infinite systems can be generated. Another strategy uses exclusively the ability of metalloporphyrins to coordinate ligands axially to the central metal ion in the macrocycle. Despite the versatility of metalloporphyrins, the abilities of metalloporphyrins to form self-assembled systems has not yet been utilized to prepare supramolecular arrays constructed from gold nanoclusters (Au NCs).

Herein, the metal-directed self-assembly route to realize extended Au_{25} -metalloporphyrin-based systems is explored. The envisioned Au NC arrays are sought by incorporating supramolecular interactions via the axial complexation of metalloporphyrins to $Au_{25}(SR)_{18}$ nanoclusters with ligands capable of

anchoring to the metal centre of a porphyrin macrocycle. The targeted assembly between the $Au_{25}(SR)_{18}$ and the metalloporphyrin building blocks is schematically presented in **Figure 4.1.** Different aspects motivated the choice of employing $Au_{25}(SR)_{18}$ nanoclusters for this study: (i) their relatively small size with well-understood structure and properties, ¹⁰ (ii) their very symmetric structure with only one type of staple unit, as revealed from single X-ray crystallographic studies ¹¹⁻¹³ and (iii) their relatively high stability. ¹⁴ Given that metalloporphyrins exhibit high affinity and strong binding for nitrogen containing ligands, the protective monolayer of Au_{25} clusters was post-synthetically functionalized with thiolate ligands bearing pyridine moiety: 4-pyridylethanemercaptan (4PEM; **Scheme 4.1**-c).

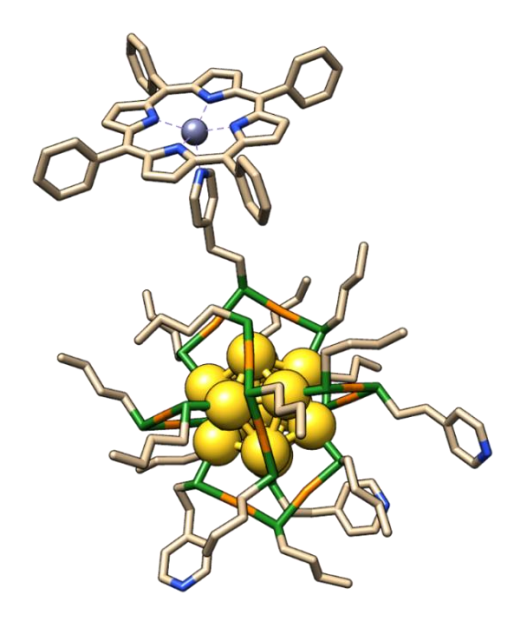


Figure 4.1 Schematic representation of the binding of metalloporphyrins to the Au25 nanocluster protected with a mixed ligand shell where some of the thiolate ligands contain pyridine moiety with high affinity for axial binding to porphyrin ring. The structure of Au25(SBu)18 nanocluster has been prepared using the crystallographic data published in Reference [13] and adapted by introducing the anchoring 4PEM ligands. Colour code: Au⁰-yellow, Au^l-orange, S-green, N-blue, C-light brown, H atoms omitted for clarity.

This Chapter is organized as follows. First, the preparation of [Au₂₅(SBu)₁₈]⁰ nanoclusters functionalized with pyridine-containing ligands is presented. The obtained systems are then characterized with MALDI-TOF-MS and electronic absorption spectroscopy. The next part describes an investigation into the formation of Au₂₅-metalloporphyrin complexes bound via the pyridine-containing ligand in the monolayer of Au₂₅ nanoclusters. Spectrophotometric (UV-vis and photoluminescence) titration experiments are conducted to shed light onto the binding constants and stoichiometry of the obtained complexes.

For simplicity, the exchanged pyridine-containing $Au_{25}(SR)_{18-x}(4PEM)_x$ species will be referred in the text as $4PEM-Au_{25}$.

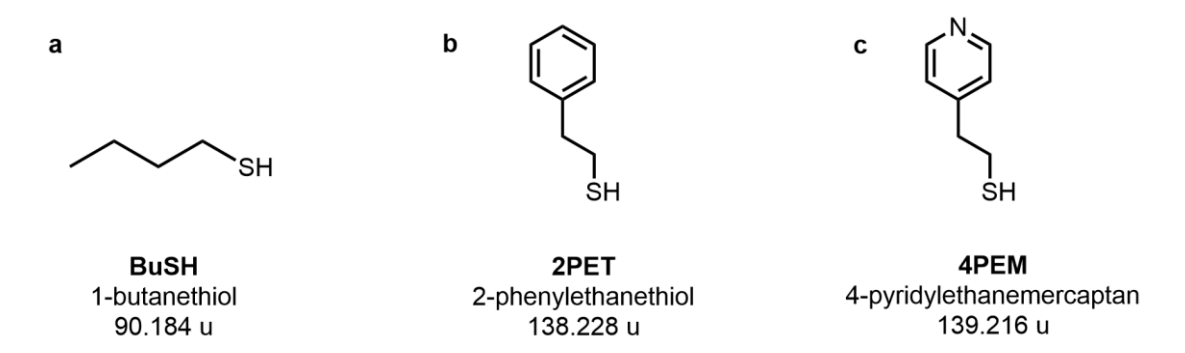
4.2 Functionalized Au₂₅(SR)₁₈ nanoclusters–synthesis and characterization

4.2.1 Synthesis of [Au₂₅(SBu)₁₈]⁰

 $[Au_{25}(SBu)_{18}]^0$ was synthesized according to the procedure reported by Maran group.¹³ The synthetic procedure is described in **Section 3.5.2**. The obtained clusters were characterized with UV-vis-NIR and ¹H NMR spectroscopy, as well as MALDI mass spectrometry which confirmed the purity of the synthesized $[Au_{25}(SBu)_{18}]^0$ clusters (data not shown here).

4.2.2 Ligand-exchange reaction of [Au₂₅(SBu)₁₈]⁰ with 4-pyridylethanemercaptan

Herein, the $[Au_{25}(SR)_{18}]^0$ nanoclusters protected with 1-butanethiolate (SBu) were subjected to partial substitution of their native SBu ligands with 4-pyridylethylmercaptan (4PEM) ligands. The choice of the 4PEM molecule was dictated by its very close structural resemblance to the 2-phenylethanethiolate (2PET) ligands that are known to yield stable $Au_{25}(2PET)_{18}$ nanoclusters. [Au₂₅(SBu)₁₈] were demonstrated to be amenable to ligand-exchange with alkyl ligands containing aromatic moieties. Furthermore, given the very close molecular mass between the 2PET and 4PEM ligands (138.23 u and 139.22 u, respectively; **Scheme 4.1**) the identification of the ligand-exchanged products from $[Au_{25}(2PET)_{18}]^0$ starting material using MALDI-MS would be very challenging. Therefore, a compromise was made to use the less stable $[Au_{25}(SBu)_{18}]^0$ clusters, the highest energy a ligand with a smaller molecular mass of 90.19 u so that the progress of the ligand-exchange reaction could be easily monitored with MALDI-MS.



Scheme 4.1 Structure of (a, b) the most typical thiol ligands used to protect the Au₂₅ nanoclusters; (c) pyridine-bearing thiol ligand used in this study.

The ligand-exchange reaction was carried out in the excess of the 4PEM ligand and with various molar ratios between cluster and ligand to produce Au₂₅ species with varying ratios of pyridine functionalized ligands in the protective monolayer, according to **Equation 4.1**:

$$[Au_{25}(SBu)_{18}]^0 + y \ 4PEM \rightarrow [Au_{25}(SBu)_{18-x}(4PEM)_x]^0 + x \ HSBu + (y-x) \ 4PEM$$
 4.1

where *y* is the molar excess of ligand and *x* is the number of exchanges per cluster. The specific samples prepared in this study are described in detail below.

Samples A and B (1:50 molar ratio)

 $1.25 \text{ mg } (1.9 \times 10^{-4} \text{ mmol}) \text{ of } [\text{Au}_{25}(\text{SBu})_{18}]^0$ —freshly purified on a SEC column (toluene as eluent)—was dissolved in 1.15 mL of dichloromethane (1.09 mg/mL) and then $1.24 \,\mu\text{L}$ (1.33 mg; $9.57 \times 10^{-3} \,\text{mmol}$) of a 4PEM solution in dichloromethane (13 mg/mL) was added. The mixture was left to react under moderate stirring (400 rpm) at ambient temperature (~301 K) for 2 h in a closed reaction flask (but under aerobic conditions). The crude sample was washed with excess of methanol to remove free thiols. Further purification and isolation of the formed 4PEM-exchanged Au₂₅ species was performed on a size-exclusion chromatography (SEC) column in dichloromethane. Two isolated products, A and B, with different ratios of 4PEM ligands were used in the study.

Sample C (1:25 molar ratio)

4.29 mg $(6.6 \times 10^{-4} \text{ mmol})$ of $[Au_{25}(SBu)_{18}]^0$ — freshly purified on a SEC column (toluene as eluent)— was dissolved in 5 mL of dichloromethane (0.86 mg/mL) and then 2.13 μ L $(2.29 \text{ mg}; 1.64 \times 10^{-2} \text{ mmol})$ of a 4PEM solution in dichloromethane (23 mg/mL) was added. The mixture was left to react under moderate stirring (400 rpm) at ambient temperature $(\sim 303 \text{ K})$ for 2 h in a closed reaction flask (but under aerobic conditions). The workup procedure of the crude product was done as described for sample A and B.

Sample D

To 0.78 mg $(1.14 \times 10^{-4} \text{ mmol})$ of an isolated $[\text{Au}_{25}(\text{SBu})_{18-x}(4\text{PEM})_x]^0$ (x = 6, by MALDI-MS) sample dissolved in 1 mL of dichloromethane a 0.11 mL of solution of freshly purified $[\text{Au}_{25}(\text{SBu})_{18}]^0$ nanocluster (1.55 mg; 2.37×10^{-4} mmol) in dichloromethane (1.41 mg/mL) was added. The mixture was left to react under moderate stirring (400 rpm) at ambient temperature (~303 K) for 70 min in a closed reaction flask (but under aerobic conditions). The workup procedure of the crude product was done as described for samples A–C.

The isolated products were characterized with UV-vis spectroscopy and MALDI mass spectrometry.

4.2.3 Characterization of the mixed ligand shell $Au_{25}(SBu)_{18-x}(4PEM)_x$ nanoclusters used for spectrophotometric titration

4.2.3.1 UV-vis-NIR spectroscopy

Figure 4.2 depicts the electronic absorption spectra of four different products of the ligand-exchange reaction that were isolated from the SEC column. The spectrum of the unreacted $[Au_{25}(SBu)_{18}]^0$ clusters in dichloromethane (grey dashed line) showed three distinctive absorption bands at ~25,000 cm⁻¹ (400 nm) ascribed to a d–sp transition, at ~22,727 cm⁻¹ (440 nm) corresponding to a HOMO–sp transition and at ~14,750 cm⁻¹ (678 nm) belonging to the highest occupied molecular orbital–lowest unoccupied molecular orbital (HOMO–LUMO) transition. ^{18, 19} Three samples containing Au_{25} clusters with modified ligand monolayers, sample A, B and C, displayed clear changes in their absorption spectra. However, the characteristic absorption features of Au_{25} clusters were still recognizable in all samples indicating that the combination of 1-butanethiolate and 4PEM ligands in the monolayer did not alter significantly the electronic properties of the $[Au_{25}(SBu)_{18-x}(4PEM)_x]^0$ species.

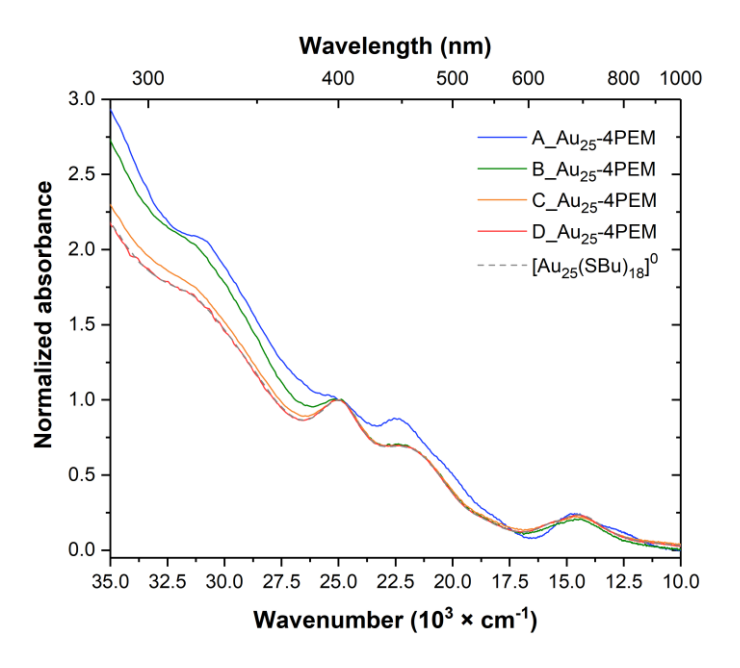


Figure 4.2 Electronic absorption spectra of different products of the ligand-exchange reaction of $[Au_{25}(SBu)_{18}]^0$ with 4-pyridylethanemercaptan (4PEM). Spectra acquired in dichloromethane (blue, green, orange, and grey spectra) or toluene (red spectrum) at ambient temperature.

4.2.3.2 MALDI-TOF-MS analysis

To identify the degree of ligand-exchange in each produced sample, MALDI-TOF-MS analysis in a DCTB matrix was performed. The analysis of the acquired spectra revealed the presence of mass peaks

corresponding to $Au_{25}(SBu)_{18-x}(4PEM)_x$ clusters with x taking the value between 0 to 11 (marked with red dashed lines in **Figure 4.3**).

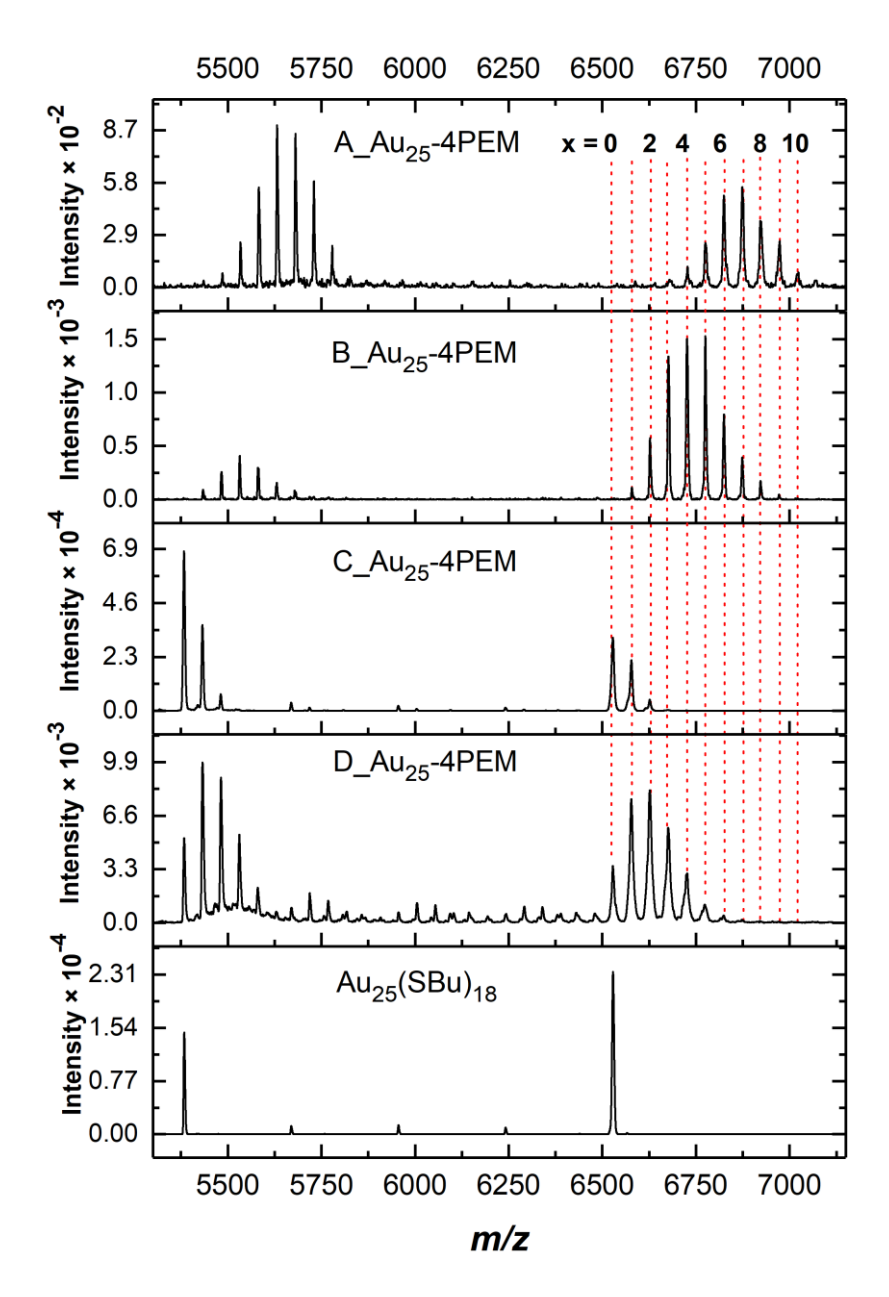


Figure 4.3 MALDI-TOF mass spectra of four samples produced in a ligand-exchange reaction between $[Au_{25}(SBu)_{18}]^0$ and 4PEM ligand. Spectrum of pure $Au_{25}(SBu)_{18}$ cluster is presented in the bottom panel for comparison. Spectra acquired in a linear positive mode.

The mass spectrum of pure $Au_{25}(SBu)_{18}$ (bottom panel) showed five characteristic mass peaks: monoisotopic mass at m/z = 6529.7 Da, the other four peaks (m/z = 6243.5, 5957.4, 5671.2 and 5385.0 Da) belong to the typical $Au_{25}(SR)_{18}$ mass fragments, corresponding to the loss of Au_mL_m (where m = 1, 2, 3, 4) unit from the intact Au_{25} cluster. All four samples, $A-D_Au_{25}-4PEM$, were a mixture of Au_{25} clusters with a different amount of 4PEM in the ligand shell. Both the $A_Au_{25}-4PEM$ and $B_Au_{25}-4PEM$ samples did not contain the pure $Au_{25}(SBu)_{18}$ clusters and were characterized by the

presence of species with a higher extent of ligand-exchange (3–11 and 1–9, respectively). On the contrary, for samples C_Au_{25} -4PEM and D_Au_{25} -4PEM, native $Au_{25}(SBu)_{18}$ clusters were present in the mixture together with clusters exhibiting a lower degree of 4PEM in the monolayer: (0–3 and 0–7, respectively). The extent of the ligand-exchange in the Au_{25} monolayer could be controlled by carefully modulating several parameters, such as molar ratio of the incoming ligand with respect to starting $Au_{25}(SBu)_{18}$ clusters, reaction time, solvent, temperature, and stirring speed.

The analysis of the acquired MALDI mass spectra allowed establishing the average amount of 4PEM ligands in the species' monolayer. This so-called average exchange number, \bar{x} , was calculated according to **Equation 4.2**:²⁰

$$\overline{x} = \sum_{x=0}^{18} x \left(\frac{I(x)}{I(x=0) + I(x=1) + I(x=2) + \dots + I(x=18)} \right)$$
 4.2

where x is the number of the 4PEM exchanged ligands, I(x)—the intensity of the MALDI mass peak corresponding to x exchanged 4PEM ligands.

Table 4.1 lists the Au₂₅(SBu)_{18-x}(4PEM)_x species for each sample A–D and their relative abundance detected using MALDI-MS. The calculated average exchange number, \bar{x} is also reported.

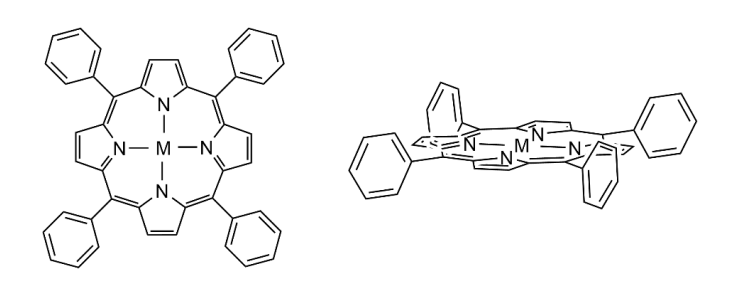
Table 4.1 Relative abundance of various $Au_{25}(SBu)_{18-x}(4PEM)_x$ clusters detected in the analysed samples together with the calculated average ligand exchange number \bar{x} .

$Au_{25}(SBu)_{18-x}(4PEM)_x$	A_Au ₂₅ -4PEM	B_Au ₂₅ -4PEM	C_Au ₂₅ -4PEM	D_Au ₂₅ -4PEM
x = 0	_	_	0.54	0.12
<i>x</i> = 1	_	0.02	0.37	0.26
x=2	_	0.09	0.08	0.27
x = 3	0.02	0.21	0.01	0.20
x = 4	0.05	0.23	-	0.10
x = 5	0.11	0.24	_	0.04
<i>x</i> = 6	0.23	0.12	_	0.02
x = 7	0.25	0.06	_	_
<i>x</i> = 8	0.17	0.03	_	_
x = 9	0.12	0.01	_	_
x = 10	0.03	_	_	_
<i>x</i> = 11	0.02	_	_	_
\overline{x}	6.8	4.4	0.6	2.1

4.3 Metalloporphyrin selection

Properties of metalloporphyrins make them excellent materials to study using spectroscopic methods. Particularly, metalloporphyrins display two types of strong and well-resolved absorption bands: high energy Soret band also known as the B band (\sim 24,000 cm⁻¹) and the low energy Q bands (14-20,000 cm⁻¹), which correspond to the transition from the occupied π HOMO levels to the empty π * LUMO levels of the porphyrin ring.²¹ The complexation of the porphyrins with metal ions increases the microsymmetry of the porphyrin ring from D_{2h} to D_{4h} and as a result the number of Q bands in the spectrum decreases from four to two.²²

Synthetic *meso*-substituted porphyrins are more accessible analogues of the chlorophylls and bacteriochlorophylls found in nature that can be more readily functionalized. Indeed, *meso*-tetraphenylporphyrins (TPPs) are widely employed in host—guest chemistry studies due to their relatively good solubility in organic solvents.²³ These macrocycles can be easily complexed with various metals and the geometry of the four aryl rings attached in the meso-position (see **Scheme 4.2**) of the porphyrin ring makes these molecules less prone to face-to-face stacking or H aggregation²⁴ where the metal ion becomes less accessible for axial coordination.



M = Zn, Co

Scheme 4.2 Structure of metalloporhysrins employed in this study: metal tetraphenylporphyrins (MTTP)

Furthermore, MTPP are known to form non-covalently bound penta- or hexa-coordinate complexes with pyridine and other *N*-containing ligands in nonpolar solvents (**Scheme 4.3**) resulting in the shift of the electronic absorption bands to lower energies.²⁵⁻²⁷

$$+ \bigvee_{N} \frac{K_{a,1}}{K_{a,-1}} + \bigvee_{N} \frac{K_{a,2}}{K_{a,-2}}$$

Scheme 4.3 Axial coordination of pyridine ligand to the central metal ion in meso-tetraphenylporphyrin macrocycle.

In this study two metalloporphyrins were employed: zinc^{II}-tetraphenylporphyrin and cobalt^{II}-tetraphenylporphyrin (henceforth denoted in the text as ZnTPP and CoTPP, respectively).

4.4 Spectrophotometric titrations: principle and data fitting

Supramolecular titration was carried out using the dilution method in which the concentration of the host (metalloporphyrin, MTPP) was fixed/kept constant whilst the concentration of the guest (py or 4PEM) was varied. During the titration, the physical changes (absorbance or PL emission) within the analysed system were monitored spectroscopically. The observed change was plotted as a function of guest equivalents (guest added to host) yielding a titration curve — binding isotherm — which was subsequently fitted to a mathematical model. The chosen model is based on the assumption that the host, guest, and the host–guest complex are in equilibrium, and correlates the observed physical change (ΔY) to the concentration of the host–guest complex, [HG], as $\Delta Y \propto [HG]$.

4.4.1 Calculation of binding constants from the UV-vis titration data

To evaluate the binding between the host and the guest complex, the equation that relates the measured signal (here, the absorbance or fluorescence) to the total concentration of the host and guest molecules via the association constant K_a is derived. These equations are obtained from the equilibrium constant equation, mass balance equations, and signal-to-concentration relations (i.e., Lambert–Beer's law for absorption and Stern–Volmer equation for fluorescence). Since the concentration of the free host and free guest in the analysed solution cannot be determined directly, two or more related equations are solved in an iterative manner to obtain the best fit to the data.

For a simple host–guest binding equilibrium, when it is assumed that both the host (H) and guest (G) have only one binding site, the equilibrium reaction equation is as follows (**Equation 4.3**):

$$H + G \rightleftharpoons HG$$
 4.3

The dissociation constant is given by **Equation 4.4**:

$$K_d = \frac{1}{K_a} = \frac{[G][H]}{[HG]} = \frac{([G]_{tot} - [HG])([H]_{tot} - [HG])}{[HG]}$$
4.4

where [HG] is the molar concentration of the 1:1 host-guest complex, $[G]_{tot}$ denotes the total concentration of the guest (here ZnTPP), $[H]_{tot}$ is the total concentration of the host (4PEM or py) and [G] and [H] are the concentration of free guest and host, respectively.

For this simple 1:1 binding, with a fixed initial concentration of host $[H]_{tot}$, that is titrated with guest ligand $[G]_{tot}$, it follows from mass conservation that:

$$[G]_{tot} = [G] + [HG] \tag{4.5}$$

$$[H]_{tot} = [H] + [HG]$$

$$4.6$$

Upon rearrangement of **Equation 4.4**, a quadratic equation in [HG] is obtained with the following solution (**Equation 4.7**):

$$[HG] = \frac{[H]_{tot} + [G]_{tot} + K_d - \sqrt{([H]_{tot} + [G]_{tot} + K_d)^2 - 4[H]_{tot}[G]_{tot}}}{2}$$
4.7

The fractional saturation, f, is defined as the fraction of binding sites occupied by the ligand and can be expressed as follows (**Equation 4.8**):

$$f = \frac{[HG]}{[H] + [HG]} = \frac{[HG]}{[H]_{tot}}$$

$$4.8$$

where [HG] is the concentration of the host–guest complex, [H] is the concentration of the unbound host, and $[H]_{tot}$ is the total host concentration.

Expressing the optical response as a function of known/measurable parameters leads to the following **Equation 4.9**, that expresses the observed absorbance as the sum of the absorbance of the host and host—guest complex. Here two assumptions are made: (i) all species present in the solution follow Lambert—Beer's law and (ii) guest molecules do not absorb at the selected wavelength.

$$A = A_0(1 - f) + A_{HG}f = A_0\left(1 - \frac{[HG]}{[H]_{tot}}\right) + A_{HG}\frac{[HG]}{[H]_{tot}}$$

$$4.9$$

where, A is the measured absorbance, A_0 absorbance of the host before guest is added, and A_{HG} is the absorbance of the formed host–guest complex.

Combining **Equation 4.7** and **4.9**, **Equation 4.10** (with two unknowns, K_d and A_{HG}) is obtained that can be solved using the non-linear regression analysis implemented in the Bindfit v. 0.5 program^{28,29} or the Origin software.³⁰

$$\frac{A_0 - A}{A_0 - A_{HG}} = \frac{[HG]}{[H]_{tot}} = \frac{[H]_{tot} + [G]_{tot} + K_d - \sqrt{([H]_{tot} + [G]_{tot} + K_d)^2 - 4[H]_{tot}[G]_{tot}}}{2[H]_{tot}}$$

$$4.10$$

The Bindfit application uses an algorithm making some initial guesses for K_a and A_{HG} to calculate $A - A_0$ and compare it to the $A - A_0$ value obtained from the experiment. Then the K_a and A_{HG} values are varied until a good fit of the acquired experimental data with the model described by **Equation 4.10** is achieved.

4.4.2 Calculation of binding constants from the fluorescence titration data

Two methodologies have been investigated in this study to estimate K_a from photoluminescence data.

Method 1. Assuming that the formed host–guest complex is fluorescent (at the same wavelength as the free host), then the measured fluorescence (F) is a simple addition of the fluorescence of the free and complexed host. If F_0 and F_{HG} are the fluorescence intensities of the free host and host–guest complex, respectively, and f is the fraction of the host bound in a complex, then the fluorescence takes the following expression:

$$F = F_0(1 - f) + F_{HG}f = F_0\left(1 - \frac{[HG]}{[H]_{tot}}\right) + F_{HG}\frac{[HG]}{[H]_{tot}}$$
4.11

Combining and rearranging Equations 4.4, 4.7 and 4.11 gives the following expression:

$$\frac{F_0 - F}{F_0 - F_{HG}} = \frac{[HG]}{[H]_{tot}} = \frac{[H]_{tot} + [G]_{tot} + K_d - \sqrt{([H]_{tot} + [G]_{tot} + K_d)^2 - 4[H]_{tot}[G]_{tot}}}{2[H]_{tot}}$$

$$4.12$$

The resulting **Equation 4.12** has two unknowns, K_d and F_{HG} , which can be solved by the nonlinear regression analysis using the Origin software package.

Method 2. This method assumes that the host–guest complex is non-fluorescent and models a process with n binding sites and infinite cooperativity, meaning that the host molecules exist in two states: unbound and fully ligated. For this scenario, the association constant is expressed by the following **Equation 4.11**:

$$K_a = \frac{[HG_n]}{[H][G]^n} \tag{4.13}$$

Assuming that the formed host–guest complex is non-fluorescent, then the measured fluorescence can be expressed as follows:

$$F = F_0 - F_0 \frac{[HG_n]}{[H]_{tot}} \tag{4.14}$$

Therefore

$$[HG_n] = \frac{F_0 - F}{F_0} [H]_{tot}$$
 4.15

$$[H] = \frac{F}{F_0} [H]_{tot} \tag{4.16}$$

Substituting Equation 4.13 and 4.14 in Equation 4.11 gives:

$$K_a [G]^n = \frac{F_0 - F}{F} \tag{4.17}$$

Taking the natural logarithm to linearize the equation yields the following expression (**Equation 4.18**):

$$ln\left[\frac{F_0 - F}{F}\right] = ln K_a + n ln[G]_{tot}$$

$$4.18$$

The treatment of the fluorescence data based on a double logarithmic plot provides an alternative to classical methods such as the Scatchard analysis³¹ or the method of continuous variations.³² It also permits to evaluate the stoichiometry of the binding process. Graphical representation of **Equation 4.18** yields a slope that corresponds to the number of guest ligands interacting simultaneously with each metalloporphyrin binding site (n) and the intercept yielding the association constant, K_a .³³

4.4.3 Solution-state UV-vis/fluorescence titration experiments

All titration experiments were performed in anhydrous toluene and deoxygenated toluene, a typical nonpolar and noncoordinating solvent. Stock solutions of the host (MTPP, M = Zn, Co), called the titrands, were prepared in toluene at a concentration of ~5 × 10^{-6} M. 0.2 - 0.4 mL of the stock solution of MTPP was then used to dissolve an accurately known mass of guest ($Au_{25}(SBu)_{18-x}(4PEM)_x$, samples A–D_Au25-4PEM), called the titrant, wherein the guest concentrations was 50–100 times greater than that of the host. Subsequently, 0.4 mL of the host solution was placed in a $2 \times 10 \text{ mm}^2$ quartz cell (Hellma Analytics) upon which 0.001 to 0.5 mL of the titrant was added gradually using Gilson MICROMAN positive-displacement pipette or a Hamilton syringe. After each addition, the solution in a cuvette was stirred to ensure the complete mixing and afterwards the UV-vis spectrum was collected at 298 K.

Also, UV-vis titration control experiments were conducted where the metalloporphyrin (MTPP, M = Zn, Co) was titrated with a simple pyridine (py) ligand in toluene solution which allowed calculating the

binding constants, K_a , for the reference system using the same fitting models that were employed for the Au₂₅(SBu)_{18-x}(4PEM)_x samples. The titrations of porphyrins with py were performed in a 10 × 10 mm² quartz cuvette (Hellma Analytics) with a screw cap, at 298 K. The toluene solutions of metalloporphyrins ($\sim 5 \times 10^{-6}$ M) were titrated with the toluene solution of py with the concentration of ~ 100 times higher than that of the host.

The fluorescence titrations of MTPP– $Au_{25}(SBu)_{18-x}(4PEM)_x$ systems were acquired at room temperature in a right-angle geometry using the same samples that were employed for the UV-vis titrations. The inner filter effect could not be completely prevented but to minimize this, a thinner cuvette was used $(2 \times 10 \text{ mm}^2)$.

The acquired fluorescence data was corrected for primary and secondary inner filter effects, using **Equation 4.19** and assuming the fluorescence originated from the exact centre of the cuvette:

$$F_{corr} = F_{obs} \times 10^{-\frac{A_{exc}d_{exc}}{2} - \frac{A_{em}d_{em}}{2}}$$
 4.19

where F_{corr} is the corrected fluorescence intensity that would be measured in the absence of inner-filter effects, F_{obs} is the observed fluorescence, d_{exc} and d_{em} correspond to the cuvette pathlength in the excitation and emission direction, respectively, A_{exc} and A_{em} are the measured changes in absorbance value at the excitation and emission wavelength, respectively, caused by the ligand addition (in a 10 mm path length cuvette).³⁴

4.5 Interactions of ZnTPP with functionalized Au₂₅ nanoclusters probed with spectrophotometric titrations

4.5.1 UV-vis titration of ZnTPP with pyridine and $Au_{25}(SBu)_{18-x}(4PEM)_x$ nanoclusters

4.5.1.1 Solution-state binding study of ZnTPP with pyridine

The control titration experiment for ZnTPP (host) was performed using pyridine (py) as a ligand (guest) to inspect the host–guest binding interaction. Titration of the ZnTPP solution $(4.89 \times 10^{-6} \text{ M})$ with py (titrant solution, $0-2.45 \times 10^{-3} \text{ M}$) was performed at 298 K, however the experiments were not carried out under temperature-controlled conditions. The absorption spectra of the ZnTPP–py system in toluene are presented in **Figure 4.4**-a. The electronic absorption spectrum of the non-coordinated ZnTPP (pink trace) exhibited characteristic maxima at 23,585 cm⁻¹ (424 nm) and 19–16,000 cm⁻¹; 525–625 nm) attributed to the Soret and Q-bands, respectively.

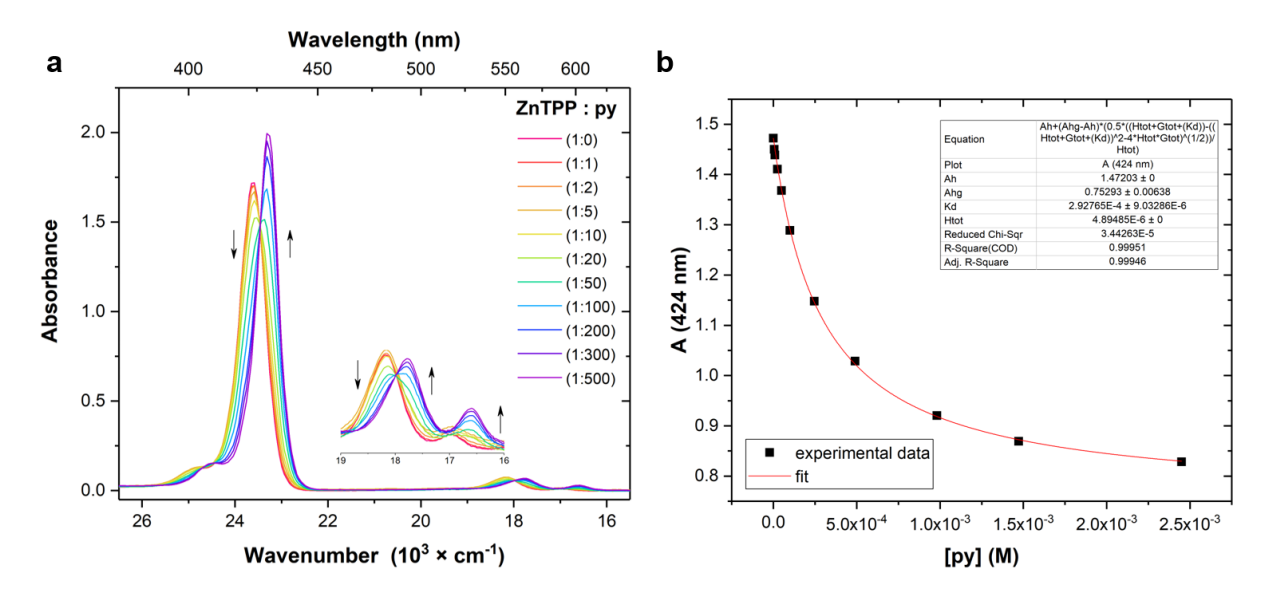


Figure 4.4 (a) Changes in the UV-vis spectra of ZnTPP) in toluene $(4.89 \times 10^{-6} \, \text{M})$ at 298 K with increasing pyridine ligand concentration [py]= $(0-2.45 \times 10^{-3} \, \text{M})$. Arrows indicate absorbance changes upon increased pyridine concentration. (b) Change in the absorbance of the Soret band of ZnTPP as a function of total py concentration. The experimental data (black squares) and fitted model curve (red trace). The 1:1 binding model, Equation 4.10, was used.

Incremental addition of the py ligand, induced significant changes in the electronic spectra. Particularly, the concomitant decrease in the absorbance of the Soret and Q bands for the pure ZnTPP and the appearance of a new Soret band at 23,256 cm⁻¹ (430 nm) and new Q bands at 17,852 and 16,639 cm⁻¹ (561 and 601 nm, respectively) was evident. The observed variations are characteristic of the axial binding of a py ligand to the central Zn²⁺ ion within the porphyrin macrocycle.²⁵

The titration curve, presented in **Figure 4.4**-b was obtained by plotting the absorbance at 424 nm (Soret band of the ZnTPP) against the total concentration of py, $[py]_{tot}$. The experimental data was fitted to a 1:1 binding model according to **Equation 4.10**. The analysis of the titration experiment data assumed that the guest (py) is 'transparent' at the wavelengths selected for the analysis (here, 424 and 430 nm). In this case the changes in absorbance can be simplified as there is only the host and host–guest complex that contribute to the observed absorbance. The calculated value of the association constant K_a was $(3.42 \pm 0.11) \times 10^3 \,\mathrm{M}^{-1}$, which was in a good agreement with the value reported in the literature $((4.8 \pm 0.5) \times 10^3 \,\mathrm{M}^{-1})$. 35

4.5.1.2 Solution-state binding study of ZnTPP with Au₂₅(SBu)_{18-x}(4PEM)_x

Titration of ZnTPP solution with $Au_{25}(SBu)_{18-x}(4PEM)_x$ was performed for 3 samples with different average numbers of 4PEM ligands in the monolayer: (i) $\bar{x} = 6.8$ (sample A_Au₂₅-4PEM); (ii) $\bar{x} = 4.4$ (sample B_Au₂₅-4PEM); and (iii) $\bar{x} = 0.6$ (sample C_Au₂₅-4PEM).

The UV-vis titration of the ZnTPP with the Au_{25} cluster containing on average 6.8 molecules of 4PEM in the monolayer is depicted in **Figure 4.5**-a. Gradual addition of the Au_{25} -4PEM solution resulted in the red-shift of the Soret band from 23,585 cm⁻¹ (424 nm) to 23,256 cm⁻¹ (430 nm), as observed in the case of the UV-vis titration of ZnTPP with py ligand (**Section 4.5.1.1**). This result confirmed the successful binding of the 4PEM-functionalized Au_{25} nanocluster to the ZnTPP macrocycle.

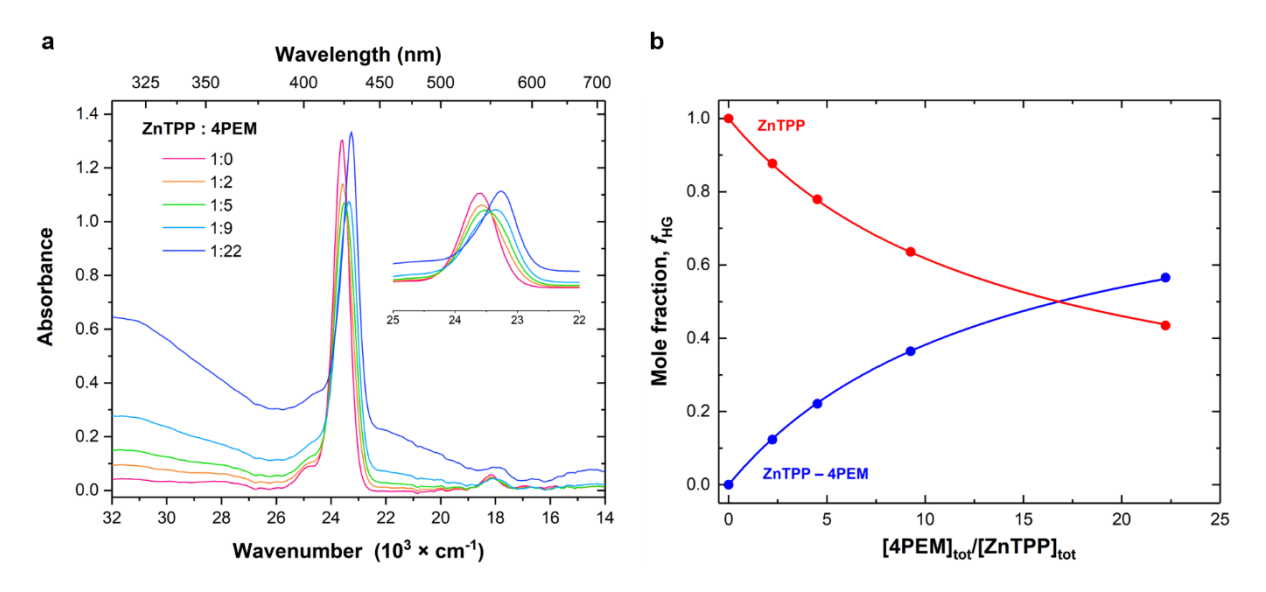


Figure 4.5 (a) Change in the absorption spectra of ZnTPP solution in toluene $(4.51-4.00 \times 10^{-6} \text{ M})$ upon titration with $Au_{25}(SBu)_{18-x}(4PEM)_x$ for $\bar{x}=6.8$ $(0-8.9\times 10^{-4} \text{ M})$. Spectra acquired at 298 K. (b) Change in the mole fraction of ZnTPP (red dots) and ZnTPP- $Au_{25}(SBu)_{18-x}(4PEM)_x$ ($\bar{x}=6.8$) complex, denoted for simplicity as ZnTPP-4PEM (blue dots). The mole fractions were obtained from the fitting using non-linear regression method employed in the Bindfit program.

The determination of the binding constant was performed using the Bindfit program assuming 1:1 binding stoichiometry and including the dilution correction, as in this experiment the concentration of the host i.e., ZnTPP varied by 12 %. The obtained value of the association constant, K_a , was $(1.50 \pm 0.01) \times 10^3 \text{ M}^{-1}$. The change in the mole fractions of ZnTPP and the ZnTPP–4PEM complex revealed that, when 16 equivalents of 4PEM ligands were added to the ZnTPP solution, half of the porphyrin was saturated with the 4PEM ligand (**Figure 4.5**-b).

Investigation of the binding of the Au₂₅ nanocluster with a lower number of anchoring 4PEM ligands in the shell ($\bar{x} = 4.4$) to the ZnTPP macrocycle with the UV-vis titration experiment revealed similar behaviour to the one observed for the sample with $\bar{x} = 6.8$ pyridine thiolate ligands. The titration led, again, to a clear red-shift of the Soret band, providing evidence for the axial binding of the functionalized cluster to the Zn centre within the macrocycle (**Figure 4.6**-a).

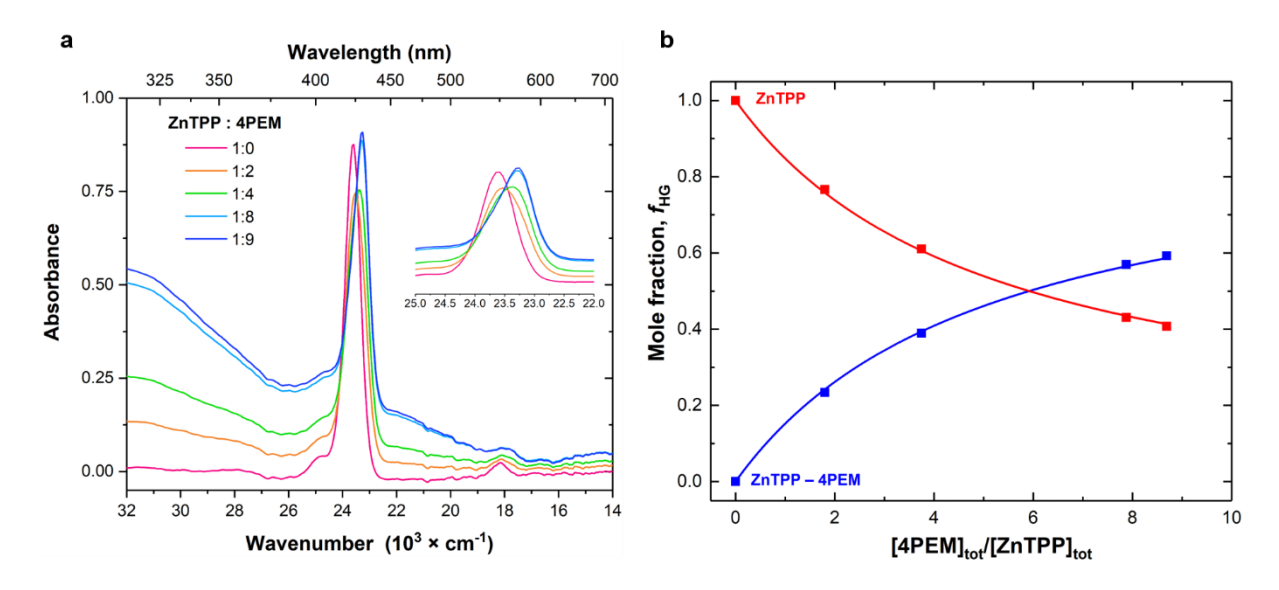


Figure 4.6 (a) Change in the absorption spectra of ZnTPP solution in toluene $(4.51-4.06 \times 10^{-6} \text{ M})$ upon titration with $Au_{25}(SBu)_{18-x}(4PEM)_x$ for $\bar{x}=4.4$ $(0-3.5\times 10^{-4} \text{ M})$. Spectra acquired at 298 K. (b) Change in the mole fraction of ZnTPP (red dots) and ZnTPP- $Au_{25}(SBu)_{18-x}(4PEM)_x$ ($\bar{x}=4.4$) complex, denoted for simplicity as ZnTPP-4PEM (blue dots). The mole fractions were obtained from the fitting using non-linear regression method employed in the Bindfit program.

Interestingly, a lower amount of the Au₂₅ cluster was necessary to ensure that half of the ZnTPP species were bound in a complex, as was shown from the data analysis performed in the Bindfit program, yielding the mole fraction values of the pure host (ZnTPP) and the formed ZnTPP–4PEM-Au₂₅ complex (**Figure 4.6**-b). The value of the association constant, $K_a = (4.02 \pm 0.05) \times 10^3 \,\text{M}^{-1}$, was higher than for the Au₂₅ cluster with the higher ratio of 4PEM in the protective ligand monolayer.

Table 4.2 Association constant values for ZnTPP-py and ZnTPP-4PEM-Au₂₅ complexes derived from UV-vis titration experiments.

	Uv-vis titration		
	ZnTDD nv	ZnTPP-4PEM@Au ₂₅	ZnTPP-4PEM@Au ₂₅
	ZnTPP–py	$\bar{x} = 6.8$	$\bar{x} = 4.4$
$K_a [M^{-1}]$	$(3.42 \pm 0.11) \times 10^3$	$(1.50 \pm 0.01) \times 10^3$	$(4.02 \pm 0.05) \times 10^3$

The results from the two titrations presented above (**Table 4.2**), showed that the Au₂₅ nanoclusters containing on average higher ratios of 4PEM in the monolayer did not preferentially bind more ZnTPP porphyrin. This can be explained by steric hindrance that prevented the macrocycle to coordinate to all available 4PEM ligands that were present in the monolayer. Hence, further investigation of the ZnTPP binding to the Au₂₅ species was undertaken using clusters with lower 4PEM exchange ratios.

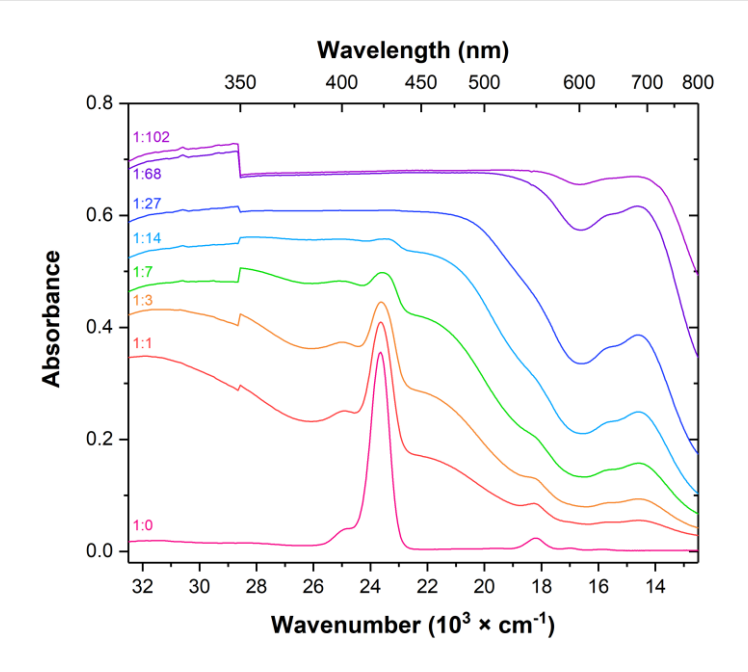


Figure 4.7 Change in the absorption spectra upon titrating ZnTPP solution in toluene $(2.50 \times 10^{-6} \text{ M})$ with the solution of $Au_{25}(SBu)_{18-x}(4PEM)_x$ for $\bar{x} = 0.6 (0-1.25 \times 10^{-4} \text{ M})$. Spectra acquired at 298 K.

Figure 4.7 presents the UV-vis titration spectra of the ZnTPP with $Au_{25}(SBu)_{18-x}(4PEM)_x$ ($\bar{x}=0.6$) nanocluster solution (sample C_Au₂₅–4PEM). The difficulty with using the Au_{25} clusters with low ratio of 4PEM in the monolayer lies in the fact that addition of few equivalents of guest causes the absorption spectra to be overwhelmed by the strong absorption of the Au_{25} nanocluster across the whole UV-vis region. Even though the Soret absorption band of ZnTPP is still recognizable in the spectrum, it became difficult to trace the evolution of the Soret band at 23,256 cm⁻¹ (430 nm) belonging to the formed ZnTPP–4PEM complex. Therefore, for this sample obtaining the binding constants from the analysis of UV-vis titration data was not straightforward. Rather, in this case the fluorescence titration data was acquired to determine the interaction between ZnTPP and 4PEM-Au₂₅ cluster with very low ratio of anchoring ligand.

4.5.2 Fluorescence titration of ZnTPP with pyridine and $Au_{25}(SBu)_{18-x}(4PEM)_x$ nanoclusters

Fluorescence spectroscopy, specifically fluorescence quenching, is used regularly to characterize the host–guest binding process. ³⁶ To determine the association constant, K_a , as defined in **Equation 4.4**, the complexation process must induce a change in the fluorescence properties of a host, guest or complex molecule.

4.5.2.1 Solution-state binding study of ZnTPP with pyridine

Fluorescence titration of ZnTPP with the py ligand was performed as a control experiment. The fluorescence spectrum of ZnTPP (pink trace in **Figure 4.8**-a) acquired after excitation at the Soret band wavelength (i.e., 424 nm) displayed two emission bands in the red region: Q(0, 0) band at 16,750 cm⁻¹ (597 nm) and Q(0, 1) band at 15,456 cm⁻¹ (647 nm). These two emission bands belong to the transition from the lowest excited singlet state S_1 to the ground state S_0 of ZnTPP.³⁷

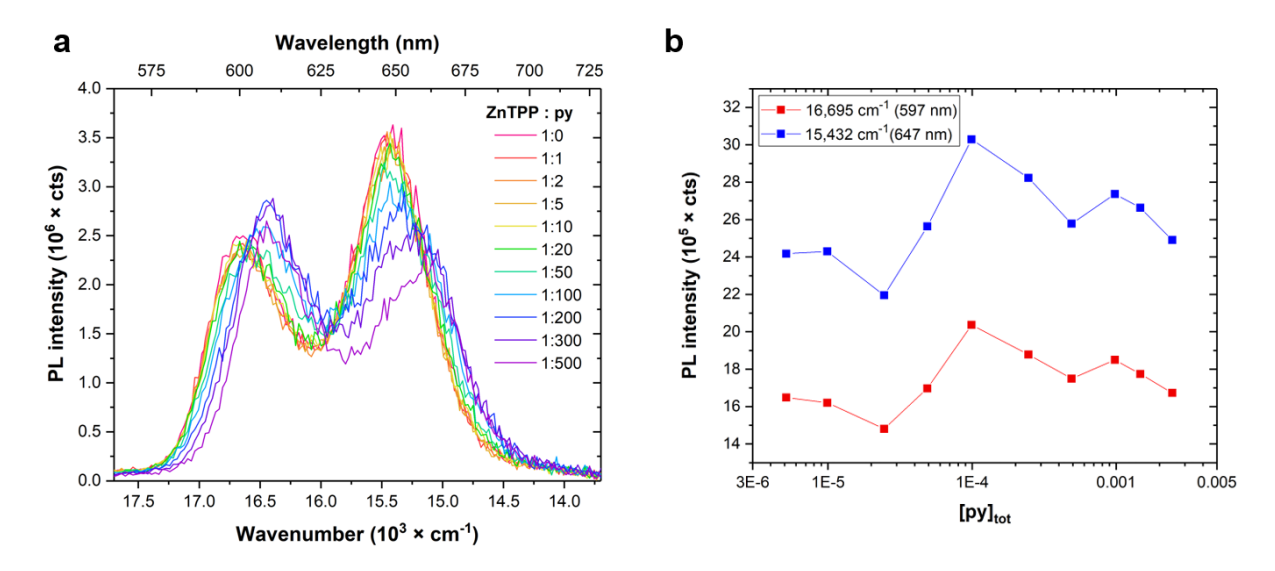


Figure 4.8 (a) Change in the PL emission of ZnTPP $(4.89 \times 10^{-6} \text{ M})$ upon gradual addition of py $([py] = 0-2.45 \times 10^{-3} \text{ M})$. Spectra recorded at 298 K in toluene after excitation at 424 nm with the size of excitation and emission slits = 3 nm. Spectra corrected for reabsorption. (b) Change in the PL emission intensity of the two Q band maxima of ZnTPP: Q(0, 0) in red and Q(0,1) in blue upon titration with py.

Gradual addition of the py ligand resulted in the red shift of the two fluorescence maxima to $16,420 \text{ cm}^{-1}$ (609 nm) and $15,221 \text{ cm}^{-1}$ (657 nm) and increase in the intensity of the Q(0, 0) band relative to Q(0, 1). This behaviour is consistent with the perturbation of the fluorescence properties of ZnTPP as a result of axial ligation of strongly coordinating ligands, such as pyridine.³⁸ Importantly, the observed changes in the fluorescence intensity of the two peaks: Q(0,0) and Q(0,1) were quite random (**Figure 4.8**-b) and did not allow for fitting of the data to the model.

Hence, the observed behaviour in the change of PL emission intensity during the titration precluded analysis of the fluorescence titration using the fitting equations described in **Section 4.4.2**.

4.5.2.2 Solution-state binding study of ZnTPP with Au₂₅(SBu)_{18-x}(4PEM)_x nanoclusters

Figure 4.9 depicts the fluorescence titration spectra of the C_Au₂₅–4PEM sample performed in a toluene solution at 298 K. The steady-state emission measurements revealed that the photoluminescence of

ZnTPP at $16,750 \text{ cm}^{-1}$ (597 nm) and $15,456 \text{ cm}^{-1}$ (647 nm), upon excitation at 424 nm, diminished gradually during titration with 4PEM in toluene, indicating that the fluorescence of the ZnTPP was quenched upon addition of Au₂₅ nanocluster containing 4PEM ligand in the protective monolayer. This could be explained by an energy transfer from the excited ZnTPP molecule to the Au₂₅ nanocluster, as has been observed for Au₃₈(2PET)₂₄ clusters functionalized with Zn S-acetylthio porphyrin.³⁹

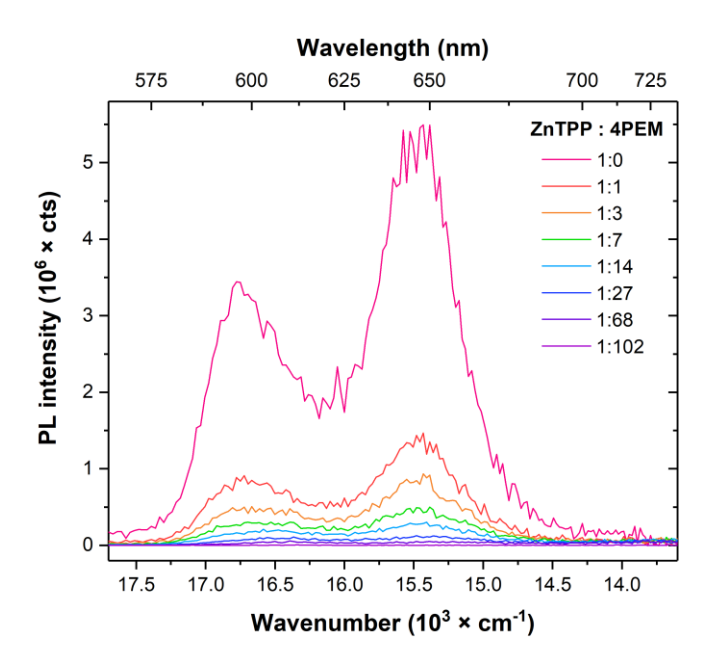


Figure 4.9 Change in the fluorescence emission spectra of ZnTPP $(2.50 \times 10^{-6} \text{ M})$ upon addition of 4PEM functionalized Au₂₅ nanocluster solution in toluene. Spectra acquired at 298 K after excitation at 550 nm were corrected for reabsorption.

Furthermore, reminiscent to the ZnTPP-py system, batochromic shifts of 275 and 235 cm $^{-1}$ for the Q(0, 0) and Q(0, 1) peaks, respectively, were observed.

To obtain the association constant value, K_a , from the fluorescence titration measurements two methodologies, discussed in **Section 4.4.2**, were employed. Firstly, the fluorescence data was fitted to the most generally valid model, **Equation 4.12**, which allows the analysis of fluorescence quenching upon ligand binding with 1:1 stoichiometry and assumes that the host–guest complex exhibits fluorescence. This method requires the observed fluorescence intensity (F) to be plotted as a function of total concentration of added guest, $[G]_{tot}$ (**Figure 4.10**).

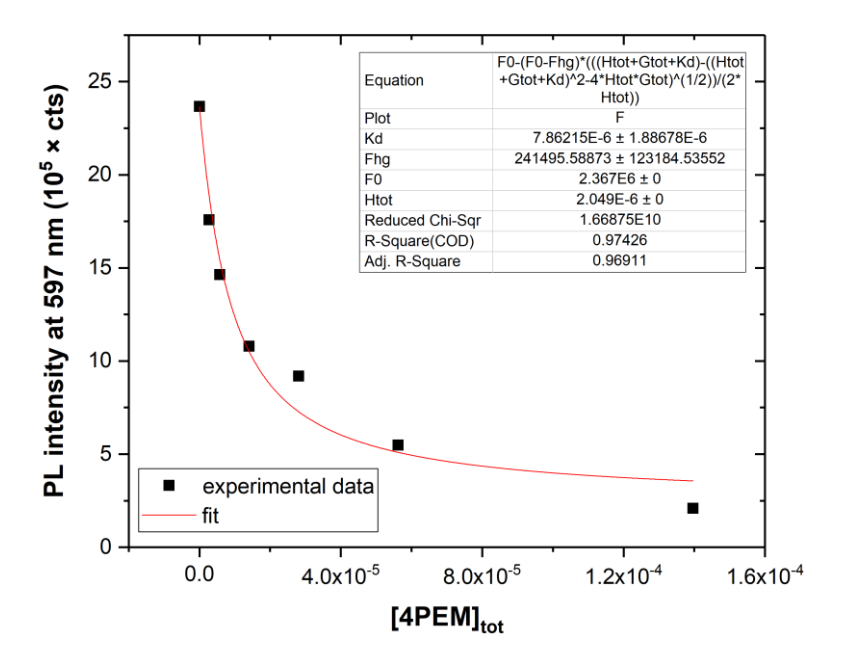


Figure 4.10 Fit of the fluorescence titration data (fluorescence intensity of the Q(0, 0) band) to Equation 4.12 obtained by nonlinear regression analysis using the Origin software.

The obtained fit of the data (red curve in **Figure 4.10**) gave the value of the association constant, $K_a = (1.27 \pm 0.31) \times 10^5 \,\mathrm{M}^{-1}$. This value was higher by two orders of magnitude than the values obtained for the other analysed 4PEM-exchanged Au₂₅ clusters.

Second method used to evaluate the association constant of the formed 4PEM–ZnTPP complex looked at quenching of an intrinsic fluorescence of a host molecule by added ligand (i.e., a quencher) through a log-log relationship (**Figure 4.11**).

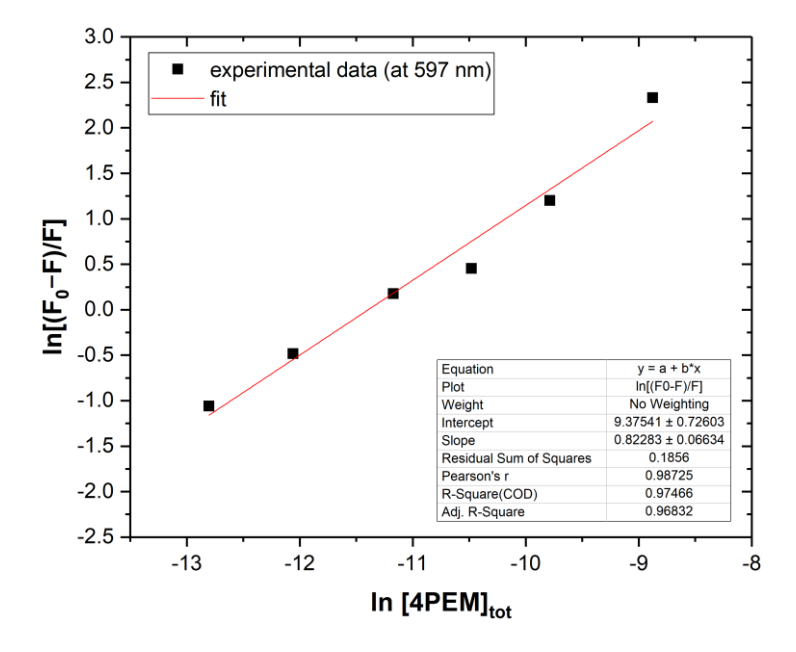


Figure 4.11 Log-log plot of the fluorescence intensity of the ZnTPP as a function of total concentration of added guest– $Au_{25}(SBu)_{18-x}(4PEM)_x$ (x=0.6). Fitting of the experimental data (black squares) to **Equation 4.18** performed using the Origin software.

The value of the binding constant, K_a obtained was $(1.18 \pm 0.09) \times 10^4$ M⁻¹, which differs significantly from the value obtained from fitting using the Method 1 (for fluorescent host–guest complex, see **Table 4.3**). Moreover, the n value of 0.82 suggested that the 4PEM-Au₂₅ was binding to ZnTPP in a 1:1 stoichiometry.

Table 4.3 Association constant values for $ZnTPP-Au_{25}(SBu)_{18-x}(4PEM)_x$ (x=2.1) calculated from fitting of the fluorescence titartion data using two methodologies.

	PL titration		
ZnTPP-4PEM@Au ₂₅	Method 1	Method 2	
ZIII F F-4F EWI @ Au25	(HG complex	(HG complex	
	photoluminescent)	non-photoluminescent)	
$K_a [M^{-1}]$	$(1.27 \pm 0.31) \times 10^5$	$(1.18 \pm 0.09) \times 10^4$	

It needs to be said that for the method using double logarithmic plot (i.e., assuming the host–guest complex is non-fluorescent) even a minor residual fluorescence will affect the outcome for both the binding constant and stoichiometry. The residual fluorescence strongly influences the slope of the curve, which defines the stoichiometry, and to a much greater extent the K_a value as the intercept corresponds to the logarithm of K_a , hence very small changes in the slope of the fitted curve will impact the K_a value significantly.

The fluorescence does not completely vanish, even at large excess of the guest py ligand. This suggests that the formed complex is fluorescent as well.

4.6 Interactions of CoTPP with functionalized Au₂₅ nanoclusters probed with spectrophotometric titrations

ZnTPP was shown to successfully bind to the 4PEM functionalized Au₂₅ nanoclusters with varying ratio of coordinating pyridyl ligand in the protective monolayer. However, the ZnTPP was shown to form penta-coordinate complexes also in the case of 4PEM-Au₂₅ clusters, making this porphyrin unsuitable as an anchoring point for pyridyl functionalized-Au₂₅ nanoclusters to enable formation of self-assembled extended Au₂₅ nanostructures. To explore the possibility of connecting the functionalized Au₂₅ to two axial positions in the macrocycle, CoTPP was chosen as it is known that cobalt porphyrins can axially bind two *N*-containing ligands in contrast to ZnTPP.^{40,41}

4.6.1 UV-vis titration of CoTPP with pyridine and $Au_{25}(SBu)_{18-x}(4PEM)_x$ nanoclusters

4.6.1.1 Solution-state binding study of CoTPP with pyridine

Investigation of the axial coordination of the *N*-containing ligand to CoTPP macrocycle began with the analysis of the simple system using py as a strongly coordinating ligand (**Scheme 4.3**). Again, the UV-vis titration experiment was conducted to understand the binding of the pyridyl ligand with the CoTPP by estimating the K_a value. The incremental addition of a toluene solution of py to a toluene solution of CoTPP (4.47 × 10⁻⁶ M) resulted in the formation of a host–guest complex which could be monitored with UV-vis absorption spectroscopy (**Figure 4.12**-a). The uncomplexed CoTPP solution in toluene (black trace in **Figure 4.12**-a) exhibited two absorption maxima: very intense Soret band at 24,213 cm⁻¹ (413 nm) and a Q band at 18,901 cm⁻¹ (529 nm). Upon complexation with the py ligand these peaks red-shifted to 22,989 cm⁻¹ (435 nm) and 18,480 cm⁻¹ (541 nm).

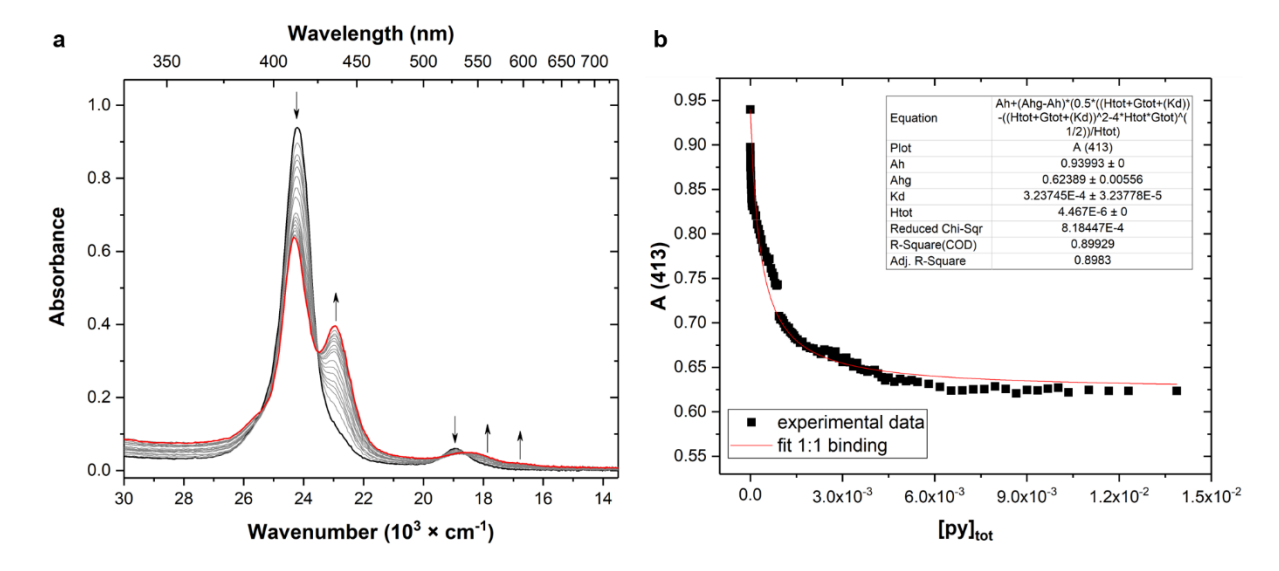


Figure 4.12 (a) Change in the absorption spectra of CoTPP in toluene $(4.47 \times 10^{-6} \, \text{M})$ upon titration with the solution of py ligand $(0-1.39 \times 10^{-2} \, \text{M})$ in toluene at 298 K. (b) Fit of the experimental data (black squares) of change in the absorbance of CoTPP Soret band as a function of total concentration of py ligand. Fitting to the 1:1 binding model was performed with Bindfit v. 0.5 program.

The changes in the absorbance of the CoTPP Soret band (24,213 cm⁻¹; 413 nm) as a function of total concentration of added py ligand are depicted in **Figure 4.12**-b. Fitting of this data, assuming both 1:1 and 1:2 host–guest binding, was performed using Bindfit v. 0.5 program. Only the 1:1 binding scenario gave meaningful results. The calculated association constant, K_a , was $(3.09 \pm 0.31) \times 10^3$ M⁻¹. This value was larger than the K_a value of $(4.85 \pm 0.29) \times 10^2$ M⁻¹ (toluene, 298 K) reported by Walker.⁴² This discrepancy could arise from the oxidation of the central Co²⁺ ion or presence of impurities (CoTPP was used as received) and was manifested by the low accuracy of the fit to the obtained experimental

data (red curve in **Figure 4.12**-b). It needs to be said that the titration was not performed under temperature-controlled conditions and each data point was measured immediately after each aliquot of py was added to the CoTPP solution, perhaps not allowing sufficient time for equilibration for this specific system.

4.6.1.2 Solution-state binding study of CoTPP with Au₂₅(SBu)_{18-x}(4PEM)_x nanoclusters

Determination of the binding affinities corresponding to the interaction between the 4PEM-functionalized Au_{25} nanoclusters and the CoTPP macrocycle was first attempted with UV-vis titration. Au_{25} nanoclusters with, $\bar{x}=2.1$ of 4PEM in the ligand shell were employed in this study (sample D_Au25-4PEM, see **Section 4.2.2**). The absorption spectral changes occurring upon incremental addition of a $Au_{25}(SBu)_{18-2.1}(4PEM)_{2.1}$ solution to the anhydrous toluene solution of CoTPP $(4.78 \times 10^{-6} \text{ M})$ are depicted in **Figure 4.13**.

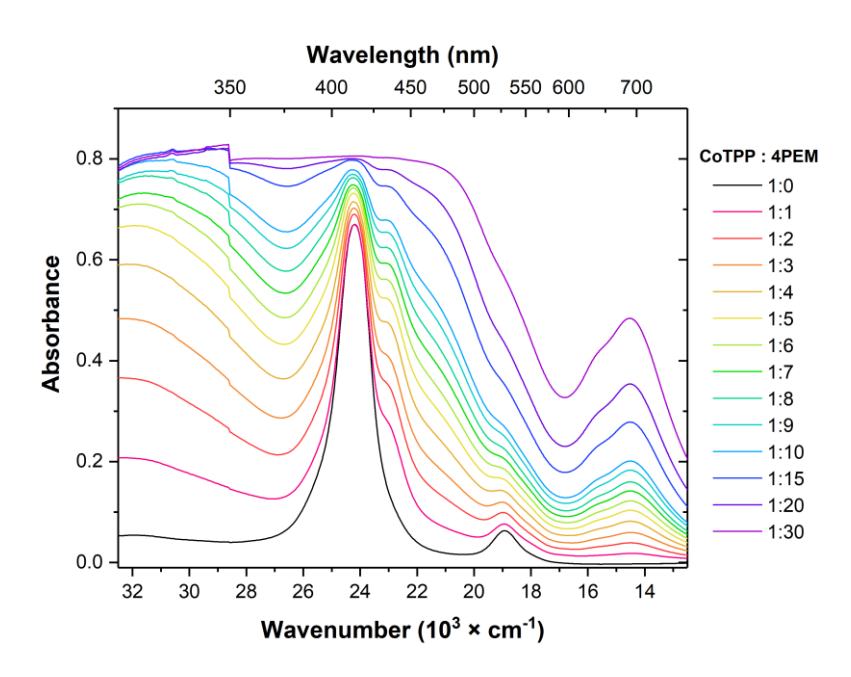


Figure 4.13 Change in the absorption spectra of CoTPP solution in toluene $(4.78 \times 10^{-6} \text{ M})$ upon titrating with $Au_{2.5}(SBu)_{18-x}(4PEM)_x$, where $\bar{x} = 2.1$ ([4PEM] = 0–1.47 × 10⁻⁴ M). Spectra measured at 298 K.

The Soret band of an unbound CoTPP at 24,213 cm⁻¹ (413 nm) was clearly visible in the spectra as the titration progressed. Incremental addition of 4PEM-Au₂₅ solution resulted in the emergence of new shoulder around ~23,006 cm⁻¹ (435 nm) that confirmed the axial ligand binding to the central Co²⁺ ion in the porphyrin macrocycle. Importantly, the contributions originating from the Au₂₅ species started dominating the absorption, e.g., the clear appearance of a band at ~14,521 cm⁻¹ (689 nm), precluding the use the UV-vis titration data to calculate binding constants employing the methodology described in **Section 4.4.1**.

4.6.2 Fluorescence titration of CoTPP with pyridine and $Au_{25}(SBu)_{18-x}(4PEM)_x$ nanoclusters

4.6.2.1 Solution-state binding study of CoTPP with pyridine

Fluorescence titration of CoTPP with the py ligand was performed as a control experiment. The fluorescence spectrum of CoTPP (black trace in **Figure 4.14**-a) acquired after excitation at the Soret band wavelength (i.e., 422 nm) displayed an emission band at 15,267 cm⁻¹ (655 nm). This emission bands belongs to the transition from the lowest excited singlet state S_1 to the ground state S_0 of CoTPP.

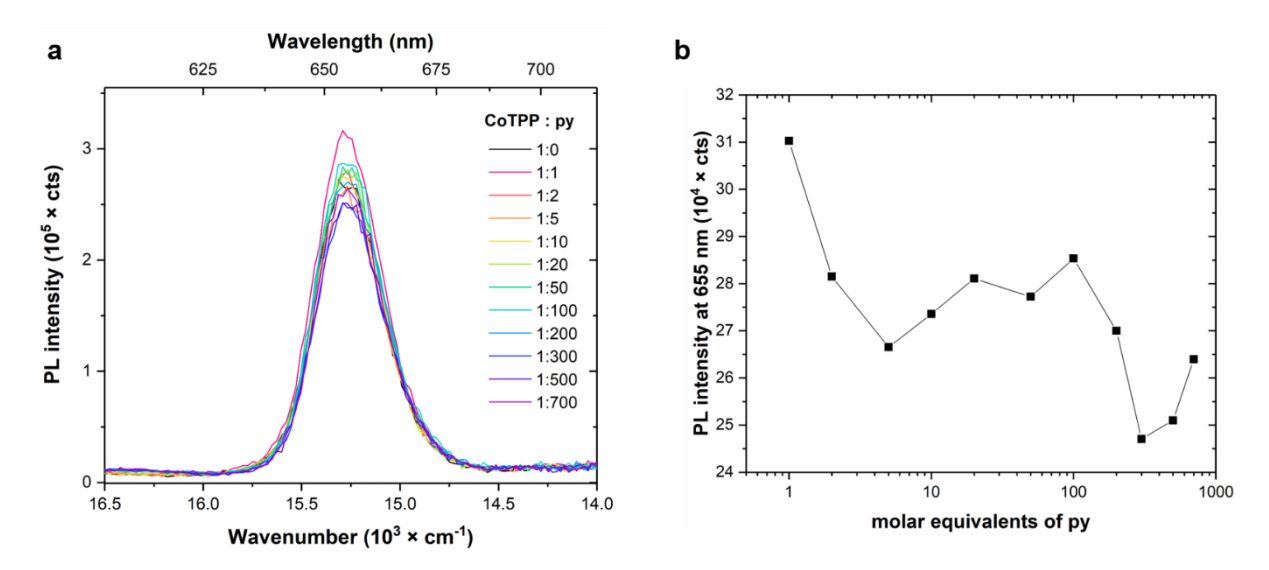


Figure 4.14 (a) Change in the PL emission of CoTPP $(4.79 \times 10^{-6} \text{ M})$ upon gradual addition of py $([py] = 0-3.50 \times 10^{-3} \text{ M})$. Spectra recorded at 298 K in toluene after excitation at 422 nm with the size of excitation and emission slits = 10 nm. Spectra corrected for reabsorption. (b) Change in the PL emission intensity at 655 nm of the Q band maximum of CoTPP upon titration with py.

Incremental addition of the py ligand resulted in an apparent decrease of the intensity of the fluorescence peak (**Figure 4.14**-a), however no clear monotonic trend in this decrease was noted (**Figure 4.14**-b). Indeed, noise in the fluorescence spectra likely contributed to the discrepancy in the observed data therefore they were considered inappropriate for fitting to the model described in **Section 4.4.2**. Further treatment of data by fitting the fluorescence spectra to a Gaussian model may help to improve the quality of the data presented in **Figure 4.14**-b. It is still unclear however if after the applied corrections the data could be fitted to a model as previously described given the discrepancy between the observed fluorescence at the 1:0 and 1:1 CoTPP:py titration points.

4.6.2.2 Solution-state binding study of CoTPP with Au₂₅(SBu)_{18-x}(4PEM)_x nanoclusters

Since the average number of 4PEM molecules within the Au_{25} monolayer was relatively low, very quickly the Au_{25} nanocluster absorption started to overshadow that of CoTPP. Therefore, even though the emergence of the Soret band at 435 nm could be followed initially, it still was coinciding with the absorption of Au_{25} species. Therefore, the evaluation of the association constant for a CoTPP-4PEM system was performed using steady-state fluorescence measurements.

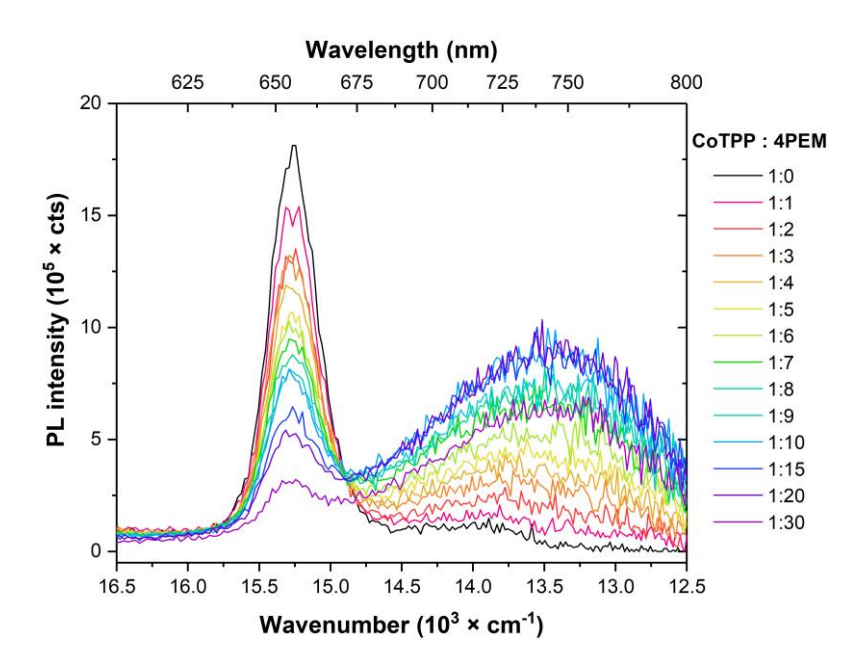


Figure 4.15 Change in steady-state photoluminescence spectra of CoTPP in toluene $(4.78 \times 10^{-6} \text{ M})$ upon addition of 4PEM-functionalized Au₂₅ nanoclusters $(0-1.47 \times 10^{-4} \text{ M})$ recorded at 298 K (in right angle geometry) after excitation at 424 nm. Spectra were corrected for reabsorption at the excitation wavelength.

The fluorescence titration (**Figure 4.15**) showed the characteristic emission band of CoTPP at 15,267 cm⁻¹ (655 nm) to decrease with gradual addition of 4PEM functionalized Au₂₅. Moreover, as the titration progressed, a steady growth of a broad emission band centred at 13,500 cm⁻¹ (742 nm) band was noted. This band was ascribed to the photoluminescence originating from the Au₂₅ clusters.⁴³ Overall, the 4PEM ligand binding to the CoTPP macrocycle caused quenching of the intrinsic CoTPP fluorescence, just like in the case of the ZnTPP macrocycle, possibly due to excitation transfer from the excited state of the porphyrin to Au₂₅ nanocluster.

Fluorescence titration data was analysed using two methods which assumed that (i) photoluminescent and (ii) non-fluorescent host–guest complex was formed.

Figure 4.16 depicts the changes in the PL emission intensity at 15,267 cm⁻¹ (655 nm) as a function of total concentration of 4PEM added to the porphyrin solution (black squares). The experimental data (titration data points up to 20 equivalents of 4PEM were used) was fitted to **Equation 4.12**. Two

assumptions were made regarding the formed host–guest complex: (i) a 1:1 binding stoichiometry (since the analysis of the model CoTPP–py system yielded 1:1 stoichiometry) and (ii) it was photoluminescent.

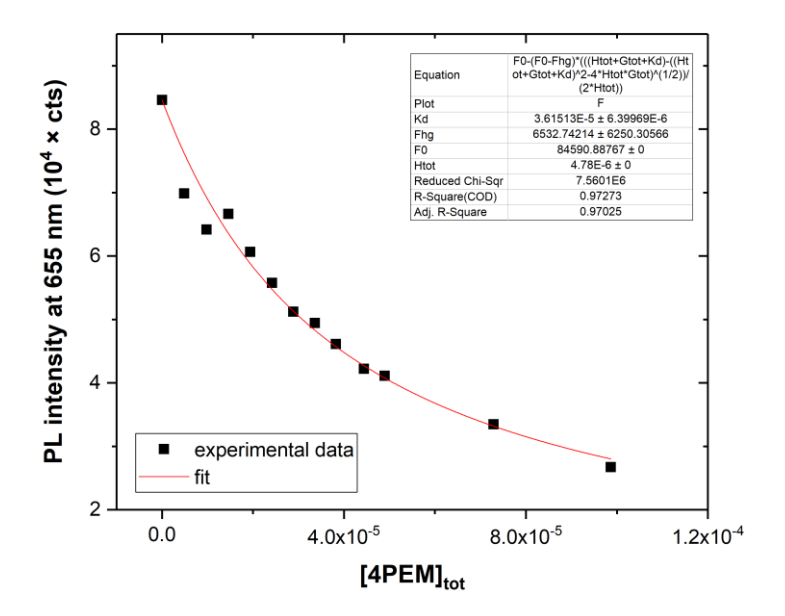


Figure 4.16 Change in the PL intensity of the 655 nm emission maxima of CoTPP upon complexation with 4PEM-functionalized Au₂₅ nanocluster (black squares). Fitting of the experimental data to Equation 4.12 was performed with nonlinear regression method using the Origin software is depicted as red curve. The applied method assumes 1:1 binding and luminescent host—guest complex. Photoluminescence intensity was corrected for inner-filter effects.

The value of the association constant, K_a obtained from the fit was $(2.77 \pm 0.49) \times 10^4$ M⁻¹. This value is ca. one order of magnitude higher than the binding constant obtained for CoTPP–py system derived from the UV-vis titration experiment.

The log-log method was also employed to analyse the same set of data. This method presumes that the host–guest complex exhibits fluorescence. Again, the changes in the PL emission intensity of CoTPP due to complexation with 4PEM-Au₂₅ were fitted to **Equation 4.18**. Much like for the method applied above, titration data points up to 20 equivalents of 4PEM were used here.

Figure 4.17 depicts a double logarithmic plot of the fluorescence emission at 15,267 cm⁻¹ (655 nm) as a function of total 4PEM concentration. Two fits were performed: first (blue curve), for which all the data points were included in the fit, yielded the value of K_a of $(3.24 \pm 0.27) \times 10^3$ M⁻¹, whereas the second fitting (red curve) that omitted the first 2 data points gave the K_a of $(3.90 \pm 0.11) \times 10^4$ M⁻¹. The former was very close to the value obtained for CoTPP–py system from the UV-vis titration experiment.

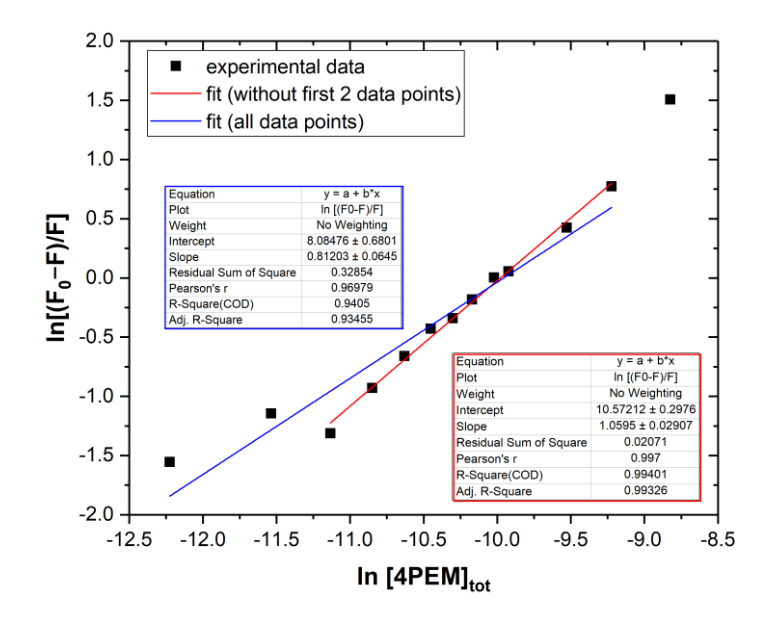


Figure 4.17 Theoretical fits (red and blue curves) using **Equation 4.18** to the fluorescence data measured at 655 nm (black squares) as function of added 4PEM ligands. Fitting was performed in the Origin software.

Very similar to the case of ZnTPP-4PEM-Au₂₅ system, the analysis of the fluorescence titration data using two methods gave K_a values that differ by one order of magnitude (**Table 4.4**). The n values of 0.81 and 1.06 (blue and red fit, respectively) indicated that the obtained 4PEM-Au₂₅ was axially ligated at 1:1 stoichiometric ratio, which revealed that CoTPP was not a suitable metalloporphyrin to form extended assemblies as the formation of 1:2 complex was not preferred.

Table 4.4 Association constant values for $CoTPP-Au_{25}(SBu)_{18-x}(4PEM)_x$ (x=2.1) calculated from fitting of the fluorescence titartion data using two methodologies.

	PL titration		
CoTPP-4PEM@Au25	Method 1	Method 2	
COTPP-4PENI@Au25	(HG complex	(HG complex	
	photoluminescent)	non-photoluminescent)	
$K_a [M^{-1}]$	$(2.77 \pm 0.49) \times 10^4$	$(1) (3.24 \pm 0.27) \times 10^3$	
	$(2.77 \pm 0.49) \times 10$	$(2) (3.90 \pm 0.11) \times 10^4$	

4.7 Conclusions

The aim of this study was to investigate the use of metalloporphyrins as effective anchoring points for Au_{25} nanoclusters making an important step towards realizing extended Au NC assemblies. The successful functionalization of the Au_{25} nanocluster monolayer and control of the ratio of the introduced anchoring ligand was demonstrated. The binding of the 4PEM-Au₂₅ species to ZnTPP and CoTPP has

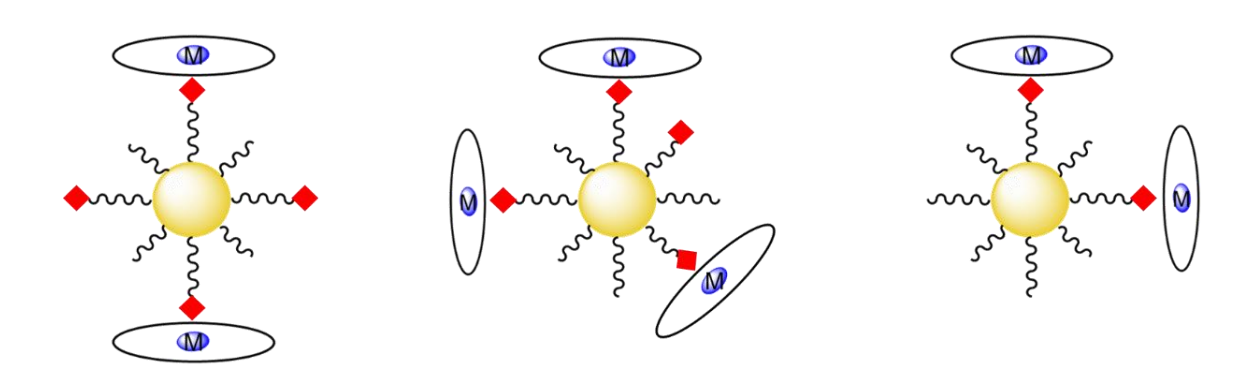
been followed spectroscopically during titration experiments by monitoring UV-vis and fluorescence. It has been shown that the employed metalloporphyrins formed coordination complexes in a 1:1 stoichiometry, reminiscent to the binding with simple py ligands. No evidence for substantial biaxial binding was found, neither for ZnTPP nor for CoTPP. The association constants were derived from fitting of the titration data to different models. For the Au₂₅ nanocluster with higher ratio of the 4PEM anchoring ligands in the monolayer (i.e, $\bar{x} = 6.8$ and 4.4), the calculated K_a were quite close in value to that found for the ZnTPP-py system. Interestingly, the half-saturation of the host metalloporphyrin was achieved with a lower amount of the introduced 4PEM-Au₂₅ species in the case of cluster with lower average exchange number, indicating that steric factors might have affected the binding. Ideally, for achieving the extended self-assembly, a low number of symmetrically distributed anchoring ligands in the Au₂₅ monolayer are required. The study of Au₂₅ species with a low 4PEM ratio showed that binding was occurring with both ZnTPP and CoTPP macrocycles, however quantitative analysis to extract the binding constants was challenging. Specifically, the applied models that correlate the concentrations of the host and guest molecules with the observed signal (absorbance or emission intensity) include coarse assumptions e.g., the added guest molecule does not exhibit any absorbance at the wavelength of interest (i.e., where the host or host-guest complex absorb). While this is true for simple organic ligands and perhaps could be accepted for the case with high 4PEM ratio in Au₂₅ monolayer (see **Figure 4.5** and **Figure 4.6**), it became problematic for the $Au_{25}(SBu)_{18-x}(4PEM)_x$ species with the low x value, as the broad absorbance from the Au₂₅ clusters dominated the spectrum.

Equally, for the fluorescence experiments, the challenge with studying the species with low ratio of anchoring ligands resided in the fluorescence quenching mechanisms that were likely not purely attributable to the host–guest complex formation (i.e., inner-filter effects, energy transfer). Of note, analysis of the fluorescence titration data requires careful and elaborate correction approaches that account for the inner filter effects⁴⁴ especially given that the solutions measured in the present study exhibited high absorbance values. The values of the K_a calculated using different approaches for the same system differed quite lot (by an order of magnitude). It can be said putatively that K_a is within the 10^4 – 10^5 M⁻¹ range of values for ZnTPP and 10^3 – 10^4 M⁻¹ for CoTPP. These values differ significantly from K_a obtained for simple MTPP–py complexes (~ 10^3 M⁻¹ for ZnTPP and ~ 10^2 for CoTPP).

To achieve extended Au₂₅-based assemblies using metalloporphyrins as the anchoring points the association constants for the axially coordinated ligands i.e., $K_{a,1}$ and $K_{a,2}$, see **Scheme 4.3**, need to be in the same order of magnitude, otherwise complexes with the 1:1 binding stoichiometry will dominate in the system. Literature does not report the $K_{a,2}$ value for $\text{Co}^{\text{II}}\text{TPP}(\text{py})_2$ formation in toluene. However, the $K_{a,1}$ and $K_{a,2}$ values calculated for py binding to $\text{Co}^{\text{II}}\text{TPP}(\text{CN})_4$ macrocycle in dichloromethane at 298 K were $1.59 \times 10^4 \,\text{M}^{-1}$ and $0.40 \,\text{M}^{-1}$, respectively. Other fluoro-substituted $\text{Co}^{\text{II}}\text{TPP}$ porphyrins, $\text{Co}(\text{F}_8\text{TPP})$ and $\text{Co}(\text{F}_{28}\text{TPP})$, also displayed low $K_{a,2}$ values for py binding in dichloromethane at 298 K:

 $0.83 \,\mathrm{M}^{-1}$ and $10.72 \,\mathrm{M}^{-1}$, respectively. ⁴⁶ Therefore, the low values of the $K_{a,2}$ support an argument against CoTPP as a suitable anchor for pyridyl-functionalized Au₂₅ nanocluster-based architectures.

Future investigation aiming at demonstrating the 1:2 binding between the host porphyrin and Au₂₅ clusters could focus on using metalloporphyrins having a centre ion that is more prone to form 1:2 complexes with pyridyl derivatives (e.g., Fe^{47,48}). Otherwise employing peripherally functionalized metalloporphyrin such as Co^{III}TPP with electron withdrawing groups in the macrocycle^{46,49} to favour the binding in both axial positions could also be considered. Alternatively, different anchoring functionality in the nanocluster monolayer (e.g., imidazole⁵⁰) might be implemented. Recently published work showed promise in employing Co^{II} porphyrins as anchor molecules. Bichan et al. demonstrated formation of the six-coordinate Co^{II}-porphyrin complex involving the self-assembly of CoOEP (OEP = 2,3,7,8,12,13,17,18-octaethylporphinato) macrocycle and two pyridyl-functionalized gold^{III} porphyrin molecules – (2,3,7,8,12,18-hexamethyl,13,17-diethyl,5-(4-pyridyl)porphinato)gold^{III} chloride).⁵¹ The association constants $K_{a,1}$ and $K_{a,2}$ were (8.40 ± 1.07) × 10⁴ and (6.09 ± 1.10) × 10⁴ M⁻¹, respectively, indicating that stable supramolecules based on cobalt porphyrins could be achieved.



Scheme 4.4 Graphical representation of the possible Au₂₅-metalloporphyrins assemblies with 1:1 binding stoichiometry.

Nonetheless, the preferred 1:1 binding led to the interesting assembled structures where the Au_{25} clusters were covered by several metalloporphyrin macrocycles (**Scheme 4.4**). These systems could be investigated for application in photocatalysis.

4.8 References

- 1. Fukuzumi, S.; Lee, Y.-M.; Nam, W., Photocatalytic Redox Reactions with Metalloporphyrins. *Journal of Porphyrins and Phthalocyanines* **2019**, 24 (01n03), 21-32.
- 2. Song, H.; Liu, Q.; Xie, Y., Porphyrin-Sensitized Solar Cells: Systematic Molecular Optimization, Coadsorption and Cosensitization. *Chemical Communications* **2018**, *54* (15), 1811-1824.
- Varchi, G.; Foglietta, F.; Canaparo, R.; Ballestri, M.; Arena, F.; Sotgiu, G.; Guerrini, A.; Nanni, C.; Cicoria, G.; Cravotto, G.; Fanti, S.; Serpe, L., Engineered Porphyrin Loaded Core-Shell Nanoparticles for Selective Sonodynamic Anticancer Treatment. *Nanomedicine* 2015, 10 (23), 3483-3494.

- Hammerer, F.; Garcia, G.; Chen, S.; Poyer, F.; Achelle, S.; Fiorini-Debuisschert, C.; Teulade-Fichou, M.-P.;
 Maillard, P., Synthesis and Characterization of Glycoconjugated Porphyrin Triphenylamine Hybrids for Targeted Two-Photon Photodynamic Therapy. *The Journal of Organic Chemistry* 2014, 79 (3), 1406-1417.
- 5. Abrahams, B. F.; Hoskins, B. F.; Michail, D. M.; Robson, R., Assembly of Porphyrin Building Blocks Into Network Structures with Large Channels. *Nature* **1994**, *369* (6483), 727-729.
- 6. Wang, X.; Nurttila, S. S.; Dzik, W. I.; Becker, R.; Rodgers, J.; Reek, J. N. H., Tuning the Porphyrin Building Block in Self-Assembled Cages for Branched-Selective Hydroformylation of Propene. *Chemistry A European Journal* **2017**, *23* (59), 14769-14777.
- 7. Beletskaya, I.; Tyurin, V. S.; Tsivadze, A. Y.; Guilard, R.; Stern, C., Supramolecular Chemistry of Metalloporphyrins. *Chemical Reviews* **2009**, *109* (5), 1659-1713.
- 8. Hiroto, S.; Miyake, Y.; Shinokubo, H., Synthesis and Functionalization of Porphyrins Through Organometallic Methodologies. *Chemical Reviews* **2017**, *117* (4), 2910-3043.
- McCallien, D. W. J.; Sanders, J. K. M., Dioxoporphyrins as Supramolecular Building Blocks: Oligomer Synthesis via Preassembly on a Ligand Template. *Journal of the American Chemical Society* 1995, 117 (24), 6611-6612.
- 10. Kang, X.; Chong, H.; Zhu, M., Au₂₅(SR)₁₈: the Captain of the Great Nanocluster Ship. *Nanoscale* **2018**, *10* (23), 10758-10834.
- 11. Zhu, M. Z.; Eckenhoff, W. T.; Pintauer, T.; Jin, R., Conversion of Anionic [Au₂₅(SCH₂CH₂Ph)₁₈]⁻ Cluster to Charge Neutral Cluster via Air Oxidation. *The Journal of Physical Chemistry C* **2008**, *112* (37), 14221-14224.
- 12. Tofanelli, M. A.; Salorinne, K.; Ni, T. W.; Malola, S.; Newell, B.; Phillips, B.; Häkkinen, H.; Ackerson, C. J., Jahn–Teller Effects in Au₂₅(SR)₁₈. *Chemical Science* **2016**, 7 (3), 1882-1890.
- 13. De Nardi, M.; Antonello, S.; Jiang, D.-e.; Pan, F.; Rissanen, K.; Ruzzi, M.; Venzo, A.; Zoleo, A.; Maran, F., Gold Nanowired: A Linear (Au₂₅)_n Polymer from Au₂₅ Molecular Clusters. *ACS Nano* **2014**, *8* (8), 8505-8512.
- 14. Yuan, X.; Goswami, N.; Mathews, I.; Yu, Y.; Xie, J., Enhancing Stability through Ligand-Shell Engineering: A Case Study with Au₂₅(SR)₁₈ Nanoclusters. *Nano Research* **2015**, 8 (11), 3488-3495.
- 15. Collins, C. B.; Tofanelli, M. A.; Crook, M. F.; Phillips, B. D.; Ackerson, C. J., Practical Stability of $Au_{25}(SR)_{18}^{-1/0/+1}$. *RSC Advances* **2017**, 7 (71), 45061-45065.
- 16. Salassa, G.; Sels, A.; Mancin, F.; Bürgi, T., Dynamic Nature of Thiolate Monolayer in Au₂₅(SR)₁₈ Nanoclusters. *ACS Nano* **2017**, *11* (12), 12609-12614.
- 17. Bhat, S.; Narayanan, R. P.; Baksi, A.; Chakraborty, P.; Paramasivam, G.; Methikkalam, R. R. J.; Nag, A.; Natarajan, G.; Pradeep, T., Detection of [Au₂₅(PET)₁₈(O₂)_n]⁻ (n = 1, 2, 3) Species by Mass Spectrometry. *The Journal of Physical Chemistry C* **2018**, *122* (34), 19455-19462.
- 18. Zhu, M.; Aikens, C. M.; Hollander, F. J.; Schatz, G. C.; Jin, R., Correlating the Crystal Structure of a Thiol-Protected Au₂₅ Cluster and Optical Properties. *Journal of the American Chemical Society* **2008**, *130* (18), 5883-5885.
- 19. Katsiev, K.; Lozova, N.; Wang, L.; Sai Krishna, K.; Li, R.; Mei, W.-N.; Skrabalak, S. E.; Kumar, C. S. S. R.; Losovyj, Y., The Electronic Structure of Au₂₅ Clusters: Between Discrete and Continuous. *Nanoscale* **2016**, 8 (31), 14711-14715.
- Hossain, S.; Kurashige, W.; Wakayama, S.; Kumar, B.; Nair, L. V.; Niihori, Y.; Negishi, Y., Ligand Exchange Reactions in Thiolate-Protected Au₂₅ Nanoclusters with Selenolates or Tellurolates: Preferential Exchange Sites and Effects on Electronic Structure. *The Journal of Physical Chemistry C* 2016, 120 (45), 25861-25869.

- 21. Gouterman, M., Spectra of Porphyrins. Journal of Molecular Spectroscopy 1961, 6, 138-163.
- 22. Annoni, E.; Pizzotti, M.; Ugo, R.; Quici, S.; Morotti, T.; Bruschi, M.; Mussini, P., Synthesis, Electronic Characterisation and Significant Second-Order Non-Linear Optical Responses of *meso*-Tetraphenylporphyrins and Their Zn(II) Complexes Carrying a Push or Pull Group in the β Pyrrolic Position. *European Journal of Inorganic Chemistry* **2005**, 2005 (19), 3857-3874.
- 23. Williams, R. J. P., The Properties of Metalloporphyrins. Chemical Reviews 1956, 56 (2), 299-328.
- 24. D'Urso, A.; Fragalà, M. E.; Purrello, R., From Self-Assembly to Noncovalent Synthesis of Programmable Porphyrins' Arrays in Aqueous Solution. *Chemical Communications* **2012**, *48* (66), 8165-8176.
- Nappa, M.; Valentine, J. S., The Influence of Axial Ligands on Metalloporphyrin Visible Absorption Spectra. Complexes of Tetraphenylporphinatozinc. *Journal of the American Chemical Society* 1978, 100 (16), 5075-5080.
- 26. Cole, S. J.; Curthoys, G. C.; Magnusson, E. A., Ligand Binding by Metalloporphyrins. I. Thermodynamic Functions of Porphyriniron(II)-Pyridine Complexes. *Journal of the American Chemical Society* **1970**, 92 (10), 2991-2996.
- 27. Cole, S. J.; Curthoys, G. C.; Magnusson, E. A.; Phillips, J. N., Ligand Binding by Metalloporphyrins. III. Thermodynamic Functions for the Addition of Substituted Pyridines to Nickel(II) and Zinc(II) Porphyrins. *Inorganic Chemistry* **1972**, *11* (5), 1024-1028.
- 28. www.supramolecular.org
- 29. Thordarson, P., Determining Association Constants from Titration Experiments in Supramolecular Chemistry. *Chemical Society Reviews* **2011**, *40* (3), 1305-1323.
- 30. http://www.originlab.com/
- 31. Scatchard, G., The Attractions of Proteins for Small Molecules and Ions. *Annals of the New York Academy of Sciences* **1949**, *51* (4), 660-672.
- 32. Renny, J. S.; Tomasevich, L. L.; Tallmadge, E. H.; Collum, D. B., Method of Continuous Variations: Applications of Job Plots to the Study of Molecular Associations in Organometallic Chemistry. *Angewandte Chemie International Edition* **2013**, *52* (46), 11998-12013.
- 33. Lissi, E.; Abuin, E., On the Evaluation of the Number of Binding Sites in Proteins From Steady State Fluorescence Measurements. *Journal of Fluorescence* **2011**, *21* (5), 1831-1833.
- 34. Lakowicz, J. R., Principles of Fluorescence Spectroscopy. 3rd edition; Springer: 2006.
- 35. Caldin, E. F.; Field, J. P., Kinetics of Complex Formation Between Zinc *meso*-Tetraphenylporphyrin and Some Nitrogen Bases in Aprotic Solvents, Studied by an Improved Microwave Temperature-Jump Method. *Journal of the Chemical Society, Faraday Transactions 1: Physical Chemistry in Condensed Phases* **1982**, 78 (6), 1923-1935.
- 36. Breen, C. J.; Raverdeau, M.; Voorheis, H. P., Development of a Quantitative Fluorescence-Based Ligand-Binding Assay. *Scientific Reports* **2016**, *6* (1), 25769.
- 37. Harriman, A., Luminescence of Porphyrins and Metalloporphyrins. Part 1.-Zinc(II), Nickel(II) and Manganese(II) Porphyrins. *Journal of the Chemical Society, Faraday Transactions 1: Physical Chemistry in Condensed Phases* **1980**, 76 (0), 1978-1985.
- 38. Humphry-Baker, R.; Kalyanasundaram, K., Influence of Axial Ligation on the Fluorescence of Tetrakisphenylporphyrins. *Journal of Photochemistry* **1985**, *31* (1), 105-112.

- 39. Varnholt, B.; Letrun, R.; Bergkamp, J. J.; Fu, Y.; Yushchenko, O.; Decurtins, S.; Vauthey, E.; Liu, S.-X.; Burgi, T., Excited State Interactions Between the Chiral Au₃₈L₂₄ Cluster and Covalently Attached Porphyrin. *Physical Chemistry Chemical Physics* **2015**, *17* (22), 14788-14795.
- 40. Fidalgo-Marijuan, A.; Barandika, G.; Bazán, B.; Urtiaga, M.-K.; Arriortua, M. I., Thermal Stability and Crystallochemical Analysis for Co(II)-Based Coordination Polymers With TPP and TPPS Porphyrins. *CrystEngComm* **2013**, *15* (20), 4181-4188.
- 41. Goodwin, J.; Bailey, R.; Pennington, W.; Rasberry, R.; Green, T.; Shasho, S.; Yongsavanh, M.; Echevarria, V.; Tiedeken, J.; Brown, C.; Fromm, G.; Lyerly, S.; Watson, N.; Long, A.; De Nitto, N., Structural and Oxo-Transfer Reactivity Differences of Hexacoordinate and Pentacoordinate (Nitro)(tetraphenylporphinato)cobalt(III) Derivatives. *Inorganic Chemistry* **2001**, *40* (17), 4217-4225.
- 42. Walker, F. A., Steric and Electronic Effects in the Coordination of Amines to a Cobalt(II) Porphyrin. *Journal of the American Chemical Society* **1973**, *95* (4), 1150-1153.
- 43. Wu, Z.; Jin, R., On the Ligand's Role in the Fluorescence of Gold Nanoclusters. *Nano Lett* **2010**, *10* (7), 2568-2573.
- 44. Gu, Q.; Kenny, J. E., Improvement of Inner Filter Effect Correction Based on Determination of Effective Geometric Parameters Using a Conventional Fluorimeter. *Analytical Chemistry* **2009**, *81* (1), 420-426.
- 45. Lin, X. Q.; Boisselier-Cocolios, B.; Kadish, K. M., Electrochemistry, Spectroelectrochemistry, and Ligand Addition Reactions of an Easily Reducible Cobalt Porphyrin. Reactions of (Tetracyanotetraphenylporphinato)Cobalt(II) (((CN)4TPF)Co(II)) in Pyridine and in Pyridine/Methylene Chloride Mixtures. *Inorganic Chemistry* **1986**, 25 (18), 3242-3248.
- 46. Smirnov, V. V.; Woller, E. K.; DiMagno, S. G., ¹⁹F NMR and Structural Evidence for Spin-State Modulation of Six-Coordinate Cobalt(II) in a Weak Field Porphyrin Ligand. *Inorganic Chemistry* **1998**, *37* (19), 4971-4978.
- 47. Patra, R.; Bhowmik, S.; Ghosh, S. K.; Rath, S. P., Effects of Axial Pyridine Coordination on a Saddle-Distorted Porphyrin Macrocycle: Stabilization of Hexa-Coordinated High-Spin Fe(III) and Air-Stable Low-Spin Iron(II) Porphyrinates. *Dalton Transactions* **2010**, *39* (25), 5795-5806.
- 48. Nasri, S.; Brahmi, J.; Turowska-Tyrk, I.; Schulz, C. E.; Nasri, H., Synthesis, UV-visible and Mössbauer Spectroscopic Studies and Molecular Structure of the Low-Spin Iron(II) Bis(Tert-Butyl Isocyanide)(5, 10, 15, 20-[4-(Benzoyloxy)Phenyl]Porphyrin) Coordination Compound. *Journal of Organometallic Chemistry* **2017**, 846, 176-184.
- 49. Terazono, Y.; Patrick, B. O.; Dolphin, D. H., X-ray Crystal Structure and Ligand Binding to β-Tetrakis (trifluoromethyl)-*meso*-Tetraphenylporphyrin Cobalt(II). *Inorganica Chimica Acta* 2003, *346*, 265-269.
- Bang, H.; Edwards, J. O.; Kim, J.; Lawler, R. G.; Reynolds, K.; Ryan, W. J.; Sweigart, D. A., Cobalt-59 NMR of Six-Coordinate Cobalt(III) Tetraphenylporphyrin Complexes. 4. The Effect of Phenyl *ortho* Substituents on Chemical Shift, Line Width, and Structure. *Journal of the American Chemical Society* 1992, 114 (8), 2843-2852.
- 51. Bichan, N. G.; Ovchenkova, E. N.; Ksenofontov, A. A.; Kudryakova, N. O.; Semeikin, A. S.; Lomova, T. N., Self-Organizing Donor-Acceptor Assemblies of Cobalt(II) Porphyrin Ligated with Gold(III) Porphyrin or Fullero[60]Pyrrolidine in Liquid Medium. *Journal of Molecular Liquids* **2021**, *326*, 115306.

Chapter 5

Synthesis of $Au_{25}(2PET)_{18}$ -based assemblies covalently bound with photoswitchable linkers

Statement of contribution

Kinetic analysis of the photoligand switching reaction was performed by Dr Arnulf Rosspeintner from Department of Physical Chemistry of University of Geneva.

SAXS measurements, data treatment and initial fittings were performed by Dr Lay-Theng Lee, Laboratoire Léon Brillouin, CEA-Saclay, France

Crystal structure determination was performed by Dr Céline Besnard from Laboratory of Crystallography of University of Geneva.

5.1 Introduction

Molecular electronics technology exploits electronic devices created from a single or group of molecules. Utilizing molecules with unique photochemical or electrochemical properties can lead to electronic devices that inherit the properties of their building blocks, or perhaps even improve them. On that account, employing metal nanoclusters to create extended networks can lead to novel functional nanomaterials that take advantage of the unique properties that nanoclusters offer, which are a direct result of their well-defined atomic structure and tuneable monolayer shell with preferred ligand exchange sites. Moreover, the bottom-up synthetic method for nanoclusters allows to approach the nanoparticle limit in a systematic and controlled manner, making nanoclusters ideal candidates for investigation of

the emergent properties in nanoparticles and higher order structures. Accordingly, understanding structure-property relationships in nanocluster-based materials would advance their application in molecular recognition, device fabrication, bioimaging, therapeutics or catalysis.

One of the strategies to create such functional nanomaterials is self-assembly. As discussed in **Chapter 2**, using multidentate ligands to bind nanoclusters is an effective approach to create extended assemblies. The careful choice of the linker molecules, in terms of their geometry and type of anchoring functionality, can result in tuneable topologies with variety of functions. Additionally, employing a bridging molecule to connect metal nanoclusters offers possibility for that bridging ligand to be a carrier of a particular functionality.

The first step towards achieving extended systems built of metal nanoclusters (NCs) is developing reliable synthetic methods to prepare discrete oligomeric systems of several clusters linked together in an organized manner. Using dithiol ligands to connect single Au NCs was shown to be a successful strategy to form oligomeric species. ²⁻⁵ A controlled, wet-chemistry synthetic method, ligand-exchange (LE) reaction, produced the Au NC assemblies. The LE strategy is used to, completely or partially, exchange ligands in the clusters' monolayer, altering their optical, electronic, and physicochemical properties, such as solubility and ability to crystallize. ⁶⁻⁸ It also serves as means to introduce a functionality into the cluster. ⁹ LE can keep the structure of the cluster intact and provides the possibility to precisely control the number of exchanged ligands, owing to the unequal exchange activities on different ligand sites on the surface of clusters.

So far only the most stable and widely-investigated Au NCs were employed to produce oligomeric structures (Au₂₅, Au₁₀₂). It has been found that dithiol ligands were very efficient in linking the Au NCs, and depending on the length of the dithiol and the Au NC structure (core size and the composition of the ligand shell), the binding of clusters may occur via disulfide bridges formed between two dithiolate ligands.² In addition to the physical properties of the dithiol, the reaction conditions (concentration of the incoming dithiol, reaction time, solvent) were shown to be of importance.^{2, 3}

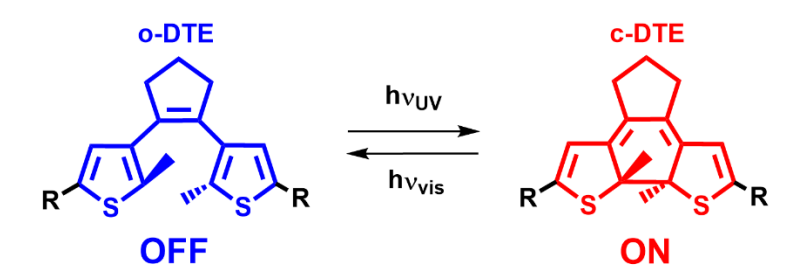
Sels et al. have demonstrated that reacting small hydrophobic $[Au_{25}(SR)_{18}]^0$ (SR= SBu, 2PET) clusters with simple dithiols led to the formation of small discrete oligomers (dimers and trimers). Moreover, the conjugated nature of the employed dithiol linkers was hypothesized to cause significant changes in the electronic properties of the linked structures. Specifically, the emergence of a new band in the NIR region has been tentatively ascribed to the electronic communication between the Au_{25} nanocluster units within the connected structures.

To investigate whether the origin of the new band could be attributed to the electronic communication between the paramagnetic $[Au_{25}(SR)_{18}]^0$ nanoclusters, herein emphasis was laid on the design of the bridging dithiol ligand. If the electronic conjugation in the linker could be controlled, then the emergence of the band could be confirmed as originating from the conjugated species.

For molecular electronics technology, switching functions play an important role, specifically when controlling the conductivity of a molecule with external stimulus (light, temperature). Molecules whose structure can be dynamically modulated using an external stimulus can be considered in applications for smart materials. Therefore, imparting a photoresponsive function in the formed Au nanoassemblies by employing an optical molecular switch function in the linker could not only contribute to the resolution of fundamental questions into electronic communication between linked Au NCs but also prove to be a promising route toward building blocks for switchable smart materials. Thus, the goal of this work is to develop a photoswitchable ligand suitable for linking $[Au_{25}(2PET)_{18}]^0$ nanoclusters into discrete oligomers.

When designing a linker molecule for this purpose, several important aspects must be considered. Firstly, a strong covalent linking to the Au NC surface is required. For this a dithiol anchoring functionality was chosen that is also of importance for the preferential thiolate-for-thiolate ligand exchange reaction. Secondly, the linker requires an appropriate length, roughly double of the thickness of the protective monolayer, to afford a successful connection between NCs. Shorter ligands could link Au NCs via disulfide bridges, as shown by Lahtinen et al.² which is undesirable since the disulfide bridge breaks the conjugation within the aromatic ligand. [Au₂₅(2PET)₁₈]⁰ nanoclusters employed in this study, have thickness of their ligand shell of ~15.7 Å as revealed from single crystal X-ray diffraction.¹⁰ Additionally, the linker should possess an extended aromatic conjugation system that affords both rigidity and electron transport between the Au NCs. Lastly, given that the electronic communication between Au NCs requires further investigation, a robust and reversible light-operated molecular switch should be included in the linker structure. For this purpose, a diarylethene moiety was chosen.

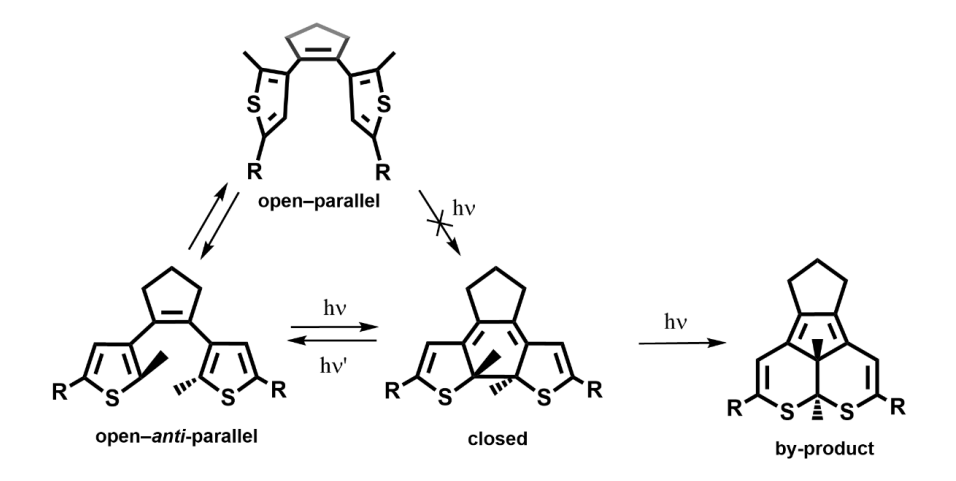
Diarylethenes (DAEs) belong to photochromic compounds characterized by the reversible change of both their geometric and electronic structures induced upon light irradiation.^{11,12} Hence, they are regarded as attractive and promising materials for many practical applications, such as molecular optoelectronic devices or ophthalmics.¹³ Specifically, dithienylethene (DTE) derivatives, a subclass of DAEs with heterocyclic thiophene rings in their photoswitching unit, have been widely investigated for applications in molecular devices.^{13,14} DTEs possess two isomers exhibiting quite different UV-vis absorption spectra. The transformation between these two isomers is induced by photoirradiation and is reversible. Exposure to ultraviolet (UV) light causes the transformation from the open-ring form (o-DTE) to the closed-ring isomer (c-DTE), whereas the visible light induces the reverse reaction (Scheme 5.1).



Scheme 5.1 Geometric structures of central photochromic units of DTE-derivatives in two isomeric forms: open-ring (o-DTE) and closed-ring (c-DTE) that can be reversibly interconverted with UV and visible light irradiation. The open-ring isomer is referred to as being in the OFF state as the π -conjugation is disconnected, whereas within the c-DTE molecule the π -conjugation is continuous (ON state).

DTEs are P-type photochromes exhibiting excellent thermal irreversibility and fatigue resistant photochromic performance. A particularly important aspect of DTE molecules is the varying topology of π -conjugation for open- and closed-ring isomers, allowing for modulation in the exchange interaction between two radical centres attached at each end. Thus, the aspect of switching of the π -connectivity further increases the attractiveness of the DTE compounds as functional materials.

The open-ring isomer of a dithienylethene photoligand (hereafter called **o-DTE**) exists in two conformers in solution, parallel and anti-parallel, in almost equal amounts, and they interconvert between each other at room temperature, $^{17, 18}$ as depicted in **Scheme 5.2**. In the parallel conformer, the two thiophene rings are in a mirror C_s symmetry, whereas in the anti-parallel one the five-membered heterocyclic rings are oriented in a C_2 symmetry. Only the antiparallel conformer is photoactive and undergoes a conrotatory photocyclization reaction to yield closed-ring isomer of a DTE photoligand, hereafter called **c-DTE**. ^{19, 20} Prolonged exposure of the closed-ring DTE isomer to UV irradiation can lead to the formation of annulated-ring by-product. ¹⁷



Scheme 5.2 Dithienylethene (DTE)-derivative isomers generated upon photoirradiation. The open-ring isomer exists in two conformers in solution: parallel and anti-parallel, out of which the latter is photoactive and can undergo cyclization reaction to closed-ring isomer. Prolonged UV illumination led to irreversible formation of the condensed ring by-product.

In this work, a symmetric dithienylethene derivative with phenylthiol groups bound at the 5,5'-positions of the thienyl ring, 1,2-bis[5-(4-mercaptophenyl)-2-methylthiophen-3-yl]cyclopent-1-ene, was employed as a linker molecule. Henceforth, the **DTE** acronym will be used to denote this ligand. The open-ring form of the DTE linker (\mathbf{o} - \mathbf{DTE}) is converted to a closed-ring form (\mathbf{c} - \mathbf{DTE}) upon irradiation with the ultraviolet (UV) light, whereas reversible reaction is induced by irradiation with visible light. This process, accompanied by a colour change from colourless to magenta, is directly related to the topological change in π -conjugation: disconnected in the \mathbf{o} - \mathbf{DTE} and continuous in the \mathbf{c} - \mathbf{DTE} (Scheme 5.3).

Scheme 5.3 Open- and closed-ring isomers of the DTE photoligand used in this study depicting the extent of the π -conjugation.

The photochromic reaction of the DEA molecules is an electrocyclic 1,3,5-hexatriene to cyclohexadiene type of reaction. In accordance with Woodward–Hoffmann rules the ring-closure occurs in a conrotatory fashion leading to the *trans*-disposition of the methyl groups.

This Chapter is organized as follows: first the synthesis of the dithiol DTE photoligand is described, followed by the full characterization of its photochromic properties (photoreaction quantum yields, fatigue). The second part describes the formation of $[Au_{25}(2PET)_{18}]^0$ assemblies linked with the photoswitchable ligand and the investigation into their size using a combination of small-angle X-ray scattering (SAXS) and matrix-assisted laser desorption/ionization (MALDI) mass spectrometry analysis.

5.2 Synthesis of dithiol photoligand

The dithiol photoligand (**o-DTE**, **7**) was synthesized in a multistep procedure, according to the protocol developed by the Feringa group, ^{21, 22} as outlined in **Scheme 5.4**.

A key intermediate, 1,5-diaryl-1,5-diketone (1), was prepared in a Friedel-Crafts acylation of 1,5-dicarboxylic dichloride with 2-chloro-5-methylthiophene which was subsequently transformed into closed-ring product 2 via McMurry reaction. The product 2 is a photochromic switch. Further functionalization of the compound 2 was conducted to produce a dithiol with extended aromatic system. First, 2 was converted into a boronic ester derivative by lithiating with n-BuLi in THF followed by reaction with B(OBu)₃ to yield bis(boronic ester), 3. The unpurified product was employed directly in the Suzuki reaction. The Suzuki cross-coupling of 3 with phenyl bromide containing protected thiol

functionality **4**, was conducted in THF with ethylene glycol as cosolvent, Na₂CO₃ as base and Pd(PPh₃)₄ as catalyst. This method led to formation of symmetrical **5** which was isolated after column chromatography in 86 % yield. The thiol deprotection was conducted in two steps, by first substituting the *t*-Bu groups by acetyl groups²³ to obtain compound **6**. The final product, **7**, was prepared according to the procedure reported by Stetsovych et al.²⁴

Scheme 5.4 Multistep synthesis of the symmetric o-DTE photoligand.

Importantly, the dithiol derivative was prepared in a separate synthetic step, rather than performing the deprotection in-situ reacting the molecule with gold samples (nanoparticles or surfaces), as has been shown in other reports.^{25, 26} Detailed synthetic procedure can be found in **Appendix A**.

5.3 The photoswitching reaction of dithienylethene (DTE) compounds

The photochromic behaviour of DTE compounds is briefly described here using the example of the target dithiol molecule: **o-DTE(SH)**.

One of the most pronounced phenomena observed in the DTE photochromes is a photoinduced colour change. When the σ -DTE solution is irradiated with the UV light, the colourless solution turns intensemagenta. This colour variation is attributed to a change in the electronic structure between open- and closed-ring isomers, more specifically the length of the π -conjugation. This is manifested in the significant difference in the absorption in the visible range of the spectrum of these two isomers, which facilitates the spectrophotometric monitoring of the light-induced cyclization and cycloreversion reaction.

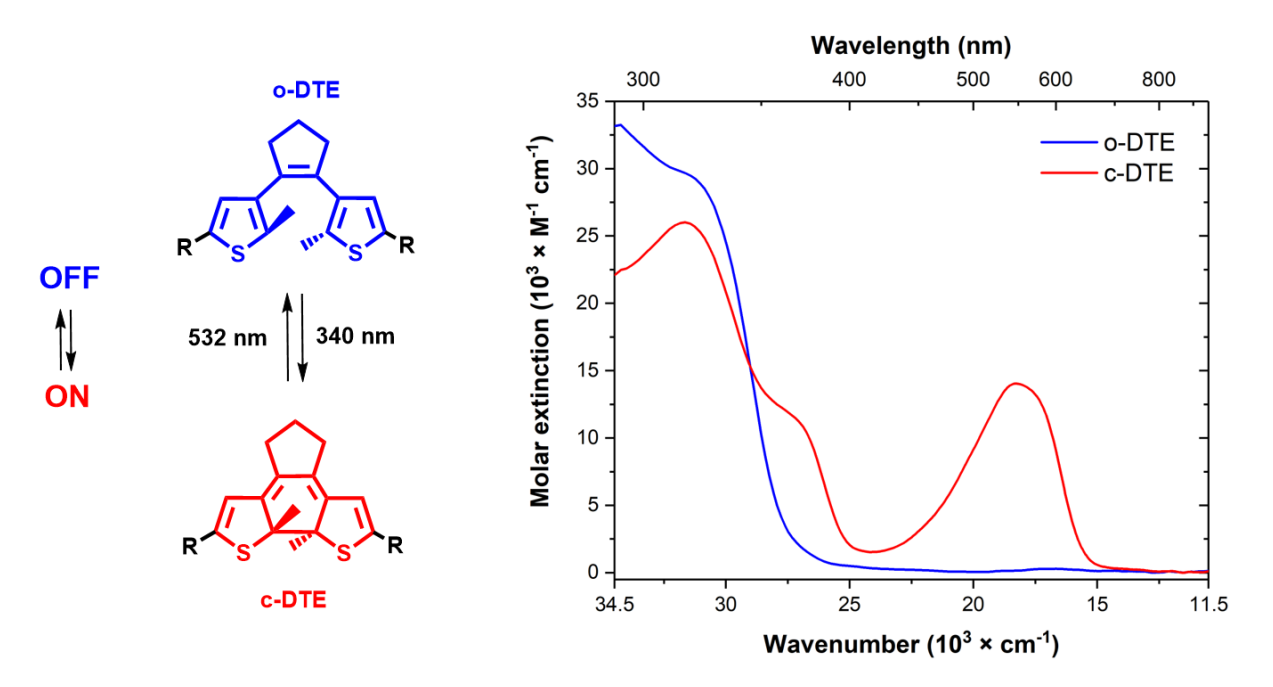


Figure 5.1 Electronic absorption spectra recorded for thiol-functionalized dithienylethene in toluene, blue line depicts the open-ring isomer (OFF state) and red trace corresponds to the closed-ring isomer in its photostationary state (ON state) after irradiation with 340 nm light.

Figure 5.1 depicts absorption spectral change of the **o-DTE(SH)** dithiol ligand in toluene induced by photoirradiation with 340 nm light. The open-ring isomer (blue trace) is colourless and exhibits only an intense absorption in the UV region with a band centred around 31,060 cm⁻¹ (321 nm). Upon irradiation with UV light a rapid spectral response is produced: a new band in the visible range appears around 18,000 cm⁻¹ (550 nm), which is very characteristic for the closed-ring isomer and is used as a diagnostic band to monitor the photoswitching reaction. Additionally, further changes could be observed in the UV range: a new broad shoulder ~28,000 cm⁻¹ (370 nm) and a more defined band at 31,440 cm⁻¹

(318 nm). The open-to-closed isomer conversion was almost quantitative (99 %) as will be discussed in **Section 5.4.1.2**.

5.4 Characterization of the photoswitching properties of DTE ligands

5.4.1 Reversible photoswitching of the DTE photoligands

5.4.1.1 Thiol-protected DTE photoligand DTE (SAc)

The analysis of the photoswitching performance was first carried out for the as-synthesized DTE ligand containing thioacetate (SAc) groups. In this case the thiol groups are protected, to avoid any side reactions. It needs to be said that free thiol/dithiol ligands have typically limited stability in solution and under aerobic conditions. These molecules are known to undergo an oxidation reaction leading to formation of disulfide molecules.²⁷ However, it is expected that upon binding of the photoligand to Au_{25} clusters the oxidative sensitivity will be reduced as the sulfhydryl (–SH) groups will engage into nanocluster linking.

Figure 5.2-a, c depicts the spectral response of the **DTE(SAc)** molecule in solution (toluene, 2.083×10^{-5} M) to UV and visible light irradiation. To start with, the open-ring isomer, **o-DTE(SAc)**, exhibited a strong absorbance in the UV region (> 31,000 cm⁻¹; < 320 nm). The irradiation with 340 nm light (0.049 mW) caused a new broad band centred at 18,114 cm⁻¹ (552 nm) to appear. This band is characteristic for the closed-ring isomer, **c-DTE(SAc)**, with the π-conjugation extending on the whole length of the molecule.

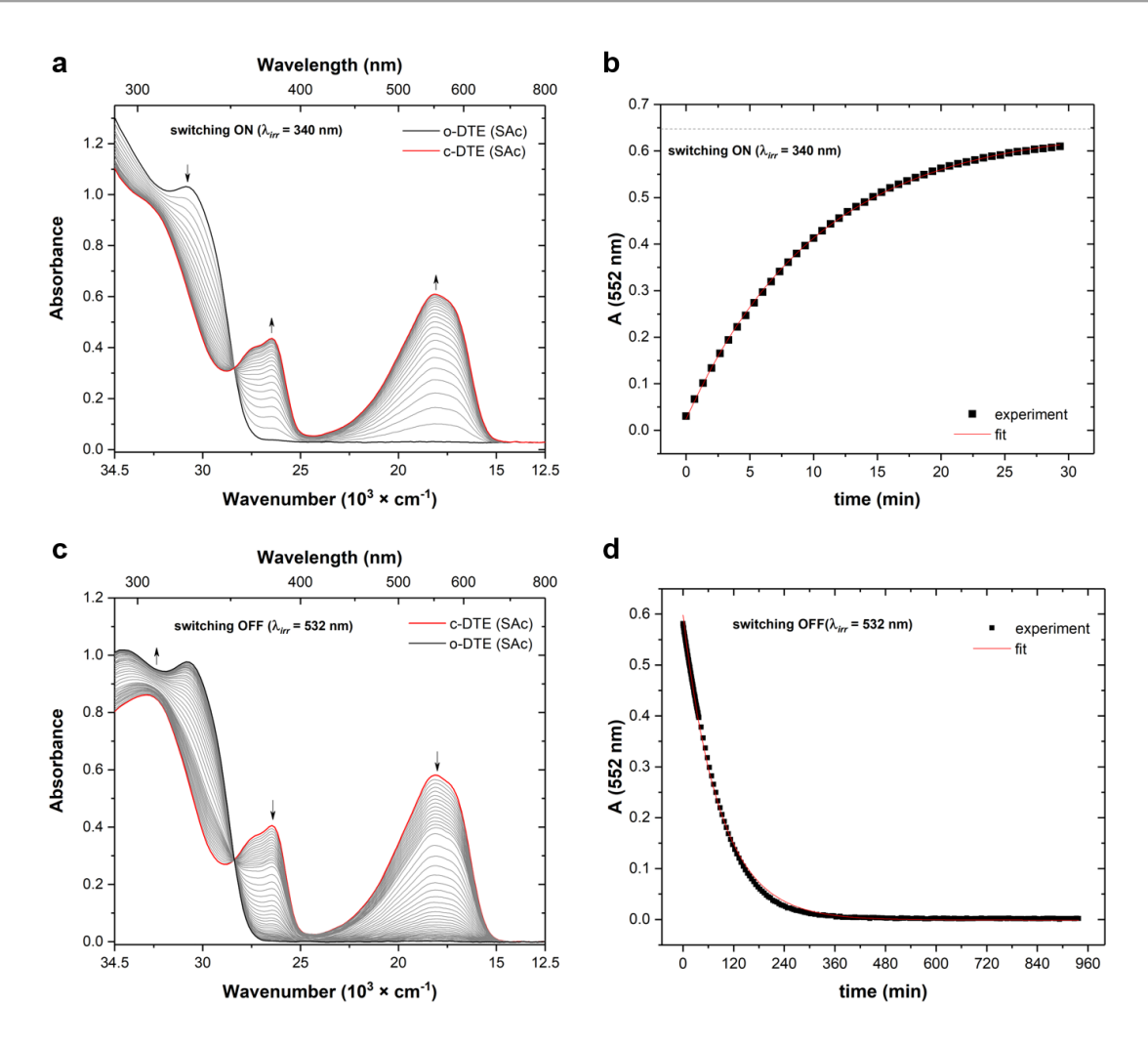


Figure 5.2 Absorption spectral change measured during (a) the ring closing process upon irradiation with 340 nm LED with an applied power of 49 μ W and (c) ring-opening reaction upon irradiation with 532 nm laser diode with an applied power of 796 μ W of 1.5 mL of a 2.1×10^{-5} M solution of o-DTE(SAc) in toluene in a 10 mm cuvette at ambient temperature. The temporal evolution of the absorption maximum at 552 nm for (b) switching ON and (d) switching OFF reactions. The experimental data is represented by black squares, and the fits are shown as red traces. The horizontal line depicts the maximum absorbance value for the open \rightarrow closed photocyclization reaction reaching 100 % conversion.

The temporal evolution of the 552 nm absorbance during UV irradiation, depicted in **Figure 5.2**-b, showed a 95 % conversion from the open- to the closed-ring isomer. The conversion has been calculated from fitting of the experimental data to the exponential decay function, as implemented in the Origin software. In this specific experiment, the photostationary state (PSS₃₄₀) was not reached, however other experiments (not shown here) confirmed that PSS can be easily achieved, especially when high photon flux is applied. Subsequent visible light irradiation (λ_{irr} = 532 nm, P = 0.796 mW) induced the completely reversible ring-opening reaction. **Figure 5.2**-d depicts the absorption at λ = 552 nm reaching a zero value after ~6 h. Complete disappearance of the 18,114 cm⁻¹ (552 nm) absorption band indicated that no by-product was formed. The time to reach a PSS for photocycloreversion reaction was much longer than for attaining a PSS after UV irradiation (~6 h and ~35 min, respectively).

5.4.1.2 Thiol-bearing DTE photoligand–DTE(SH)

Similar to the **DTE**(**SAc**) molecule, the absorption spectrum of the open-ring isomer of **o-DTE**(**SH**) in toluene $(2.45 \times 10^{-5} \text{ M})$, displayed a strong absorption at $\lambda > 350 \text{ nm}$ and no absorption in the visible part of the spectrum (black trace in **Figure 5.3-a**). Irradiation of the sample at 340 nm led to appearance of a broad absorption band centred at $18,315 \text{ cm}^{-1}$ (546 nm), weaker absorption around $27,027 \text{ cm}^{-1}$ (370 nm), and a strong band in the UV region, at $31,447 \text{ cm}^{-1}$ (318 nm) (red trace in **Figure 5.3-a**). These spectral changes are characteristic of the formation of the closed-ring isomer, **c-DTE**(**SH**). Temporal changes in absorption at 546 nm, depicted in **Figure 5.3-b**, showed that 99 % species reached a photostationary state (PSS₃₄₀) after less than 8 min of irradiation (1.24 mW). Irradiation with visible light (532 nm, 23.7 mW, 35 min) caused the reversal of the spectral changes. Analysis of the kinetics of the photoswitching (**Figure 5.3-d**) demonstrated that 99 % of the species attained a PSS₅₃₂ within 30 min of the light irradiation.

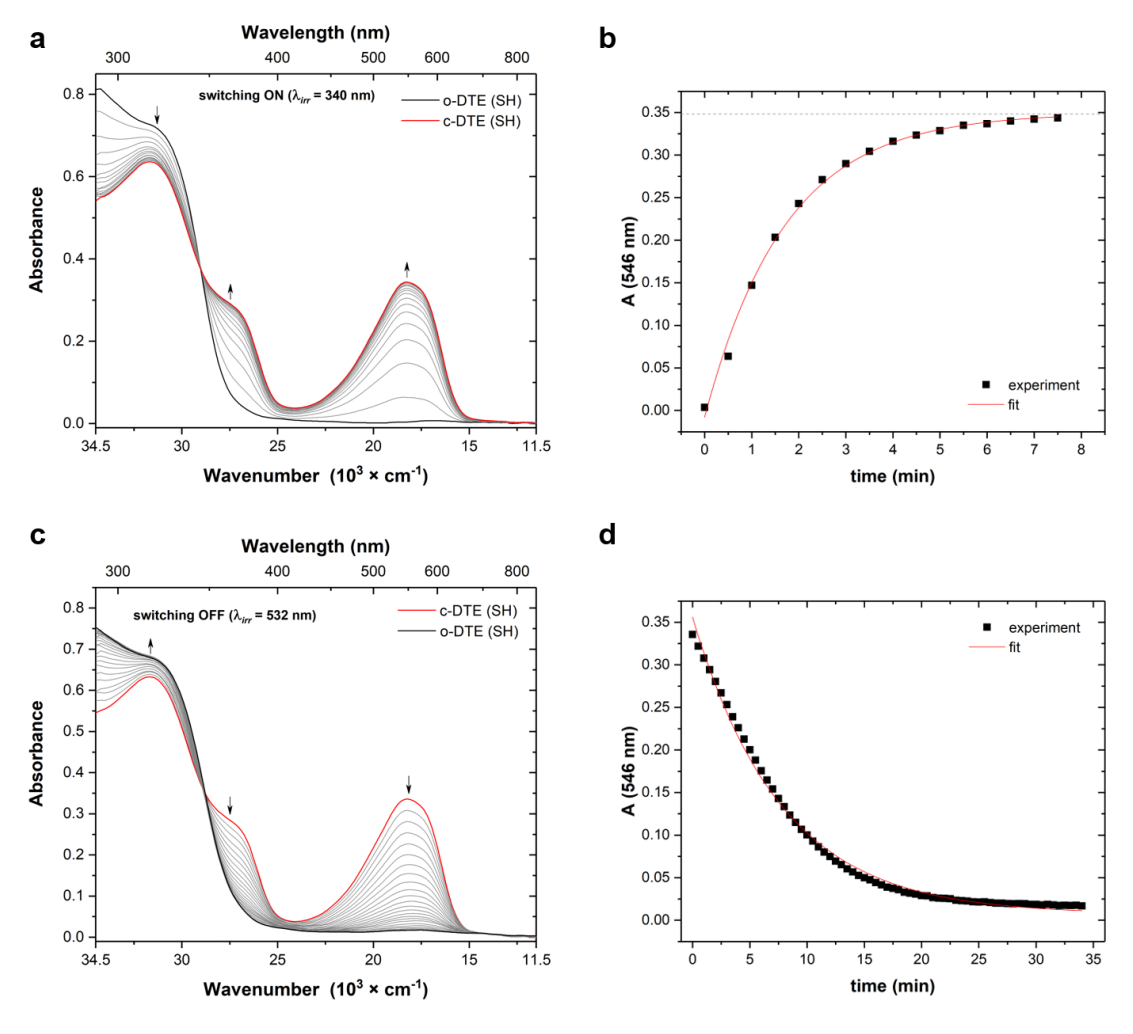


Figure 5.3 UV-vis spectra of DTE(SH) (1.5 mL in toluene, 2.4×10^{-5} M, 10×10 mm² cuvette) during irradiation with (a) 340 nm light, with an applied power of 1.24 mW, until reaching a PSS₃₄₀, (c) 532 nm light, with an applied power of 23.7 mW until reaching a PSS₅₃₂. Temporal changes in the diagnostic band (546 nm) absorbance recorded for (b) photocyclization and (d) photocycloreversion reactions (black squares). Data fitted to the exponential function (red traces).

5.4.2 Quantum yield of the photocyclization (Φ_C) and photocycloreversion (Φ_O) reaction of DTE ligands

The quantum yield (Φ) of a reaction describes how many molecules of a product are generated from one absorbed photon,²⁸ according to **Equation 5.1**

$$\Phi(\lambda) = \frac{N_{prod}}{N_{abs.\ photons}}$$
 5.1

where N_{prod} and $N_{abs.\ photons}$ correspond to the number of molecules converted and the number of absorbed photons, respectively. To precisely determine the Φ , the quantification of both N_{prod} and $N_{abs.\ photons}$ are necessary. In this work, the concentration of formed molecules of product was measured with UV-vis spectrophotometry. The number of photons that the system of interest absorbed was determined with the chemical actinometry method. Actinometry requires a standardized chemical reaction to effectively measure the amount of light that was absorbed under given experimental conditions, which could then be compared to the amount of light absorbed by the DTE molecular switches.

The quantum yields of photocyclization (\mathbf{o} -DTE \rightarrow \mathbf{c} -DTE) and photocycloreversion (\mathbf{c} -DTE \rightarrow \mathbf{o} -DTE) reactions for the \mathbf{o} -DTE(SAc) and \mathbf{o} -DTE(SH) ligands were determined in toluene by measuring the rate of the photoisomerization reaction in the initial stage of the reactions. The light intensity was measured with a photometer that was calibrated with o-nitrobenzaldehyde chemical actinometer (see Section A3, Appendix A). To determine the Φ of the \mathbf{o} -DTE \rightarrow \mathbf{c} -DTE reaction the procedure involving LED illumination and photometric measurement of the absorbed light amount, established by Megerle et al.²⁹ was followed.

The number of photons absorbed by the sample per second and wavelength interval is directly proportional to the radiant power and can be expressed by **Equation 5.2**:

$$N_{abs.\ photons}(\lambda)[s^{-1}] = \frac{P_0 f(\lambda)}{E_{photon}(\lambda)} A(\lambda)$$
 5.2

where P_0 is the incoming power, $f(\lambda)$ is the spectral distribution of the LED light source, $E_{photon}(\lambda)$ is expressed as $\lambda/(h \cdot c)$, h – Planck's constant, c – the speed of light, and the $A(\lambda)$ is the absorbance of the sample expressed as A = 1 - T.

The absorbance value is dependent on the cuvette thickness, d, the concentration of both open- (c_0) and closed-ring (c_C) DTE isomers, as well as their molar extinction coefficients, ε_0 and ε_C , according to **Equation 5.3**:

$$A(\lambda, t) = 1 - 10^{-d \cdot [c_0(t) \cdot \epsilon_0(\lambda) + c_C(t) \cdot \epsilon_C(\lambda)]}$$
5.3

The change in the number of the DTE isomers per irradiation time interval can be expressed by the differential equations presented in **Equations 5.4** and **5.5**:

$$\frac{dN_{0}(t)}{dt} = -\Phi_{0\to c} \int \frac{c_{0}(t) \cdot \varepsilon_{0}(\lambda)}{c_{0}(t) \cdot \varepsilon_{0}(\lambda) + c_{c}(t) \cdot \varepsilon_{c}(\lambda)} \cdot N_{photons}(\lambda) + \Phi_{c\to 0} \int \frac{c_{c}(t) \cdot \varepsilon_{c}(\lambda)}{c_{0}(t) \cdot \varepsilon_{0}(\lambda) + c_{c}(t) \cdot \varepsilon_{c}(\lambda)} \cdot N_{photons}(\lambda)$$

$$5.4$$

$$\frac{dN_{c}(t)}{dt} = -\boldsymbol{\Phi}_{c \to 0} \int \frac{c_{c}(t) \cdot \varepsilon_{c}(\lambda)}{c_{o}(t) \cdot \varepsilon_{o}(\lambda) + c_{c}(t) \cdot \varepsilon_{c}(\lambda)} \cdot N_{photons}(\lambda) + \boldsymbol{\Phi}_{o \to c} \int \frac{c_{o}(t) \cdot \varepsilon_{o}(\lambda)}{c_{o}(t) \cdot \varepsilon_{o}(\lambda) + c_{c}(t) \cdot \varepsilon_{c}(\lambda)} \cdot N_{photons}(\lambda)$$

$$5.5$$

In this work, the change in the concentration of the open and closed DTE isomers (instead of the change in the number of DTE molecules) per irradiation time interval was calculated for both **DTE(SAc)** and **DTE(SH)** photoligands, using the same procedure that was employed for *o*-nitrobenzaldehyde actinometer photoreaction analysis (see **Section A3** in **Appendix A**).

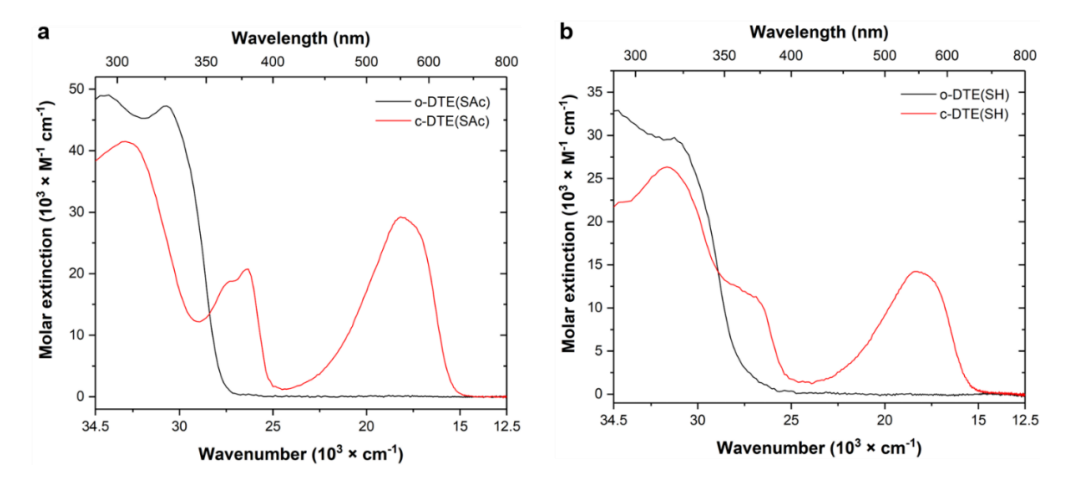


Figure 5.4 Molar absorptivities of both the reactants and the products of the photoswitching reaction of (a) DTE(SAc) and (b) DTE(SH) molecules recorded after irradiating the toluene solution with 340 nm LED.

For determination of the quantum yields of the molecular photoswitches the molar absorptivity spectra in toluene of the two DTE isomers (**Figure 5.4**) as well as the spectrum of the LED excitation light (**Figure 3.1**) was used. Of note, the full ranges of experimental data (**Figure 5.2**-a, c and **Figure 5.3**-a,c) from the start of the photoisomerization until the photostationary state were evaluated. The acquired spectra (at each time interval) were decomposed to extract the spectra of the open- and closed-ring isomers which were used to determine the concentration of both species at each time point (**Figure 5.5** and **Figure 5.6**).

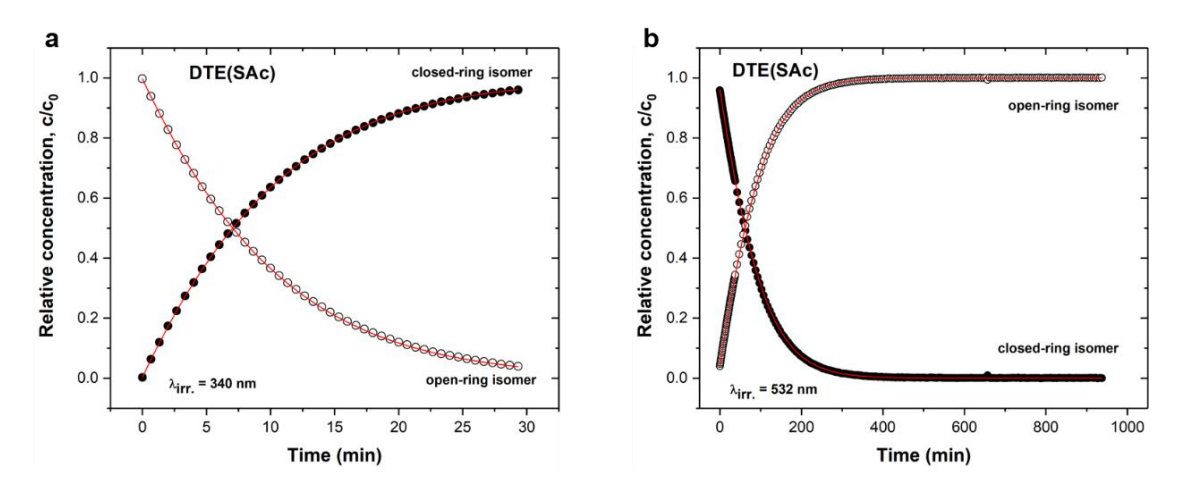


Figure 5.5 Temporal evolution of the concentrations of the open- and closed-ring DTE(SAc) isomers (open and closed symbols, respectively) during the (a) 340 nm and (b) 532 nm illumination. Corresponding fits depicted as red traces.

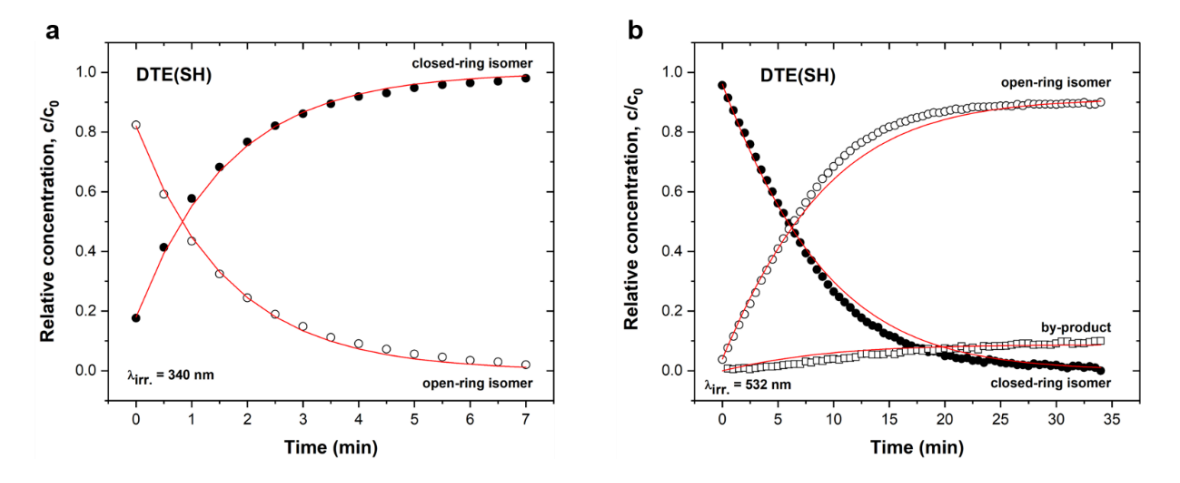


Figure 5.6 Temporal evolution of the concentrations of the open- and closed-ring **DTE(SH)** isomers (open and closed symbols, respectively) during the **(a)** 340 nm and **(b)** 532 nm illumination. Corresponding fits depicted as red traces.

The calculated values of the Φ for the photoreaction for the analysed DTE photoligands are presented in **Table 5.1**. The efficiency of the ring-opening process was found to be much lower for both photoswitches than the ring-closing reaction, in accordance with the observed DTE photoswitching behaviour reported in the literature.^{30, 31}

Table 5.1 Photocyclization and photocycloreversion quantum yields of the investigated DTE photoligands.

	$\lambda_{max}/\text{nm} \ (\epsilon/10^4 \text{M}^{-1} \text{cm}^{-1})$		PSS yield		$\Phi_{o \to c} (\lambda / nm)$	$\Phi_{c \to o}$ (λ /nm)
photoligand	open-ring	closed-ring	(340 nm) (532 nm)	(532 nm)		
	isomer	isomer		(332 1111)		
DTE(SAc)	326 (4.73)	552 (2.91)	0.99	0.99	0.53	1.85×10^{-3}
DTE(SH)	321 (2.96)	546 (1.42)	0.94*/0.99	0.99	0.21	1.00×10^{-3}

Additionally, for the **DTE(SH)** photoligand the formation of a by-product during the 532 nm irradiation experiment was observed (**Figure 5.6**-b). To the best of our knowledge, such a behaviour was not reported in the literature and requires further investigation which lies outside the scope of this thesis. The formation of a by-product during the visible light illumination could explain the observed photofatigue during the ON/OFF cycling experiment described in **Section 5.4.3.2**.

The obtained values of the extinction coefficients, ε , for the open-ring isomer of **DTE(SAc)** ligand in this work is in very good agreement with the value of $4.9 \times 10^4 \,\mathrm{M}^{-1} \,\mathrm{cm}^{-1}$ ($\lambda_{max} = 322 \,\mathrm{nm}$, acetonitrile) reported by Browne et al.³² However, they did not report the ε value for the closed-ring isomer, nor the quantum yield given the very low solubility of the **DTE(SAc)** in acetonitrile.

The ε values for both the open- and closed ring isomer of **DTE(SH)** and quantum yields for the ring-opening and ring-closing reaction have not yet been reported in the literature as usually this molecule is prepared in situ from the protected analogue. Therefore, this study reports for the first time the photochemical properties of the isolated **DTE(SH)** ligand in toluene.

5.4.3 Photofatigue of DTE ligands

As demonstrated in **Section 5.4.1**, the **DTE** photoligands could be reversibly switched between the ON and OFF states using UV and visible light, respectively. The changes in absorption were conveniently monitored with the UV-vis spectrophotometry in a non-destructive fashion.

The prolonged photoswitching between the open- and closed-ring isomers of the DTE molecule monitored at the probe wavelength can provide insight into the stability of the photochromic switch under repeated irradiation cycles. One irradiation cycle comprises of two switching events: switching ON via 340 nm illumination leading to formation of a closed-ring DTE isomer with characteristic absorption around 550 nm. The subsequent switching OFF reaction is ensured by 532 nm illumination during which the cycloreversion process takes place, manifested by the gradual disappearance of the 550 nm band. Consequently, recording the changes in the 550 nm-absorbance during each irradiation event allowed monitoring the photoswitching process over time. A fatigue resistance is an important property of photochromic compounds and can be described as an ability of the photoswitching molecule/system to maintain its photoswitching property during the ON/OFF irradiation cycles.

5.4.3.1 Thiol-protected DTE photoligand DTE (SAc)

Repeated photoswitching (ON/OFF) was first investigated for the **DTE(SAc)** molecule. Irradiation times necessary to reach a near photostationary states under constant illumination with either UV (340 nm) or visible (532 nm) light were determined prior to irradiation cycling experiments. The experimental setup

involved the combination of LED and laser as light sources and shutters to control the light irradiation. A 1.0 mL of **DTE(SAc)** solution (toluene, 2.25×10^{-5} M) in a closed quartz cuvette (10×10 mm²) was irradiated alternatively with UV (340 nm, 90 s) and visible light (532 nm, 480 s) under constant stirring to ensure a homogeneity of the irradiated sample.

The **DTE(SAc)** ligand was exposed to 120 ON/OFF switching cycles (total irradiation time of 20 h), and the photoswitching behaviour was monitored by recording a change in absorbance at the probing wavelength of 552 nm, which corresponded to the maximum absorbance of the characteristic band of the closed-ring isomer. **Figure 5.7** depicts the results of this experiment.

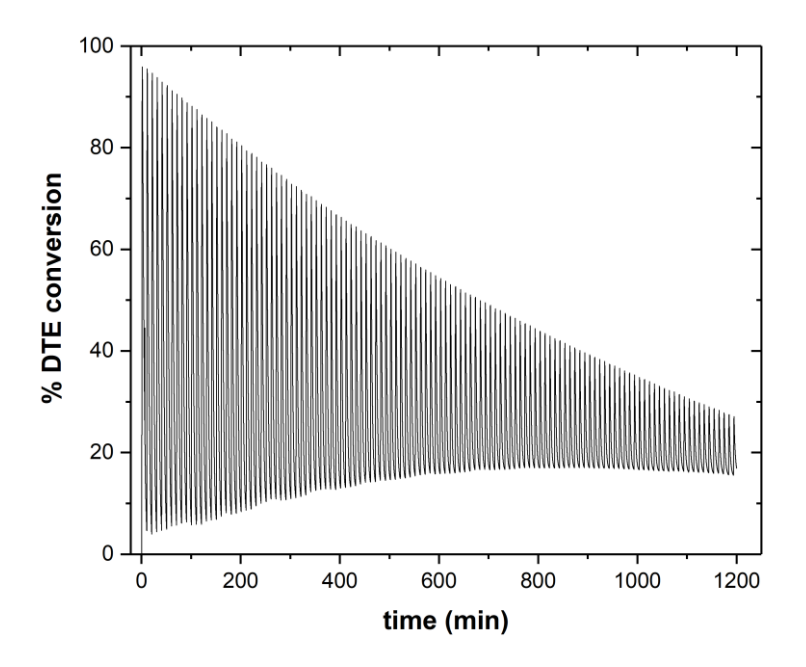


Figure 5.7 Evolution of absorbance at 552 nm of the **DTE(SAc)** photoligand during repetitive switching cycles comprising alternating UV (340 nm, 90 s) and visible (532 nm, 480 s) irradiation.

Overall, the photoswitching performance decreased with prolonged irradiation cycles. However, during the first 10 irradiation cycles the photofatigue is quite small (from 96 to 92 %) which contrasts with results found for a similar molecule, in which the two sulfhydryl groups were protected with a methyl functionality. For this molecule, a 50 % decrease in absorbance maximum was observed after 7 ON/OFF cycles. The authors argued that this significant photofatigue was due to by-product formation during the UV irradiation (having a condensed ring in its structure, **Scheme 5.2**). This reaction was inhibited for the perfluorocyclopentene-derivative. However, it needs to be said that the UV irradiation was conducted at 365 nm corresponding to a wavelength where one of the bands of the closed-ring isomer appeared. Therefore, the closed-ring isomer has been selectively irradiated facilitating the formation of by-product. Based on our observation however, it is argued that the perhydrocyclopentene derivatives could exhibit improved photorecyclability performance with a careful choice of the UV irradiation wavelength and control over the irradiation power.

5.4.3.2 Thiol-bearing DTE photoligand DTE(SH)

The investigation of the effects of the repeated ON/OFF switching on the fatigue performance was also carried out for the **DTE(SH)** sample in toluene solution (toluene, 2.45×10^{-5} M). As depicted in **Figure 5.8**, the photochemical switching fatigue is apparent already after the second UV irradiation, manifested in the decrease of the maximum absorbance at 546 nm from 99 to 73 %. Additionally, after the first 532 nm irradiation cycle the 546 nm band did not disappear entirely and the residual absorption increased in the following irradiation cycles.

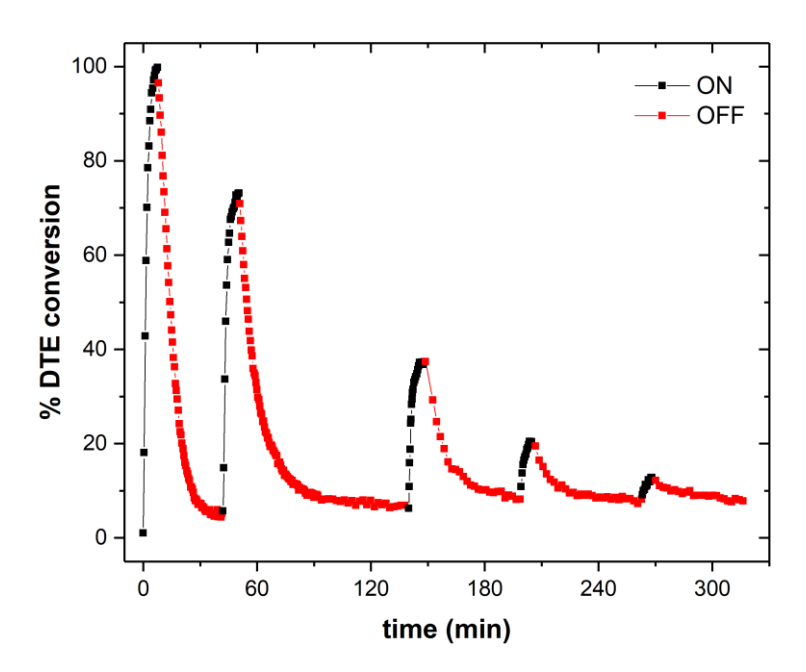


Figure 5.8 Photofatigue of the DTE(SH) ligand measured during the ON/OFF switching cycles in solution (toluene, $2.45 \times 10^{-5} \, \text{M}$) monitored at the 546 nm.

The degree of switching between the open- and closed-**DTE**(**SH**) isomer was found to decrease drastically with each irradiation cycle. After four cycles, only ~17 % of the initial value of maximum absorbance for the ON product could be reached. The slow increase in the base value for the absorbance of the isomer in the OFF state (from 0 to 9 %) indicated that the photoligand was degrading. It appeared that the 532 nm irradiations were causing the photoligand to undergo a structural transformation, similarly to the **DTE**(**SAc**) ligand, however in this case this process was much faster. This finding needs to be investigated further and requires coupling other techniques, like NMR spectroscopy, that would help to identify the structural changes induced by the photoirradiation. However, it can already be stated that this result is remarkable, since while multiple reports exist on the damage to the DTE photochromic molecules induced by the extensive UV irradiation (i.e., irreversible transformation to the annulated isomer as a by-product, **Scheme 5.2**), the influence of visible light induced damaged has not yet been reported to the best of our knowledge.

The conducted ON/OFF switching irradiations for both DTE(SAc) and DTE(SH) ligands have shown an enhanced photocycling stability of the DTE(SAc) ligand with respect to its free thiol-counterpart, **DTE(SH)**. The **DTE(SAc)** ligand lost ~69 % of its photochromic property after 120 ON/OFF cycles, whereas for the **DTE(SH)** the loss of 83.5 % of its photoswitching performance occurred already after 5 cycles. This photofatigue could be partially explained by the irreversible conversion of the closed-ring DTE isomer into its by-product isomer when irradiating with the UV light (Scheme 5.2), as argued by Irie et al.³³ It seems however that the functional group substituted on the phenyl ring attached to the thienyl ring could also be a contributing factor to the photoswitching performance. Irie et al. have demonstrated the effect of various substituents at para-positions of the phenyl groups of DTE molecules on their photochemical reactivity.³⁰ Furthermore, a perhydrocyclopentene unit on the DTE is known to be less fatigue resistant than a perfluorocyclopentene counterparts.³⁴ Recent studies have shown however, that fatigue resistance of photochromic 1,2-diarylethenes is strongly dependent on the illumination process, more specifically on the UV source (wavelength and light dose) and on the absorption characteristics of the molecule at the irradiation wavelength.³⁵ For the two photoligand systems presented herein, additional NMR investigations are necessary to gain insight into possible byproduct formed during a photoswitching reaction. Moreover, a more systematic study that involves the photoswitching using various wavelengths of light (both UV and visible), including the dependence of the specific light dose on the photoswitching performance is of interest to gain more insight into the intrinsic differences between the DTE(SH) and DTE(SAc) molecules.

5.5 Synthesis of photoswitchable Au₂₅ assemblies

Assemblies of Au NCs linked by the **DTE**(**SH**) ligand were produced via the ligand-exchange method in solution by mixing discrete $[Au_{25}(SC_2H_4Ph)_{18}]^0$ clusters (hereafter denoted as $[Au_{25}(2PET)_{18}]^0$ for simplicity) dissolved in toluene solution (2.5 mg/mL) with the freshly synthesized photoligand in a 2:1 Au₂₅-to-**DTE** molar ratio. The reaction mixture was left to stir under nitrogen at ambient temperature in the dark for 24 h. Then, the crude product was washed with MeOH to remove free thiols. The product mix was fractionated on a size-exclusion chromatography (SEC) column (BioBeads S-X1) in toluene. Typically, 3 main separation bands were observed on the column (see **Appendix A**), and were isolated as main fractions denoted, **F1**, **F3**, and **F5**. All fractions were analysed with standard characterization techniques: UV-vis-NIR spectroscopy and MALDI-MS analysis and compared against the pure $[Au_{25}(2PET)_{18}]^0$ clusters.

5.6 Characterization of the formed Au_{25} assemblies linked with a DTE photoligand

5.6.1 Steady-state UV-vis-NIR spectroscopy in solution

The observation of three main bands on the SEC column suggests that three distinct sizes of species were formed (**Figure A.4**-b). It should be noted that the synthesis was repeated many times, and each time a similar separation was obtained. To characterize the isolated species, the electronic absorption spectra for each eluted fraction (denoted as **Fn**, n = 1-6, based on their elution sequence from the column) were recorded and compared to the spectrum of unreacted monomeric $[Au_{25}(2PET)_{18}]^0$ clusters to offer a first insight into the structure of the formed Au_{25} assemblies.

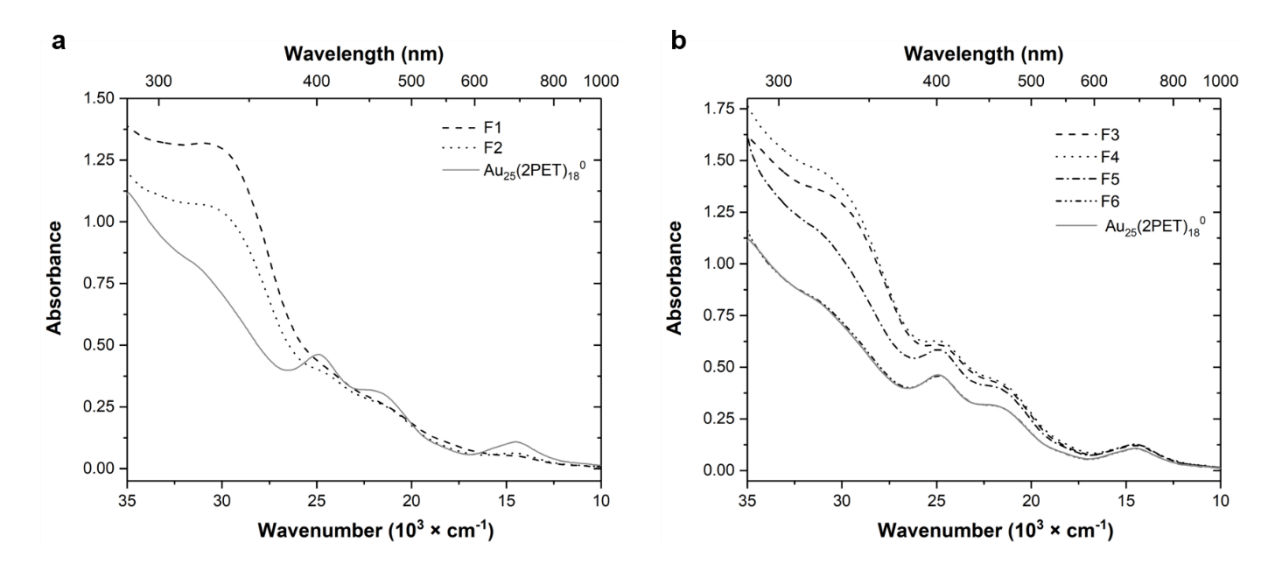


Figure 5.9 Electronic absorption spectra of fractions isolated on SEC column (a) fractions containing larger Au_{25} assemblies; (b) smaller Au_{25} assemblies with their spectra preserving the spectral features of $[Au_{25}(SR)_{18}]^0$ clusters (solid grey line). Spectra recorded in toluene at ambient temperature.

Typical spectral traces of the isolated SEC fractions are depicted in **Figure 5.9**. The largest (in size) fractions, (**F1** and **F2** in **Figure 5.9**-a), displayed spectra with a monotonic absorbance increase in the visible range, and intense broad absorption in the UV region (> 25,000 cm⁻¹; < 400 nm). Based on the SEC elution sequence, it is reasonable to presume that **F1** and **F2** are comprised of larger Au₂₅ multimers. Consequently, the contribution to the absorption originating from the **o-DTE** linker was expected to be stronger, given their higher fraction in the multimeric structure. It is known that larger species exhibit larger absorption cross-section which enhances Rayleigh scattering. Since scattered light has a λ^{-4} dependence, it is expected that larger multimers would distort the UV regime the most. Importantly, the optical spectra of larger species show no characteristic bands of [Au₂₅(2PET)₁₈]⁰. This finding is in

agreement with other study that has shown that multimeric Au_{25} assemblies lost the absorption band of the parent nanocluster.⁵

In contrast, the spectra of smaller size fractions, presented in **Figure 5.9**-b, displayed the characteristic absorption bands observed in the spectra of discrete $[Au_{25}(SR)_{18}]^0$ species, that is the peak at ~14,750 cm⁻¹ (678 nm) corresponding to the highest occupied molecular orbital–lowest unoccupied molecular orbital (HOMO–LUMO) transition, peak at ~22,727 cm⁻¹ (440 nm) ascribed to HOMO–sp transition and at ~25,000 cm⁻¹ (400 nm) to d–sp transition.^{36,37} Therefore, the as-formed small assemblies, in their non-irradiated state, exhibited the electronic structure that greatly resembled that of single $[Au_{25}(2PET)_{18}]^0$ nanocluster building unit.

5.6.2 Identification of the separated fractions with MALDI-TOF mass spectrometry

The spectra of all isolated fractions were acquired under the same conditions in the 10-20,000 Da range (see **Section 3.2.2**) and compared with the spectrum of the parent cluster, $[Au_{25}(2PET)_{18}]^0$.

As depicted in **Figure 5.10**, the mass signals of the parent $[Au_{25}(2PET)_{18}]^0$ cluster were observed across all fractions (grey dashed lines in Figure 5.10-a). It needs to be said that even when applying the mildest parameters for ionizing, the pure Au₂₅ cluster fragmented quite extensively. Next to the typical fragmentation peaks corresponding to the loss of Au_nL_n (where n = 1, 2, 3, 4) unit³⁸ more peaks were observed in the lower mass range (i.e., m/z = 5722.51 Da attributed to the loss of Au₅L₅, or m/z = 5847.66 Da, not assigned). Moreover, the appearance of signals in the higher mass region, above the monoisotopic mass of Au₂₅(2PET)₁₈ of m/z = 7391 Da, was apparent. Given that the analysed cluster sample was purified on the SEC column before MALDI-MS analysis, the higher mass fragments are most likely produced during the MA laser desorption-ionization process. The occurrence of these peaks could be related to the applied laser pulse intensity and the dilution of the analyte within the matrix solution. Furthermore, additional peaks at $m/z \sim 7591$, 7791 and 7991 Da were detected (blue and red dashed lines in Figure 5.10-a). These signals were assigned to the Au₂₅ clusters having a mixed monolayer ligand shell containing next to the monodentate 2PET ligands, up to three bidentate o-DTE ligands (henceforth denoted as o-DTE²). The assignment of the MALDI mass peaks to the corresponding species is presented in **Table 5.2**. The inspection of the spectra of the isolated fractions in the mass range between 8–12 kDa allowed identification of several new peaks at $m/z \sim 10,527; 10,559; 10,662; 10,862;$ 10,997; 11,197 Da, not present in the spectrum of pure $[Au_{25}(2PET)_{18}]^0$ cluster.

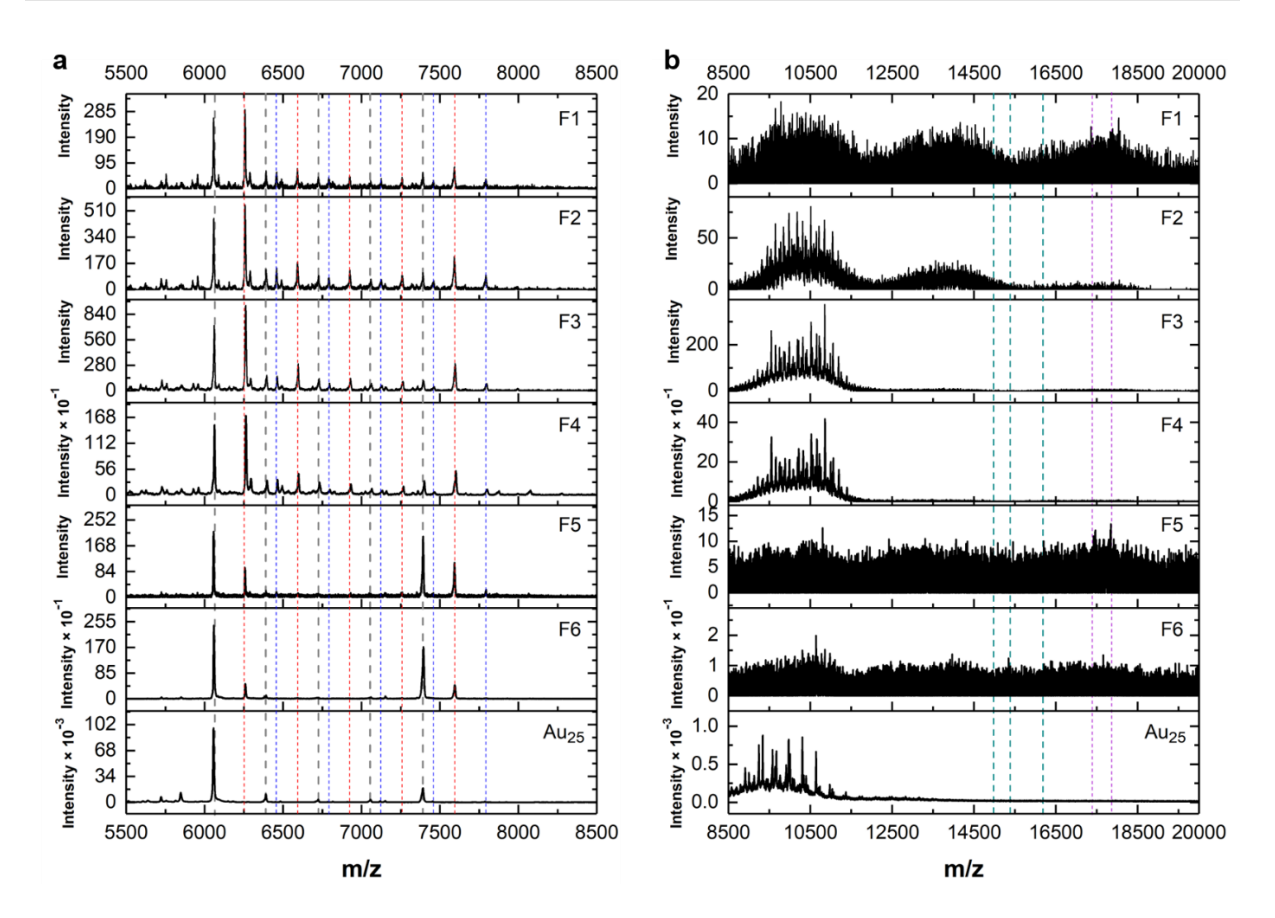


Figure 5.10 Typical MALDI-TOF-MS spectra of the fractions isolated from the SEC column after the ligand-exchange reaction of $[Au_{25}(2PET)_{18}]^0$ with the **o-DTE** dithiol linker. (a) The low mass region depicts the peaks originating from pure $[Au_{25}(2PET)_{18}]^0$ cluster (denoted Au_{25} ; grey dashed lines); the Au_{25} clusters with one and two exchanged **o-DTE** ligands within the Au_{25} monolayer are represented by red and blue lines, respectively. (b) The high mass region does not show clear peaks belonging to monocharged dimeric species (D^+) or doubly charged trimers. The green lines show the region where the symmetric and non-symmetric D^+ peaks should be observed. The peaks marked with magenta lines could be ascribed to higher multimeric fragments (see description in the text). All spectra were acquired in linear positive mode at 15 % laser fluence.

While the assignment of these peaks is not trivial, the mass separation between them, $\Delta m \sim 200$ or 334 Da, corresponds to **o-DTE**²-2 × 2PET or Au-2PET difference, respectively, indicating these may correspond to the fragments from the larger species having both 2PET and **o-DTE** ligands in their structure.

Needless to say, the peaks corresponding to dimeric species, like the simplest symmetrical $Au_{25}(PET)_{17}$ —**o-DTE**– $Au_{25}(PET)_{17}$ dimer (**1-1** dimer, notation describing each Au_{25} cluster with one bidentate **o-DTE**² ligand in the monolayer), in a singly (m/z = 14,982 Da) or doubly charged state (m/z = 7,491 Da) were not found. Here, the notion of symmetrical and non-symmetrical dimers is used, which is related to the ligand shell of the Au_{25} units that build the dimer. When both Au_{25} units have the same number of exchanged **o-DTE**² ligands in the monolayer, they are being referred to as symmetrical dimers. Of note, $Au_{25}(2PET)_{17}$ –oDTE– $Au_{25}(2PET)_{17}$ dimer can also be regarded as symmetrical.

Table 5.2 Calculated and experimentally acquired MALDI m/z (for z=1) values of the intact $Au_{25}(2PET)_{18}$ clusters and mixed ligand shell $Au_{25}(2PET)_{18-x}(\textbf{o-DTE}^2)_x$ (x=1, 2, 3) clusters and their most characteristic fragments corresponding to the loss of $Au_n(2PET)_n$ units.

m/z (experiment)	m/z (calculated)	Assigned species
	Intact spo	ecies
7391.4198	7390.9394	$Au_{25}(PET)_{18}$
7591.7616	7590.9149	$Au_{25}(PET)_{16}(\mathbf{o-DTE}^2)$
7792.6085	7790.8904	$Au_{25}(PET)_{14}(\mathbf{o-DTE}^2)_2$
7991.0429	7990.8659	$Au_{25}(PET)_{12}(\mathbf{o-DTE}^2)_3$
	Mass fragments of	Au ₂₅ (2PET) ₁₈
7056.1604	7056.9298	$Au_{25}(PET)_{18} - Au(2PET)$
6723.4348	6722.9202	$Au_{25}(PET)_{18} - Au_2(2PET)_2$
6388.6428	6388.9106	$Au_{25}(PET)_{18} - Au_3(2PET)_3$
6053.5273	6054.9009	$Au_{25}(PET)_{18} - Au_4(2PET)_4$
	Mass fragments of Au ₂₅ ($(2PET)_{18-x}(0-DTE^2)_x$
7257.8623	7256.9053	$Au_{25}(PET)_{16}(\textbf{o-DTE}^2) - Au(2PET)$
6923.3344	6922.8957	$Au_{25}(PET)_{16}(\textbf{o-DTE}^2) - Au_2(2PET)_2$
6589.2150	6588.8861	$Au_{25}(PET)_{16}(\textbf{o-DTE}^2) - Au_3(2PET)_3$
6255.2625	6254.8764	$Au_{25}(PET)_{16}(\textbf{o-DTE}^2) - Au_4(2PET)_4$
7455.5542	7456.8808	$Au_{25}(PET)_{14}(\mathbf{o-DTE}^2)_2 - Au(2PET)$
7123.2426	7122.8712	$Au_{25}(PET)_{14}(\mathbf{o-DTE}^2)_2 - Au_2(2PET)_2$
6789.5424	6788.8616	$Au_{25}(PET)_{14}(\mathbf{o-DTE}^2)_2 - Au_3(2PET)_3$
6455.1283	6454.8519	$Au_{25}(PET)_{14}(\mathbf{0-DTE}^2)_2 - Au_4(2PET)_4$

The green dashed lines in **Figure 5.10**-b indicate where the monoisotopic masses of the symmetrical and non-symmetrical (in terms of their ligand shell) dimers should appear (see **Table A.8** listing some examples of dimers). Similarly, no peaks corresponding to trimers in any charged state were found in the spectrum. The magenta colour lines in **Figure 5.10**-b could potentially be ascribed to the fragments of higher species since their mass is higher than that of the symmetrical (3-3) dimers and their separation ($\Delta m = 474 \,\mathrm{Da}$) corresponds to the mass of the **o-DTE** ligand. All things considered, the lack of dominant peaks belonging to dimers or trimers in the higher mass range of the spectrum cannot definitively exclude the presence these species in the analysed sample.

Hitherto, MALDI-MS technique has been unsuccessful in detecting the intact dimers and higher order species of Au NCs connected with a linker molecule. Instead, the mass peaks of the monomeric units were detected.^{4,39} The report by Sels et al. showed no clear mass peaks belonging to intact Au₂₅-based oligomeric species, rather the presence of multiple peaks in the spectrum was ascribed to the extensive fragmentation of the oligomeric species.⁴ Since MALDI-MS analysis requires uniform cocrystallization of the analyte with a large excess of matrix, it is probable that for the multimeric Au₂₅ assemblies the

quality of cocrystallization with the DCTB matrix was lower than for pure Au₂₅ clusters, which affected the ionization and detection of the species. Also, multimeric species may be prone to decomposition when undergoing the ionization process. Nonetheless, MALDI-MS is a technique that can provide the insight into the ligand composition of the formed assemblies, i.e., the extent of the ligand exchange and possibly number of potential linkers available per one cluster. However, it needs to be stressed that this information does not complete the picture of the types of assemblies formed and a complementary analysis into the size and nature of the species is required.

The attempts were made to analyse the formed products with mass spectrometry coupled with softer ionization method, electrospray ionization ESI-MS, but they were proven unsuccessful. Nevertheless, further optimization of the analysis parameters is expected to give the evidence of multimeric species as it was depicted for Au_{25} and Ag_{25} fullerene adducts.⁴⁰

5.6.3 Small angle X-ray scattering (SAXS) analysis of the formed Au₂₅ assemblies

Given the challenges in identifying the size of the formed species using mass spectrometry (MALDI and ESI-MS), complementary information was provided by the SAXS analysis in solution (here, toluene). This powerful technique allows deriving the size and shape parameters of the scattering species and hence offers the global structural information about the assemblies in solution. This technique was shown previously to be effective in describing Au₂₅(SR)₁₈ multimers linked with organic dithiol linkers.⁴ The SAXS technique is based on the scattering length electronic density, therefore in the case of the Au₂₅ assemblies, the scattering signal originates from the gold atoms (both kernel and staples) owing to their high scattering power.

5.6.3.1 Analysis of the SAX scattering profiles

The SAXS analysis was performed for the three representative fractions isolated on the SEC column, that is **F2**, **F3**, and **F5** (see **Figure A.4**-b). Their scattering intensities (normalized by concentration), presented in **Figure 5.11** as a function of the scattering vector Q, were contrasted against that of unreacted $[Au_{25}(2PET)_{18}]^0$ (black diamonds).

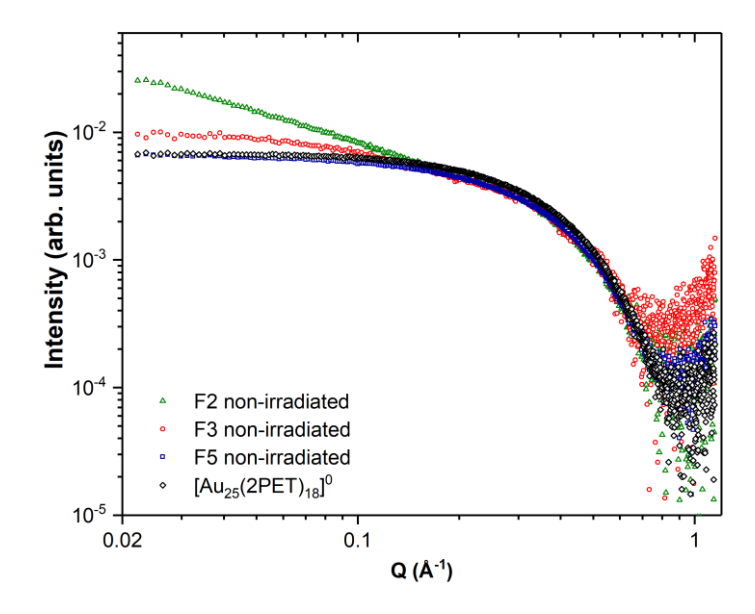


Figure 5.11 Log-log plot of scattering intensity, I, as a function of the scattering vector, Q, for three isolated fractions: F2 (green), F3 (red) and F5 (blue symbols) after the Au_{25} assembly formation contrasted with the scattering profile of pure $[Au_{25}(PET)]_{18}]^0$ clusters (black diamonds).

The scattering curves of $[Au_{25}(2PET)_{18}]^0$, **F3** and **F5** exhibited a clear plateau at low Q values (so-called Guinier plateau). The scattering profile of **F2** fraction however differed markedly from the other three samples as the significant increase in intensity at small angle was apparent. Even though the scattering signal rose rather steeply at low Q, the onset of plateauing within the Q-range of measurement could just be detected. The levelling-off of the scattering curve indicated a finite size of the scattering species. It could therefore be concluded that the isolated Au_{25} assemblies were not agglomerated but discrete in size. Additionally, the Guinier plateau cut-off appeared at a lower Q value for both **F2** and **F3** fractions, whereas the scattering profile of fraction **F5** almost coincided with that of unreacted $[Au_{25}(2PET)_{18}]^0$ nanoclusters. The nature of the scattering profiles of the analysed samples showed that **F2** and **F3** contained larger species than monomeric Au_{25} and species in fraction **F5** had a size similar to the pure $[Au_{25}(2PET)_{18}]^0$ cluster.

Since the scattering intensity, I, at a very low Q is proportional to the volume of the scatterer, relating the scattering intensity of each fraction to that of pure $[Au_{25}(2PET)_{18}]^0$ cluster could provide insight into the size of the assemblies that each fraction contained.

Qualitative analysis was attempted by comparing the scattering intensities of the measured fractions with that of unreacted Au₂₅ nanoclusters at $I(Q)_{Q\to 0}$, according to **Equation 5.6**:

$$N = \frac{I(Q)_{n-mer}}{I(Q)_{Au25}} \quad at \ Q \to 0$$
 5.6

The resulting approximate relative volumes of the **F2**, **F3**, and **F5** fractions were 3.50, 1.34, and 0.99, respectively (**Table 5.3**)

Table 5.3 Relative scattering volumes of SEC isolated **o-DTE** linked Au₂₅ assemblies obtained from the analysis of the SAXS intensity profiles.

	Au ₂₅ (2PET) ₁₈	F2	F3	F5
$I(Q)_{Q o 0}$	0.0072	0.0253	0.0095	0.0071
N	1	3.50	1.32	0.99

The obtained values implied that the species in **F2** were, on average, 3–4 times larger in volume than $[Au_{25}(2PET)_{18}]^0$ monomers. Similarly, the smaller **F3** fraction contained species with volume almost 1.32 larger than pure $[Au_{25}(2PET)_{18}]^0$ clusters, whereas the **F5** fraction species matched the $[Au_{25}(2PET)_{18}]^0$ volume almost perfectly. Moreover, the scattering curves showed a lack of well-defined peaks or shoulders at higher Q values (> 0.3 Å⁻¹) suggesting high polydispersity in the population of scattering species. Additionally, a monotonic increase in the scattering intensity with the onset at $Q \sim 0.2$ Å that was observed for the larger Au_{25} assemblies (i.e., **F2** and **F3**), was caused by the larger species present in the fractions, as the size of the largest object within the mixture dominates the scattering at the lowest Q region, even if these species are not the prevalent ones. The levelling-off of the scattering curve however indicates the size of these larger species was finite.

5.6.3.2 Fitting of the experimental SAX scattering data

To obtain the information about the size and shape of the formed assemblies, all the experimental scattering curves were fitted to the models embedded in the SasView 4.2.2 software.⁴¹

Fitting of the scattering profiles of pure $[Au_{25}(2PET)_{18}]^0$ clusters (black diamond symbols in **Figure 5.12**) was performed with a spherical model (hard sphere), since the shape of the Au_{25} nanocluster can be approximated by the sphere, as corroborated by X-ray analysis.⁴²

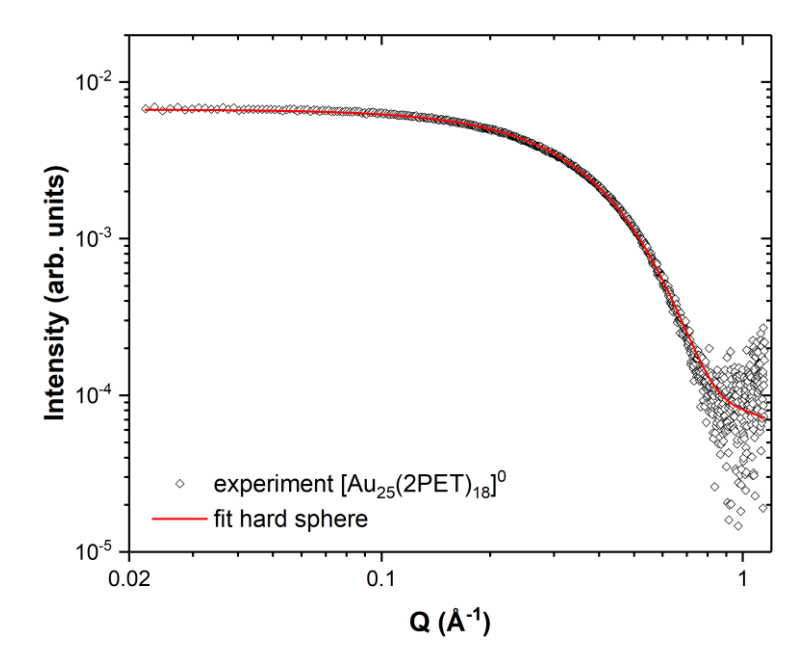


Figure 5.12 SAXS profile of pure [Au₂₅(2PET)₁₈]⁰ clusters measured in toluene (diamond symbols) fitted to the hard-sphere model (red curve).

The fitted curve (red trace in **Figure 5.12**) perfectly matched the experimental data. The value of the $[Au_{25}(2PET)_{18}]^0$ cluster radius, R = 4.56 Å, that was obtained from the fitting was in excellent agreement with the 4.6 Å value devised from SAXS measurements for $Au_{25}(SBu)_{18}$ reported by Sels et al.⁴ Moreover, the value of the radius obtained from SAXS analysis was in good agreement with the Au–Au distances between the most peripheral gold atoms in the $[Au_{25}(2PET)_{18}]^0$ cluster structure of 4.90 ± 0.02 Å obtained from X-ray crystallographic analysis as reported by Tofanelli et al.¹⁰

The cylindrical pearl-necklace structural model was chosen to quantitatively explain the acquired SAXS pattern in isolated **F2**, **F3**, and **F5** fractions. This model treats Au₂₅ clusters as hard spheres ('pearls') that are linearly connected by strings, in no preferential orientation, and was shown to be successful to describe the multimers of Au₂₅ connected with covalent linkers.⁴ For each of the analysed fractions a different number of 'pearls' was used in the fits. The fits produced the set of parameters that characterized the synthesized Au₂₅ assemblies: radius of Au₂₅ nanocluster in the multimer, *R*, and the edge-to-edge distance between the 'pearls', *L*, corresponding to the length of the linker (see **Scheme 3.1**).

Figure 5.13 depicts the experimental profiles (open black symbols) of **F2**, **F3**, and **F5** samples and their respective fits (red traces).

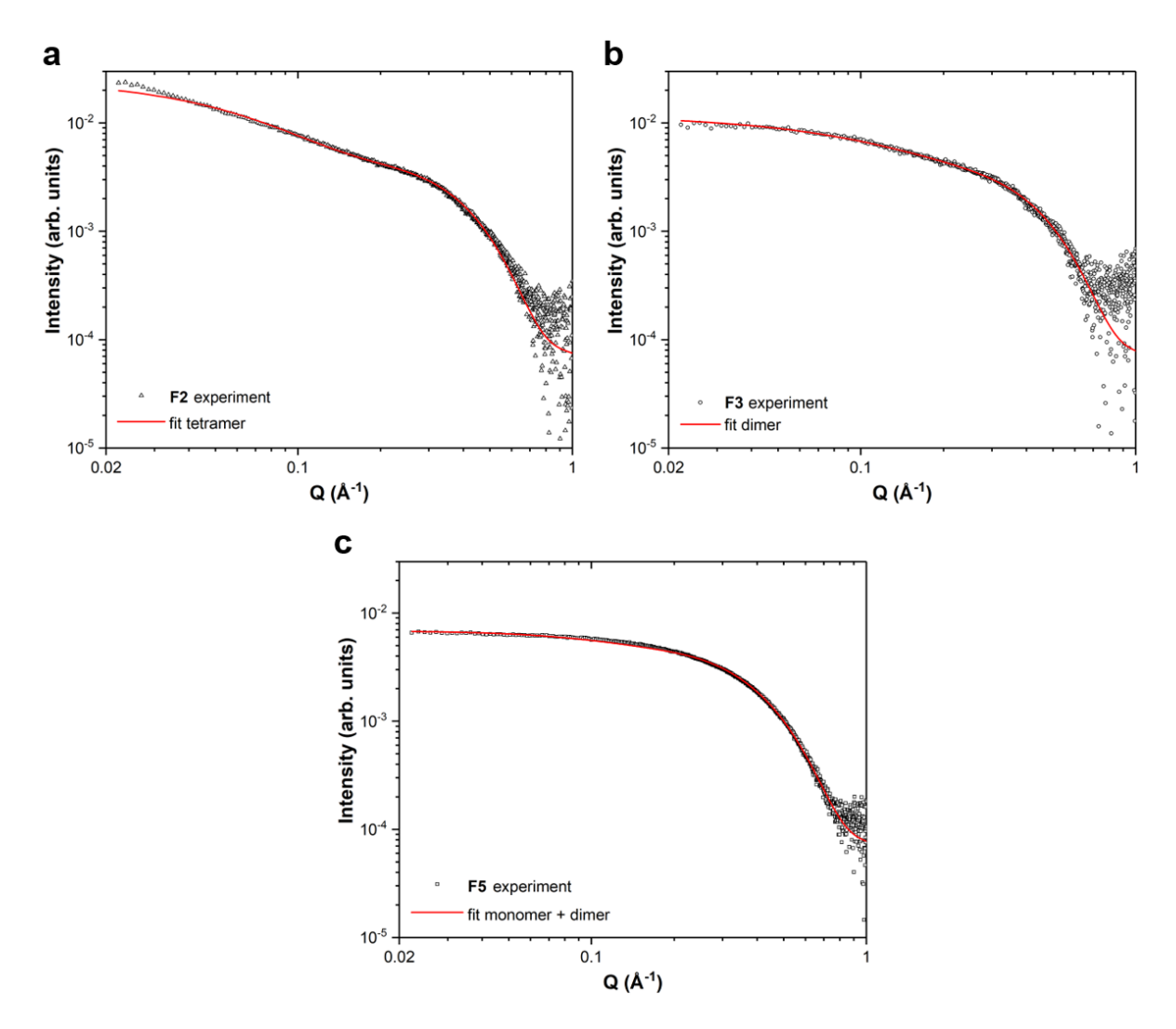


Figure 5.13 Fitting of the SAXS data to the pearl-necklace model (a) fraction F2 (n = 4); (b) fraction F3 (n = 2); (c) fraction F5 to the mixed 'sphere + pearl-necklace' model (n = 2). The experimental data depicted as black open symbols; fitting profiles depicted in red.

The fitted curves showed a very good agreement between the model and experiment and the parameters obtained from the fits for each sample are presented in **Table 5.4**.

The **F2** sample was best fitted with tetrameric structure (no. of 'pearls' = 4) yielding the cluster radius R = 4.80 Å and edge-to-edge distance of 18.78 Å. This result matched the qualitative description of the **F2** sample (i.e., the relative volume of the scattering species N = 3.5) based on the scattering intensity. The experimental data for the **F3** fraction was fitted to a dimeric model (no. of 'pearls' = 2, fitting range 0.024 - 0.7 Å), with a satisfactory result, generating values of 4.45 Å and 15.62 Å for the Au₂₅ radius and the intercluster distance, respectively. Again, the value of N = 1.34 provided a strong indication that the fraction **F3** may constitute of dimeric species.

For the fraction F5 however, even though the N value of 0.99 indicated that the sample contained predominantly monomers, fitting of the experimental data to the spherical model furnished the sphere

radius value of 3.94 ± 0.03 Å (not shown here), which markedly underestimated the $[Au_{25}(2PET)_{18}]^0$ nanocluster size. The pearl-necklace model for dimeric species, on the other hand, overestimated the experimental data. Therefore, the mixed 'sphere + pearl-necklace' model, which treats part of the sample as spherical monomers and the other as dimeric species ('2 pearls'), was employed to obtain the quantitative fit for the **F5** fraction. This approach allowed obtaining a satisfactory fit to the experimental data. It provided the descriptor values of R and L for the species within the **F5** sample (see **Figure 5.13-c**). More importantly, it allowed determination of the relative abundance of monomers and dimers in the sample, since each component of the mixed model (i.e., sphere and pearl-necklace) has its own scaling factor. The monomer-to-dimer ratio was found to be 7.73, and this explained why the sample was showing largely monomeric character, given the dominant monomeric population in the **F5** sample.

Table 5.4 Fitted SAXS parameters of **F2** and **F3** fractions using pearl-necklace model for tetramers and dimers, respectively and for the **F5** sample with a mixed 'sphere + pearl-necklace' model.

	Au25(2PET)18	F2	F3	F5
Fitting model	hard sphere	pearl-necklace	pearl-necklace	sphere +
				pearl-necklace
Core radius, R (Å)	4.55*	4.80 ± 0.01	4.45 ± 0.01	$R_s = 4.51$
				$R_{p-n}=4.53$
Edge-to-edge distance, L (Å)	n/a	18.78 ± 0.08	15.62 ± 0.70	15.00 ± 2.85
No. pearls (n)	n/a	4	2	2
R polydispersity	0.20 (fixed)	0.20 (fixed)	0.20 (fixed)	sphere $= 0.203$
				p-n = 0.211
L polydispersity	n/a	1.120 ± 0.003	1.337 ± 0.005	0.405 ± 0.042
M/D ratio from the model	n/a	n/a	n/a	7.73

^(*) very small error 0.003

The fitting of the experimental data yielded the size of Au_{25} clusters, and the linker length for each fraction (**Table 5.4**). Overall, the size of the Au_{25} clusters was consistent across all samples and was in excellent agreement with the value of 4.6 Å obtained from SAXS measurements of $Au_{25}(SBu)_{18}$ clusters fitted with the hard sphere model. The mean separation values of connected pearls (*L*) for each analysed fraction were in close agreement with the value of terminal sulfur-to-sulfur distance of 18.5 Å in the **o-DTE** linker, obtained from the DFT modelling of dimeric $Au_{25}(SCH_3)_{18}$ species (**Appendix B**).

5.7 Conclusions

Herein, the successful synthesis of the designed dithiol linker molecule bearing the molecular photoswitching functionality is reported. The synthetic methodology extended on the already reported method by the Feringa group^{22, 43} and effectively introduced the thiol functionality in a separate synthetic step rather than forming it *in-situ* when reacting with Au species, as shown by others.^{25, 26}

The photoswitching properties of the thiol-protected, **DTE(SAc)** and the thiol-bearing **DTE(SH)** molecules were characterized in detail. The ON/OFF photoswitching experiments demonstrated that the **DTE(SAc)** ligand was significantly more photostable than its **DTE(SH)** analogue. Interestingly, it was the visible light irradiation experiment of the **DTE(SH)** ligand that induced the photofatigue. The analysis of the UV-vis spectra acquired during the ring-opening reaction showed the formation of a by-product. This is quite unexpected, as the literature reports show the emergence of the annulated-ring by-product (**Scheme 5.2**) during the UV irradiation. The by-product formed upon 532 nm illumination requires further identification using e.g., NMR analysis. For both DTE-based ligands the ring-opening reactions, measured at 532 nm, were much less efficient ($\Phi_{CO} = \sim 0.1-0.19$ %) that the photocyclization reactions as evidenced by the quantum yields of 21 % and 53 % for **DTE(SH)** and **DTE(SAc)**, respectively, which is a known phenomenon for the DTE photoswitches.³¹ Moreover, it is known that not only the substituents in the 5, 5'-position of the thienyl rings affect the quantum yields but even the *para-*substituents of the phenyl ring attached to these 5, 5'-positions could influence the Φ values.^{30,44}

The formation of nanocluster assemblies based on the $[Au_{25}(2PET)_{18}]^0$ cluster connected with the dithiol (**o-DTE**) linker was achieved via wet-chemistry method in which the protective 2PET ligands were exchanged for the **o-DTE** dithiols and subsequently oligomeric species emerged. These species were then isolated using the standard size-exclusion chromatography (SEC) technique employed for Au NC purification. Analysis of the Au_{25} assemblies revealed that the reaction produced a mixture of tetramers, dimers and monomers with a mixed monolayer ligand shell.

5.8 Acknowledgements

This work benefited from the use of the SasView application, originally developed under NSF Award DMR-0520547. SasView also contains code developed with funding from the EU Horizon 2020 programme under the SINE2020 project Grant No 654000.

5.9 References

- Sun, L.; Diaz-Fernandez, Y. A.; Gschneidtner, T. A.; Westerlund, F.; Lara-Avila, S.; Moth-Poulsen, K., Single-Molecule Electronics: from Chemical Design to Functional Devices. *Chemical Society Reviews* 2014, 43 (21), 7378-7411.
- 2. Lahtinen, T.; Hulkko, E.; Sokołowska, K.; Tero, T.-R.; Saarnio, V.; Lindgren, J.; Pettersson, M.; Häkkinen, H.; Lehtovaara, L., Covalently Linked Multimers of Gold Nanoclusters Au₁₀₂(p-MBA)₄₄ and Au~₂₅₀(p-MBA)_n. *Nanoscale* **2016**, *8* (44), 18665-18674.
- 3. Sokolowska, K.; Hulkko, E.; Lehtovaara, L.; Lahtinen, T., Dithiol-Induced Oligomerization of Thiol-Protected Gold Nanoclusters. *The Journal of Physical Chemistry C* **2018**, *122* (23), 12524-12533.
- 4. Sels, A.; Salassa, G.; Cousin, F.; Lee, L.-T.; Bürgi, T., Covalently Bonded Multimers of Au₂₅(SBut)₁₈ as a Conjugated System. *Nanoscale* **2018**, *10* (26), 12754-12762.
- 5. Ho-Wu, R.; Sun, K.; Goodson, T., Synthesis and Enhanced Linear and Nonlinear Optical Properties of Chromophore–Au Metal Cluster Oligomers. *The Journal of Physical Chemistry C* **2018**, *122* (4), 2315-2329.
- 6. Heinecke, C. L.; Ni, T. W.; Malola, S.; Mäkinen, V.; Wong, O. A.; Häkkinen, H.; Ackerson, C. J., Structural and Theoretical Basis for Ligand Exchange on Thiolate Monolayer Protected Gold Nanoclusters. *Journal of the American Chemical Society* **2012**, *134* (32), 13316-13322.
- 7. Yan, N.; Xia, N.; Wu, Z., Metal Nanoparticles Confronted with Foreign Ligands: Mere Ligand Exchange or Further Structural Transformation? *Small* **2020**, 2000609.
- 8. Rambukwella, M.; Sakthivel, N. A.; Delcamp, J. H.; Sementa, L.; Fortunelli, A.; Dass, A., Ligand Structure Determines Nanoparticles' Atomic Structure, Metal-Ligand Interface and Properties. *Frontiers in Chemistry* **2018**, *6* (330).
- Shibu, E. S.; Muhammed, M. A. H.; Tsukuda, T.; Pradeep, T., Ligand Exchange of Au₂₅SG₁₈ Leading to Functionalized Gold Clusters: Spectroscopy, Kinetics, and Luminescence. *The Journal of Physical Chemistry* C 2008, 112 (32), 12168-12176.
- 10. Tofanelli, M. A.; Salorinne, K.; Ni, T. W.; Malola, S.; Newell, B.; Phillips, B.; Häkkinen, H.; Ackerson, C. J., Jahn–Teller effects in Au₂₅(SR)₁₈. *Chemical Science* **2016**, *7* (3), 1882-1890.
- 11. Irie, M.; Mohri, M., Thermally Irreversible Photochromic Systems. Reversible Photocyclization of Diarylethene Derivatives. *The Journal of Organic Chemistry* **1988**, *53* (4), 803-808.
- 12. Asano, Y.; Murakami, A.; Kobayashi, T.; Goldberg, A.; Guillaumont, D.; Yabushita, S.; Irie, M.; Nakamura, S., Theoretical Study on the Photochromic Cycloreversion Reactions of Dithienylethenes; on the Role of the Conical Intersections. *Journal of the American Chemical Society* **2004**, *126* (38), 12112-12120.
- 13. Irie, M.; Fukaminato, T.; Matsuda, K.; Kobatake, S., Photochromism of Diarylethene Molecules and Crystals: Memories, Switches, and Actuators. *Chemical Reviews* **2014**, *114* (24), 12174-12277.
- 14. Irie, M.; Uchida, K., Synthesis and Properties of Photochromic Diarylethenes with Heterocyclic Aryl Groups. *Bulletin of the Chemical Society of Japan* **1998**, *71* (5), 985-996.
- 15. Irie, M., Diarylethenes for Memories and Switches. Chemical Reviews 2000, 100 (5), 1685-1716.
- 16. Szalóki, G.; Pozzo, J.-L., Synthesis of Symmetrical and Nonsymmetrical Bisthienylcyclopentenes. *Chemistry A European Journal* **2013**, *19* (34), 11124-11132.
- 17. Uchida, K.; Nakayama, Y.; Irie, M., Thermally Irreversible Photochromic Systems. Reversible Photocyclization of 1,2-Bis(benzo[b]thiophen-3-yl)ethene Derivatives. *Bulletin of the Chemical Society of Japan* **1990**, *63* (5), 1311-1315.

- 18. Taniguchi, H.; Shinpo, A.; Okazaki, T.; Matsui, F.; Irie, M., Photodegradation Mechanism of Photochromic Diarylethene Derivatives. *Nippon Kagaku Kaishi* **1992**, *1992* (10), 1138-1140.
- 19. Irie, M.; Lifka, T.; Kobatake, S.; Kato, N., Photochromism of 1,2-Bis(2-methyl-5-phenyl-3-thienyl)perfluorocyclopentene in a Single-Crystalline Phase. *Journal of the American Chemical Society* **2000**, *122* (20), 4871-4876.
- 20. Uchida, K.; Guillaumont, D.; Tsuchida, E.; Mochizuki, G.; Irie, M.; Murakami, A.; Nakamura, S., Theoretical Study of an Intermediate, a Factor Determining the Quantum Yield in Photochromism of Diarylethene Derivatives. *Journal of Molecular Structure: THEOCHEM* **2002**, *579* (1), 115-120.
- 21. N. Lucas, L.; van Esch, J.; M. Kellogg, R.; L. Feringa, B., A New Class of Photochromic 1,2-Diarylethenes; Synthesis and Switching Properties of Bis(3-Thienyl)Cyclopentenes. *Chemical Communications* **1998**, (21), 2313-2314.
- 22. Lucas, Linda N.; Jong, Jaap J. D. d.; Esch, Jan H. v.; Kellogg, Richard M.; Feringa, Ben L., Syntheses of Dithienylcyclopentene Optical Molecular Switches. *European Journal of Organic Chemistry* **2003**, 2003 (1), 155-166.
- 23. Stuhr-Hansen, N.; Christensen, J. B.; Harrit, N.; Bjørnholm, T., Novel Synthesis of Protected Thiol End-Capped Stilbenes and Oligo(phenylenevinylene)s (OPVs). *The Journal of Organic Chemistry* **2003**, *68* (4), 1275-1282.
- 24. Stetsovych, O.; Mutombo, P.; Švec, M.; Šámal, M.; Nejedlý, J.; Císařová, I.; Vázquez, H.; Moro-Lagares, M.; Berger, J.; Vacek, J.; Stará, I. G.; Starý, I.; Jelínek, P., Large Converse Piezoelectric Effect Measured on a Single Molecule on a Metallic Surface. *Journal of the American Chemical Society* 2018, 140 (3), 940-946.
- 25. Kudernac, T.; van der Molen, S. J.; van Wees, B. J.; Feringa, B. L., Uni- and Bi-Directional Light-Induced Switching of Diarylethenes on Gold Nanoparticles. *Chemical Communications* **2006**, (34), 3597-3599.
- 26. von Irmer, J.; Frieß, F.; Herold, D.; Kind, J.; Thiele, C. M.; Gallei, M., Photochromic Dithienylethenes Characterized by In Situ Irradiation NMR-Spectroscopy and Electrochemically Induced Responsiveness on Gold Substrates. *Journal of Materials Chemistry C* **2019**, *7* (45), 14088-14097.
- 27. Singh, R.; Whitesides, G. M., Thiol-Disulfide Interchange. In *The Chemistry of Sulfur-Containing Functional Groups*, Patai, S., Ed. J. Wiley and Sons, Ltd.: London, 1993; Vol. Supplement S, pp 633-658.
- 28. Rubin, M. B.; Braslavsky, S. E., Quantum Yield: the Term and the Symbol. A Historical Search. *Photochemical & Photobiological Sciences* **2010**, *9* (5), 670-674.
- 29. Megerle, U.; Lechner, R.; König, B.; Riedle, E., Laboratory Apparatus for the Accurate, Facile and Rapid Determination of Visible Light Photoreaction Quantum Yields. *Photochemical & Photobiological Sciences* **2010**, *9* (10), 1400-1406.
- 30. Irie, M.; Sakemura, K.; Okinaka, M.; Uchida, K., Photochromism of Dithienylethenes with Electron-Donating Substituents. *The Journal of Organic Chemistry* **1995**, *60* (25), 8305-8309.
- 31. Sumi, T.; Takagi, Y.; Yagi, A.; Morimoto, M.; Irie, M., Photoirradiation Wavelength Dependence of Cycloreversion Quantum Yields of Diarylethenes. *Chemical Communications* **2014**, *50* (30), 3928-3930.
- 32. Browne, W. R.; de Jong, J. J. D.; Kudernac, T.; Walko, M.; Lucas, L. N.; Uchida, K.; van Esch, J. H.; Feringa, B. L., Oxidative Electrochemical Switching in Dithienylcyclopentenes, Part 2: Effect of Substitution and Asymmetry on the Efficiency and Direction of Molecular Switching and Redox Stability. *Chemistry A European Journal* **2005**, *11* (21), 6430-6441.
- 33. Irie, M.; Lifka, T.; Uchida, K.; Kobatake, S.; Shindo, Y., Fatigue Resistant Properties of Photochromic Dithienylethenes: By-Product Formation. *Chemical Communications* **1999**, (8), 747-750.

- 34. Hanazawa, M.; Sumiya, R.; Horikawa, Y.; Irie, M., Thermally Irreversible Photochromic Systems. Reversible Photocyclization of 1,2-Bis (2-Methylbenzo[β]Thiophen-3-yl)Perfluorocyclocoalkene Derivatives. *Journal of the Chemical Society, Chemical Communications* **1992**, (3), 206-207.
- 35. Pariani, G.; Quintavalla, M.; Colella, L.; Oggioni, L.; Castagna, R.; Ortica, F.; Bertarelli, C.; Bianco, A., New Insight into the Fatigue Resistance of Photochromic 1,2-Diarylethenes. *The Journal of Physical Chemistry C* **2017**, *121* (42), 23592-23598.
- 36. Zhu, M.; Aikens, C. M.; Hollander, F. J.; Schatz, G. C.; Jin, R., Correlating the Crystal Structure of a Thiol-Protected Au₂₅ Cluster and Optical Properties. *Journal of the American Chemical Society* **2008**, *130* (18), 5883-5885.
- 37. Katsiev, K.; Lozova, N.; Wang, L.; Sai Krishna, K.; Li, R.; Mei, W.-N.; Skrabalak, S. E.; Kumar, C. S. S. R.; Losovyj, Y., The Electronic Structure of Au₂₅ Clusters: Between Discrete and Continuous. *Nanoscale* **2016**, 8 (31), 14711-14715.
- 38. Dass, A.; Stevenson, A.; Dubay, G. R.; Tracy, J. B.; Murray, R. W., Nanoparticle MALDI-TOF Mass Spectrometry without Fragmentation: Au₂₅(SCH₂CH₂Ph)₁₈ and Mixed Monolayer Au₂₅(SCH₂CH₂Ph)_{18-x}(L)_x. *Journal of the American Chemical Society* **2008**, *130* (18), 5940-5946.
- 39. Ho-Wu, R.; Yau, S. H.; Goodson, T., Linear and Nonlinear Optical Properties of Monolayer-Protected Gold Nanocluster Films. *ACS Nano* **2016**, *10* (1), 562-572.
- 40. Chakraborty, P.; Nag, A.; Mondal, B.; Khatun, E.; Paramasivam, G.; Pradeep, T., Fullerene-Mediated Aggregation of M₂₅(SR)₁₈⁻ (M = Ag, Au) Nanoclusters. *The Journal of Physical Chemistry C* **2020**, *124* (27), 14891-14900.
- 41. Doucet, M.; Cho, J. H.; Alina, G.; Bakker, J.; Bouwman, W.; Butler, P.; ...; Washington, A., SasView version 4.2.2. Zenodo. **2019**.
- 42. Zhu, M. Z.; Eckenhoff, W. T.; Pintauer, T.; Jin, R., Conversion of Anionic [Au₂₅(SCH₂CH₂Ph)₁₈]⁻ Cluster to Charge Neutral Cluster via Air Oxidation. *The Journal of Physical Chemistry C* **2008**, *112* (37), 14221-14224.
- 43. Lucas, L. N.; van Esch, J.; Kellogg, R. M.; Feringa, B. L., A New Synthetic Route to Symmetrical Photochromic Diarylperfluorocyclopentenes. *Tetrahedron Letters* **1999**, *40* (9), 1775-1778.
- 44. Guillaumont, D.; Kobayashi, T.; Kanda, K.; Miyasaka, H.; Uchida, K.; Kobatake, S.; Shibata, K.; Nakamura, S.; Irie, M., An Ab Initio MO Study of the Photochromic Reaction of Dithienylethenes. *The Journal of Physical Chemistry A* **2002**, *106* (31), 7222-7227.

Chapter 6

Photoresponsive Au₂₅ nanoassemblies: structural and spectroscopic investigations

Statement of contribution

DFT calculations were performed by Dr Latévi Max Dawson Daku from Department of Physical Chemistry of University of Geneva.

SAXS measurements, data treatment and initial fittings were performed by Dr Lay-Theng Lee, Laboratoire Léon Brillouin, CEA-Saclay, France

HRTEM measurements were performed by Dr Mohammad M. Dadras, CSEM Centre Suisse d'Electronique et de Microtechnique SA, Neuchâtel, Switzerland

6.1 Introduction

A few examples of light responsive $Au_{25}(SR)_{18}$ nanoclusters are known in the literature. ¹⁻³ These species have been created by functionalizing the protective monolayer with thiolate ligands containing photoswitchable moiety based on either azobenzene^{1,2} or spiropyran³ units. Importantly, these clusters have shown reversible photoisomerization confirming that Au NCs are a suitable vehicle for photoligands. Recently, Rival et al. demonstrated the application of a photoresponsive ligand to stimulate a Au_{25}^- reversible dipole-induced self-assembly. ¹ Au_{25} nanoclusters capped with an azobenzene-alkyl

monothiol (C₃-AMT) were shown to form disc-like superstructures upon exposure to ultraviolet (345 nm) irradiation. These stable superstructures could be readily disassembled with exposure to visible light (435 nm). However, so far, photoswitching behaviour performed with Au NC assemblies has not been described.

However, dithienylethene (DTE) photoswitches have been implemented as part of various systems: self-assembled monolayers (SAMs) on either Au surfaces⁴ or Au and Ag nanoparticles⁵, Au–DTE–Au junctions⁶ or as molecular bridges connecting single-walled carbon nanotubes (SWNTs)⁷. It needs to be said that the photoswitching of the DTE molecule when incorporated into various architectures is not always reversible, as has been shown in the work of Dulić et al. where thiol functionalized DTE switch connecting two gold electrodes demonstrated only one-way switching.⁶ However, molecular bridges connecting two SWNTs were reversible when the central photochromic moiety contained pyrrole rather than a thiophene unit,⁷ suggesting that with careful molecular engineering photoswitching can be enabled with the DTE moiety even in challenging environments. The incorporation of the DTE photoswitching bridge to link Au NCs is therefore investigated in this work.

Specifically, the photoresponsive performance of the covalently linked Au₂₅ assemblies (synthesis described in Section 3.5.1) is presented. As a reminder, detailed characterization of the free photoligand (Section 5.4), established that the free DTE(SH) linker exhibited photofatigue much faster than its acetate-protected analogue–DTE(SAc). This process was caused by the irreversible formation of the isomer containing an annulated ring system (see Scheme 5.2) and was especially pronounced in perhydro-DTE derivatives in solution.^{8, 9} However, formation of such a by-product when the DTE is used as a linker molecule (as here to bind Au₂₅ clusters) is unknown. In fact, the formation of this by-product could be attenuated as recent studies by Pijper et al. using surface-enhanced Raman spectroscopy (SERS) showed that the formation of the condensed by-product was successively inhibited when DTE molecules were immobilized on gold surfaces.¹⁰ The high intermolecular interactions of DTEs in densely packed self-assembled monolayers (SAMs) or in crystalline phases were hampering the isomerization reaction by impeding conformational changes. It is therefore reasonable to assume that the DTE(SH) linker would show different behaviour once the thiolate functionality was covalently linked to the Au₂₅ nanoclusters.

This Chapter is organized as follows: first the reversible photoswitching of different sizes of Au₂₅ assemblies in solution phase is investigated with optical spectroscopy. Then the effect of light irradiation on the structure of the assemblies is analysed using small-angle X-ray scattering (SAXS) and MALDI-MS. Finally, considerable effort has been devoted to understanding the effects of photoirradiation on small Au₂₅ assemblies (mixture of monomers and dimers). Specifically, insights into photophysical and structural changes are sought by a combined approach involving various spectroscopic (UV-vis, PL, NMR, SAXS) and imaging (HRTEM) techniques.

For the clarity of reading, the photocyclization reaction will be also referred to in the text as the switching ON reaction or UV (340 nm) light irradiation. During this reaction, the open-ring isomer is converted to the closed-ring isomer, according to the reaction presented in **Scheme 5.1**. The photocycloreversion process is referred to in the text as the switching OFF or visible (532 nm) light irradiation.

6.2 Reversible photoswitching of DTE-linked Au₂₅ assemblies

6.2.1 Principle of photoswitching reaction

The photoswitching reaction, presented in **Scheme 5.3**, can be viewed as a switching between different states of π -conjugation: 'ON state' with the extended π -conjugation (**c-DTE**) and 'OFF state' where the π -conjugation is disconnected (**o-DTE**). The photoisomerization of the central DTE chromophore corresponds to a conversion from a non-planar, conformationally flexible molecule to a rigid and planar structure. The wavelengths of light chosen to switch between the two different states are dictated by the absorption characteristics of each isomer, considering that **o-DTE** \rightarrow **c-DTE** reaction is driven by UV light, and the reverse reaction, **c-DTE** \rightarrow **o-DTE** is activated by visible light. Ideally, the wavelengths of light used for the photoswitching reaction should be selectively tuned to the absorption band of the targeted isomer. For illumination of the open-ring isomer, 340 nm light was chosen as it avoids directly irradiating the absorption maximum band belonging to the closed-ring isomer. Correspondingly, for the photocycloreversion reaction the irradiation of the **c-DTE** species was achieved by illuminating in the characteristic absorption band in the visible range of the spectrum (~18,000 cm⁻¹, 550 nm). The idea was to irradiate at the wavelength with the highest absorption coefficient for a given DTE isomer, avoiding the wavelengths where both species absorb.

6.2.2 Reversible photoswitching of the DTE-linked Au₂₅ assemblies—qualitative inspection using the UV-vis-NIR spectroscopy

This Section qualitatively describes the photoswitching behaviour of different sizes of Au₂₅ assemblies prepared as described in **Section 5.5**. In total, five fractions of the **S1** sample were subjected to several 340/532 nm irradiation cycles in solution and the progress of the photoisomerization reaction was monitored with UV-vis spectroscopy. The photoswitching of each isolated fraction was performed in toluene by subjecting the sample first to ultraviolet (UV), and then to visible light illumination. Of note, the photoirradiation experiments of the various fractions of the **S1** sample were not conducted with an aim to reach the photostationary state (PSS) during each irradiation event. Rather, they probed whether the formed Au₂₅ assemblies responded to the light stimuli and determined whether the changes in the

diagnostic band region could be readily monitored during the photoreaction. Moreover, the first demonstration of the photoswitching reversibility for the formed Au_{25} assemblies was of primary interest.

Temporal changes in the absorption spectra of one of the fractions of the **S1** sample (**S1-F1**) exposed alternately to UV and vis light is presented in **Figure 6.1**. The photoinduced spectral changes for the other fractions (**F2–F5**) after each irradiation event can be found in **Appendix A** (**Figure A.9**). The irradiation times required to bring the **S1** sample to a PSS_{340} were considerably longer than for a pure **DTE(SH)** ligand, when applying the same irradiation power (8 vs 40 min). This is understandable given that the Au₂₅ clusters also absorb photons at 340 nm. Since the reverse reaction, is much less efficient ($\Phi = 1 \times 10^{-3}$), substantially more time was required to reach a PSS_{532} for the Au₂₅ assemblies (e.g., after 60 min the absorbance at the characteristic band maximum was brought to the half of the original value).

The electronic absorption spectrum of the non-irradiated **S1-F1** sample (black trace in **Figure 6.1**), displayed no characteristic features of [Au₂₅(2PET)₁₈]⁰ building units. However, the presence of a new band around 11,900 cm⁻¹ (840 nm) was noted. Appearance of such NIR band has been shown for larger Au₂₅ aggregates, constituting between 10–20 Au₂₅ clusters, formed by linking Au₂₅(SBu)₁₈ clusters via simple conjugated dithiol linkers.¹¹ This band was attributed to the electronic coupling of the Au₂₅ units through the aromatic bridging molecules.

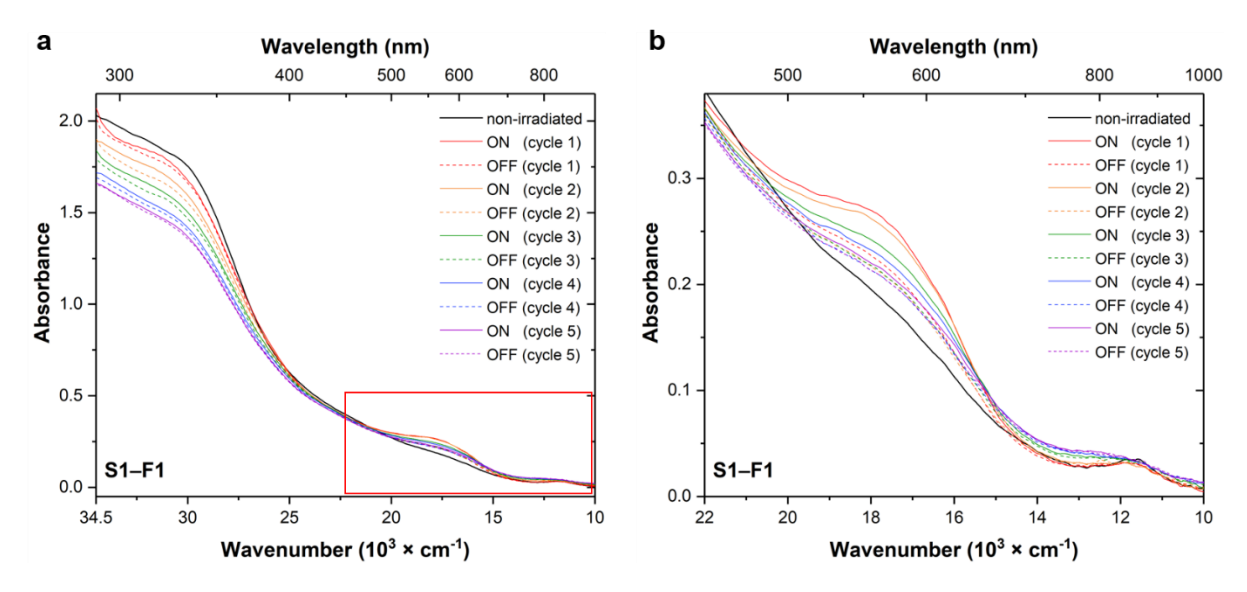


Figure 6.1 The optical absorption spectra of the **S1-F1** sample after different irradiation events. The UV irradiation led to a closed-ring DTE isomer (ON state), and the visible light irradiation produced the OFF state of the DTE linker. (a) full range spectrum; (b) enlarged region of the spectrum indicated by the red square.

The first illumination with 340 nm light (\sim 1.24 mW) led to a gradual increase in absorbance at \sim 18,000 cm⁻¹ (550 nm, red solid line in **Figure 6.1**). Similar but opposite behaviour was observed for

the switching OFF reaction (532 nm illumination): the band at ~18,000 cm⁻¹ (550 nm) decreased in intensity (red dotted line). This new band originated from the π - π * transition in the closed-ring isomer of the dithiol linker, since the **c-DTE** moiety exhibits a strong band at 18,315 cm⁻¹ (546 nm) after the UV light-induced cyclization reaction (as shown in **Figure 5.3**-a).

It is important to note, that the 532 nm irradiation (the switching OFF reaction) was not conducted for a duration sufficiently long to return the $A_{546 nm}$ to its initial value. However, at the time of experiment, after 60 min of irradiation, the absorbance changes ($\Delta A_{546 nm}$) were very small and hence difficult to observe by visual inspection. The detailed investigation of the photoswitching process will be described in **Section 6.4**.

Besides the fluctuation in the diagnostic band region, the subsequent irradiation cycles have substantially impacted the overall optical spectra. The 11,900 cm⁻¹ (840 nm) band observed in the spectra of the large fractions (e.g., **F1-F2**) was flattened and blue-shifted while the absorbance in the UV region gradually diminished. Moreover, if an extent of the photoswitching is defined as a change in absorbance of the diagnostic band maximum ($\Delta A_{546 nm}$) at the beginning and end of each irradiation experiment, it is clear that this value dampened considerably with increasing cycle number (**Figure 6.2**).

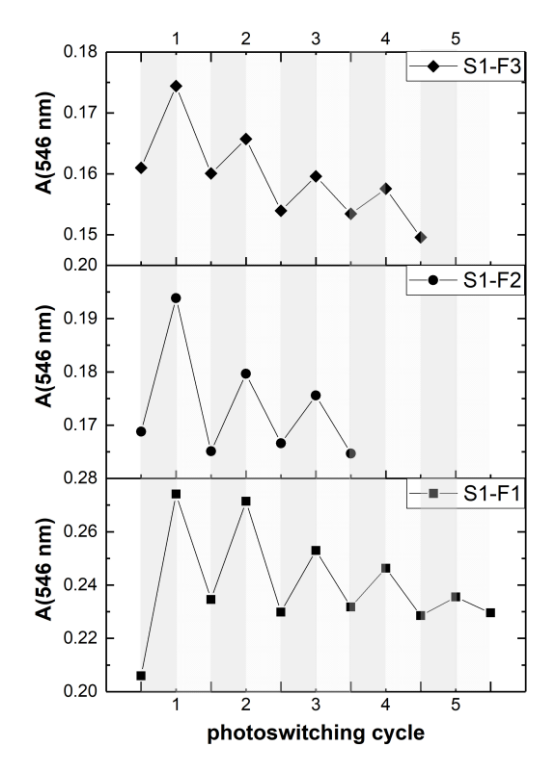


Figure 6.2 Changes in the absorbance of the diagnostic band (546 nm) for different fractions of the **S1** sample. The photoswitching cycle consisted of two irradiation events: UV illumination (grey bands) and visible light illumination (white bands).

Remarkably, all **S1** fractions exhibited similar behaviour in the diagnostic band region when exposed to the 340/532 nm light irradiation cycles, confirming their photoswitching abilities. Interestingly, the

optical traces of the smaller SEC fractions ($\mathbf{F3}$ – $\mathbf{F5}$) in their non-irradiated state exhibited the spectral features of the starting $[\mathrm{Au}_{25}(\mathrm{2PET})_{18}]^0$ cluster suggesting that the linking reaction did not induce considerable changes in their electronic structure. However, the extent of the photoswitching varied across the fractions: it was significantly greater for the larger fractions ($\mathbf{F1}$, $\mathbf{F2}$) than for the smaller ones which could be explained by the higher ratio of the bridging photoligands in larger and more highly interconnected Au_{25} assemblies.

The observed behaviour in the diagnostic band region during irradiation cycles could be explained by a considerable photofatigue of the DTE linker, similar to the pure **DTE(SH)** ligand (**Section 5.4.3.2**). Due to the incomplete switching OFF the remaining **c-DTE** isomer population have been exposed to UV light in a subsequent irradiation experiment, possibly leading to the formation of the annulated-ring by-product. Furthermore, it is hypothesized that the photoswitching of the larger Au₂₅ assemblies could not occur in a synchronized fashion. That is, only a fraction of the DTE linkers were in a favourable conformation to undergo the photoisomerization reaction.

6.2.3 MALDI-TOF-MS analysis of photoirradiated Au₂₅ assemblies

Insights into the molecular composition of the irradiated species was provided by MALDI mass analysis and the obtained spectra were compared with the pure $Au_{25}(2PET)_{18}$ nanocluster. Herein, the mass spectrometry results of the **S1-F1** sample in different irradiation states are presented. Other analysed fractions displayed very similar MALDI-MS spectra, with observed signals originating from both unexchanged $Au_{25}(2PET)_{18}$ and Au_{25} clusters with one or two molecules of the bidentate **o-DTE**² ligand in the protective monolayer, as discussed in **Section 5.6.2**.

The acquired MALDI mass spectra of the non-irradiated **S1-F1** sample (**Figure 6.3**) showed the presence of peaks originating from the Au₂₅(2PET)₁₈ cluster (marked with blue dotted lines). Furthermore, the appearance of peaks corresponding to exchanged species, Au₂₅(2PET)₁₆(**o-DTE**²) marked with red lines, confirmed that Au₂₅ species with unaltered protective ligand shell (i.e., eighteen 2PET ligands) and the modified ligand shell were coexisting in the sample. Analysis of the relative intensities of these species revealed that the ratio of the unexchanged to singly-exchanged Au₂₅ clusters was 1:1.1 and doubly-exchanged species, Au₂₅(2PET)₁₄(**o-DTE**²)₂ was 1:0.88. Interestingly, upon UV light photoirradiation, the peaks corresponding to the monoisotopic species of pure Au₂₅(2PET)₁₈ (m/z = 7390.94 Da), Au₂₅(2PET)₁₆(**o-DTE**²) (m/z = 7590.92 Da) and Au₂₅(2PET)₁₄(**o-DTE**²)₂ (m/z = 7790.89 Da) were no longer observed in the mass spectrum. However, the presence of characteristic fragmentation peaks: Au₂₄L₁₇, Au₂₃L₁₆, Au₂₂L₁₅, and Au₂₁L₁₄, where L = 2PET, for both exchanged Au₂₅(2PET)₁₆(**o-DTE**²) and pure Au₂₅(2PET)₁₈ clusters, confirmed that the assemblies were not decomposed, but rather suggested that their molecular composition was modified. This conclusion is supported by the presence of intense fragmentation peaks of pure Au₂₅(2PET)₁₈, indicating that the

free single clusters underwent linking reaction after photoirradiation. Additionally, the emergence of new relatively intense peaks below $m/z \sim 4750$ Da and in the region of $\sim 10,000$ Da in the spectra of photoirradiated samples, suggests that new species with more complex fragmentation patterns were formed upon photoswitching.

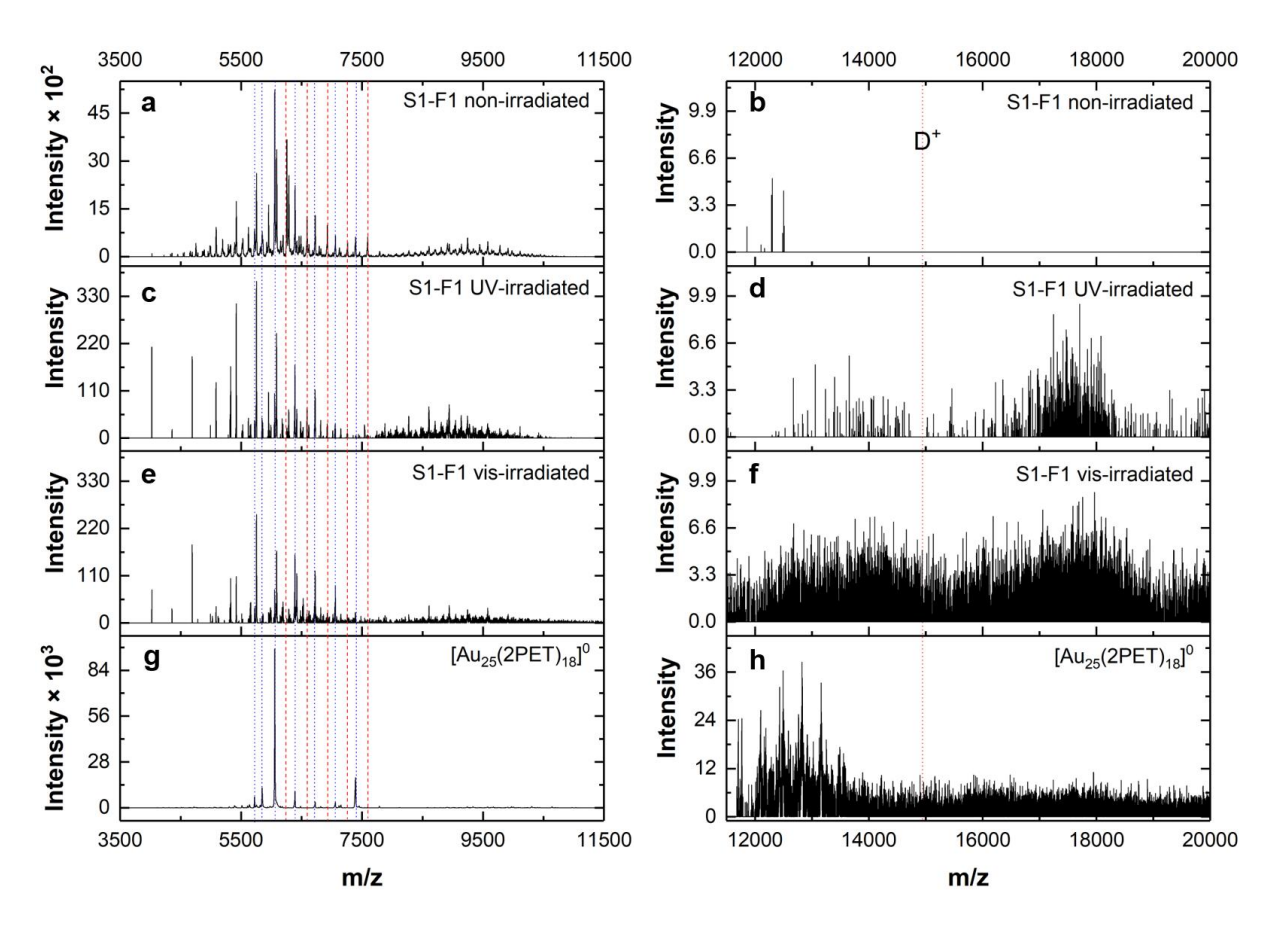
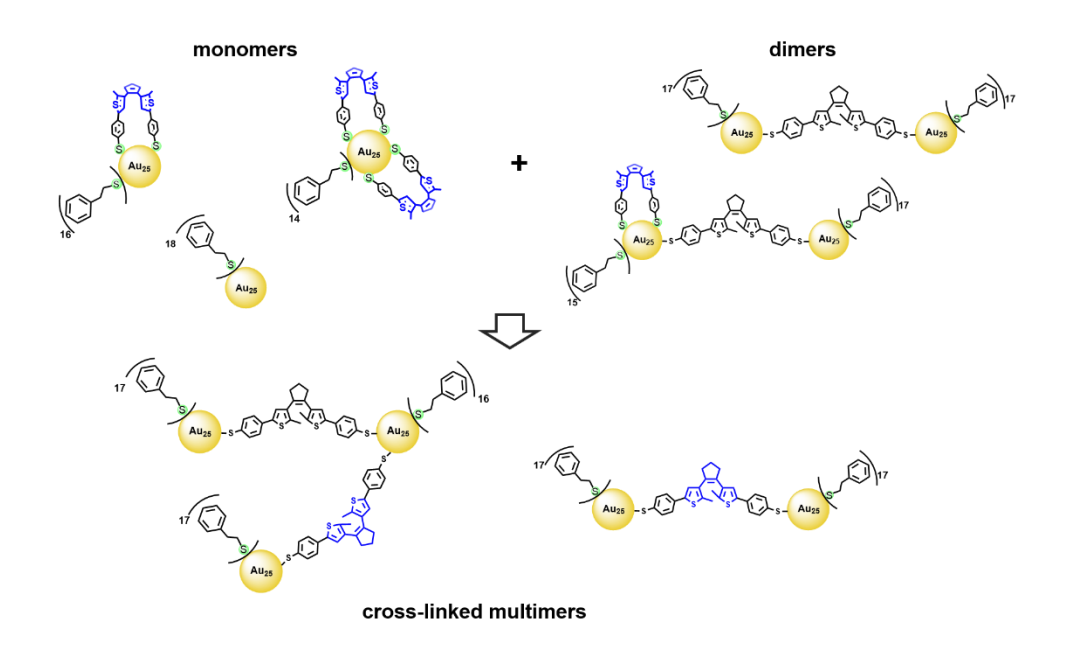


Figure 6.3 (a, b, c) low-mass and (d, e, f) high-mass MALDI mass spectra of S1-F1 sample in various stages of photoirradiation. The dotted blue lines show the signals of pure $Au_{25}(2PET)_{18}$ cluster and its most characteristic fragmentation peaks. The red dashed lines depict the mass peaks of $Au_{25}(2PET)_{16}(\textbf{o-DTE}^2)$ and the corresponding fragments. The dotted line in the high-mass region denotes the mass of the simplest dimer.

It is postulated that for the Au_{25} clusters with exchanged bidentate **o-DTE**² thiolates in their ligand shell, one of the thiolate bonds was broken and the as-formed dangling bond subsequently became available for linking with another Au_{25} cluster. In other words, the photoirradiation caused higher extent of intercluster linking, as depicted in **Scheme 6.1**.

This hypothesis is consistent with the observed lack of mass signals originating from monomeric $Au_{25}(2PET)_{18}$ clusters in the photoirradiated samples. The mass peaks detected in the low mass region could be originating from the multimeric fragments produced in the matrix assisted ionization-desorption process. No peaks corresponding to the singly charged dimeric or trimeric species were detected, but it has been shown previously that MALDI-MS analysis of Au nanocluster assemblies performed under the

same conditions may not be the optimal method to detect such singly charged species^{11, 12} (see discussion in **Section 5.6.2**).



Scheme 6.1. Proposed scenario for light induced assembly formation in the mixture of monomers and dimers. The DTE ligands depicted in blue correspond to the bidentate ligands (o-DTE²) that are postulated to serve as linkers when one of the Au–S bonds is cleaved after photoirradiation.

6.2.4 Photoluminescence behaviour of photoirradiated Au₂₅ assemblies

In addition to the UV-vis absorption, the photoluminescence properties of the Au₂₅ assemblies before and after photoirradiation were also examined. The steady-state photoluminescence (PL) spectra of the various size fractions of the S1 sample, described in Section 6.2.2, in their non-irradiated state (black traces) and after several UV/vis irradiation cycles (red traces), are presented in Figure 6.4. The SEC isolated Au₂₅ assemblies showed a broad emission signal in the red-NIR region centred around 12,000 cm⁻¹ (833 nm) with intensities increasing with the size of the S1 sample.

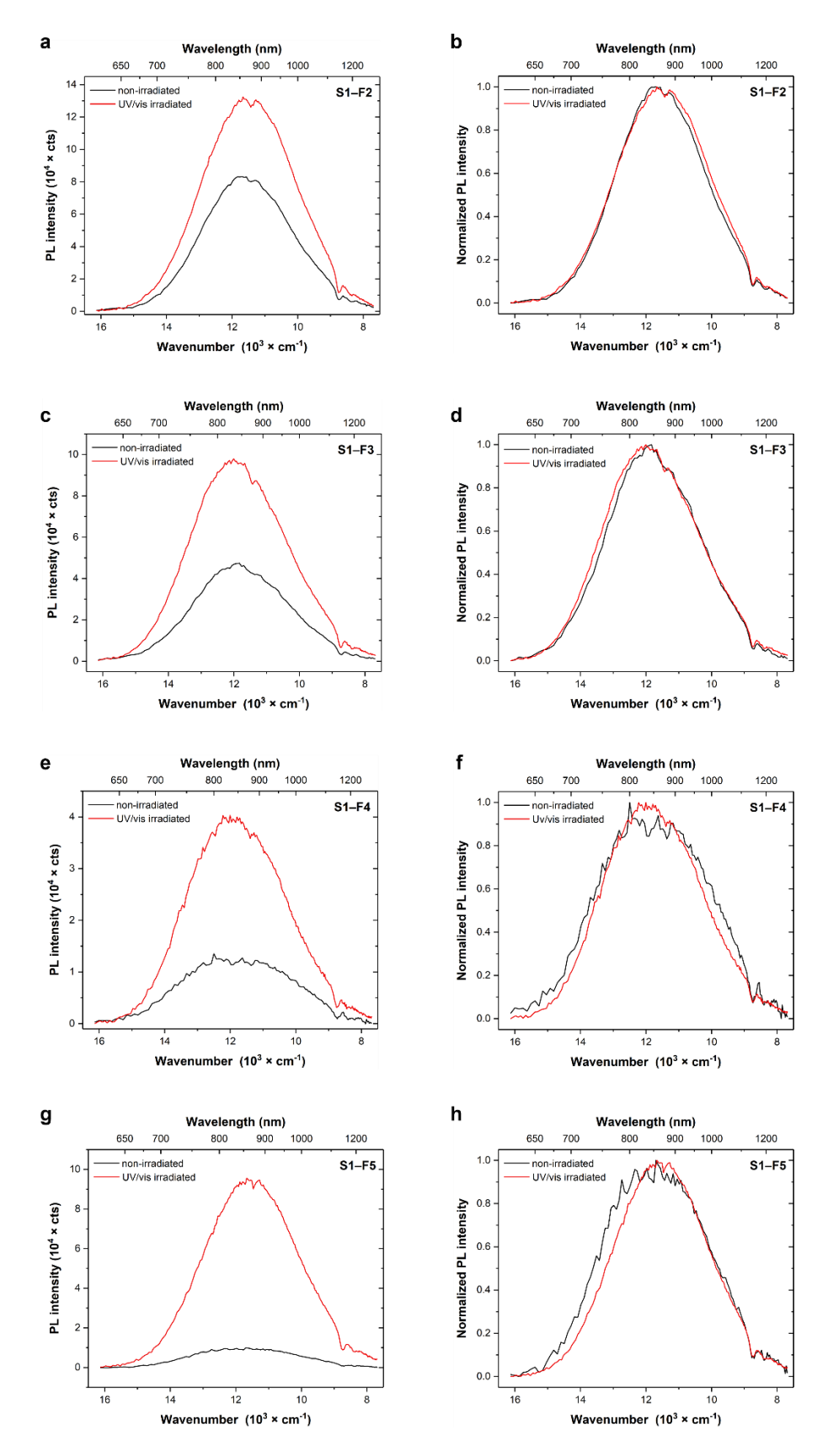


Figure 6.4 Steady-state photoluminescence (PL) spectra of the different size fractions of the S1 sample in their non-irradiated state (black traces) and after several UV/vis irradiation cycles. The left side panels (a, c, e, g) depict the changes in the PL intensity upon photoirradiation of the corresponding fraction. The panels on the right (b, d, f, h) display the shift in the PL spectra and changes in the spectral width of the PL band (spectra were scaled). Spectra were acquired in toluene at 293 K after excitation at 440 nm.

The PL emission of the Au_{25} assemblies was significantly enhanced with respect to single $[Au_{25}(2PET)_{18}]^0$ nanoclusters (data not shown here). Remarkably, an even further increase in the PL intensity was observed for the photoirradiated (i.e., after several ON/OFF cycles) assemblies (**Figure 6.4**-a, c, e, g). In addition, the PL emission bands were showing changes in their spectral widths (**Figure 6.4**-b, d, f, h) with the most pronounced effect noted for the smallest size fractions (i.e., **F4** and **F5**). The detected variations in the optical spectra across the different fractions of the **S1** sample were consistent with the expected size-dependent behaviour. For the absorption spectra of the large fractions (**F1–F3**) a band at ~11,900 cm⁻¹ (840 nm) emerged that was characteristic of large Au_{25} assemblies in agreement with the finding by Sels et al. ¹¹ Furthermore, the rise of the PL emission with the increasing size of the Au_{25} assemblies can be explained by a decrease in non-radiative deactivation pathways, which is consistent with the formation of larger and more rigid Au_{25} network. ¹³

6.3 Investigation of the light-induced structural changes within the Au₂₅ assemblies using small angle X-ray scattering

The photoswitching reaction induced considerable changes in the photophysical properties of the Au_{25} assemblies, as evidenced by the spectroscopic study discussed in **Section 6.2**. Moreover, the MALDI-MS analysis of the irradiated samples (**Figure 6.3**), allowed speculation about the possible structural transformation of the Au_{25} assemblies, based on the changes within the ligand shell of single Au_{25} clusters detectable by the MALDI-MS technique. Further investigation was aimed at gaining more insight into the size and structure of Au_{25} assemblies and how these properties evolved with the photoirradiation cycles.

Yet again, the SAXS technique was chosen as an invaluable technique to address these questions. Accordingly, samples containing different sizes of Au₂₅ assemblies (separated using SEC) in both the ON and OFF states were analysed by SAXS. Essentially, the samples in the OFF state were linked with the open-ring isomer of a DTE linker (**o-DTE**), whereas the sample in the ON state should contain the closed-ring DTE from (**c-DTE**). The primary interest was to identify whether the photoswitching reaction induced significant geometric changes to the DTE linker that were further translated to the size/shape evolution of the Au₂₅ assemblies.

Since the SAXS measurements required a substantially larger amount of analyte than the other characterization techniques employed so far, the sample was prepared in a few synthetic batches according to the procedure described in **Appendix A**. The crude products were fractionated on a SEC column yielding three separate bands (see **Figure A.4**-b). These SEC isolated fractions were characterized by UV-vis-NIR spectroscopy (shown in **Section 6.3.1**) and subsequently combined according to the resemblance of their optical absorption spectra. In total three fractions, **S2-F2**, **S2-F3**

and **S2-F5**, were subjected to evaluation with the SAXS technique. Each fraction was divided into two portions, one of which was exposed to UV light irradiation. In this way, samples containing different isomers of the photoligand could be analysed: the open-ring isomer (i.e., the OFF state, denoted **S2-Fm_o-DTE**), and the closed-ring DTE isomer sample (ON state, **S2-Fm_c-DTE**) produced during the UV-irradiation experiment.

6.3.1 Steady-state absorption spectroscopy of the Au₂₅ assemblies connected with o-DTE and c-DTE photoligand isomers

The electronic absorption spectra of the three fractions of the **S2** sample containing the open DTE isomer (red traces) and the closed-isomer (blue traces) are presented in **Figure 6.5**. For comparison, the absorption spectrum of $[Au_{25}(2PET)_{18}]^0$ was also included (dotted trace).

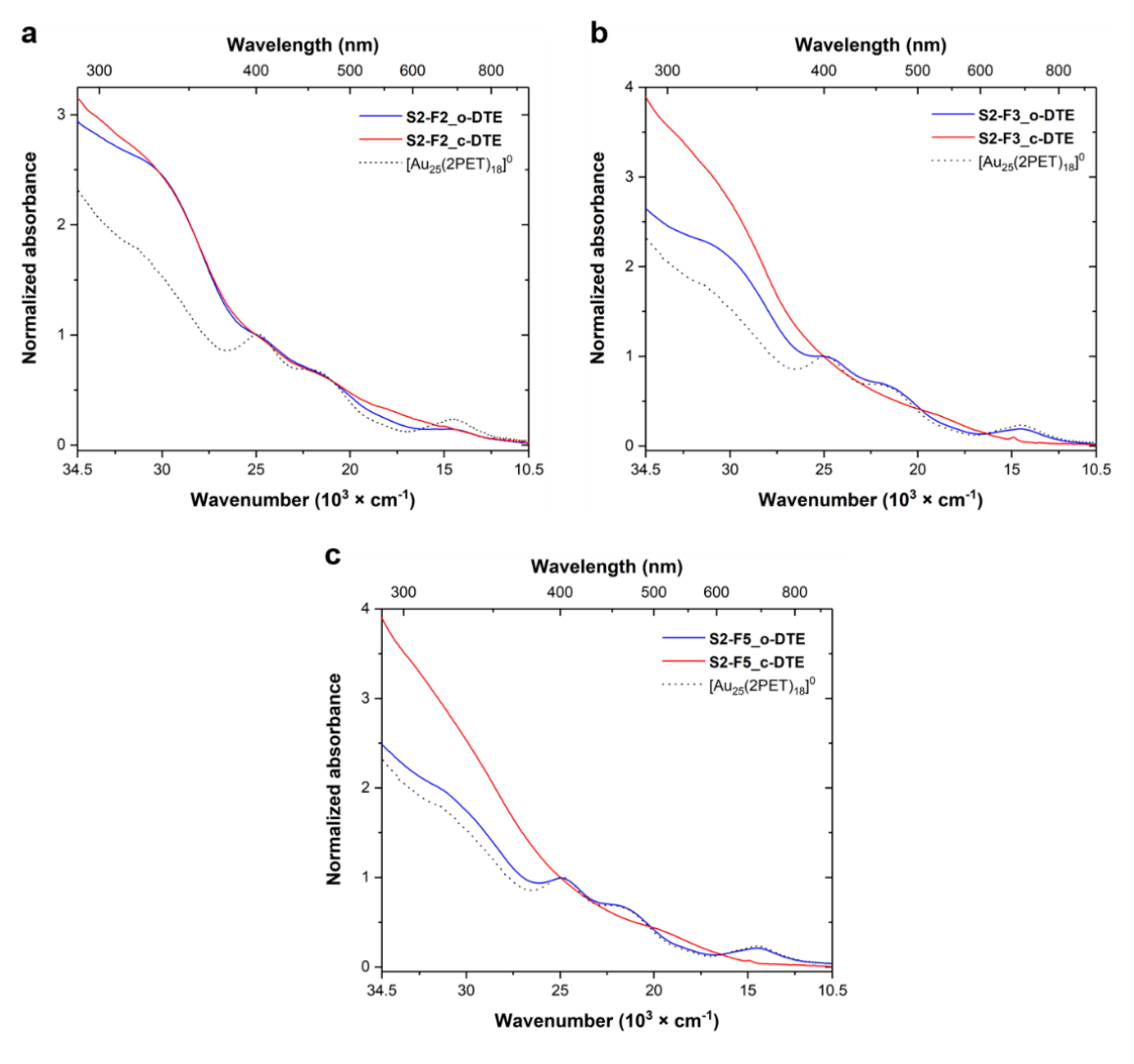


Figure 6.5 Normalized optical absorption spectra of three different size fractions of the S2 sample: (a) S2-F2, (b) S2-F3, and (c) S2-F5 subjected to SAXS analysis in their non-irradiated state (blue traces) and irradiated with UV light (red traces). The spectra of $[Au2s(2PET)18]^0$ (dotted traces) are shown for comparison.

Evidently, the as-formed Au_{25} assemblies, in their non-irradiated state, are characterized by absorption spectra that greatly resembled that of single $[Au_{25}(2PET)_{18}]^0$ nanoclusters. The exposure of the samples to 340 nm irradiation resulted in their photoswitching to the ON state, as evidenced by the emergence of the band at ~18,000 cm⁻¹ (550 nm).

The absorption spectra of the larger fractions (**S2-F2** and **S2-F3**) displayed clear features of $[Au_{25}(2PET)_{18}]^0$ cluster and were similar to that of the **S1-F4** sample shown in **Appendix A** (**Figure A.9-**e). It needs to be said however that the **S2** sample was obtained using an optimized synthetic procedure that gave product separation into well-defined bands on the SEC column. Based on the appearance of the optical spectra, it is expected that the samples **S2-F2** and **S2-F3** will contain smaller assemblies. Another indication of the smaller size of the formed Au_{25} assemblies was provided by the lack of characteristic absorption band around 11,900 cm⁻¹ (840 nm) exhibited by aggregates constituting 10-20 Au₂₅ nanoclusters covalently-linked with dithiol molecules.

6.3.2 SAXS investigation into photoinduced structural changes of Au₂₅ assemblies

Figure 6.6 displays the SAX scattering profiles of three different fractions of the **S2** sample: **S2-F2**, **S2-F3** and **S2-F5** measured in toluene in OFF (open symbols) and ON (filled symbols) state. The qualitative analysis, based on the ratio of scattering intensities I(Q) at $Q \to 0$, showed clearly that the volume of the species in all three fractions increased upon 340 nm illumination. Of note, the **F3** sample presented unusual scattering profile at $Q < 0.5 \text{ Å}^{-1}$ (**Figure 6.6**-b) therefore a quantitative analysis of the volume of the scattering species could not be undertaken, since the applied model relies on reaching the so-called Guinier plateau at low Q values, which signifies the finite volume of the scatterer.

In contrast to the **S2-F3** sample, the profiles for both the **S2-F2** and **S2-F5** sample displayed a Guinier plateau indicating a finite size of the scattering objects, accessible within the *Q*-range of the measurement.

The ratio of the scattering intensities $I(Q)_{Q\to 0}$ for the fractions connected with two different DTE photoisomers, N, describes the change in the volume of the sample as a result of UV irradiation, according to **Equation 6.1**:

$$N = \frac{I(Q)_{Q \to 0}[S2 - Fm_x - DTE]}{I(Q)_{Q \to 0}[Au_{25}(2PET)_{18}]}$$
6.1

where m = 2, 3, 5 and x-DTE corresponds to **o-DTE** or **c-DTE**.

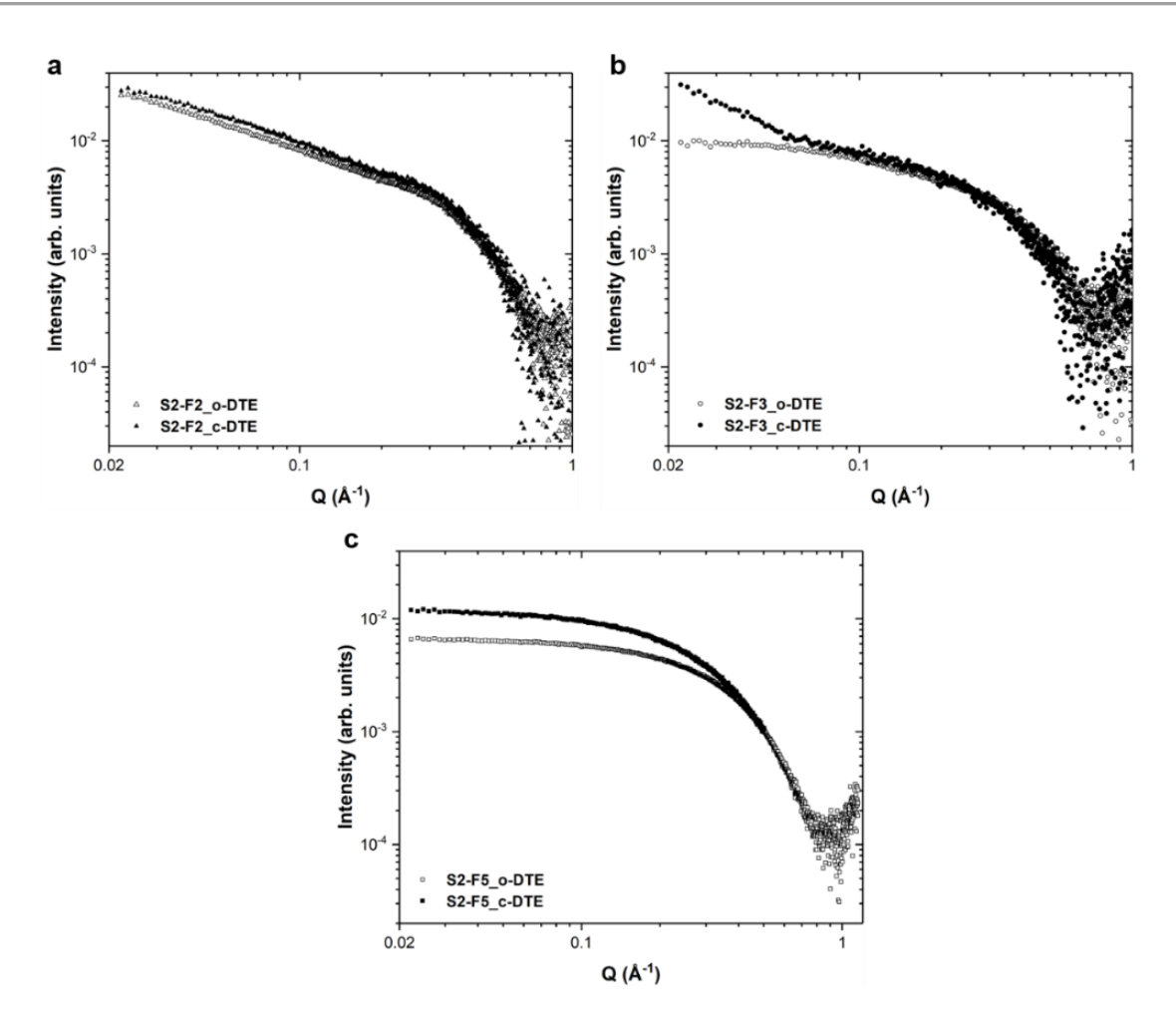


Figure 6.6 SAX scattering profiles of three different size fractions of the S2 sample (a) F2, (b)F3, and (c) F5 with o-DTE (open symbols) and c-DTE (closed symbols) photoisomers of the linker.

For the S2-F2_(c-DTE) fraction (Figure 6.6-a) the ratio N of 4.02 showed a 15 % increase in the volume of the scattering species compared to the **o-DTE** counterpart. The S2-F5 sample however exhibited a more significant 75 % increase in the volume of the c-DTE containing Au₂₅ assemblies (Figure 6.6-c). Therefore, the most significant evolution of size and/or shape was observed for the smallest Au₂₅ assemblies after switching under UV light. The summary of the experimental data for all three analysed samples after photoirradiation experiments is presented in **Table 6.1**.

Table 6.1 Qualitative analysis of the SAXS data of three different fractions of the **S2** sample containing **o-DTE** and **c-DTE** linker photoisomers.

	[Au ₂₅ (2PET) ₁₈] ⁰	S2-F2		S2-F3		S2-F5	
		o-DTE	c-DTE	o-DTE	c-DTE	o-DTE	c-DTE
$I(Q)_{Q \to 0}$	0.0072	0.0253	0.0290	0.0095	n/a	0.0071	0.0125
N	1	3.51	4.02	1.32	_	0.99	1.73

All in all, the approximation of the relative volume of the scattering species for each of the fractions of the S2 sample before and after UV irradiation revealed photoinduced size and/or shape increase of the Au_{25} assemblies.

The fitting of the SAXS data for the non-irradiated fractions of the **S2** sample was described in **Section 5.6.3.2**. For the UV irradiated **S2-F2** and **S2-F3** samples the experimental data were fit to the same model than their non-irradiated counterparts. i.e., a pearl-necklace model¹⁴ that assumed tetramers for **S2-F2**, and dimers in the case of **S2-F3** sample. The **S2-F5_c-DTE** sample, which showed an almost doubling of the scattering volume, did not converge with a dimeric pearl-necklace model, however the mixed 'sphere¹⁵ + pearl-necklace' model gave a satisfactory fit. The fitting curves for the samples in the ON state (with **c-DTE** isomer) are depicted in **Figure 6.7** as red traces. The parameters obtained from the fits of the photoirradiated samples (i.e., Au_{25} radius, R, and intercluster distance, L) are presented in **Table 6.2**.

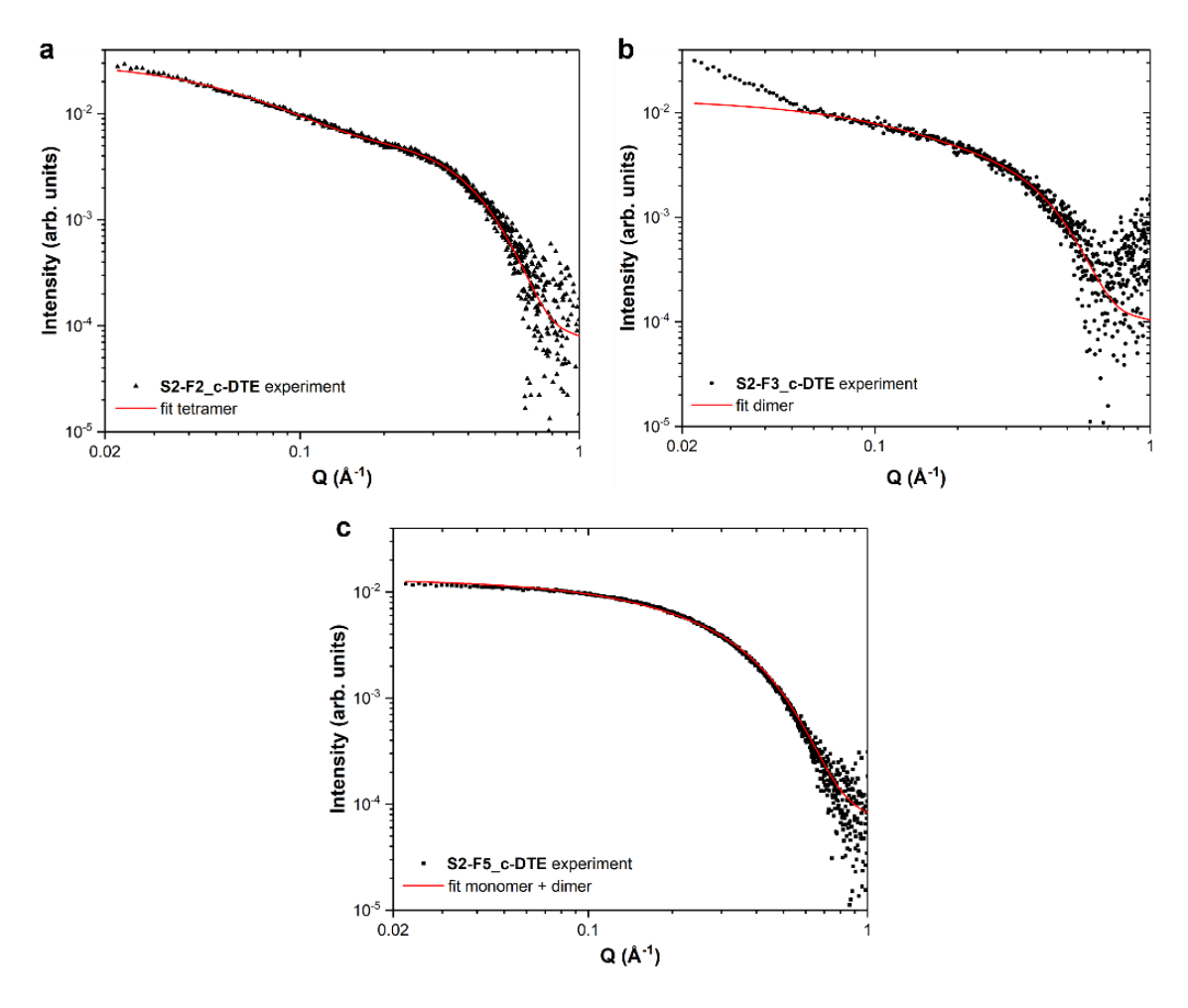


Figure 6.7 Fitting of the experimental SAXS data of the different S2 sample fractions connected with the c-DTE isomer of the linker, to the pearl-necklace model: (a) fraction F2 (n = 4); (b) fraction F3 (n = 2); and to the mixed 'sphere + pearl-necklace' model (c) fraction F5 (n = 2). Fitted curves (in red) are presented against the experimental data (black filled symbols).

The fitting for the **S2-F2** sample with the **c-DTE** linker (**Figure 6.7**-a) gave a satisfactory result up to low Q value range. However, the fit slightly underestimated the experimental data for $Q < 0.03 \text{ Å}^{-1}$. This could be explained by the presence of multimers larger than tetramers, given that the contribution of bigger species to the scattering intensity is the highest at low Q values. The applied model yielded the cluster size of 4.90 Å, in good agreement with the size of the pure $[Au_{25}(2PET)_{18}]^0$ cluster. The cluster edge-to-edge distance value (L) of 18.20 Å, which is related to the length of the DTE linker, matched very well the value of 18.04 Å obtained from the DFT calculations of Au_{25} dimers linked with a **c-DTE** photoligand (**Appendix B**).

The **S2-F3_c-DTE** sample showed an unusual scattering profile (**Figure 6.6**-b) with a sudden sharp increase in intensity around $Q \sim 0.05 \text{ Å}^{-1}$. Without any follow-up measurements, it is difficult at this stage to speculate about the possible origin of this behaviour. Therefore, the fitting for the **S2-F3_c-DTE** sample was performed using the pearl-necklace model for dimeric species in the limited range of $0.055-0.7 \text{ Å}^{-1}$. Again, the pearl-necklace model for dimers gave a reasonable outcome, with R = 5.10 Å and a lower value of the edge-to-edge distance (14.77 Å; **Table 6.2**). The **S2-F5_c-DTE** sample was fit to a mixed 'sphere + pearl necklace' model that assumed coexistence of monomers and dimers in the solution.

Table 6.2 Parameters obtained by fitting the data from SAXS measurements for UV-irradiated fractions of the **S2** sample using a pearl-necklace and a mixed 'sphere + pearl-necklace' model.

	$[Au_{25}(2PET)_{18}]^0$	S2-F2_c-DTE	S2-F3_c-DTE	S2-F5_c-DTE
Fitting model	hard sphere	pearl-necklace	pearl-necklace	sphere + pearl-necklace
Core radius, R (Å)	$R_{\rm s} = 4.55*$	$R_{\text{p-n}} = 4.90 \pm 0.01$	$R_{\rm p-n} = 5.10 \pm 0.01$	$R_{\rm s} = 4.48 \pm 0.08$ $R_{\rm p-n} = 4.82 \pm 0.18$
Edge-to-edge distance, <i>L</i> (Å)	n/a	18.20 ± 0.06	14.77 ± 0.23	13.08 ± 2.05
No. pearls (n)	n/a	4	2	2
R polydispersity	0.20 (fixed)	0.20 (fixed)	0.20 (fixed)	sphere = 0.22 (fixed) p-n = 0.24 (fixed)
L polydispersity	n/a	1.032 ± 0.016	1.691 ± 0.007	1.951 ± 0.035
<i>M/D</i> ratio from the model	n/a	n/a	n/a	1.14

^(*) very small error of 0.003

From fitting of the experimental data, the monomer-to-dimer ratio, M/D = 1.14 was obtained. This value for the S2-F5_c-DTE sample was found to decrease almost 7-fold in comparison to the value obtained for the S2-F5_o-DTE analogue (see Table 5.4). Therefore, the significant increase in the population of dimers at the expense of monomers after UV irradiation has been revealed by the SAXS data analysis. Based on the results obtained from MALDI-MS measurements (described in Section 6.2.3), it is reasonable to conclude that this phenomenon was facilitated by the DTE photoligands that were present in the ligand shell of Au₂₅ clusters as bidentate ligands (o-DTE²). It is postulated that one of the surface Au-S_{DTE} bonds was cleaved, and the as-created dangling thiolate bond became available for linking together Au₂₅ clusters. The size of the Au₂₅ clusters (R = 4.48 Å) was in good agreement with the one obtained for the other S2 fractions, however the edge-to edge distance of 13 Å was lower compared to the theoretical predictions. Note that the DFT simulations assumed a perfect dimeric system which was modelled in vacuum. In contrast, the SAXS measurements were acquired for a sample in solution, and the solvent could affect the conformation of the linker molecule, especially in a system as small as a dimer. Given the dynamic nature of Au NCs in solution, 16, 17 it is anticipated that the monomers and dimers were constantly undergoing a collision-driven disassembly and reassembly, affecting the L values obtained from fits.

6.4 Photoinduced self-assembly of Au₂₅ dimers: insight into structure and photophysical properties

As demonstrated in **Section 6.3.2**, the isolated fractions **S2-F2**, **S2-F3** and **S2-F5** exhibited structural transformation when exposed to UV irradiation. In particular, the most significant changes were observed for the sample containing the mixture of monomers and dimers. These findings motivated further exploration of the photophysical properties of the Au₂₅ assemblies and their structure-dependence. In order to gain clear insights into structure-property relationships of the Au₂₅ assemblies and how they were dictated by the photoirradition, the photophysical properties of the smaller Au₂₅ assemblies and their morphological changes induced by the photoirradiation were studied in detail. Herein, a systematic study is presented.

Herein, the investigation of the sample originated from the same synthetic batch as the three isolated fractions (**S2-Fm**; m = 2, 3, 5) analysed with the SAXS technique, is described. This sample was isolated from the size-exclusion column as fraction **F4**. Based on the SAXS analysis (**Section 5.6.3**) that identified the species in **F3** as a mixture of dimers and monomers, and **F5** as consisting mainly monomeric species, the fraction **F4** had to therefore contain mixture of monomers, $Au_{25}(2PET)_{18-x}(\mathbf{oDTE}^2)_x$ (x = 0, 1, 2, 3), and dimers. Henceforth, this sample is denoted as **S2-F4**. The **S2-F4** sample was subjected to photoswitching experiments, in a similar fashion to the other samples

described in **Section 6.2.2**. After each irradiation event, the photoluminescence properties of the sample were analysed.

6.4.1 Photoswitching of Au₂₅ dimers and mixed ligand shell Au₂₅ monomers

The photoswitching of the **S2-F4** sample dissolved in toluene (concentration of ~0.11 mg/mL, total volume 2.0 mL) was monitored with UV-vis spectrophotometry. The duration of irradiation necessary for the sample to reach a photostationary state (PSS) were significantly longer than for the free DTE photoligand described in **Section 5.4.1**, given the slower response of the sample to the same dose of light. The duration of each irradiation experiment (i.e., the half-irradiation cycle) was dictated by either the increase or the decrease of the characteristic band ~18,000 cm⁻¹ (550 nm). When, upon visual inspection, no more changes were detected, the photostationary state (PSS) was assumed. In general, the PSS for the ON state (PSS_{340}) was attained much faster than the PSS after visible light illumination (PSS_{532}).

Figure 6.8 presents the absorption spectral changes resulting from the total of 2 photoswitching cycles of the S2-F4 sample: the monitoring of the UV-activated switching ON is depicted in Figure 6.8-a, e and switching OFF in Figure 6.8-c, g. The corresponding kinetic profiles are presented in Figure 6.8-b, f and Figure 6.8-d, h for the first and second cycle, respectively. The spectrum of the nonirradiated **S2-F4** sample (black trace in **Figure 6.8**-a) displayed features typical for the [Au₂₅(SR)₁₈]⁰ species, implying that the assemblies preserved the electronic structure of their Au₂₅ cluster building unit. It is important to mention that monomeric Au₂₅ species with a mixed ligand shell can have identical electronic absorption spectrum, on the condition that newly introduced ligands do not perturb the electronic structure of the cluster in a significant way. 18-20 The first irradiation with UV light caused the three characteristic Au₂₅ bands to disappear and a broad band emerged centred around ~18,000 cm⁻¹ (550 nm; diagnostic band) ascribed to the **c-DTE** ligand. The first photoswitching process reached a 99.4 % conversion (discounting the by-product formation, data were fit to the exponential decay model) after ca. 40 minutes of irradiation (~1.24 mW) at ambient temperature (**Figure 6.8**-b). The reverse reaction, induced via visible light irradiation, took significantly longer than the switching ON reaction (~15 h, 23.7 mW; Figure 6.8-d). During the switching OFF reaction a steady decrease in the diagnostic band was observed, as expected for the ring-opening reaction. Remarkably, the [Au₂₅(SR)₁₈]⁰ absorption features observed in the spectrum of the non-irradiated S2-F4 sample (containing the openring isomer of the photoligand), could not be restored upon the 532 nm illumination. Furthermore, the absorption changes in the UV region ($\bar{\nu} > 30,300 \text{ cm}^{-1}$; $\lambda < 330 \text{ nm}$) were also ascribed to the cycloreversion reaction of the photoligand (Figure 5.3-c).

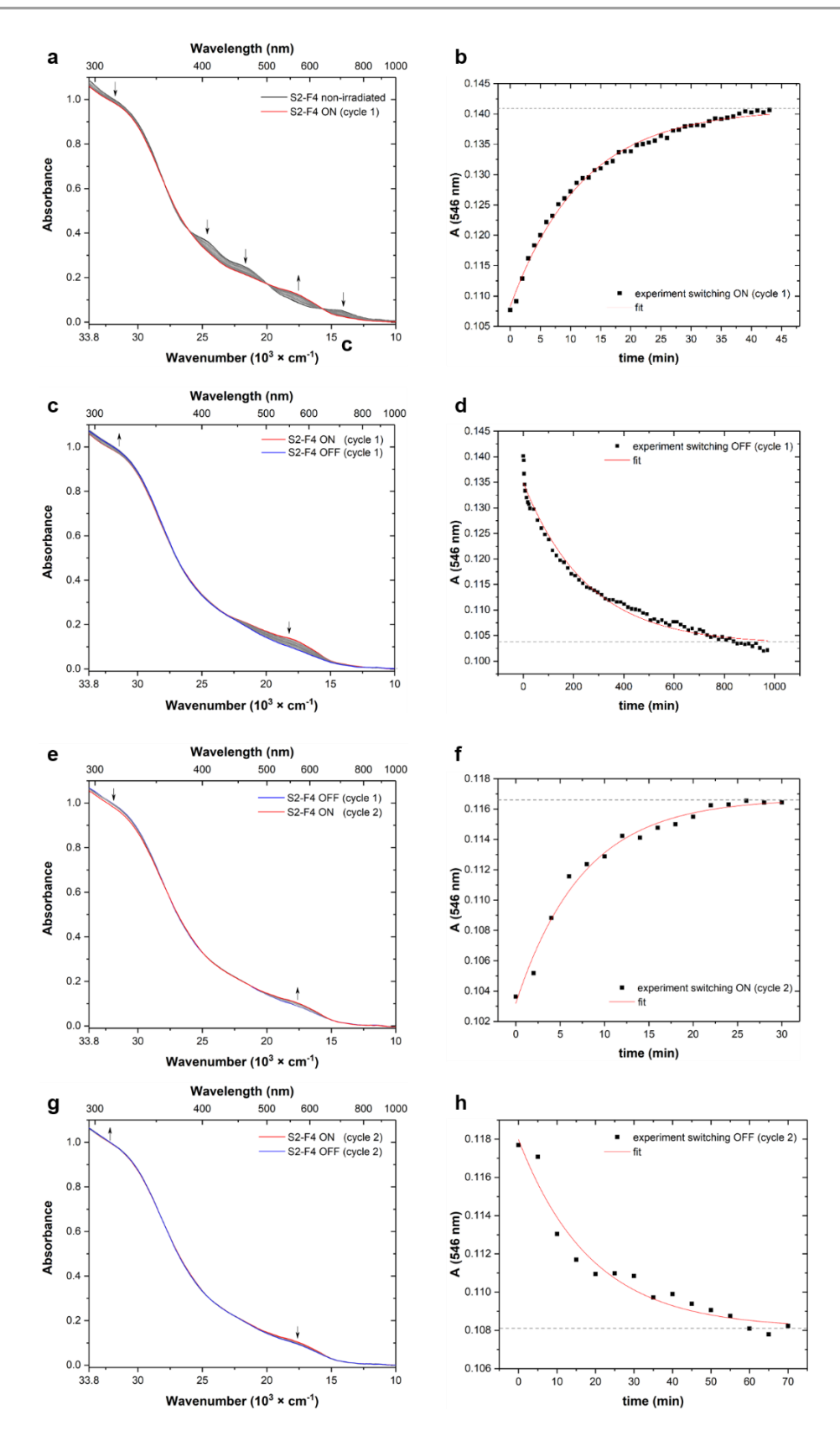


Figure 6.8 Two photoswitching cycles of the S2-F4 sample in toluene with 340 nm light (a, e) and 532 nm light (c, g) followed by absorption spectroscopy. Kinetic traces depict the changes in the diagnostic band intensity (546 nm) with the irradiation time. (b, f) 546 nm-absorbance increase upon UV irradiation leading to ON state of the DTE photoligand; (d, h) 546 nm-absorbance decrease upon visible light irradiation yielding the OFF state of the DTE photoligand. The experimental date (black squares) was fitted to the single exponential function (red traces that allowed to calculate the 100 % conversion of the one isomer into another (grey dashed lines).

These two irradiation events completed one photoswitching cycle. The subsequent second UV irradiation, presented in **Figure 6.8**-e, again showed the growth of the diagnostic band, however the extent of the photoswitching ($\Delta A_{546 nm}$) was lower. Monitoring the temporal changes of the diagnostic band absorbance (**Figure 6.8**-f) led to the estimation that the conversion from the open- to closed-ring isomer reached 99.7 % after 30 min of UV illumination, which was 30 % faster than the switching ON reaction in the first cycle. The second switching OFF with visible light (**Figure 6.8**-g) caused, as expected, disappearance of the ~18,000 cm⁻¹ (550 nm) band. Owing to a significantly lower switching ON performance in the second cycle, the 532 nm illumination experiment required only 70 min to reach a photostationary state (PSS_{532}), which corresponded to ca. $1/16^{th}$ of the time required to reach a PSS_{532} after the first cycle.

The observed spectral changes across all irradiation events suggest that, next to the photoswitching of the central DTE moiety embedded in the linker molecule, structural transformations of the species took place as evidenced by the difference in their electronic structure. These changes pertained to the switching of the DTE linker functionality but were reversible to a certain degree. Indeed, the original electronic structure exhibited by the non-irradiated assemblies could not be restored once light irradiation was applied to the sample. Notably, the most significant changes occurred after the first irradiation with the visible light. Identical photofatigue behaviour was seen for pure DTE(SH) ligand in solution. Moreover, the control irradiation experiments of a toluene solution of pure [Au₂₅(SR)₁₈]⁰ clusters (Figure A.11 Appendix A) confirmed the stability of the single clusters to prolonged 532 nm-irradiation (17 h, 23.7 mW). It is hence reasoned that the DTE-Au₂₅ assemblies demonstrate photofatigue behaviour that is ascribed to the DTE linker moiety. An alternative explanation could also be offered that ascribes the observed behaviour to the formation of larger assemblies during photoirradiation. Indeed, Ho-Wu et al. reported that multimeric Au₂₅ assemblies exhibited both higher absorption coefficients and hypsochromic shifts of their absorption bands with growing size. 12 This hypothesis however requires further corroboration and insights from a theoretical study of the electronic structure of the Au₂₅ assemblies.

6.4.2 Photoluminescent properties of the Au₂₅ assemblies linked with DTE ligand

6.4.2.1 Steady-state photoluminescence

In **Section 6.2.4**. the photoluminescent properties of various Au₂₅ assemblies were shown to depend on their size. Herein, the evolution of the photoluminescence with the photoirradiation of the sample is systematically investigated.

Figure 6.9 depicts the photoluminescence (PL) emission spectra of the **S2-F4** sample after four irradiation events (i.e., 2 full ON/OFF cycles). Spectra have been acquired in toluene in a right-angle geometry at the 440 nm excitation wavelength with bandpass slits of 3 nm. Long-pass filter (610 nm) was placed at the emission collection side. All spectra were corrected for absorbance. The emission spectra were found to be excitation wavelength independent. The quantum efficiency relative to Rhodamine 6G was calculated according to the **Equation 3.1**. Sample solutions were analysed immediately after each irradiation experiment.

Evidently, the photoluminescence emission intensities/photoluminescence quantum yields (Φ_{PL}) varied widely. All analysed samples displayed a broad band shapes (FWHM ~3500 cm⁻¹) and emitted over the same range of energies, from ~ 16,000 cm⁻¹ (620 nm) to ~7,500 cm⁻¹ (1300 nm). For comparison, the spectrum of pure [Au₂₅(2PET)₁₈]⁰ (grey trace) showed a very weak emission intensity signal ($\Phi_{PL} = 0.15$ %, **Figure 6.9**-c), in accordance with the reports of other groups.²¹

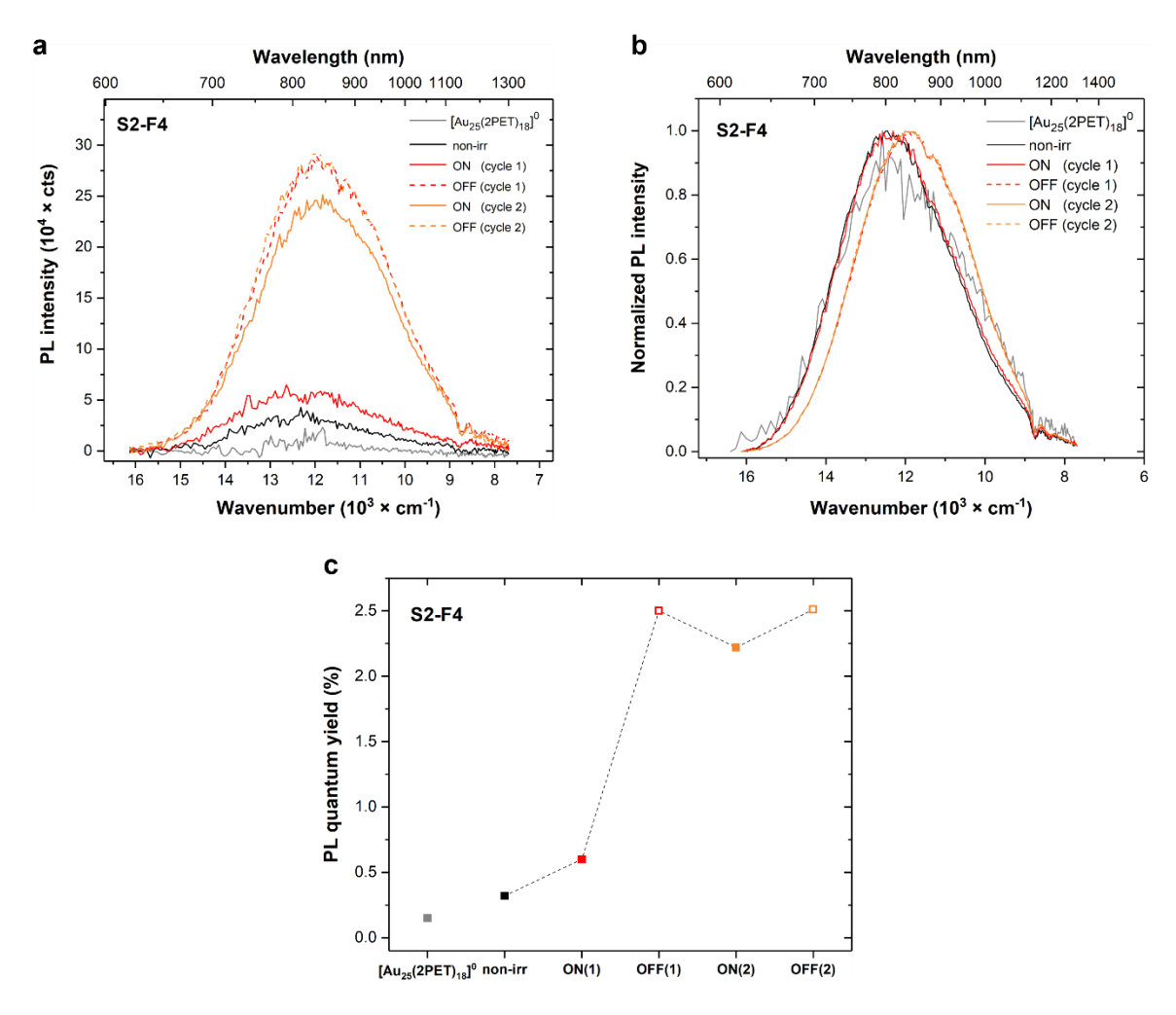


Figure 6.9 (a, b) Steady-state photoluminescence spectra of the S2-F4 sample measured in non-irradiated state (black trace), after first irradiation cycle (red traces, solid for 340 nm and dashed for 532 nm irradiation) and after second irradiation cycle (orange traces). Solid lines correspond to the PL emission measured after 340 nm irradiation and the dashed lines-after 532 nm irradiation. (c) Change in the PL quantum yields evolving with photoirradiation. Φ_{PL} of $[Au_{25}(2PET)_{18}]^0$ cluster is shown for comparison. Spectra acquired after 440 nm excitation, in toluene solution at 293 K.

The non-irradiated **S2-F4** sample exhibited more intense emission ($\Phi_{PL} = 0.32$ %) than the pure $[\mathrm{Au}_{25}(\mathrm{2PET})_{18}]^0$ cluster in the visible to near-infrared (NIR) region with the emission peak centred around 12,500 cm⁻¹ (800 nm) at 293 K. The first photoswitching induced significant changes in the PL emission behaviour of the **S2-F4** sample, leading to a two-fold increase in PL intensity ($\Phi_{PL} = 0.60$ %) after the first irradiation with UV light (40 min, ~1.24 mW). Interestingly, switching the sample OFF using the 532 nm light led to a 4-fold increase in emission intensity (red dashed trace, $\Phi_{PL} = 2.50$ %). The second 340 nm irradiation caused a slight decrease in the emission signal (solid orange line, $\Phi_{PL} = 2.22$ %) that was restored to the highest observed value with the second 532 nm-irradiation (dashed orange line, $\Phi_{PL} = 2.51$ %).

Furthermore, after one full irradiation cycle a highly emissive species emerged that exhibited a PL band at $11,905 \text{ cm}^{-1}$ (840 nm) with a batochromic shift of 590 cm^{-1} (**Figure 6.9**-b). This behaviour is consistent with the observations by Wang et al. for Au₂₅(2PET)₁₈ upon introduction of new ligands to the ligand shell.^{22, 23} It needs to be said, that the origin of photoluminescence in metal nanoclusters is still not well-understood. It is postulated that it may originate from the nanocluster core, as research shows that diminishing the size of the metal kernel results in significant enhancement of Φ_{PL} .²⁴ A second theory attributes the photoluminescence to the ligand effect. Numerous reports reveal a strong PL emission dependency on the protective ligand.²⁵ Specifically, the PL intensity was shown to scale with the electron donating capacity of the protective ligands.²¹ Moreover, Au NCs with mixed ligand shells exhibited stronger photoluminescence than their analogues protected with a monolayer containing only one type of ligand.²⁶ In the case of **S2-F4** sample, it is most reasonable to conclude that the observed PL originated from the Au₂₅ species as the **o-DTE** ligand shows no emission (**Appendix A, Figure A.12**).

Additionally, the broadening of the emission band was observed for the highly emissive species (**Figure 6.9**-b). More experiments are required to explain the origin of this behaviour. It is however consistent with the formation of larger assemblies during the photoirradiation. It is anticipated that the nanocluster oligomers would exhibit lowering of the HOMO–LUMO gap as their size increases, in analogy to organic polymers with the extended π -conjugation. ^{13, 27}

Further insights into the nature of the emissive species in the **S2-F4** sample was provided by the PL excitation (PLE) study. The PLE spectra were acquired in the 320–850 nm region using an emission wavelength of 950 nm (the highest photon count) and were corrected for the inner filter effect according to the procedure reported by Larsson et al.²⁸ **Figure 6.10** depicts the excitation spectra (red traces) with the corresponding absorption and emission spectra (black and blue traces, respectively) of the **S2-F4** sample after various photoswitching experiments. Noticeably, the shape the of the PLE spectra differed significantly from the corresponding absorption spectra for the **S2-F4** sample in all five irradiation states: non-irradiated, ON(1), OFF(1), ON(2), and OFF(2). The major divergence was observed between the absorption and PLE spectra of the non-irradiated **S2-F4** sample. Specifically, the

pronounced absorption features at 25,000; 22,727 and 14,750 cm⁻¹ (400, 440 and 680 nm, respectively) were not present in the PLE spectra (**Figure 6.10**-a).

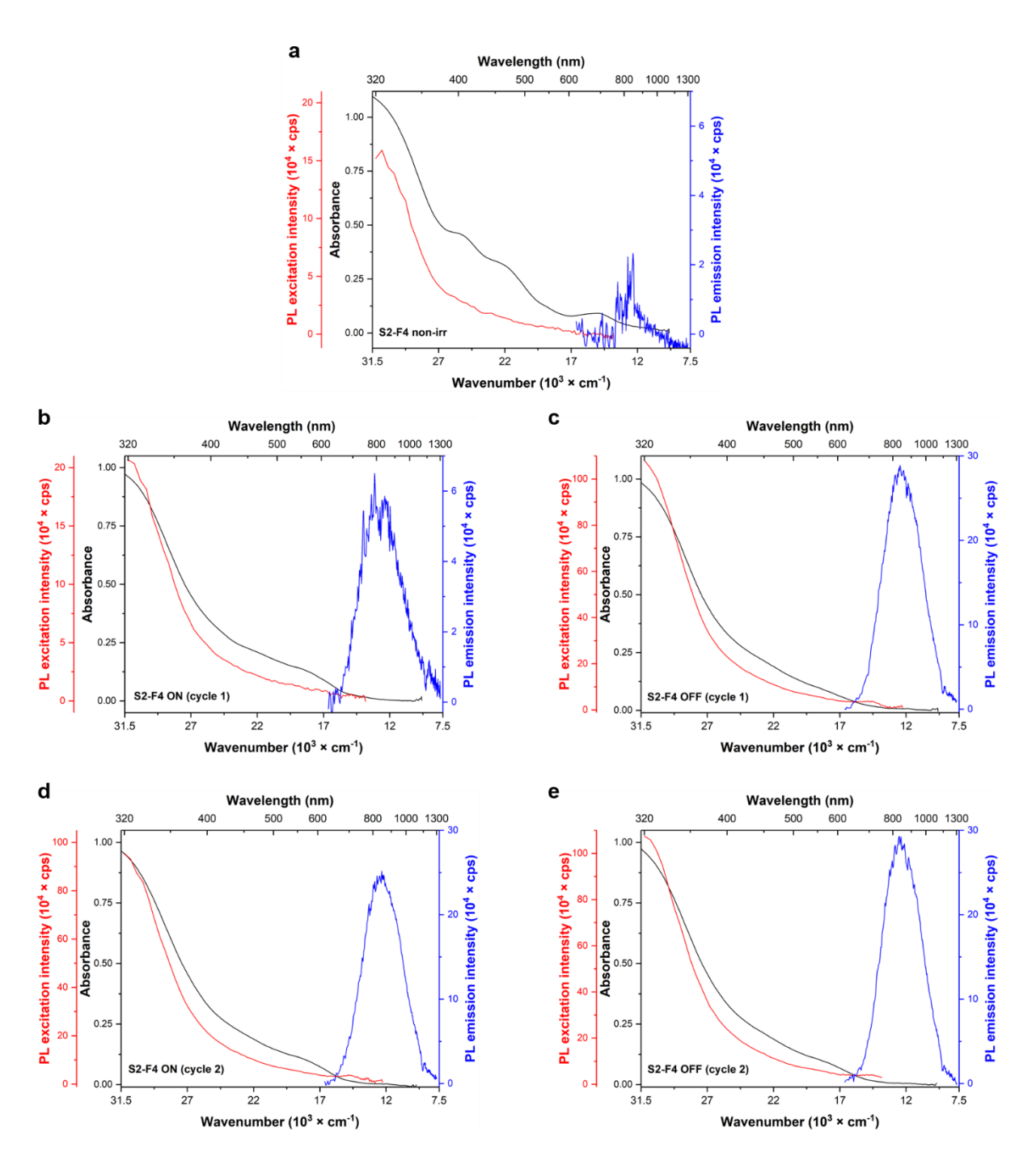


Figure 6.10 PL excitation (PLE) spectra (red) taken 320–850 nm with $\lambda_{em} = 950$ nm, PL emission spectra (blue) with $\lambda_{exc} = 440$ nm. Samples in toluene at 293 K and corresponding absorption spectra (black) of S2-F4 sample in different irradiation states: (a) non-irradiated; (b) after 40 min of 340 nm irradiation (cycle 1)-switching ON; (c) after 15 h of 532 nm irradiation (cycle 1)-switching OFF; (d) after 30 min of 340 nm irradiation (cycle 2)-switching ON and (e) after 70 min of 532 nm irradiation (cycle 2)-switching OFF. PLE spectra were corrected for the inner-filter effect, PL emission spectra were corrected for the absorption at the excitation wavelength.

Markedly, a new band around 14,500 cm⁻¹ (690 nm) emerged after illuminating the sample with 532 nm light. This feature was persistent in the spectra of ON(2) and OFF(2) samples (**Figure 6.10**-d,e) and its appearance was accompanied by the red-shift and increase of PL emission intensity.

Since PL excitation is a photoluminescence detected absorption, the difference between the two spectra supports the conclusion that only a subpopulation of the light-absorbing species relaxed via photoluminescence. Interestingly, the population of PL emissive species was found to have evolved further after the first full irradiation cycle, as manifested by the appearance of a 14,500 cm⁻¹ (690 nm) band in the PLE spectra of OFF(1), ON(2) and (OFF 2) samples.

As was previously observed in Figure 6.9, Figure 6.10 (blue curves) also shows the significant enhancement of PL in the photoirradiated Au₂₅ assemblies. One of the reasons for increased photoluminescence in Au NCs is the diminishing size of the Au core.²⁹ This possibility is excluded here as the SAXS data showed that upon irradiation the size of the species increased (more specifically, the ratio of dimers over monomers: M/D ratio). Moreover, during the SAXS measurements, as well as irradiation experiments, no decomposition of the sample was observed, which would have been a tell-tale sign of the NCs size transformation to lower nuclearity gold species. It is therefore reasonable to argue that stronger PL emission in the non-irradiated Au₂₅ assemblies could originate from the modified ligand shell in the Au₂₅ units. Indeed, the MALDI-MS analysis confirmed the presence of Au₂₅ species with mixed ligand shells (2PET and o-DTE²). The further enhancement of the PL emission after photoirradiation can be attributed to a rigidified ligand shell after a cross-linking reaction, as was proposed in **Scheme 6.1**. This is in accordance with the report by Pyo et al. demonstrating the significant increase in the PL of the Au NCs after reducing the flexibility of its ligand shell with bulky cations.³⁰ Lastly, changes in the electronic structure of the formed assemblies as a contributing factor to the photoluminescence should be considered. Indeed, a theoretical investigation into the structure and stability of a model system of Au₂₅ dimers connected with the DTE linker shows the presence of a triplet ground state lying quite close in energy to the singlet ground state. Based on this result, it can be speculated that both singlet and triplet states could contribute to the PL signal (see **Appendix B**).

6.4.2.2 Time-resolved photoluminescence

In order to obtain more information about the complex nature of the photoluminescent species in the **S2-F4** sample the emission time dependence was measured at ambient temperature by time-correlated single photon detection (details in **Section 3.2.4**). The photoluminescence decays were recorded for the sample in two states: non-irradiated and OFF(2), as well as for pure [Au₂₅(2PET)₁₈]⁰ cluster. As presented in **Figure 6.11**, the three samples displayed different photoluminescence decay behaviour. First, both the non-irradiated (black trace) and photo-irradiated (blue trace) **S2-F4** samples exhibited a multiexponential decay. This could be explained by the existence of multiple different chemical

species in the solution contributing to the PL emission of the S2-F4 sample. Secondly, the photoluminescent population underwent changes upon the photoswitching experiments as evidenced by the altered time dependence of the emission decay (blue trace). In the case of photoirradiated S2-F4 sample, the PL signal decayed much slower which could be explained by the generation of species with longer emission due to structural rearrangement within the Au_{25} assemblies induced by the photoirradiation. Given that the PL lifetimes are a reciprocal sum of the radiative (k_r) and non-radiative (k_{nr}) decay rates (Equation 6.2):

$$\tau_{PL} = \frac{1}{k_{rad} + k_{non-rad}}$$
 6.2

it is reasonable to argue that the increased rigidity of the Au₂₅ assemblies caused by a higher degree of cross linking would contribute to diminishing of the number on non-radiative relaxation channels, thus increasing the PL emission lifetime.³¹ Remarkably, the shape of the PL decay for the pure [Au₂₅(2PET)₁₈]⁰ clusters also suggests that multiple processes with different time scales contribute to the PL emission—revealing the complex photophysical nature of single Au₂₅ clusters. So far, no comprehensive study exists in the literature that addresses this aspect, which requires its own independent investigation. Hence, only qualitative description of the time range of the emissive events in the S2-F4 sample could be provided, with more in-depth analysis being out of scope of the present work.

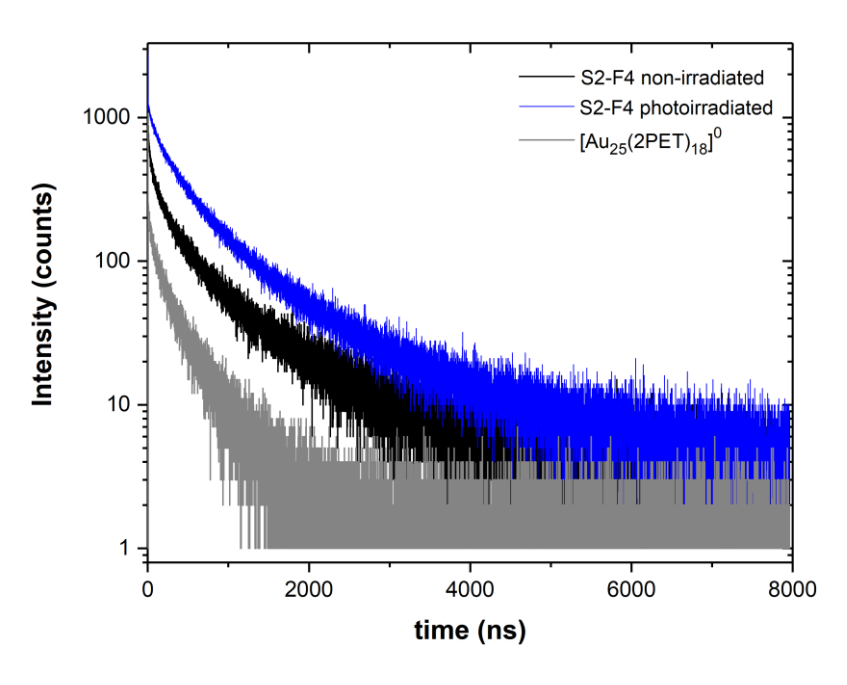


Figure 6.11 Time-resolved photoluminescence decay profiles of the S2-F4 non-irradiated sample (black), S2-F4 photoirradiated after 2 cycles (blue) and $[Au_{25}(2PET)_{18}]^0$ (grey) in toluene solution. The samples were excited at $\lambda_{exc} = 635$ nm and the decay profiles were measured at 800, 839 and 750 nm, respectively, at 298 K.

6.4.3 Characterization of the photoinduced structural changes in small Au₂₅ assemblies

6.4.3.1 High-resolution transmission electron microscopy (HR-TEM)

Investigations of the morphology changes of the Au₂₅ assemblies after photoirradiation were performed with high-resolution transition electron microscopy (HRTEM). Samples for TEM analysis were prepared by drop-casting a freshly prepared solution of either non-irradiated or irradiated S2-F4 sample (after two ON/OFF switching cycles) in a toluene:dichloromethane solution (4:1, vol/vol) on a carbon-coated copper TEM grid. Samples were then allowed to air-dry overnight prior to imaging. The electron micrographs of both S2-F4 samples showed a uniform size distribution with an average size of ~1.5 nm, which corresponded well to the size of $[Au_{25}(2PET)_{18}]^0$ reported in the literature.³² Moreover, the comparable morphologies of the two S2-F4 samples (Figure 6.12-a, b) suggested that Au_{25} assemblies did not undergo a decomposition after photoirradiation experiments. Importantly, the TEM images of monomeric $[Au_{25}(2PET)_{18}]^0$ clusters (Figure A.13, Appendix A) revealed that their average size (~2.5 nm) was larger than the value of obtained from the single X-ray analysis, implying that clusters coalesced after the electron beam irradiation. Since, no aggregation was observed for the S2-F4 samples, it was postulated that the linked Au_{25} assemblies were less prone to aggregation under the e-beam.

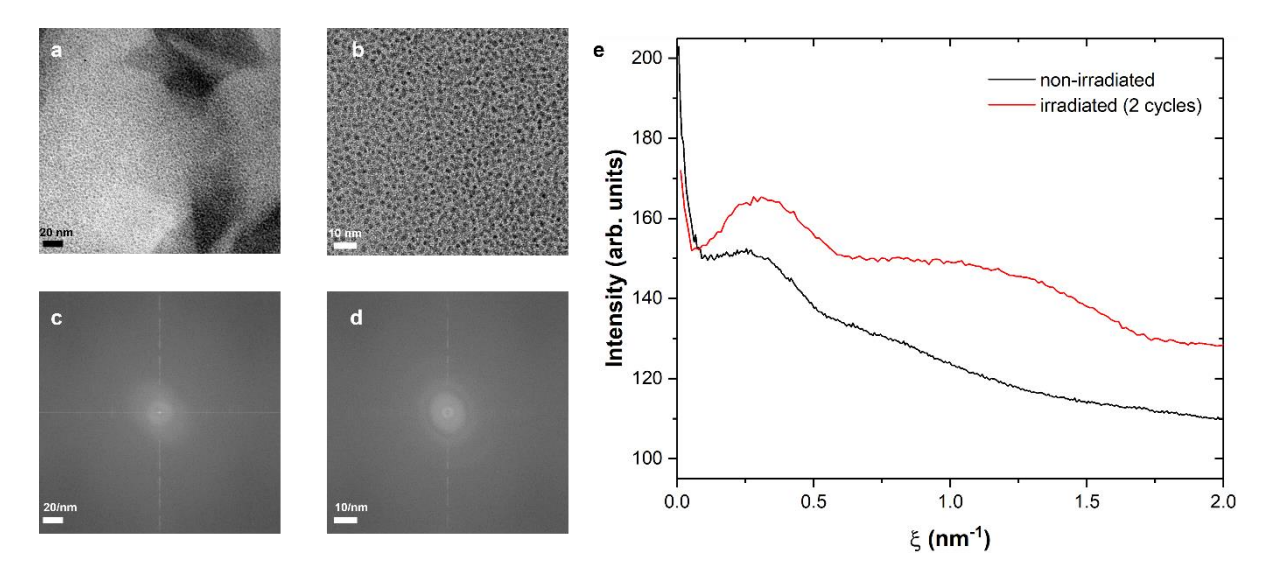


Figure 6.12 HRTEM characterization of the Au₂₅ assemblies before and after photoirradiation. Images of a sample containing a mixture of Au₂₅ monomers and dimers (a) non-irradiated and (b) irradiated after two ON/OFF switching cycles. The scale bar is (a) 20 nm and (b) 10 nm. (c) and (d) depict the fast Fourier transform (FFT) of the (a) and (b) TEM images, respectively. (e) Amplitude of the spatial frequency obtained from the FFT analysis of image of non-irradiated sample (black trace) and irradiated sample (red trace).

The analysis of the microtexture of the Au_{25} assemblies was provided by TEM image processing technique.³³ The fast Fourier transforms (FFTs) of the images, performed with ImageJ (1.53E) software,³⁴ allowed to estimate the average distance between the nanoclusters.

The integrated radial profiles of the FFTs of the **S2-F4** sample TEM images (**Figure 6.12**-c, d) produced amplitude plots as a function of the spatial frequency, ξ , which quantified the periodicity of the features (here, Au₂₅ clusters) observed by TEM (**Figure 6.12**-e). The peaks at approximately $\xi = 0.3 \text{ nm}^{-1}$ corresponded to a distance between the centre of the features of ~3.3 nm and were assigned to the distance between the Au₂₅ clusters. A small change could be observed between the non-irradiated sample and the sample after two irradiation cycles, where the intensity peak maximum was seen at $\xi = 0.248 \text{ nm}^{-1}$ and $\xi = 0.307 \text{ nm}^{-1}$, respectively, corresponding to distances of 4.03 nm and 3.25 nm. This result provided additional evidence for the light induced reorganization of Au₂₅ assemblies, which caused the formation of more tightly bound network of Au₂₅ clusters.

6.4.3.2 Small angle X-ray scattering (SAXS)

The unexpected rise in the photoluminescence intensity/quantum yield observed after irradiating the Au_{25} assemblies with UV and visible light motivated the further exploration of the possible origins of the electronic changes in the photoirradiated samples. It has been shown earlier (**Section 6.3.2**) that upon UV irradiation the population of dimers increased in the fraction containing the smallest Au_{25} assemblies. To corroborate whether this phenomenon persisted when sample was subsequently irradiated with visible light, the SAXS analysis was employed. In this study, the investigation was continued with a new sample containing the mixture of monomers and dimers, herein denoted as **S3**.

The **S3** sample was produced in the non-irradiated, UV-irradiated (ON) and vis-irradiated (OFF) states see **Figure A.16**-b. These samples were then analysed with SAXS to investigate the structural changes that occur due to UV and vis light irradiation. Already, in case of the **S2** sample, it was demonstrated that UV-irradiation induced structural changes to the Au₂₅ assemblies, as the ratio of larger assemblies increased within the sample. The observed upsurge in the PL emission intensity for the sample irradiated with visible light (**S2-F4**), sparked interest in pursuing structural characterization of the sample after a full photoswitching cycle. The characterization of the **S3** sample and the photoirradiation experiments are described in **Section A.8** (**Appendix A**).

The SAXS profiles of the non-irradiated, UV-irradiated, and vis-irradiated samples are presented in **Figure 6.13**.

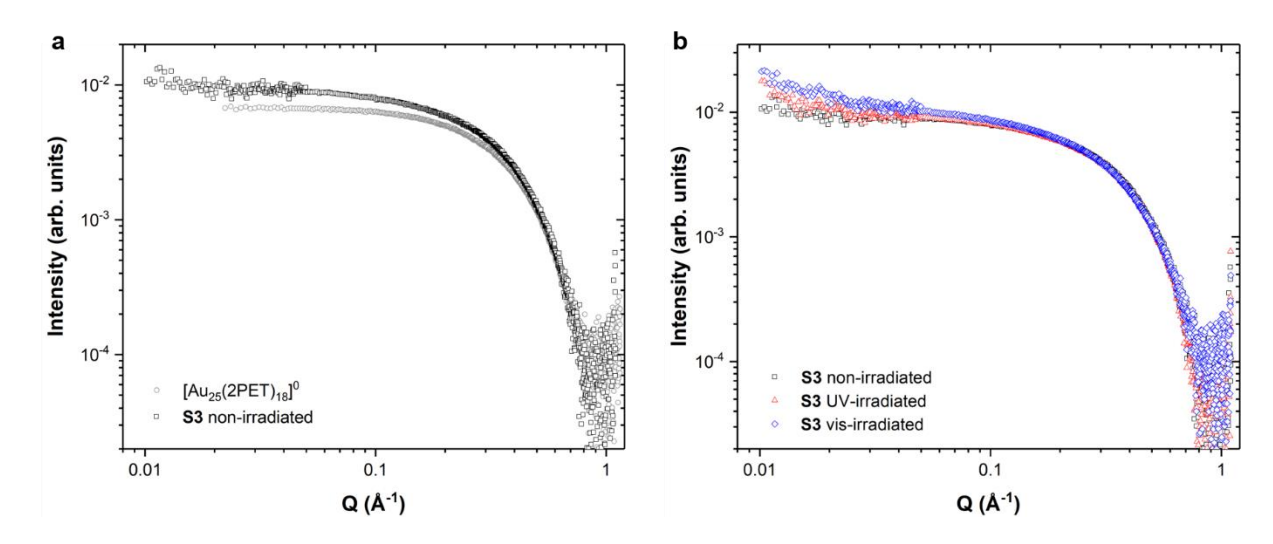


Figure 6.13 Comparison of SAXS profiles of (a) non-irradiated S3 sample (squares) with pure [Au₂₅(2PET)₁₈]⁰ cluster (circles); (b) S3 sample in three different irradiation states: non-irradiated (black squares), UV-irradiated (red triangles) and vis-irradiated (blue diamonds).

The scattering profile of the non-irradiated **S3** sample exhibited higher intensity than that of a pure $[Au_{25}(2PET)_{18}]^0$ cluster. According to the SAXS results depicted in **Figure 6.13**-a, the non-irradiated **S3** sample closely resembled monomeric species, however the scattering intensity at low Q values indicated presence of larger species. Indeed, the N value $(N = \frac{I(Q)_{Q \to 0}[S3 \ non-irradiated]}{I(Q)_{Q \to 0}[Au_{25}(2PET)_{18}]})$ of 1.34 supported this observation. The scattering profiles of the **S3** sample in all three irradiation states, presented in **Figure 6.13**-b, showed that the scattering intensity, $I(Q)_{Q \to 0}$, increased with the number of irradiation events. The qualitative analysis, presented in **Table 6.3**, was based on small but noticeable differences in the scattering intensities at $I(Q)_{Q \to 0}$. A steady increase in the volume of scatterers, from 1.34 to 1.70 for the vis-irradiated **S3** sample, has been observed.

Table 6.3 Qualitative analysis of the SAXS data of the S3 sample in three different irradiation states.

	$[Au_{25}(2PET)_{18}]^0$	S3 non-irr	S3 UV-irr	S3 vis-irr
$I(Q)_{Q o 0}$	0.0066	0.0097	0.0108	0.0123
N	1	1.34	1.50	1.70

Since the N values for all S3 samples fell between one and two, it was reasonable to assume that the sample was composed of mainly monomers and dimers. Even though the scattering profiles of the three S3 samples closely resembled that of monomeric Au_{25} species, fitting of the data to the sphere model did not converge. In view of the above, the mixed 'sphere + pearl-necklace' model (for dimers) was employed, and it was shown to fit the data properly.

The experimental data for all three samples was fitted within the range of $0.027-0.7 \text{ Å}^{-1}$. The obtained fits are presented in **Figure 6.14** and showed reasonable agreement with the experimental data. The noise

in the data at low Q was partially ascribed to the background subtraction and was therefore not included in the fits. The obtained parameters describing the size and shape of the assemblies in all three S3 samples are presented in Table 6.4.

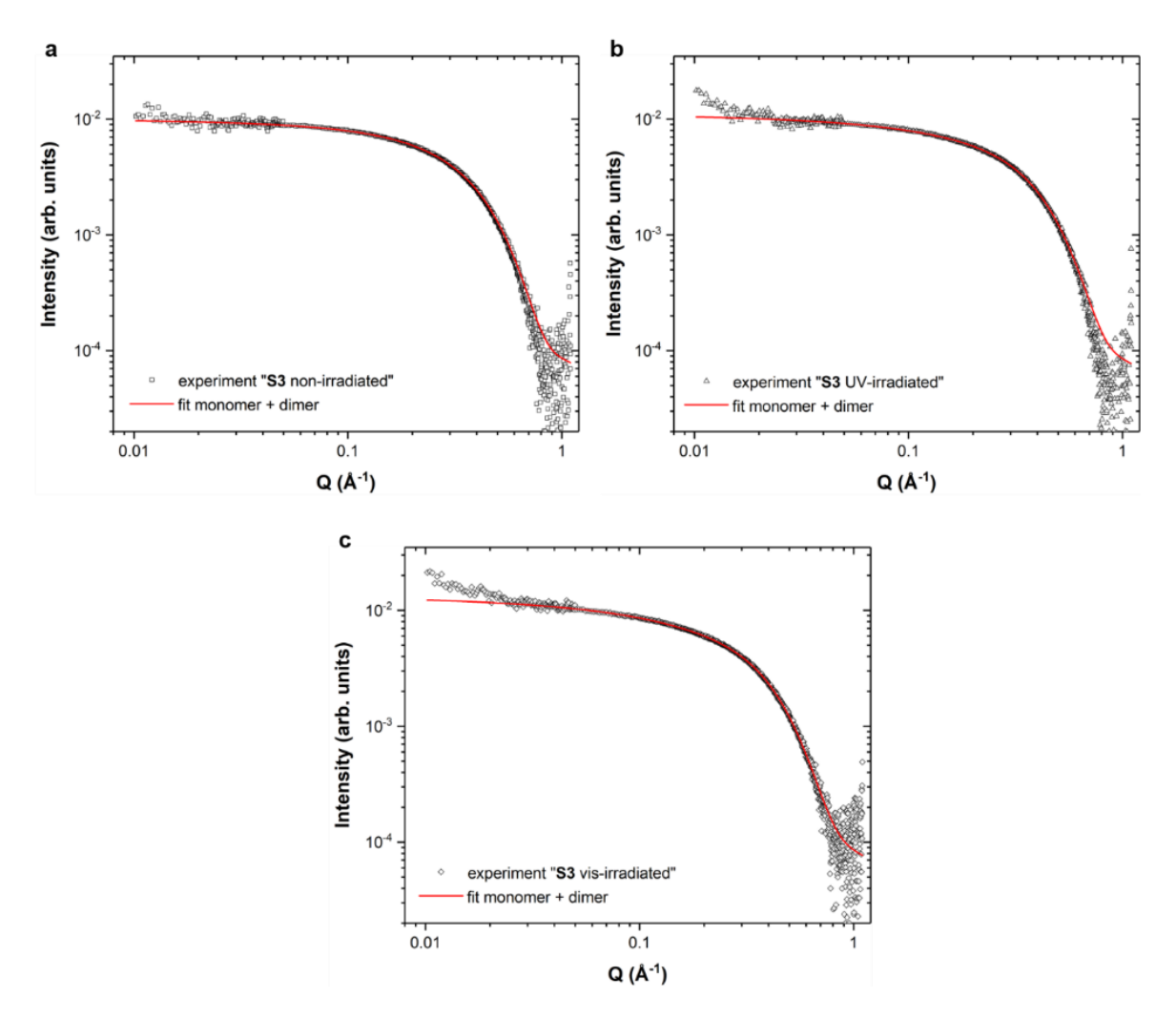


Figure 6.14 Fit to the experimental SAXS data of the S3 sample in three different irradiation states. Fitted curves (in red) presented against the experimental data (black open symbols).

The radius for the Au₂₅ clusters, R, was fixed at ~4.5 Å when fitting the SAXS data of each S3 sample, as this was the SAXS-fitted value obtained for the monomeric $[Au_{25}(2PET)_{18}]^0$ clusters (Table 5.4). The value of the intercluster distance, L, did not vary much for S3 sample in all irradiation states and was in good agreement with the DFT calculations (Appendix B). The lowest value of 18.29 Å was obtained for the UV-irradiated sample, and the value for non-irradiated and vis-irradiated sample was 19.90 and 18.99 Å, respectively. This result was in agreement with the anticipated structural changes for the switchable linker upon photoirradiation. Indeed, a small contraction of the terminal sulfur-to-sulfur distance, as a result of the cyclization of the central DTE moiety, was revealed by the DFT calculations. The increase in the linker length for the vis-irradiated S3 sample was an indication of the ring-opening reaction.

Table 6.4 Parameters for the S3 sample in different irradiation states obtained from fitting SAXS data to a mixed 'sphere + pearl-necklace' model.

	$[Au_{25}(2PET)_{18}]^0$	S3 non-irr	S3 UV-irr	S3 vis-irr
Model	hard sphere	sphere +	sphere +	sphere +
		pearl-necklace	pearl-necklace	pearl-necklace
Core radius (R)	4.553 ± 0.003	4.55 (fixed)	4.55 (fixed)	4.52 (fixed)
Edge-to-edge distance (L)	n/a	19.903 ± 3.499	18.291 ± 1.316	18.992 ± 0.800
No of pearls (n)	n/a	2	2	2
R polydispersity	0.20 (fixed)	0.20 (fixed)	0.21 (fixed)	0.22 (fixed)
L polydispersity	n/a	1.8908±0.0079	1.9728 ±0.0001	1.9725 ±
$I(Q)_{Q o 0}$	0.0066	0.0097	0.0108	0.0123
M/D ratio from the model	n/a	2.50	1.56	0.67

Furthermore, the fitting of the SAXS data yielded the ratio of monomeric to dimeric species in the solution (M/D ratio, **Table 6.4**). A notable decrease in the M/D ratio from 2.50 for the non-irradiated sample, to 1.56 for the UV-irradiated and finally to 0.67 for the vis-irradiated sample was observed. In other words, an overall four-fold increase in dimers relative to monomers has been induced by one photoswitching cycle. These structural changes could explain the increase in the photoluminescence intensity for the samples after ON/OFF switching experiment, as the dimers are expected to have decreased non-radiative relaxation channels compared to monomeric $[Au_{25}(2PET)_{18}]^0$ clusters.

6.4.3.3 Diffusion-ordered NMR spectroscopy (DOSY)

Diffusion-ordered NMR spectroscopy was employed to further ascertain the possible structural changes of Au_{25} assemblies after the irradiation experiments. Given that the diffusion of species in solution depends on their size and shape, the quantification of the diffusion coefficient, D, inversely related to size, could provide valuable insights into the size of the irradiated Au_{25} species in comparison to the non-irradiated ones. The D values obtained from DOSY NMR measurements are shown in **Table 6.5**.

Table 6.5 Diffusion coefficient values of the S3 sample in different irradiation states obtained from DOSY NMR measurements.

	[Au ₂₅ (2PET) ₁₈] ⁰	S3	S3	S3
	[Au25(2PE1)18]	non-irradiated	UV-irradiated	vis-irradiated
Diffusion coefficient,	7.80×10^{-10}	9.14×10^{-10}	1.02×10^{-9}	5.85×10^{-10}
$D (m^2 s^{-1})$	7.80 × 10 ···			

The value of the diffusion coefficient, D, obtained for the monomeric $[Au_{25}(2PET)_{18}]^0$ clusters in dichloromethane was 7.80×10^{-10} m² s⁻¹ which gave the diameter of nanoclusters, d = 1.28 nm, when plugged into Stokes–Einstein relation (**Equation 6.3**):

$$D = \frac{k_B T}{6\pi \eta r} \tag{6.3}$$

where k_B is Boltzmann constant $(1.381 \times 10^{-23} \text{ m}^2 \cdot \text{kg} \cdot \text{s}^{-2} \cdot \text{K}^{-1})$; T is temperature (293 K); η is the viscosity (0.43 mPa·s for CH₂Cl₂- d_2), and r is the particle hydrodynamic radius. This value was lower than the value of 1.7 nm reported for $[\text{Au}_{25}(2\text{PET})_{18}]^0$ clusters in CHCl₃ solution at 298 K.³⁵ However, the diffusion coefficients of particles in solution depend strongly on the effective size and shape under the given conditions (temperature, solvent).³⁶ Even though a single crystal structure of $[\text{Au}_{25}(2\text{PET})_{18}]^0$ revealed an average cluster diameter of 1.9 nm³⁷, it was found that the flexible ligand monolayer undergoes some degree of folding, which is more pronounced in solution than in the solid state, yielding a smaller nanocluster diameter.³⁸

For the non-irradiated **S3** species, the diffusion coefficient ($D = 9.14 \times 10^{-10} \text{ m}^2 \text{ s}^{-1}$) was found to be ~1.2 higher than for pure $[\text{Au}_{25}(2\text{PET})_{18}]^0$ species. Plugging this obtained diffusivity into the Stokes-Einstein equation would yield a d value that was smaller than for the pure $[\text{Au}_{25}(2\text{PET})_{18}]^0$ clusters. However, **Equation 6.3** is valid only for spherical (or nearly spherical) particles. Since the Au_{25} dimers and higher assemblies are expected to have more elongated (boomerang like) shape, this relation cannot be used for estimating the size of Au_{25} assemblies. Moreover, the analysed **S3** samples were not uniformly dispersed, i.e., they contained the mixture of monomers with mixed ligand shell and dimers. Hence the obtained D value was averaged over all species that existed in the solution. Therefore, the extracted D values for the **S3** sample after different irradiation stages provided only qualitative evidence of the size of the Au_{25} assemblies.

Despite this, the diffusion coefficient for the UV-irradiated S3 sample increased to 1.02×10^{-9} m² s⁻¹, indicating that the species were diffusing faster in solution. Interestingly, for the sample irradiated with visible light the diffusion coefficient was found to decrease even below the value found for the non-irradiated species (5.85×10^{-10} m² s⁻¹). This lower value may signify that the translational motion of the sample after one switching cycle was reduced with respect to the non-irradiated species containing the photoligand in the OFF state. This observed trend in diffusion coefficients is coherent with theoretical findings of Hammouda for a dumbbell model (i.e., two beads connected with a linker) wherein the linker rigidity affected the diffusion behaviour of the molecule in solution.³⁹ More specifically, the flexibility of the linker dictated how the whole structure responded to collisions in the solution. The enhanced flexibility of the linker ensured that the whole structure could bend and, in this way, absorb the collision energy, whereas for the more rigid molecule this energy was converted into translational motion.

6.5 Conclusions

Herein, the reversible photoswitching of different size Au₂₅ assemblies (higher aggregates, tetramers, dimers) connected with a photoswitchable DTE linker was demonstrated for the first time. This process could be observed for several ON/OFF cycles when monitoring with UV-vis spectroscopy. During the cycling experiments signs of photofatigue were observed in all Au₂₅ assemblies. Even though it was shown by Pijper et al. that the irreversible by-product formation could be prevented when DTE molecules were assembled in a monolayer on gold surfaces¹⁰ the results presented herein suggest that this does not hold for DTE-linked Au₂₅ assemblies. The strong interactions between DTE molecules within the monolayer hampered conformational transformations that led to annulated-ring by-products. However, such conformational changes could not be completely precluded in the case of Au₂₅ assemblies given their dispersion in solution. Moreover, the dynamic behaviour that Au NCs exhibit in solution (collision induced ligand-exchange between the species)^{16,17} also facilitated the conformational changes within the DTE-linked Au₂₅ assemblies during the photoirradiation experiments.

Interestingly, the photoirradiation was also shown to induce structural rearrangements of the assemblies. The examination of the ligand composition of Au₂₅ assemblies by MALDI-MS analysis depicted that the nature of the species changed after light exposure. The lack of a signal (or a very low one) from intact Au₂₅(2PET)₁₈ clusters combined with the decrease of the mass peaks from the **o-DTE**² exchanged Au₂₅ species was interpreted as a growth of the population of linked Au₂₅ species. Additionally, the SAXS analysis confirmed the increasing size of the assemblies after UV/vis light irradiation cycles. It is therefore proposed that photoinduced assembly of Au₂₅ and cross-linking was occurring. This effect was more pronounced for the smaller Au₂₅ assemblies given their more dynamic nature in solution which facilitated their interlinking. The network of Au₂₅ clusters became more tightly bound after photoirradiation as shown by HRTEM. Furthermore, a difference in the diffusion behaviour was observed when the Au₂₅ assemblies were linked with open- and closed-ring DTE isomer.

The observed photoluminescent properties of the irradiated Au_{25} assemblies (enhanced emission/quantum yield, increase of PL lifetimes) further supported the formation of photoinduced cross-linking of Au_{25} assemblies. In addition, a supporting DFT study showed that the in Au_{25} assemblies a triplet ground state was more energetically favourable but still very close in energy to the singlet ground state. Therefore, it is postulated that multiple states could contribute to the photoluminescence in the formed Au_{25} assemblies.

6.6 References

1. Rival, J. V.; Nonappa; Shibu, E. S., Light-Triggered Reversible Supracolloidal Self-Assembly of Precision Gold Nanoclusters. *ACS Applied Materials & Interfaces* **2020**, *12* (12), 14569-14577.

- 2. Negishi, Y.; Kamimura, U.; Ide, M.; Hirayama, M., A Photoresponsive Au₂₅ Nanocluster Protected by Azobenzene Derivative Thiolates. *Nanoscale* **2012**, *4* (14), 4263-4268.
- 3. Udayabhaskararao, T.; Kundu, P. K.; Ahrens, J.; Klajn, R., Reversible Photoisomerization of Spiropyran on the Surfaces of Au₂₅ Nanoclusters. *ChemPhysChem* **2016**, *17* (12), 1805-1809.
- Katsonis, N.; Kudernac, T.; Walko, M.; van der Molen, S. J.; van Wees, B. J.; Feringa, B. L., Reversible Conductance Switching of Single Diarylethenes on a Gold Surface. *Advanced Materials* 2006, 18 (11), 1397-1400.
- 5. Ikeda, M.; Tanifuji, N.; Yamaguchi, H.; Irie, M.; Matsuda, K., Photoswitching of Conductance of Diarylethene-Au Nanoparticle Network. *Chemical Communications* **2007**, (13), 1355-1357.
- Dulić, D.; van der Molen, S. J.; Kudernac, T.; Jonkman, H. T.; de Jong, J. J. D.; Bowden, T. N.; van Esch, J.; Feringa, B. L.; van Wees, B. J., One-Way Optoelectronic Switching of Photochromic Molecules on Gold. *Physical Review Letters* 2003, 91 (20), 207402.
- 7. Whalley, A. C.; Steigerwald, M. L.; Guo, X.; Nuckolls, C., Reversible Switching in Molecular Electronic Devices. *Journal of the American Chemical Society* **2007**, *129* (42), 12590-12591.
- 8. Uchida, K.; Nakayama, Y.; Irie, M., Thermally Irreversible Photochromic Systems. Reversible Photocyclization of 1,2-Bis(benzo[b]thiophen-3-yl)ethene Derivatives. *Bulletin of the Chemical Society of Japan* **1990**, *63* (5), 1311-1315.
- 9. Herder, M.; Schmidt, B. M.; Grubert, L.; Pätzel, M.; Schwarz, J.; Hecht, S., Improving the Fatigue Resistance of Diarylethene Switches. *Journal of the American Chemical Society* **2015**, *137* (7), 2738-2747.
- 10. Pijper, T. C.; Ivashenko, O.; Walko, M.; Rudolf, P.; Browne, W. R.; Feringa, B. L., Position and Orientation Control of a Photo- and Electrochromic Dithienylethene Using a Tripodal Anchor on Gold Surfaces. *The Journal of Physical Chemistry C* **2015**, *119* (7), 3648-3657.
- 11. Sels, A.; Salassa, G.; Cousin, F.; Lee, L.-T.; Bürgi, T., Covalently Bonded Multimers of Au₂₅(SBut)₁₈ as a Conjugated System. *Nanoscale* **2018**, *10* (26), 12754-12762.
- 12. Ho-Wu, R.; Sun, K.; Goodson, T., Synthesis and Enhanced Linear and Nonlinear Optical Properties of Chromophore–Au Metal Cluster Oligomers. *The Journal of Physical Chemistry C* **2018**, *122* (4), 2315-2329.
- 13. Lee, K.-M.; Huang, C.-H.; Chang, C.-Y.; Chang, C.-C., The Optical and Microstructural Characterization of the Polymeric Thin Films with Self-Assembly Nanoparticles Prepared by Spin-Coating Techniques. *Crystals* **2020**, *10* (5).
- 14. Schweins, R.; Huber, K., Particle Scattering Factor of Pearl Necklace Chains. *Macromolecular Symposia* **2004**, *211* (1), 25-42.
- 15. Guinier, A.; Fournet, G.; Walker, C. B.; Yudowitch, K. L., Small-Angle Scattering of X-rays. Wiley: 1955.
- 16. Salassa, G.; Sels, A.; Mancin, F.; Bürgi, T., Dynamic Nature of Thiolate Monolayer in Au₂₅(SR)₁₈ Nanoclusters. *ACS Nano* **2017**, *11* (12), 12609-12614.
- 17. Zhang, B.; Salassa, G.; Bürgi, T., Silver Migration between $Au_{38}(SC_2H_4Ph)_{24}$ and Doped $Ag_xAu_{38-x}(SC_2H_4Ph)_{24}$ Nanoclusters. *Chemical Communications* **2016**, *52* (59), 9205-9207.
- 18. Tlahuice-Flores, A.; Whetten, R. L.; Jose-Yacaman, M., Ligand Effects on the Structure and the Electronic Optical Properties of Anionic Au₂₅(SR)₁₈ Clusters. *The Journal of Physical Chemistry C* **2013**, *117* (40), 20867-20875.
- 19. Hossain, S.; Kurashige, W.; Wakayama, S.; Kumar, B.; Nair, L. V.; Niihori, Y.; Negishi, Y., Ligand Exchange Reactions in Thiolate-Protected Au₂₅ Nanoclusters with Selenolates or Tellurolates: Preferential Exchange Sites and Effects on Electronic Structure. *The Journal of Physical Chemistry C* **2016**, *120* (45), 25861-25869.

- Matsuyama, T.; Hirayama, J.; Fujiki, Y.; Kikkawa, S.; Kurashige, W.; Asakura, H.; Kawamura, N.; Negishi, Y.; Nakatani, N.; Hatada, K.; Ota, F.; Yamazoe, S., Effect of Ligand on the Electronic State of Gold in Ligand-Protected Gold Clusters Elucidated by X-ray Absorption Spectroscopy. *The Journal of Physical Chemistry C* 2021, 125 (5), 3143-3149.
- 21. Wu, Z.; Jin, R., On the Ligand's Role in the Fluorescence of Gold Nanoclusters. *Nano Lett* **2010**, *10* (7), 2568-2573.
- 22. Wang, S.; Zhu, X.; Cao, T.; Zhu, M., A Simple Model for Understanding the Fluorescence Behavior of Au₂₅ Nanoclusters. *Nanoscale* **2014**, *6* (11), 5777-5781.
- 23. Wang, G.; Guo, R.; Kalyuzhny, G.; Choi, J.-P.; Murray, R. W., NIR Luminescence Intensities Increase Linearly with Proportion of Polar Thiolate Ligands in Protecting Monolayers of Au₃₈ and Au₁₄₀ Quantum Dots. *The Journal of Physical Chemistry B* **2006**, *110* (41), 20282-20289.
- Yang, T.-Q.; Peng, B.; Shan, B.-Q.; Zong, Y.-X.; Jiang, J.-G.; Wu, P.; Zhang, K., Origin of the Photoluminescence of Metal Nanoclusters: From Metal-Centered Emission to Ligand-Centered Emission. *Nanomaterials* 2020, 10 (2), 261.
- 25. Chen, T.; Yang, S.; Chai, J.; Song, Y.; Fan, J.; Rao, B.; Sheng, H.; Yu, H.; Zhu, M., Crystallization-Induced Emission Enhancement: A Novel Fluorescent Au-Ag Bimetallic Nanocluster with Precise Atomic Structure. *Science Advances* **2017**, *3* (8), e1700956.
- 26. Mohanty, J. S.; Baksi, A.; Lee, H.; Pradeep, T., Noble Metal Clusters Protected with Mixed Proteins Exhibit Intense Photoluminescence. *RSC Advances* **2015**, *5* (59), 48039-48045.
- 27. Luscombe, C. K.; Maitra, U.; Walter, M.; Wiedmer, S. K., Theoretical Background on Semiconducting Polymers and Their Applications to OSCs and OLEDs. *Chemistry Teacher International* **2021**.
- 28. Larsson, T.; Wedborg, M.; Turner, D., Correction of Inner-Filter Effect in Fluorescence Excitation-Emission Matrix Spectrometry Using Raman Scatter. *Analytica Chimica Acta* **2007**, *583* (2), 357-363.
- 29. Bain, D.; Maity, S.; Paramanik, B.; Patra, A., Core-Size Dependent Fluorescent Gold Nanoclusters and Ultrasensitive Detection of Pb²⁺ Ion. *ACS Sustainable Chemistry & Engineering* **2018**, *6* (2), 2334-2343.
- 30. Pyo, K.; Thanthirige, V. D.; Kwak, K.; Pandurangan, P.; Ramakrishna, G.; Lee, D., Ultrabright Luminescence from Gold Nanoclusters: Rigidifying the Au(I)–Thiolate Shell. *Journal of the American Chemical Society* **2015**, *137* (25), 8244-8250.
- 31. Kang, X.; Zhu, M., Tailoring the Photoluminescence of Atomically Precise Nanoclusters. *Chemical Society Reviews* **2019**, *48* (8), 2422-2457.
- 32. Zhu, M.; Aikens, C. M.; Hollander, F. J.; Schatz, G. C.; Jin, R., Correlating the Crystal Structure of a Thiol-Protected Au₂₅ Cluster and Optical Properties. *Journal of the American Chemical Society* **2008**, *130* (18), 5883-5885.
- 33. Oshida, K.; Nakazawa, T.; Miyazaki, T.; Endo, M., Application of Image Processing Techniques for Analysis of Nano- and Micro-Spaces in Carbon Materials. *Synthetic Metals* **2001**, *125* (2), 223-230.
- 34. Schneider, C. A.; Rasband, W. S.; Eliceiri, K. W., NIH Image to ImageJ: 25 Years of Image Analysis. *Nature Methods* **2012**, *9* (7), 671-675.
- 35. Salorinne, K.; Lahtinen, T.; Koivisto, J.; Kalenius, E.; Nissinen, M.; Pettersson, M.; Häkkinen, H., Nondestructive Size Determination of Thiol-Stabilized Gold Nanoclusters in Solution by Diffusion Ordered NMR Spectroscopy. *Analytical Chemistry* **2013**, *85* (7), 3489-3492.
- 36. Chow, B. C.; Cohen, I. A., Derivatives of Tetraphenylporphineruthenium (II). *Bioinorganic Chemistry* **1971**, *1* (1), 57-63.

- 37. Zhu, M. Z.; Eckenhoff, W. T.; Pintauer, T.; Jin, R., Conversion of Anionic [Au₂₅(SCH₂CH₂Ph)₁₈]⁻ Cluster to Charge Neutral Cluster via Air Oxidation. *The Journal of Physical Chemistry C* **2008**, *112* (37), 14221-14224.
- 38. Heaven, M. W.; Dass, A.; White, P. S.; Holt, K. M.; Murray, R. W., Crystal Structure of the Gold Nanoparticle $[N(C_8H_{17})_4][Au_{25}(SCH_2CH_2Ph)_{18}]$. *Journal of the American Chemical Society* **2008**, *130* (12), 3754-3755.
- 39. Hammouda, B., Brownian Dynamics Simulation of Stiff Dumbbells. *The Journal of Chemical Physics* **1985**, 82 (1), 401-405.

General conclusions and outlook

The objective of this dissertation was to assess different approaches that could be employed to prepare extended assemblies of atomically precise gold nanoclusters (Au NCs) with the idea to bring these systems closer to application as functional nanomaterials, e.g., fundamental components of molecular electronic devices. This goal has been accomplished by exploring two distinct avenues that differed in the type of chemical interaction responsible for linking the nanoclusters.

The prototypical Au₂₅(SR)₁₈ nanoclusters were utilized in the study presented in this thesis due to their established stability and versatility for ligand exchange. The main approach towards achieving self-assembled systems involved modification of the protective ligand shell of nanoclusters via the ligand exchange reaction in a solution phase. This afforded species capable of interlinking and was shown to be a successful method to obtain assemblies of different sizes. Specifically, the two approaches studied, and the overall results are as follows:

Metalloporphyrins as anchoring points for gold nanocluster assemblies formed via supramolecular interactions.

In this project the functionalization of the surface of Au₂₅(SBu)₁₈ nanoclusters by introducing pyridyl-thiolate ligands was demonstrated. Importantly, the careful purification of a polydisperse mixture of clusters yielded species with varying ratio of the exchanged ligands, which were shown to bind to the metalloporphyrin with different affinity. The obtained supramolecular assemblies for two probed metallocycles, ZnTPP and CoTPP, exhibited 1:1 binding stoichiometry with the pyridyl-thiolate ligand, hence this specific configuration of building blocks did not produce the assemblies via a biaxial coordination mode. However, while the 1:1 binding stoichiometry between pyridyl-thiolate ligand and metalloporphyrins limits the applications of the latter as anchor nodes for extended self-assembled systems, nevertheless this approach gives access to discrete Au₂₅ clusters with metalloporphyrindecorated surface. Such architectures could be explored as photocatalytic systems.

Generally, the question remains open whether the metalloporphyrins could be used as effective structural elements in Au NC-based assembled systems since the strong binding of Au NC to both axial positions (as yet not demonstrated) is pivotal for obtaining stable architectures. There are several possibilities to consider when designing and/or optimizing the metalloporphyrins as reliable anchoring points. These

involve the changing the electronic properties by introducing peripheral substituents on the porphyrin macrocycle. Indeed, it is desirable that, after the first axial coordination, the central metal ion remain in the plane of the macrocycle hence making the other axial coordination site accessible for binding. Otherwise, employing metalloporphyrins with a central ion that is more prone to form 1:2 complexes with pyridyl derivatives is a viable way forward. Alternatively, different anchoring functionalities in the nanocluster monolayer (e.g., imidazole) might be implemented with improved success. Crucially, to realize extended Au NC-based assemblies using metalloporphyrins as the anchoring points, the values of the two association constants for the axially coordinated ligands need to be on the same order of magnitude, otherwise supramolecular complexes with the 1:1 binding stoichiometry will dominate in the system.

Dithiolate photoswitchable ligands as potential linkers for gold nanocluster assemblies formed via covalent bonding.

In this project all the objectives were met. First, the synthesis of the dithiol photoligand with a photoswitching functionality based on the dithienylethene moiety was accomplished in a multistep reaction and purification process. The obtained dithiol ligand was shown to be effective in linking $[Au_{25}(2PET)_{18}]^0$ nanoclusters with a strong covalent bond. Consequently, oligomeric species with different sizes were isolated and they all underwent reversible photoswitching behaviour, which represents the first demonstration of Au NC-based assemblies with a light-controlled ON/OFF functionality. Overall, this is an important finding showcasing that Au NCs can be suitable building blocks for the formation of superstructures that carry out functions controlled by external stimuli.

Interestingly for the already linked Au₂₅–photoligand structures, the light-induced cross-linking reaction yielded assemblies with more compact geometries, as determined by SAXS and NMR measurements. This was hypothesized to be facilitated by the dithiols that were present in the protective shell of Au₂₅ nanoclusters as exchanged bidentate ligands. This behaviour demonstrates the flexibility and dynamics of the assembled system.

Generally, the nanocluster species exhibit a very dynamic behaviour and undergo a constant exchange of ligands when in solution phase. This is true not only for the discrete nanoclusters but also for their assemblies. Therefore, the isolation of uniformly dispersed multimeric species (i.e., dimers, trimers, etc) could be of interest for the systematic study of the evolution of properties exhibited by nanoclusters in assembled structures in comparison to single clusters. Potentially, for future consideration, the design of a photoswitchable linker with a (bidentate) dithiol functionality on both terminal sites of the photoligand could be attempted. Indeed, it has been demonstrated that dithiol ligands form more robust and stable structures with Au NC core since the two sulfhydryl groups have a separation distance that is very close to the distance between two S atoms on adjacent staple motifs of the cluster. (Świerczewski et al., *manuscript under revision*)

This strategy could also be employed to investigate the impact of the photo-induced cross-linking within the formed Au₂₅ assemblies on their limited cyclability of the ON/OFF switching. Indeed, since a low photostability has been observed in the dithiol linker, one could hypothesize that this might not necessarily occur for more robustly linked Au₂₅ assemblies. In fact, the ability of a linker, which is an integral part of an assembled system, to undergo photoswitching is expected to be reduced when the bridging molecule is 'locked' in a specific geometry within the superstructure. This would prohibit the photocyclization or photocycloreversion reaction. Therefore, the photoswitching might be more of a localized process that slowly propagates through the formed structure as certain domains undergo conformational changes that release the photoligand from an unfavourable steric environment. For the same reasons, photoswitching could be completely hindered in this type of system. To investigate this hypothesis, the possibility of cross-linking should be eliminated by using the rigid bis(dithiol) linkers.

The photostability of the dithienylethene(DTE)-based ligand could also be improved by employing perfluoro-dithienylethene moiety. Indeed, this structure was shown to exhibit a much higher photostability than the perhydro-analogues that were employed in this thesis.

Moreover, the stability of the free photoligand after the 532 nm irradiation, which caused the deterioration of the dithienylethene(DTE)-based linker, should also be addressed. A future study investigating the decomposition reaction and/or a by-product formation could perhaps provide some answers into the limited cycling of the ON/OFF switchability. Possibly, different irradiation wavelengths for the ON/OFF switching reaction could be explored to identify the dependence of the degree of photoligand decomposition on the photon wavelength. Ideally wavelengths could be identified to minimize the photodegradation. Indeed, a systematic investigation of the irradiation at various wavelengths on the stability of the parent Au₂₅(SR)₁₈ nanocluster would complement this future study.

Appendix A

A.1 Photoligand Synthesis and Characterization

A.1.1 General remarks

Reagents and starting materials were used as supplied, unless mentioned otherwise. All reactions were carried under nitrogen using the standard Schlenk techniques. Distilled and degassed solvents were employed in all syntheses. Silica gel (230-400 mesh) was used for column chromatography. Analytical thin layer chromatography (TLC) was performed on commercially coated 60 mesh F_{254} aluminium plates. Spots were rendered visible by exposing the plate to UV light.

A.1.2 Chemicals

2-chloro-5-methylthiophene (95 %, Fluorochem); glutaryl dichloride (97 %, Acros Organics); aluminium chloride AlCl₃ (98.5 %, Acros Organics); nitromethane (98+%, Alfa Aesar); zinc powder (99.995 % trace metal basis, Sigma Aldrich); titanium tetrachloride TiCl₄ (99.0 %, Brunschwig); potassium carbonate K₂CO₃ (≥99.0 %, Sigma Aldrich); 4-bromothiophenol (97 %, Apollo Scientific); 2-chloro-2-methylpropane (Acros Organics); *n*-butyllithium *n*-BuLi (1.6 M in hexanes, Acros Organics); tributyl borate B(*n*-BuO)₃ (Bachem); tetrakis(triphenylphosphine)-palladium(0) [Pd(PPh₃)₄] (98 %, Fluorochem); sodium carbonate Na₂CO₃ (≥99.5 %, Sigma Aldrich); ethylene glycol (99.8 %, Acros Organics); sodium sulfate Na₂SO₄ (anhydrous, Reactolab); acetyl chloride, AcCl (99 %, Fluorochem); boron tribromide BBr₃ (99.9 %, Sigma Aldrich); caesium hydroxide monohydrate CsOH · H₂O (99.95 %, Sigma Aldrich), *tert*-butyl methyl ether MTBE (99 %, Acros Organics);

Solvents: diethylether Et₂O, *n*-pentane, tetrahydrofuran THF, dichloromethane CH₂Cl₂, methanol MeOH (ACS grade, Fisher Scientific).

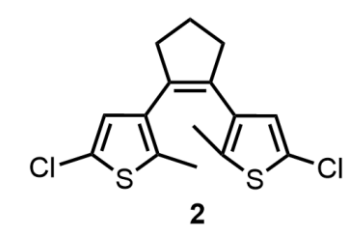
1,5-bis(5-chloro-2-methylthiophen-3-yl)pentane-1,5-dione (1)

2-chloro-5-methylthiophene (4.13 mL, 37.7 mmol) and glutaryl dichloride (2.41 mL, 18.9 mmol) were dissolved in dry and degassed nitromethane CH_3NO_2 (75 mL) under nitrogen and then cooled to 0 °C. AlCl₃ (5.78 g, 43.3 mmol) was added slowly to the solution and

was left to stir at ambient temperature for 4 h. Then the reaction mixture was poured into ice-cold water (15 mL). Crude product was extracted with CH_2Cl_2 (3 × 75 mL), dried over anhydrous Na_2SO_4 , filtered and concentrated in vacuo. The purification was done with flash chromatography (silica gel 60 Å, CH_2Cl_2) to obtain light brown powder (3.50 g, 51 %).

¹H NMR (CDCl₃, 300 MHz): δ (ppm) = 7.18 (s, 2H), 2.86 (t, *J*=6.85 Hz, 4H), 2.66 (s, 6H), 2.10–2.01 (m, 2H)

1,2-bis(5-chloro-2-methylthiophen-3-yl)cyclopent-1-ene (2)

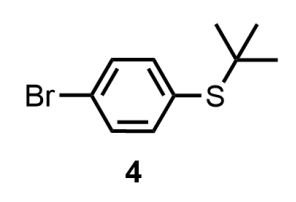


Zinc powder (2.53 g, 38.49 mmol) was suspended in 100 mL of anhydrous THF and cooled to 0 °C. TiCl₄ (2.14 mL, 19.37 mmol) was added cautiously dropwise under nitrogen. The solution was stirred at 50 °C for 2 h. Then pyridine (1.58 mL, 19.37 mmol) was added. After 10 min, compound **1** (3.50 g, 9.69 mmol) dissolved in anhydrous THF (10 mL)

was added to the stirring mixture. Reaction was left to stir overnight in dark. After cooling the reaction mixture to ambient temperature, aqueous K_2CO_3 (2 mL, 1.46 M) was added followed by Et_2O (5 mL). The reaction mixture was filtered and washed with a small amount of Et_2O . The organic phase was placed in the cold bath for 30 min to form a precipitate that was then filtered. The organic phase was washed with 2N HCl (3 × 10 mL), dried with anhydrous Na_2SO_4 , filtered, and concentrated in vacuo to obtain an orange oil. The purification was done with column chromatography (silica gel 60 Å, hexane) to obtain light brown powder (0.99 g, 79 %).

¹H NMR (CDCl₃, 300 MHz): δ (ppm) = 6.57 (s, 2H), 2.71 (t, J=7.43 Hz, 4H), 2.07–1.97 (m, 2H), 1.89 (s, 6H)

1-Bromo-4-tert-butylsulfanylbenzene (4)



Synthesis was followed according to the procedure reported by Pinault et al.¹ Briefly, 4-bromothiophenol (5.03 g, 26.6 mmol) was dissolved in 2-chloro-2-methylpropane (20 mL). To the stirring mixture aluminium chloride (179 mg, 1.34 mmol) was added portionwise. Reaction was left to stir for 1 h at ambient

temperature and the solution became light orange in colour. The reaction mixture was extracted with Et_2O (3 × 25 mL). The combined organic layers were washed with water (3 × 30 mL), dried over anhydrous MgSO₄, and solvent was removed under reduced pressure. The purification of the crude light-yellow oil was done using column chromatography (silica gel 60 Å, n-pentane) to afford colourless oil (4.1 g, 62 % yield).

¹H NMR (CDCl₃, 400 MHz): δ (ppm) = 7.46 (d, 2H), 7.38 (d, 2H), 1.27 (s, 9H)

¹³C NMR (CDCl₃, 101 MHz): δ (ppm) = 139.07, 131.93, 131.78, 123.60, 46.29, 31.01

1,2-bis(5-di-*n*-butoxyboryl-2-methylthiophen-3-yl)cyclopent-1-ene (3)

Synthesis was following the procedure reported by Lucas et al.²

Compound **2** (1.02 g, 3.1 mmol) was dissolved in anhydrous THF (40 mL) under nitrogen, and n-BuLi (4.45 mL, 7.1 mmol, 1.6 M in hexane) was added by syringe. The solution was left to stir at

-78 °C for 1 h, and B(n-BuO) $_3$ (2.0 mL, 7.41 mmol) was added dropwise. The solution was left to stir for 2 h and used directly for Suzuki cross-coupling reaction without any workup.

1,2-bis(5-(4-(tert-butylthio)phenyl)-2-methylthiophen-3-yl)cyclopent-1-ene (5)

Compound 4 (1.20 mL, 6.47 mmol) was dissolved in THF (25 mL), and freshly activated [Pd(PPh₃)₄] (0.18 g, 0.16 mmol) was added under nitrogen. The solution was left to stir for 15 min at ambient temperature. Aqueous Na₂CO₃ (5 mL, 2 M) and 15 drops of ethylene glycol were

added, and the solution was heated until reflux (80 °C). The solution of **3** was added dropwise over a period of 50 min. The solution was then left to react under reflux (73 °C) overnight. After cooling the reaction mixture to ambient temperature, Et₂O and H₂O were added. The organic layer was collected and dried with anhydrous Na₂SO₄, and the solvent was removed under reduced pressure. The purification of dark orange oil was done using column chromatography (silica gel 60 Å, *n*-pentane: Et₂O, 100:1) to afford magenta-hued solid (1.55 g, 86 % yield).

¹H NMR (CDCl₃, 400 MHz): δ (ppm) = 7.50–7.43 (m, 8H), 7.07 (s, 2H), 2.84 (t, *J*=7.5 Hz, 4H), 2.14–2.04 (m, 2H), 1.99 (s, 6H), 1.29 (s, 18H)

¹³C NMR (CDCl₃, 101 MHz,): δ (ppm) = 139.01, 138.00, 136.96, 135.27, 134.92, 134.76, 131.25, 125.25, 124.62, 46.30, 38.66, 31.08, 23.12, 14.67

1,2-bis[5-(4-acetylthiophenyl)-2-methylthiophen-3-yl]cyclopent-1-ene (6)

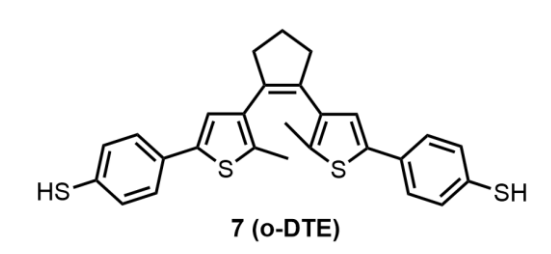
Compound 5 (0.49 g, 0.83 mmol) was dissolved in anhydrous CH_2Cl_2 (10 mL) under nitrogen, and AcCl (0.4 mL, 5.63 mmol) was added to a stirring solution at 0 °C. The solution of BBr_3 (0.18 mL, 1.90 mmol) in CH_2Cl_2 (4 mL) was then added dropwise and solution was

stirred for 24 h at ambient temperature. The reaction mixture was diluted with Et₂O (10 mL) and poured over ice. The combined organic phases were dried with anhydrous Na₂SO₄, and the solvent was removed under reduced pressure. The purification of dark green crude product was done using column chromatography (silica gel 60 Å, petroleum ether: ethyl acetate, 4:1) to afford white crystals with magenta hue (0.31 g, 67 % yield).

¹H NMR (CDCl₃, 400 MHz,): δ (ppm) = 7.56–7.50 (m, 4H), 7.40–7.34 (m, 4H), 7.08 (s, 2H), 2.85 (t, *J*=7.5 Hz, 4H), 2.43 (s, 6H), 2.14–2.06 (m, 2H), 2.01 (s, 6H)

¹³C NMR (CDCl₃, 101 MHz,): δ (ppm) = 194.28, 138.71, 136.93, 135.72, 135.59, 134.96, 134.80, 126.13, 125.97, 124.94, 38.54, 30.27, 23.10, 14.58, 14.31

1,2-bis[5-(4-mercaptophenyl)-2-methylthiophen-3-yl]cyclopent-1-ene (7)



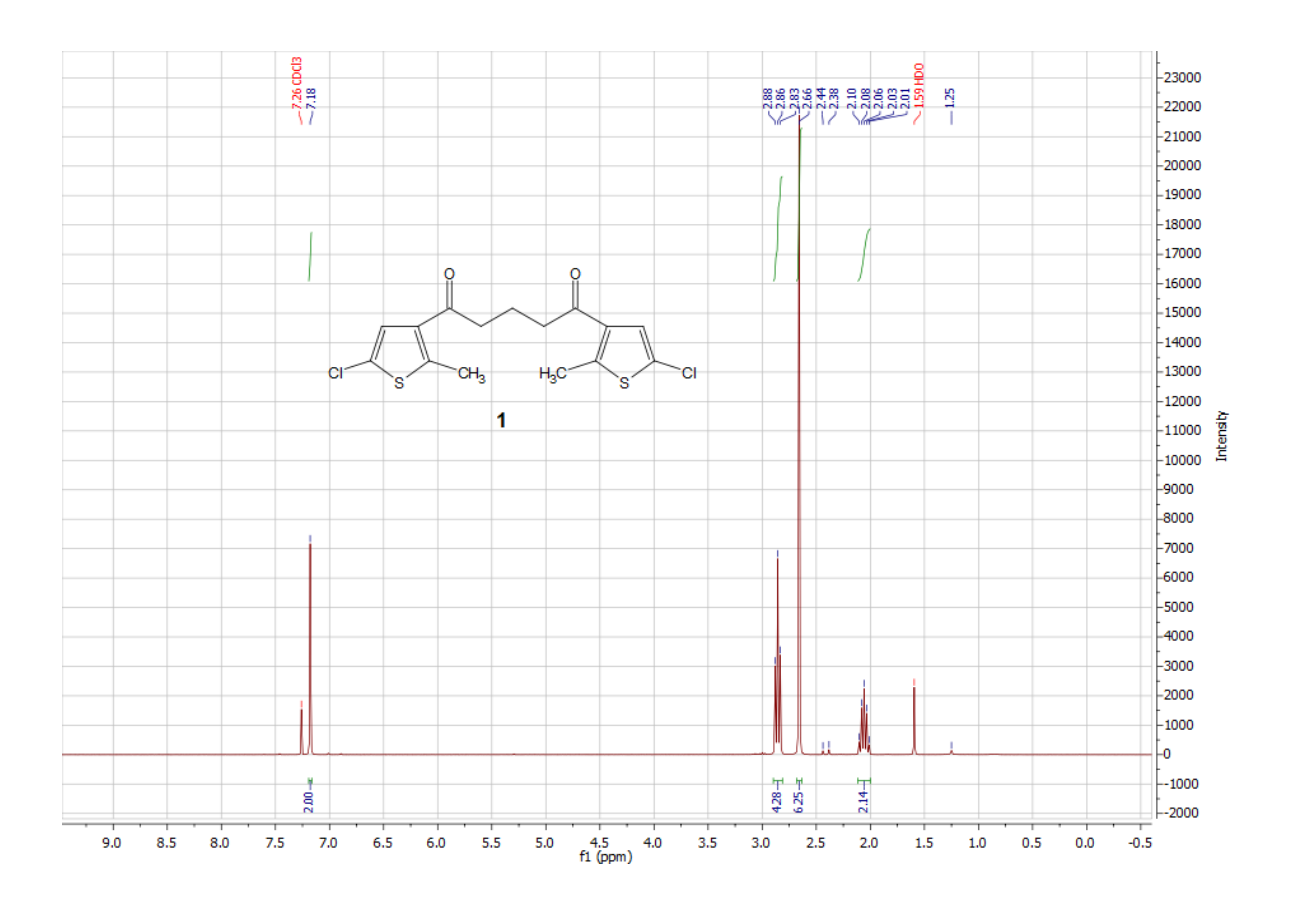
Compound **6** (0.021 g, 0.037 mmol) was dissolved in degassed methyl *tert*-butyl ether (MTBE, 10 mL) and a solution of caesium hydroxide monohydrate (0.106 g, 0.632 mmol) in degassed methanol (MeOH, 0.3 mL) was added dropwise at ambient temperature. The reaction

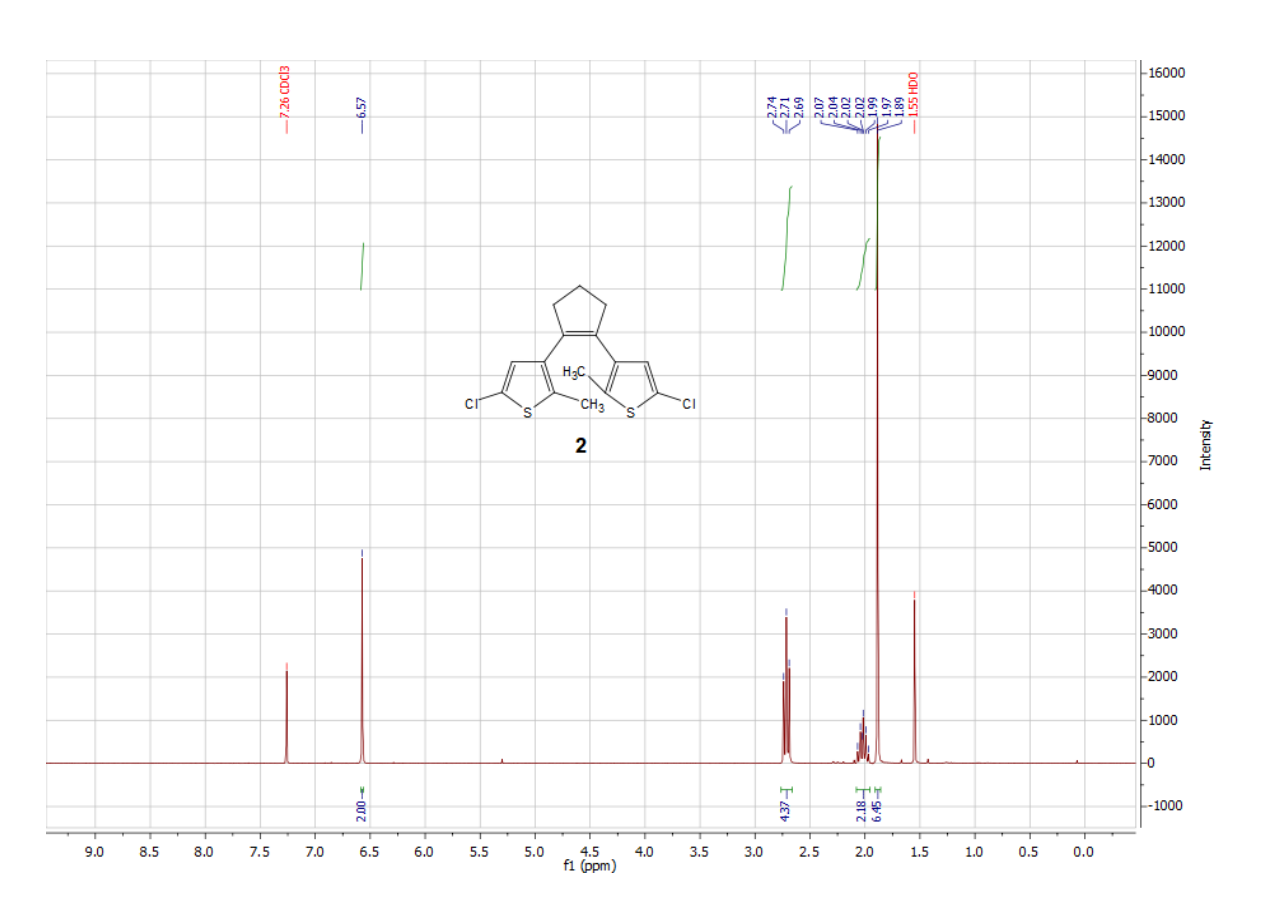
mixture was stirred for 10 min and then slowly acidified with aqueous hydrochloric acid (1.48 mL, 1 M). The reaction mixture was extracted with MTBE (3×10 mL), dried with anhydrous Na₂SO₄, and the solvent was removed under reduced pressure to afford a pink film.

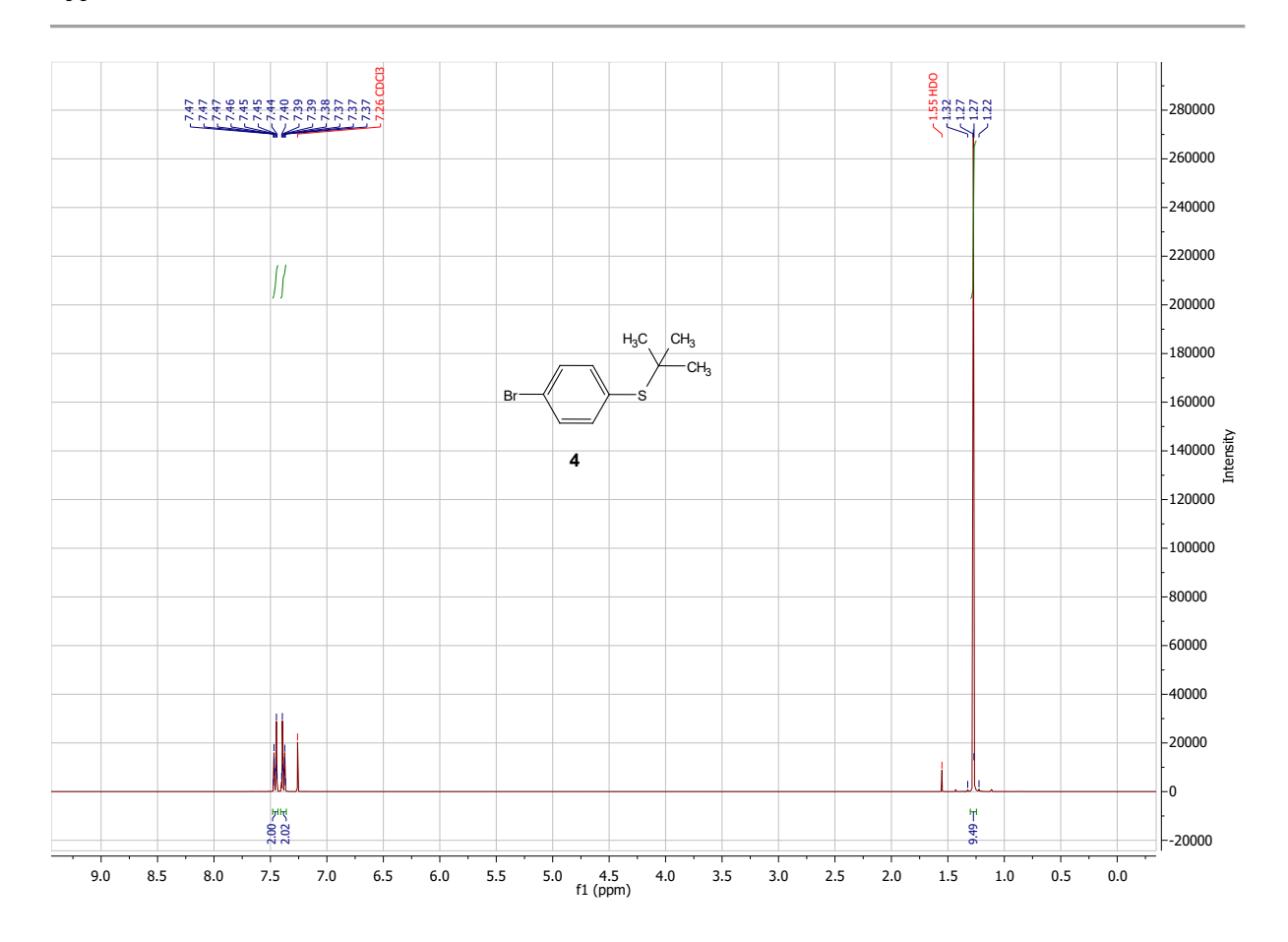
¹H NMR (CDCl₃, 400 MHz,): δ (ppm) = 7.38–7.33 (m, 4H), 7.25–7.21 (m, 4H), 6.98 (s, 2H), 3.45 (s, 2H), 2.83 (t, J = 7.5, 4H), 2.11–2.03 (m, 2H), 1.99 (s, 6H)

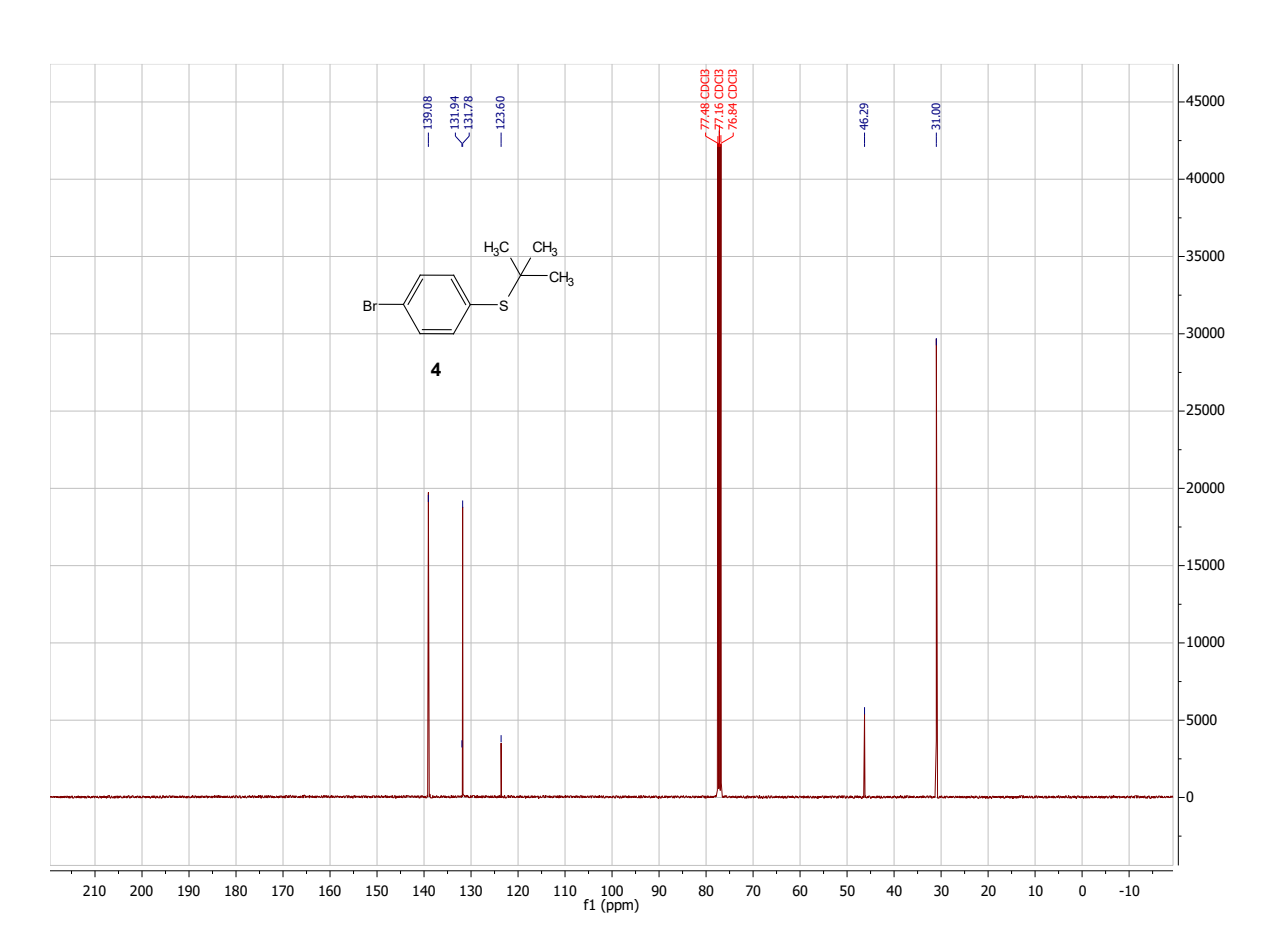
¹³C NMR (CDCl₃, 101 MHz,): δ (ppm) = 139.03, 136.82, 134.78, 134.59, 132.29, 129.98, 129.25, 126.01, 124.02, 38.56, 27.12, 23.15, 14.56

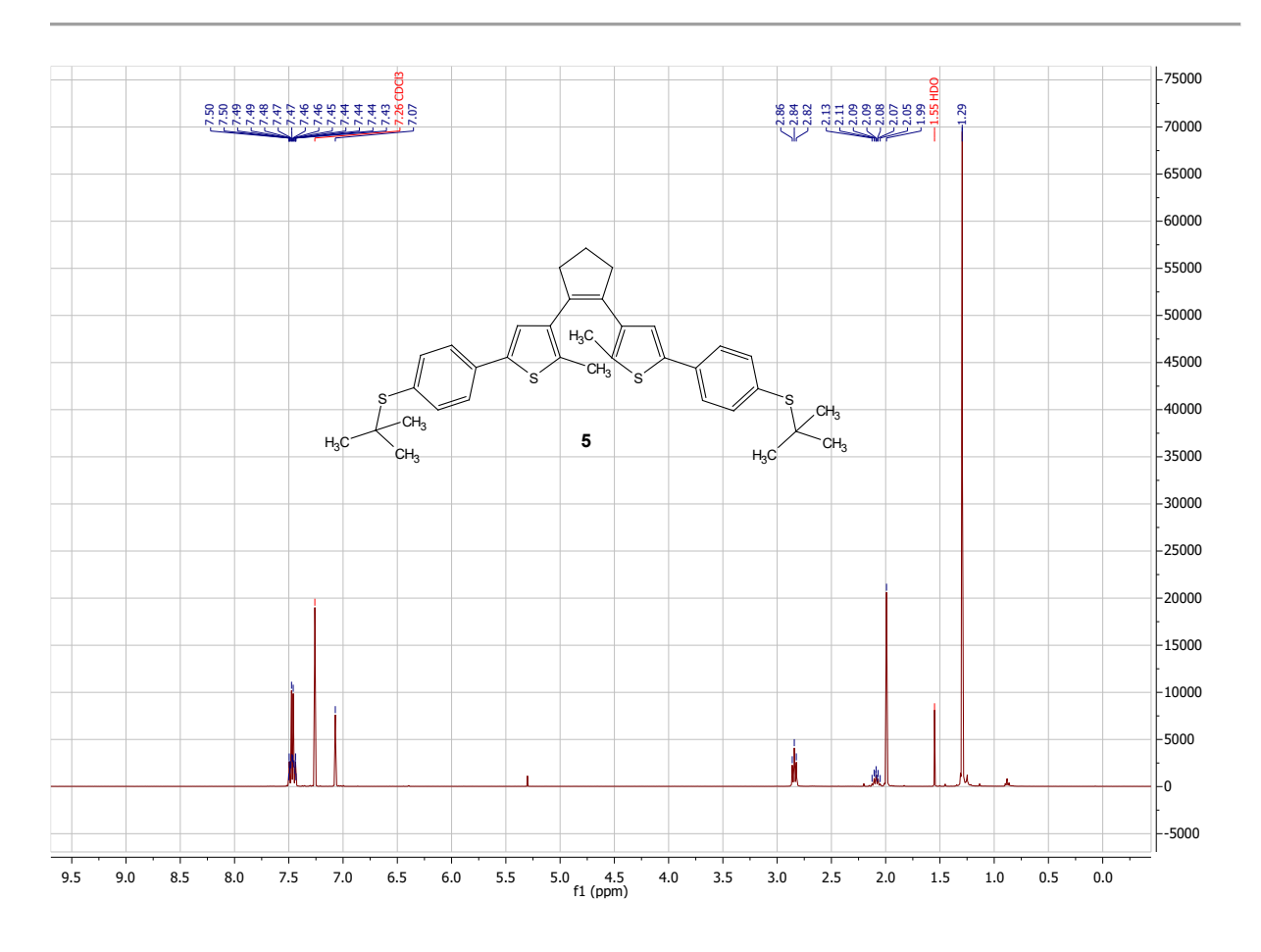
A.1.3 ¹H and ¹³C NMR spectra of 1–7

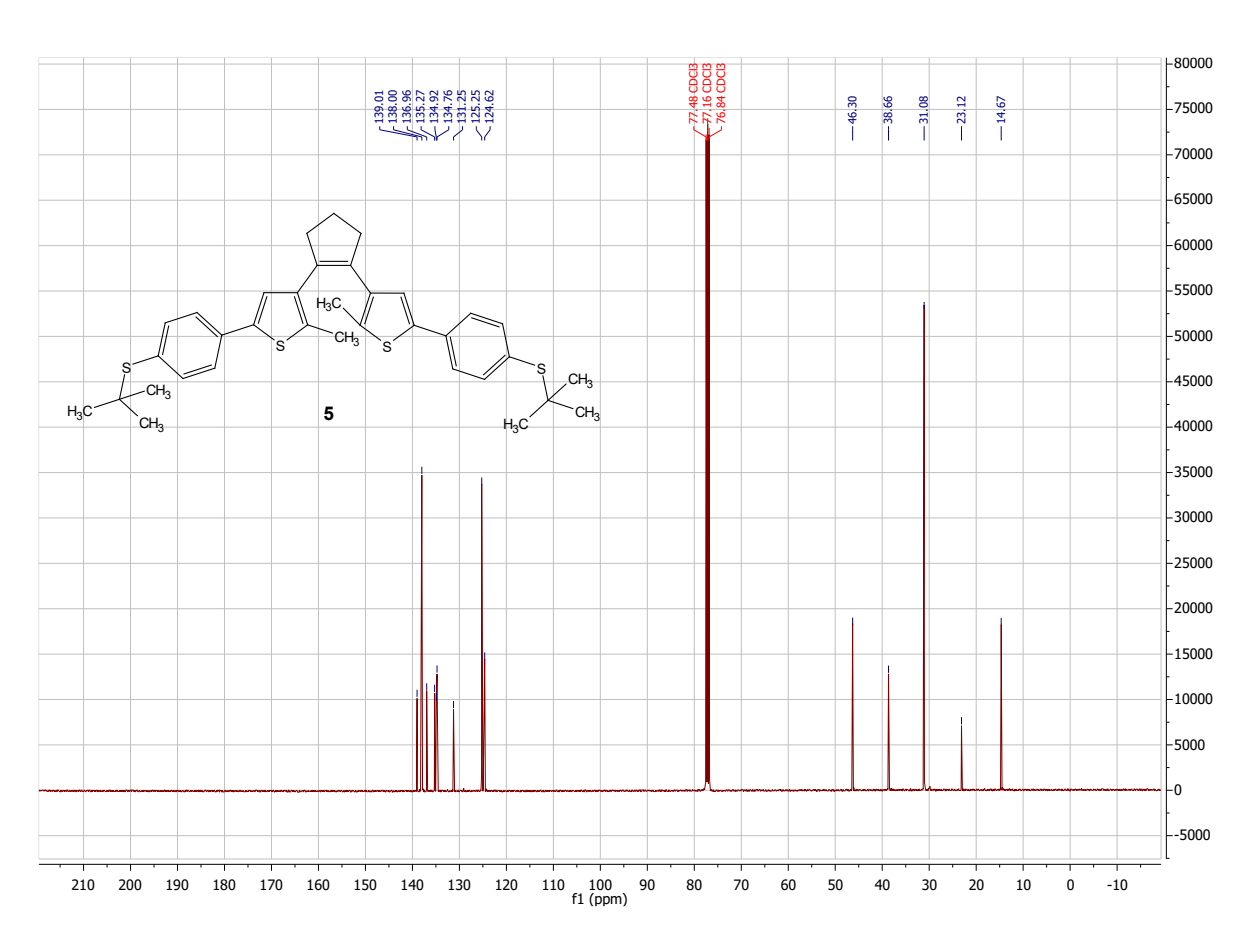


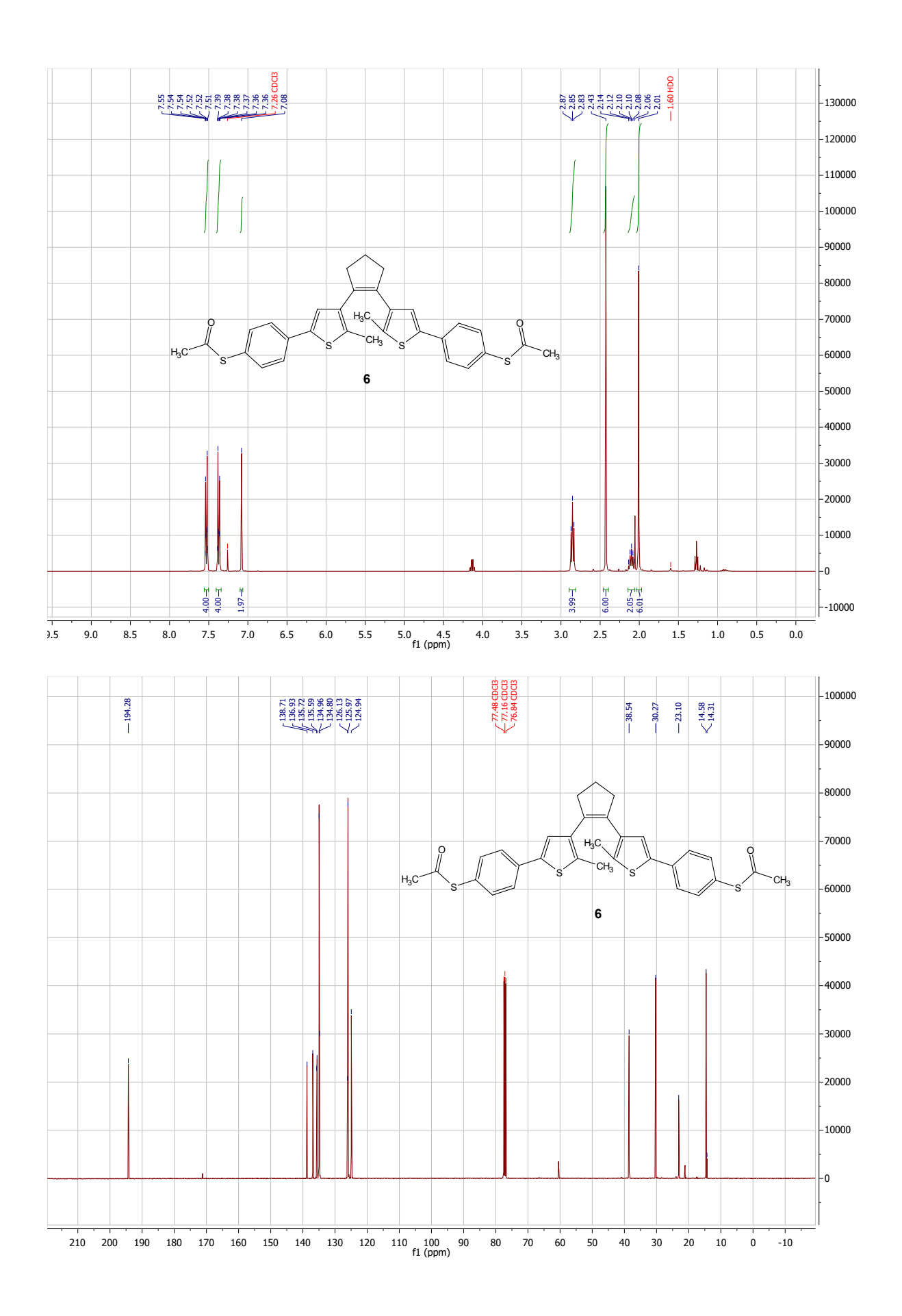


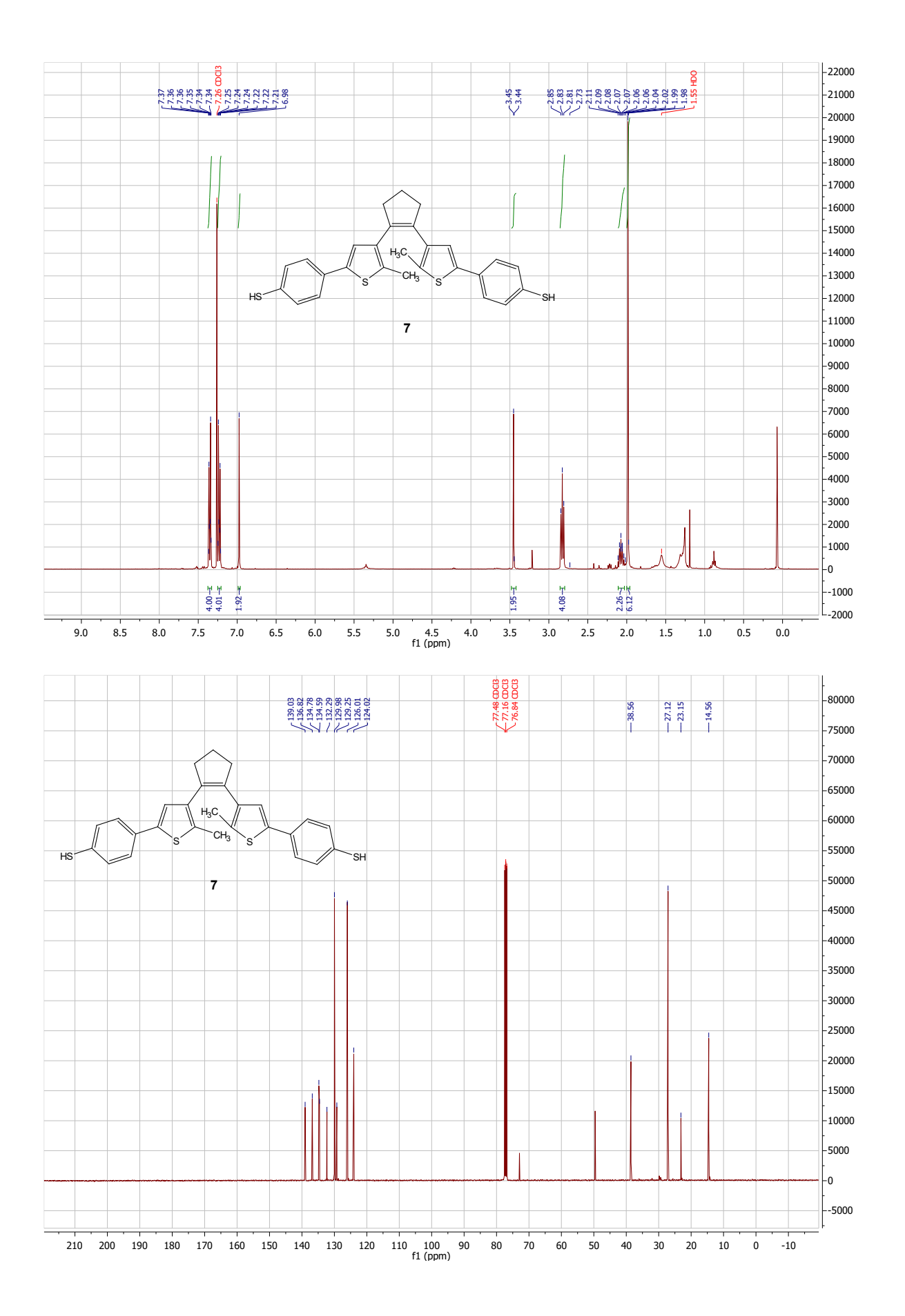












A.1.4 X-ray structure determination of 1,2-bis[5-(4-acetylthiophenyl)-2-methylthiophen-3-yl]cyclopent-1-ene (6)

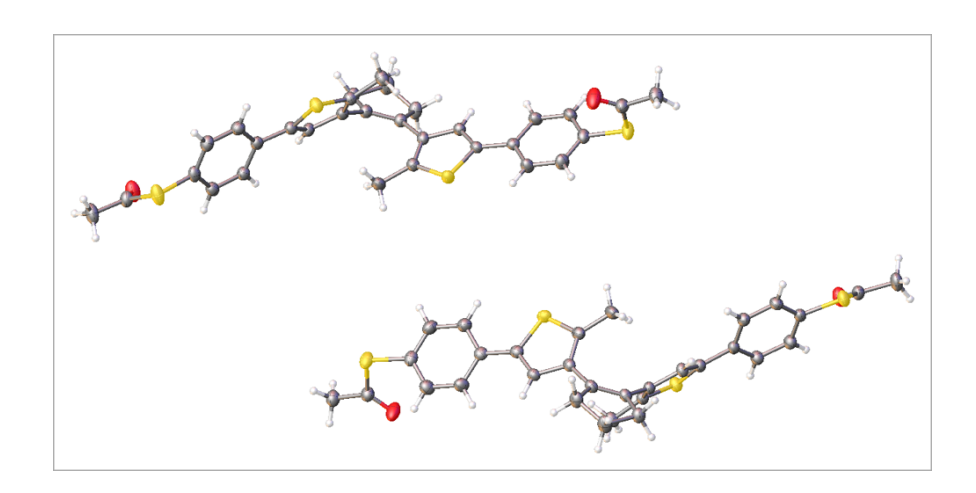


Figure A.1 The crystal structure of 1,2-bis[5-(4-acetylthiophenyl)-2-methylthiophen-3-yl]cyclopent-1-ene (6). Colour code: C-black, S-yellow, O-red, H-white.

 $\textbf{\textit{Table A.1 Crystal data and structure refinement for 1,2-bis [5-(4-acetylthiophenyl)-2-methylthiophen-3-yl] cyclopent-1-ene~(\textbf{6}).}$

Empirical formula	C ₃₁ H ₂₈ O ₂ S ₄
Formula weight	560.77
Temperature/K	149.99(10)
Crystal system	triclinic
Space group	P-1
a/Å	11.90785(17)
b/Å	13.22890(19)
c/Å	18.0154(3)
a /°	94.0296(12)
β/°	98.1658(12)
γ/°	103.5219(12)
Volume/Å ³	2715.45(7)
Z	4
ρ _{calc} g/cm ³	1.372
μ/mm ⁻¹	3.431
F(000)	1176.0
Crystal size/mm ³	$0.255 \times 0.208 \times 0.096$
Radiation	Cu K α ($\lambda = 1.54184$)
2Θ range for data collection/°	4.984 to 149.188
Index ranges	$-14 \le h \le 14, -16 \le k \le 13, -22 \le l \le 22$
Reflections collected	56794
Independent reflections	$10704 \; [R_{int} = 0.0268, R_{sigma} = 0.0149]$

Data/restraints/parameters	10704/0/675
Goodness-of-fit on F ²	1.091
Final R indexes [I>=2σ (I)]	$R_1 = 0.0380, wR_2 = 0.1042$
Final R indexes [all data]	$R_1 = 0.0396$, $wR_2 = 0.1054$
Largest diff. peak/hole / e Å-3	1.26/-0.38

Table A.2 Fractional atomic coordinates ($\times 10^4$) and equivalent isotropic displacement parameters ($\mathring{A}^2 \times 10^3$) for 1,2-bis[5-(4-acetylthiophenyl)-2-methylthiophen-3-yl]cyclopent-1-ene (**6**). U_{eq} is defined as 1/3 of the trace of the orthogonalised U_{II} tensor.

Atom	x	у	z	U(eq)
S1	6002.4(4)	1577.7(3)	9897.1(2)	30.51(10)
S2	4593.3(4)	1292.2(3)	6710.2(2)	29.5(1)
S3	6935.3(4)	6208.8(4)	12228.8(3)	42.12(13)
S4	1587.8(4)	-2860.3(4)	3890.9(3)	37.93(12)
О3	9230.9(12)	6806.8(12)	12378.6(9)	46.4(4)
O31	592.2(16)	-3316.2(14)	5083.9(8)	57.3(5)
C1	8359.4(19)	7822.1(18)	13177.8(13)	45.5(5)
C2	8371.2(16)	6966.2(15)	12587.6(10)	32.8(4)
C4	7162.1(15)	5201.1(15)	11610.2(10)	31.4(4)
C5	6647.0(16)	4180.2(16)	11719.4(10)	33.7(4)
C6	6667.8(16)	3359.9(15)	11208.9(10)	31.6(4)
C7	7213.5(15)	3541.5(14)	10575.0(10)	27.3(3)
C8	7758.1(15)	4570.8(14)	10482.2(10)	28.9(4)
C9	7725.2(15)	5396.8(14)	10990.3(10)	30.4(4)
C10	7160.6(15)	2673.9(14)	10010.2(10)	27.8(3)
C11	7884.0(15)	2568.5(14)	9501.5(9)	26.9(3)
C12	7499.5(15)	1623.1(14)	9003.5(10)	26.8(3)
C13	6486.0(15)	995.4(14)	9162.7(10)	28.3(4)
C14	5826.1(17)	-63.7(15)	8803.2(11)	35.5(4)
C15	8139.9(15)	1329.4(14)	8420.3(10)	26.8(3)
C16	9415.5(16)	1317.7(16)	8618.3(10)	34.3(4)
C17	9585.6(17)	587.9(18)	7968.8(11)	39.7(5)
C18	8664.3(16)	676.5(17)	7302.4(11)	34.8(4)
C19	7731.0(15)	1004.1(14)	7683.8(10)	26.6(3)
C20	6572.9(15)	961.0(13)	7248.7(9)	26.0(3)
C21	6016.5(15)	138.8(13)	6662.9(9)	25.1(3)
C22	4933.1(14)	188.4(13)	6326.7(9)	24.2(3)
C23	5905.5(16)	1671.6(14)	7326.4(10)	28.3(4)
C24	6150.4(19)	2677.3(15)	7822.6(11)	37.4(4)
C25	3048.7(16)	-344.9(14)	5418.3(10)	30.9(4)

C26	2276.7(16)	-1044.1(16)	4860.3(11)	34.5(4)
C27	2557.0(16)	-1949.4(14)	4600.5(10)	30.0(4)
C28	3623.3(17)	-2139.0(14)	4892.5(10)	32.2(4)
C29	4388.4(16)	-1440.1(14)	5448.3(10)	30.9(4)
C30	558.2(17)	-3543.4(15)	4424.6(10)	33.5(4)
C32	-359.0(19)	-4415.1(16)	3960.1(12)	41.5(5)
C38	4116.5(14)	-530.7(13)	5728.1(9)	24.5(3)
S1B	4888.1(4)	3445.3(3)	3330.4(2)	30.07(10)
S2B	3885.7(4)	3132.6(3)	105.6(2)	27.57(10)
S3B	8341.7(4)	7574.5(4)	6049.4(2)	37.37(12)
S4B	1353.5(4)	-1770.3(4)	-2171.6(3)	33.50(11)
ОЗВ	8968.3(15)	8565.7(12)	4894.9(8)	51.1(4)
O31B	3529.4(13)	-1443.0(12)	-2457.7(9)	44.7(3)
C1B	10178.2(17)	9265.2(16)	6074.0(11)	36.9(4)
C2B	9181.3(16)	8524.7(15)	5559.9(10)	31.8(4)
C4B	7349.6(16)	6750.5(15)	5302.7(10)	31.2(4)
C5B	6534.5(17)	7127.5(15)	4840.0(11)	36.0(4)
C6B	5743.5(16)	6462.8(15)	4278.5(11)	33.6(4)
C7B	5713.2(15)	5401.0(14)	4168.6(10)	26.9(3)
C8B	6544.1(17)	5038.4(15)	4632.0(10)	32.9(4)
C9B	7353.4(17)	5706.5(16)	5191.0(11)	35.5(4)
C10B	4823.3(15)	4711.0(13)	3588.8(10)	26.3(3)
C11B	3851.7(15)	4910.0(13)	3187.1(10)	26.1(3)
C12B	3167.7(15)	4063.1(13)	2652.8(9)	25.5(3)
C13B	3627.6(16)	3203.2(14)	2673.3(10)	29.0(4)
C14B	3177(2)	2142.8(15)	2243.2(11)	40.2(5)
C15B	2073.0(15)	4122.0(13)	2179.9(10)	26.3(3)
C16B	1167.7(16)	4537.3(16)	2532.3(11)	33.5(4)
C17B	263.2(18)	4618.7(17)	1860.1(12)	39.4(4)
C18B	481.6(15)	3945.0(15)	1194.9(10)	31.3(4)
C19B	1700.7(14)	3807.2(13)	1442.0(10)	25.5(3)
C20B	2335.7(15)	3377.1(13)	902.6(9)	24.8(3)
C21B	1886.7(15)	2391.8(13)	457.4(10)	27.1(3)
C22B	2624.4(15)	2137.2(13)	0.1(9)	26.2(3)
C23B	3412.2(15)	3880.8(13)	759.6(9)	25.3(3)
C24B	4132.0(16)	4948.6(14)	1073.2(11)	31.6(4)
C25B	1759.0(16)	237.7(14)	-337.5(10)	29.5(4)
C26B	1507.5(16)	-664.0(14)	-831.5(10)	30.1(4)
C27B	1927.2(15)	-648.4(14)	-1512.5(10)	27.9(3)

C28B	2649.1(16)	268.4(14)	-1679.7(10)	30.7(4)
C29B	2910.3(16)	1167.2(14)	-1178.1(10)	29.9(4)
C30B	2538.4(17)	-1952.9(14)	-2631.5(10)	32.2(4)
C32B	2123.4(19)	-2829.5(17)	-3260.8(12)	42.0(5)
C38B	2443.7(15)	1178.9(13)	-510.1(9)	26.0(3)

Table A.3 Anisotropic displacement parameters ($\mathring{A}^2 \times 10^3$) for 1,2-bis[5-(4-acetylthiophenyl)-2-methylthiophen-3-yl]cyclopent-1-ene (**6**). The anisotropic displacement factor exponent takes the form: $-2\pi^2[h^2a^{*2}U_{11}+2hka^*b^*U_{12}+...]$.

Atom	U ₁₁	U ₂₂	U33	U23	U ₁₃	U ₁₂
S1	28.6(2)	29.0(2)	32.8(2)	-0.93(17)	9.63(17)	3.40(17)
S2	30.0(2)	27.5(2)	31.2(2)	-0.06(16)	0.23(16)	11.52(17)
S3	25.9(2)	46.3(3)	48.6(3)	-18.6(2)	5.40(19)	5.3(2)
S4	37.8(2)	39.5(3)	27.6(2)	-4.73(18)	5.55(18)	-5.8(2)
03	30.2(7)	53.9(9)	50.5(9)	-15.2(7)	7.0(6)	7.2(6)
O31	64.8(11)	59.9(10)	31.8(8)	-0.3(7)	10.1(7)	-15.0(8)
C1	37.8(11)	49.0(12)	43.3(11)	-16.1(10)	8.8(9)	3.0(9)
C2	29.1(9)	37.6(10)	29.3(9)	-2.7(7)	3.8(7)	5.8(8)
C4	24.2(8)	35.6(10)	31.6(9)	-5.3(7)	-0.6(7)	7.1(7)
C5	29.9(9)	41.5(10)	28.4(9)	0.2(8)	5.5(7)	6.5(8)
C6	31.3(9)	31.4(9)	31.3(9)	4.5(7)	4.8(7)	6.2(7)
C7	25.1(8)	29.3(9)	26.9(8)	1.1(7)	0.9(6)	8.1(7)
C8	28.0(8)	30.0(9)	27.2(8)	1.5(7)	2.6(7)	5.9(7)
C9	27.4(8)	28.4(9)	32.8(9)	0.8(7)	0.8(7)	5.1(7)
C10	26.1(8)	26.3(8)	29.3(8)	1.6(7)	2.2(7)	4.9(7)
C11	24.5(8)	28.6(9)	24.4(8)	1.7(7)	1.5(6)	1.7(7)
C12	25.3(8)	27.2(8)	26.7(8)	1.7(7)	0.1(6)	6.9(7)
C13	27.6(8)	27.8(9)	29.1(8)	1.5(7)	4.5(7)	6.6(7)
C14	35.0(10)	30.6(9)	37.7(10)	-3.3(8)	10.0(8)	1.7(8)
C15	23.5(8)	28.1(8)	27.9(8)	1.8(7)	3.7(6)	5.1(7)
C16	24.5(9)	46.6(11)	30.2(9)	0.2(8)	1.6(7)	8.2(8)
C17	27.2(9)	53.5(12)	38.8(10)	-3.3(9)	3.2(8)	14.4(9)
C18	26.2(9)	46.7(11)	30.9(9)	-2.8(8)	5.8(7)	9.1(8)
C19	23.0(8)	28.8(8)	27.1(8)	1.9(7)	4.7(6)	4.4(7)
C20	26.9(8)	26.4(8)	23.3(8)	2.1(6)	5.9(6)	2.8(7)
C21	24.7(8)	25.3(8)	25.6(8)	1.4(6)	4.9(6)	6.9(6)
C22	25.5(8)	22.0(8)	25.5(8)	2.6(6)	5.9(6)	5.6(6)
C23	29.7(9)	26.0(8)	28.5(8)	1.7(7)	4.1(7)	6.5(7)

C24	46.0(11)	27.4(9)	36.9(10)	-0.9(8)	-4.3(8)	13.5(8)
C25	28.0(9)	29.2(9)	34.9(9)	-2.5(7)	1.4(7)	9.5(7)
C26	26.9(9)	37.6(10)	36.7(10)	-1.7(8)	-0.4(7)	8.4(8)
C27	30.0(9)	29.6(9)	26.2(8)	0.9(7)	5.3(7)	-0.7(7)
C28	39.0(10)	23.9(8)	33.2(9)	0.5(7)	6.0(8)	7.4(7)
C29	29.7(9)	27.6(9)	35.0(9)	2.3(7)	1.5(7)	8.8(7)
C30	35.7(10)	31.1(9)	30.5(9)	2.3(7)	3.1(7)	3.5(8)
C32	38.9(11)	38.9(11)	38.7(10)	-2.3(8)	6.8(8)	-4.3(9)
C38	23.9(8)	23.6(8)	26.0(8)	4.7(6)	5.4(6)	4.1(6)
S1B	35.0(2)	29.6(2)	29.7(2)	5.06(17)	7.34(17)	14.28(18)
S2B	23.8(2)	27.4(2)	30.6(2)	-1.70(16)	7.27(16)	4.17(16)
S3B	37.2(2)	43.9(3)	24.7(2)	4.31(18)	5.26(18)	-2.7(2)
S4B	31.9(2)	30.5(2)	34.0(2)	-7.20(18)	3.05(18)	3.96(18)
ОЗВ	59.8(10)	50.6(9)	28.1(7)	7.0(6)	1.7(7)	-13.3(7)
O31B	36.3(8)	43.7(8)	48.2(8)	-10.2(7)	6.6(6)	2.6(6)
C1B	34.1(10)	39.6(10)	32.7(9)	-0.4(8)	3.9(8)	3.1(8)
C2B	32.5(9)	33.6(9)	28.1(9)	2.0(7)	6.4(7)	5.3(8)
C4B	27.2(8)	37.4(10)	26.1(8)	4.0(7)	6.8(7)	0.8(7)
C5B	32.7(9)	31.4(9)	41.8(10)	2.2(8)	4.8(8)	5.0(8)
C6B	28.7(9)	31.5(9)	39.7(10)	5.2(8)	1.1(7)	7.8(7)
C 7B	24.2(8)	30.0(9)	27.4(8)	5.9(7)	8.9(6)	4.9(7)
C8B	34.3(9)	32.0(9)	33.2(9)	5.7(7)	4.7(7)	9.6(8)
C9B	33.5(10)	40.2(11)	32.5(9)	9.5(8)	2.0(7)	8.6(8)
C10B	27.8(8)	26.3(8)	26.9(8)	5.2(7)	9.8(7)	6.6(7)
C11B	27.1(8)	23.7(8)	28.4(8)	2.8(6)	7.1(7)	7.0(7)
C12B	27.9(8)	25.2(8)	24.3(8)	2.1(6)	9.0(6)	6.0(7)
C13B	36.1(9)	27.2(9)	25.9(8)	3.5(7)	9.6(7)	9.6(7)
C14B	61.7(13)	26.0(9)	34.2(10)	-0.3(8)	5.6(9)	15.8(9)
C15B	26.6(8)	22.6(8)	29.9(8)	0.0(6)	7.8(7)	5.3(6)
C16B	30.9(9)	38.6(10)	32.8(9)	-4.4(8)	7.6(7)	12.9(8)
C17B	33.0(10)	45.3(11)	40.8(11)	-7.5(9)	2.4(8)	17.2(9)
C18B	26.2(8)	34.8(9)	32.4(9)	-0.4(7)	4.2(7)	7.9(7)
C19B	23.4(8)	22.7(8)	29.1(8)	-0.4(6)	5.7(6)	3.0(6)
C20B	25.1(8)	23.4(8)	24.6(8)	0.2(6)	2.0(6)	5.7(6)
C21B	25.3(8)	25.8(8)	27.2(8)	-1.7(7)	4.4(6)	1.7(7)
C22B	26.2(8)	25.4(8)	25.9(8)	0.8(6)	3.0(6)	5.7(7)
C23B	24.5(8)	24.2(8)	26.3(8)	0.2(6)	2.3(6)	6.1(7)
~	27.5(9)	26.7(9)	37.4(10)	-2.3(7)	5.9(7)	1.8(7)
C24B	27.3()	` '				

C26B	33.9(9)	24.0(8)	31.5(9)	2.5(7)	5.6(7)	5.4(7)
C27B	30.3(9)	25.8(8)	26.8(8)	-0.7(7)	0.6(7)	9.0(7)
C28B	33.8(9)	31.5(9)	27.1(8)	1.2(7)	7.3(7)	8.1(7)
C29B	31.3(9)	28.2(9)	29.9(9)	1.4(7)	7.9(7)	5.5(7)
C30B	36.6(10)	30.6(9)	28.2(9)	-1.4(7)	2.3(7)	9.1(8)
C32B	43.1(11)	41.9(11)	36.7(10)	-12.3(9)	1.2(9)	10.5(9)
C38B	26.6(8)	26.0(8)	24.5(8)	-0.7(6)	1.2(6)	8.0(7)

 $\textbf{\textit{Table A.4} Bond lengths for 1,2-bis [5-(4-acetylthiophenyl)-2-methylthiophen-3-yl] cyclopent-1-ene~(\textbf{\textit{6}}).}$

Atom	Atom	Length/Å	Atom	Atom	Length/Å
S1	C10	1.7291(18)	S1B	C10B	1.7283(18)
S1	C13	1.7193(18)	S1B	C13B	1.7246(19)
S2	C22	1.7284(17)	S2B	C22B	1.7276(17)
S2	C23	1.7286(18)	S2B	C23B	1.7240(17)
S3	C2	1.7717(19)	S3B	C2B	1.7821(19)
S3	C4	1.7712(19)	S3B	C4B	1.7703(19)
S4	C27	1.7698(18)	S4B	C27B	1.7684(17)
S4	C30	1.784(2)	S4B	C30B	1.7887(19)
О3	C2	1.197(2)	ОЗВ	C2B	1.196(2)
O31	C30	1.197(2)	O31B	C30B	1.199(2)
C1	C2	1.502(3)	C1B	C2B	1.498(3)
C4	C5	1.387(3)	C4B	C5B	1.393(3)
C4	C9	1.391(3)	C4B	C9B	1.383(3)
C5	C6	1.379(3)	C5B	C6B	1.379(3)
C6	C7	1.400(2)	C6B	C7B	1.396(3)
C7	C8	1.397(2)	С7В	C8B	1.396(3)
C7	C10	1.463(2)	С7В	C10B	1.465(2)
C8	C9	1.387(3)	C8B	C9B	1.387(3)
C10	C11	1.365(2)	C10B	C11B	1.365(2)
C11	C12	1.427(2)	C11B	C12B	1.430(2)
C12	C13	1.375(2)	C12B	C13B	1.374(3)
C12	C15	1.465(2)	C12B	C15B	1.474(2)
C13	C14	1.488(2)	C13B	C14B	1.494(2)
C15	C16	1.514(2)	C15B	C16B	1.513(2)
C15	C19	1.349(2)	C15B	C19B	1.344(2)
C16	C17	1.531(3)	C16B	C17B	1.530(3)
C17	C18	1.538(3)	C17B	C18B	1.531(3)

C18	C19	1.515(2)	C18B C19B 1.513(2)	
C19	C20	1.473(2)	C19B C20B 1.474(2)	
C20	C21	1.428(2)	C20B C21B 1.426(2)	
C20	C23	1.377(3)	C20B C23B 1.368(2)	
C21	C22	1.363(2)	C21B C22B 1.367(2)	
C22	C38	1.462(2)	C22B C38B 1.467(2)	
C23	C24	1.494(2)	C23B C24B 1.494(2)	
C25	C26	1.386(3)	C25B C26B 1.383(2)	
C25	C38	1.397(2)	C25B C38B 1.401(2)	
C26	C27	1.385(3)	C26B C27B 1.389(2)	
C27	C28	1.389(3)	C27B C28B 1.392(3)	
C28	C29	1.380(3)	C28B C29B 1.387(2)	
C29	C38	1.396(2)	C29B C38B 1.396(2)	
C30	C32	1.496(3)	C30B C32B 1.504(2)	

 $\textbf{\textit{Table A.5} Bond angles for 1,2-bis [5-(4-acetylthiophenyl)-2-methylthiophen-3-yl] cyclopent-1-ene~(\textbf{\textit{6}}).}$

Atom	Atom	Atom	Angle/°	Atom	Atom	Atom	Angle/°
C13	S 1	C10	92.91(9)	C13B	S1B	C10B	92.96(8)
C22	S2	C23	92.95(8)	C23B	S2B	C22B	92.84(8)
C4	S3	C2	103.63(9)	C4B	S3B	C2B	102.23(8)
C27	S4	C30	101.34(8)	C27B	S4B	C30B	106.16(9)
О3	C2	S3	123.60(15)	ОЗВ	C2B	S3B	123.62(15)
О3	C2	C1	125.13(18)	ОЗВ	C2B	C1B	123.93(18)
C1	C2	S3	111.27(14)	C1B	C2B	S3B	112.45(13)
C5	C4	S3	117.06(14)	C5B	C4B	S3B	121.07(15)
C5	C4	C9	119.75(17)	C9B	C4B	S3B	119.67(15)
С9	C4	S3	122.87(15)	C9B	C4B	C5B	119.23(17)
C6	C5	C4	120.41(17)	C6B	C5B	C4B	120.06(18)
C5	C6	C7	120.72(17)	C5B	C6B	C7B	121.62(18)
C6	C7	C10	120.25(16)	C6B	С7В	C8B	117.54(17)
C8	C7	C6	118.35(16)	C6B	C7B	C10B	119.94(16)
C8	C7	C10	121.34(16)	C8B	C7B	C10B	122.52(16)
C9	C8	C7	120.93(17)	C9B	C8B	C7B	121.09(18)
C8	C9	C4	119.80(17)	C4B	C9B	C8B	120.42(18)
C7	C10	S1	119.50(13)	С7В	C10B	S1B	121.50(13)
C11	C10	S1	109.86(13)	C11B	C10B	S1B	109.72(13)
C11	C10	C7	130.60(16)	C11B	C10B	С7В	128.77(16)

C10	C11	C12	114.24(16)	C10B	C11B	C12B	114.52(16)
C11	C12	C15	124.13(16)	C11B	C12B	C15B	122.40(15)
C13	C12	C11	111.82(16)	C13B	C12B	C11B	111.67(16)
C13	C12	C15	123.96(16)	C13B	C12B	C15B	125.85(16)
C12	C13	S 1	111.13(13)	C12B	C13B	S1B	111.11(13)
C12	C13	C14	129.07(17)	C12B	C13B	C14B	129.84(18)
C14	C13	S1	119.79(13)	C14B	C13B	S1B	119.02(14)
C12	C15	C16	120.54(15)	C12B	C15B	C16B	119.86(15)
C19	C15	C12	128.32(16)	C19B	C15B	C12B	128.83(15)
C19	C15	C16	111.08(15)	C19B	C15B	C16B	111.24(15)
C15	C16	C17	102.81(15)	C15B	C16B	C17B	104.27(15)
C16	C17	C18	104.68(15)	C16B	C17B	C18B	105.82(15)
C19	C18	C17	103.29(15)	C19B	C18B	C17B	104.07(14)
C15	C19	C18	110.63(15)	C15B	C19B	C18B	111.31(15)
C15	C19	C20	128.88(16)	C15B	C19B	C20B	127.59(16)
C20	C19	C18	120.48(15)	C20B	C19B	C18B	121.10(15)
C21	C20	C19	121.50(15)	C21B	C20B	C19B	123.74(15)
C23	C20	C19	126.84(16)	C23B	C20B	C19B	124.18(15)
C23	C20	C21	111.65(15)	C23B	C20B	C21B	112.07(15)
C22	C21	C20	114.68(15)	C22B	C21B	C20B	114.18(15)
C21	C22	S2	109.77(12)	C21B	C22B	S2B	109.80(13)
C21	C22	C38	129.06(15)	C21B	C22B	C38B	127.95(16)
C38	C22	S2	121.17(13)	C38B	C22B	S2B	122.24(13)
C20	C23	S2	110.89(13)	C20B	C23B	S2B	111.07(13)
C20	C23	C24	131.00(17)	C20B	C23B	C24B	128.23(16)
C24	C23	S2	118.09(14)	C24B	C23B	S2B	120.66(13)
C26	C25	C38	121.34(17)	C26B	C25B	C38B	120.94(16)
C27	C26	C25	119.94(17)	C25B	C26B	C27B	120.27(17)
C26	C27	S4	121.05(14)	C26B	C27B	S4B	116.63(14)
C26	C27	C28	119.55(16)	C26B	C27B	C28B	119.59(16)
C28	C27	S4	119.40(14)	C28B	C27B	S4B	123.31(14)
C29	C28	C27	120.24(17)	C29B	C28B	C27B	119.86(16)
C28	C29	C38	121.24(17)	C28B	C29B	C38B	121.21(17)
O31	C30	S4	123.27(15)	O31B	C30B	S4B	124.25(15)
O31	C30	C32	123.71(18)	O31B	C30B	C32B	124.87(18)
C32	C30	S4	113.01(14)	C32B	C30B	S4B	110.89(14)
C25	C38	C22	122.14(15)	C25B	C38B	C22B	119.57(15)
C29	C38	C22	120.19(15)	C29B	C38B	C22B	122.42(16)
C29	C38	C25	117.67(16)	C29B	C38B	C25B	118.00(16)

 $\textbf{\textit{Table A.6} Torsion angles for 1,2-bis [5-(4-acetylthiophenyl)-2-methylthiophen-3-yl] cyclopent-1-ene~(\textbf{\textit{6}}).}$

A	В	С	D	Angle/°	A	В	C	D	Angle/°
S1	C10	C11	C12	1.7(2)	S1B	C10B	C11B	C12B	-1.75(19)
S2	C22	C38	C25	2.4(2)	S2B	C22B	C38B	C25B	149.59(14)
S2	C22	C38	C29	-177.34(13)	S2B	C22B	C38B	C29B	-31.8(2)
S3	C4	C5	C6	172.40(15)	S3B	C4B	C5B	C6B	-177.75(15)
S3	C4	C9	C8	-172.82(14)	S3B	C4B	C9B	C8B	176.85(14)
S4	C27	C28	C29	-179.72(14)	S4B	C27B	C28B	C29B	169.58(14)
C2	S3	C4	C5	126.73(15)	C2B	S3B	C4B	C5B	-63.32(17)
C2	S3	C4	C9	-59.69(17)	C2B	S3B	C4B	C9B	118.94(16)
C4	S3	C2	О3	4.7(2)	C4B	S3B	C2B	ОЗВ	5.9(2)
C4	S3	C2	C1	-175.47(16)	C4B	S3B	C2B	C1B	-174.28(14)
C4	C5	C6	C7	0.4(3)	C4B	C5B	C6B	C7B	1.6(3)
C5	C4	C9	C8	0.6(3)	C5B	C4B	C9B	C8B	-0.9(3)
C5	C6	C7	C8	1.4(3)	C5B	C6B	C7B	C8B	-2.3(3)
C5	C6	C7	C10	-175.76(17)	C5B	C6B	C7B	C10B	177.11(17)
C6	C7	C8	C9	-2.2(3)	C6B	С7В	C8B	C9B	1.3(3)
C6	C7	C10	S1	26.2(2)	C6B	С7В	C10B	S1B	169.69(14)
C6	C7	C10	C11	-156.24(19)	C6B	C7B	C10B	C11B	-11.4(3)
C7	C8	C9	C4	1.2(3)	C7B	C8B	C9B	C4B	0.3(3)
C7	C10	C11	C12	-176.02(17)	C7B	C10B	C11B	C12B	179.24(16)
C8	C7	C10	S 1	-150.85(14)	C8B	C7B	C10B	S1B	-11.0(2)
C8	C7	C10	C11	26.7(3)	C8B	C7B	C10B	C11B	167.95(18)
С9	C4	C5	C6	-1.4(3)	C9B	C4B	C5B	C6B	0.0(3)
C10	S1	C13	C12	-0.44(14)	C10B	S1B	C13B	C12B	-0.17(14)
C10	S1	C13	C14	178.46(16)	C10B	S1B	C13B	C14B	-178.22(15)
C10	C7	C8	C9	174.93(16)	C10B	С7В	C8B	C9B	-178.05(17)
C10	C11	C12	C13	-2.1(2)	C10B	C11B	C12B	C13B	1.7(2)
C10	C11	C12	C15	-178.91(16)	C10B	C11B	C12B	C15B	178.53(15)
C11	C12	C13	S1	1.44(19)	C11B	C12B	C13B	S1B	-0.77(19)
C11	C12	C13	C14	-177.32(18)	C11B	C12B	C13B	C14B	177.02(18)
C11	C12	C15	C16	53.2(3)	C11B	C12B	C15B	C16B	-46.5(2)
C11	C12	C15	C19	-129.8(2)	C11B	C12B	C15B	C19B	136.66(19)
C12	C15	C16	C17	158.43(17)	C12B	C15B	C16B	C17B	172.40(16)
C12	C15	C19	C18	-174.15(17)	C12B	C15B	C19B	C18B	175.93(16)
C12	C15	C19	C20	7.2(3)	C12B	C15B	C19B	C20B	-4.2(3)
C13	S1	C10	C7	177.29(14)	C13B	S1B	C10B	С7В	-179.81(14)
C13	S1	C10	C11	-0.71(14)	C13B	S1B	C10B	C11B	1.09(14)
C13	C12	C15	C16	-123.3(2)	C13B	C12B	C15B	C16B	129.91(19)

C13	C12	C15	C19	53.7(3)	C13B	C12B	C15B	C19B	-46.9(3)
C15	C12	C13	S1	178.30(14)	C15B	C12B	C13B	S1B	-177.50(13)
C15	C12	C13	C14	-0.5(3)	C15B	C12B	C13B	C14B	0.3(3)
C15	C16	C17	C18	26.7(2)	C15B	C16B	C17B	C18B	17.0(2)
C15	C19	C20	C21	-144.20(19)	C15B	C19B	C20B	C21B	124.4(2)
C15	C19	C20	C23	37.1(3)	C15B	C19B	C20B	C23B	-56.8(3)
C16	C15	C19	C18	3.1(2)	C16B	C15B	C19B	C18B	-1.1(2)
C16	C15	C19	C20	-175.65(17)	C16B	C15B	C19B	C20B	178.77(16)
C16	C17	C18	C19	-25.1(2)	C16B	C17B	C18B	C19B	-17.6(2)
C17	C18	C19	C15	14.2(2)	C17B	C18B	C19B	C15B	12.0(2)
C17	C18	C19	C20	-166.99(16)	C17B	C18B	C19B	C20B	-167.92(16)
C18	C19	C20	C21	37.2(2)	C18B	C19B	C20B	C21B	-55.7(2)
C18	C19	C20	C23	-141.53(19)	C18B	C19B	C20B	C23B	123.06(19)
C19	C15	C16	C17	-19.0(2)	C19B	C15B	C16B	C17B	-10.2(2)
C19	C20	C21	C22	178.15(15)	C19B	C20B	C21B	C22B	-179.28(16)
C19	C20	C23	S2	-178.77(14)	C19B	C20B	C23B	S2B	179.29(13)
C19	C20	C23	C24	3.0(3)	C19B	C20B	C23B	C24B	-3.0(3)
C20	C21	C22	S2	2.06(19)	C20B	C21B	C22B	S2B	-0.9(2)
C20	C21	C22	C38	-178.33(16)	C20B	C21B	C22B	C38B	178.38(16)
C21	C20	C23	S2	2.39(19)	C21B	C20B	C23B	S2B	-1.80(19)
C21	C20	C23	C24	-175.88(19)	C21B	C20B	C23B	C24B	175.91(17)
C21	C22	C38	C25	-177.15(17)	C21B	C22B	C38B	C25B	-29.6(3)
C21	C22	C38	C29	3.1(3)	C21B	C22B	C38B	C29B	148.95(19)
C22	S2	C23	C20	-1.09(14)	C22B	S2B	C23B	C20B	1.11(14)
C22	S2	C23	C24	177.43(15)	C22B	S2B	C23B	C24B	-176.80(15)
C23	S2	C22	C21	-0.55(13)	C23B	S2B	C22B	C21B	-0.09(14)
C23	S2	C22	C38	179.79(14)	C23B	S2B	C22B	C38B	-179.45(15)
C23	C20	C21	C22	-2.9(2)	C23B	C20B	C21B	C22B	1.8(2)
C25	C26	C27	S4	179.77(15)	C25B	C26B	C27B	S4B	-169.33(14)
C25	C26	C27	C28	-1.2(3)	C25B	C26B	C27B	C28B	3.0(3)
C26	C25	C38	C22	-178.87(17)	C26B	C25B	C38B	C22B	175.64(17)
C26	C25	C38	C29	0.9(3)	C26B	C25B	C38B	C29B	-3.0(3)
C26	C27	C28	C29	1.3(3)	C26B	C27B	C28B	C29B	-2.2(3)
C27	S4	C30	O31	3.4(2)	C27B	S4B	C30B	O31B	5.6(2)
C27	S4	C30	C32	-177.48(15)	C27B	S4B	C30B	C32B	-174.50(14)
C27	C28	C29	C38	-0.2(3)	C27B	C28B	C29B	C38B	-1.2(3)
C28	C29	C38	C22	178.91(16)	C28B	C29B	C38B	C22B	-174.80(17)
C28	C29	C38	C25	-0.9(3)	C28B	C29B	C38B	C25B	3.8(3)
C30	S4	C27	C26	-79.55(17)	C30B	S4B	C27B	C26B	-143.47(14)

C30	S4	C27	C28	101.44(16)	C30B	S4B	C27B	C28B	44.50(18)
C38	C25	C26	C27	0.1(3)	C38B	C25B	C26B	C27B	-0.4(3)

Table A.7 Hydrogen atom coordinates $(\mathring{A} \times 10^4)$ and isotropic displacement parameters $(\mathring{A}^2 \times 10^3)$ for 1,2-bis[5-(4-acetylthiophenyl)-2-methylthiophen-3-yl]cyclopent-1-ene (6).

Atom	X	y	z	U(eq)
H1A	7971.19	8324.98	12944.81	68
H1B	9165.42	8179.11	13404.26	68
H1C	7933.89	7520.78	13569.58	68
Н5	6277.45	4044.87	12148.55	40
Н6	6307.95	2664.25	11288.25	38
Н8	8156.62	4706.72	10065.09	35
Н9	8085.96	6094.21	10915.43	36
H11	8583.47	3080.63	9480.89	32
H14A	5088.88	-17.66	8503.88	53
H14B	5658.6	-529.2	9194.88	53
H14C	6296.17	-342.12	8474.12	53
H16A	9570.35	1040.2	9108.68	41
H16B	9933.68	2026.84	8638.83	41
H17A	9455.17	-140.52	8099.29	48
H17B	10385.41	812.49	7846.69	48
H18A	9000.54	1209.05	6982.26	42
H18B	8343.69	-2.76	6988.41	42
H21	6372.94	-400.07	6518.85	30
H24A	5712.82	3142.93	7583.36	56
H24B	6990.49	3011.09	7899.19	56
H24C	5908.64	2537.56	8310.77	56
H25	2847.87	273.29	5593.67	37
H26	1555.69	-902.53	4656.32	41
H28	3826.51	-2752.05	4708.93	39
H29	5113.68	-1580.33	5644.28	37
H32A	-247.18	-4424.47	3431.37	62
H32B	-1136.13	-4309	4001.46	62
H32C	-294.54	-5082.76	4143.29	62
H1BA	9983.68	9322.86	6583.4	55
H1BB	10319.22	9954.97	5888.11	55
H1BC	10884.08	9002.17	6087.01	55

Н5В	6523.61	7843.36	4911.51	43
H6B	5205.95	6734.07	3958.57	40
H8B	6555.47	4322.51	4563.33	39
H9B	7913.68	5445	5499.03	43
H11B	3646.67	5558.41	3256.74	31
H14D	3479.64	2138.49	1765.13	60
H14E	2319.35	1971.57	2141.21	60
H14F	3435.93	1623.06	2541.32	60
H16C	1523.67	5230.84	2820.88	40
H16D	805.23	4051.24	2874.03	40
H17C	365.28	5354.19	1749.33	47
H17D	-540.91	4355	1966.09	47
H18C	-101.02	3261.13	1100.3	38
H18D	444.47	4302.66	730.69	38
H21B	1139.52	1950.47	476.92	33
H24D	4537.7	4921.21	1581.53	47
H24E	3621.24	5429.29	1096.44	47
H24F	4709.26	5195.62	747.36	47
H25B	1463.34	218.74	125.5	35
H26B	1045.7	-1296.52	-704.49	36
H28B	2962.19	278.34	-2136.41	37
H29B	3415.94	1786.33	-1291.17	36
H32D	1275.65	-3106.56	-3303.3	63
H32E	2519.33	-3386.88	-3153.07	63
H32F	2304.88	-2566.07	-3736.05	63

A.2 Au₂₅-DTE assemblies

A.2.1 Synthesis of [Au₂₅(2PET)₁₈]⁰ building blocks

Purity of the synthesized $[Au_{25}(2PET)_{18}]^0$ clusters was assessed by electronic absorption spectrophotometry, MALDI-TOF-MS and 1H NMR spectroscopy (**Figure A.2** and **Figure A.3**). The MALDI mass spectrum of pure $Au_{25}(2PET)_{18}$ is presented in **Figure 6.3**-g, h.

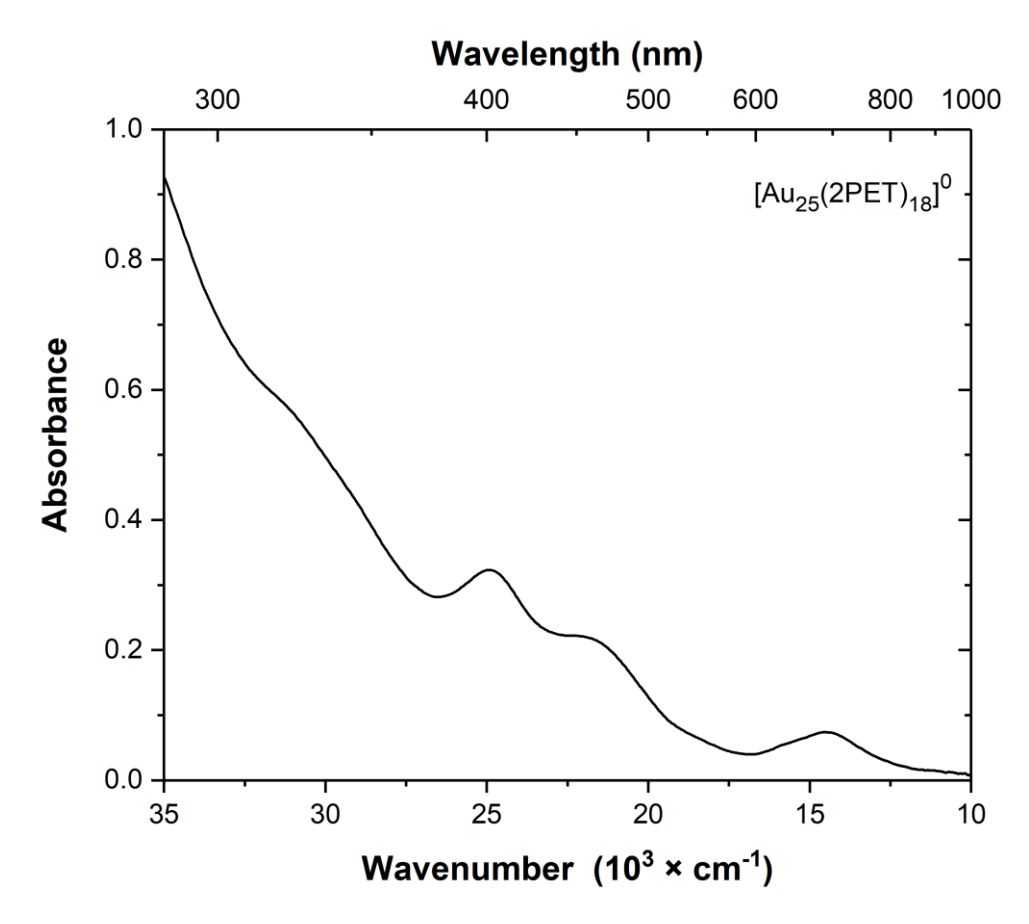


Figure A.2 Steady-state electronic absorption spectrum of [Au₂₅(2PET)₁₈]⁰ in toluene recorded at 298 K.

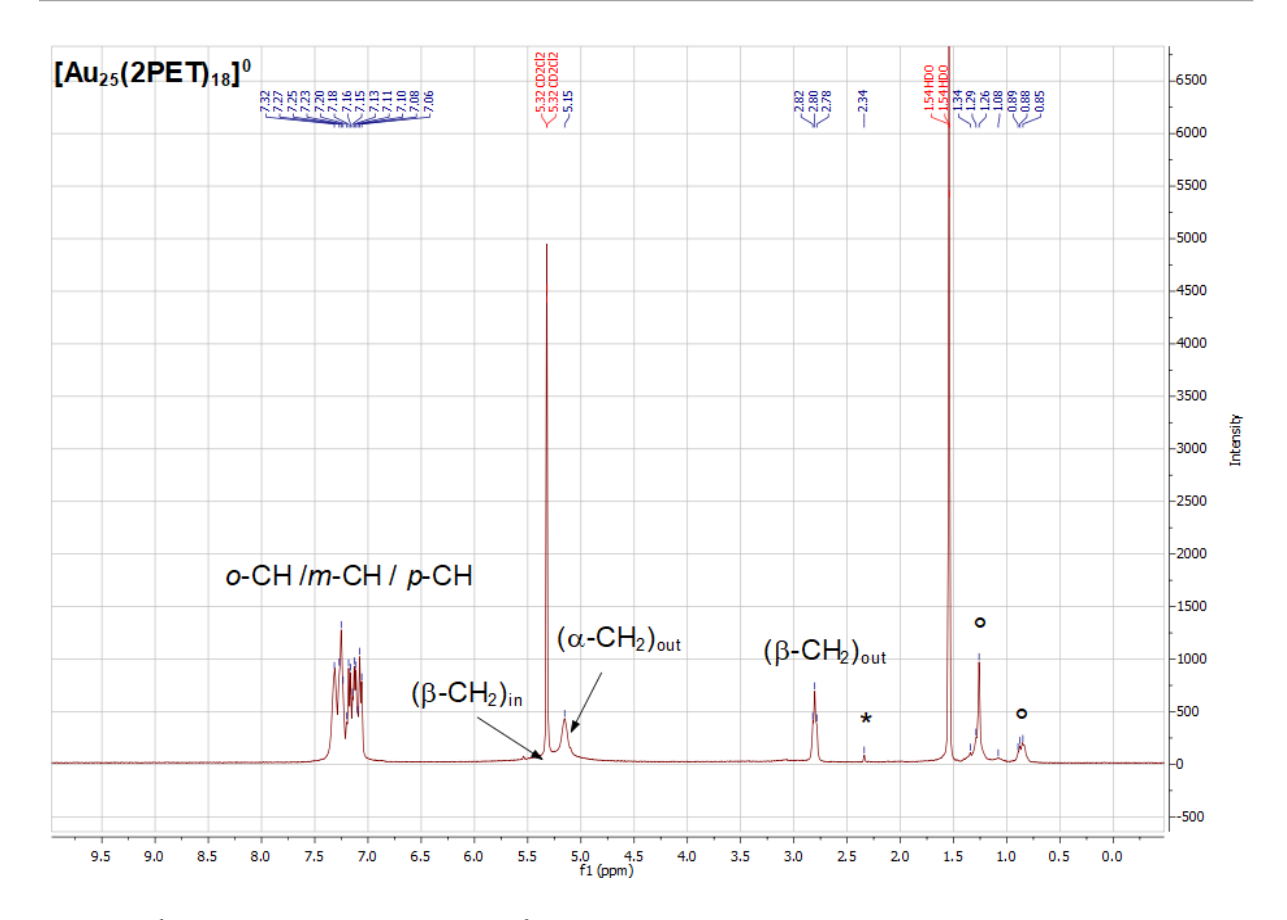


Figure A.3 1 H NMR spectrum of $[Au_{25}(2PET)_{18}]^{0}$ in $CH_{2}Cl_{2}$ - d_{2} at 298 K. (*) denotes the signal from residual toluene; (°) signals are attributed to the pump oil. Assignments made according to Fulmer et al. 3 The 1 H NMR spectrum of $[Au_{25}(2PET)_{18}]^{0}$ in accordance with the reported spectra in the literature. 4

A.2.2 Synthesis of Au₂₅-DTE linked assemblies

Assemblies of Au NCs linked by the **DTE(SH)** ligand were produced via the ligand-exchange method in solution by mixing discrete $[Au_{25}(SC_2H_4Ph)_{18}]^0$ clusters with the freshly synthesized photoligand in a 2:1 Au_{25} -to-**DTE** molar ratio.

Method A:

Freshly purified (SEC column) $[Au_{25}(2PET)_{18}]^0$ clusters (5.12 mg; 0.692 µmol) were dissolved in 0.6 mL of toluene- d_8 and then 20 µL (0.16 mg; 0.336 µmol) of the newly synthesized DTE photoligand in toluene (1.68 mM) was added. The reaction mixture was kept in a dark and slowly mixed for 18 h at 293 K. Next, the sample was loaded on a SEC column and eluted with toluene yielding 3 different colour bands that were isolated as 5 fractions (**Figure A.4**-a).

Method B:

Freshly purified (SEC column) $[Au_{25}(2PET)_{18}]^0$ clusters (5.90 mg; 0.798 μ mol) were dissolved in 3 mL of degassed toluene and then 75 μ L (0.20 mg; 0.425 μ mol) of the newly synthesized DTE photoligand

in degassed toluene (5.66 mM) was added. The reaction mixture was left to stir under nitrogen at ambient temperature in the dark for 24 h. Then, the crude product was washed with MeOH to remove free thiols. The product mix was fractionated on a size-exclusion chromatography (SEC) column (BioBeads S-X1) in toluene. Typically, 3 main separation bands were observed on the column (see **Figure A.4**-b), and were isolated as main fractions denoted, **F1**, **F3**, and **F5**. All fractions were analysed with standard characterization techniques: UV-vis-NIR spectroscopy and MALDI-MS analysis and compared with the pure [Au₂₅(2PET)₁₈]⁰ clusters.

A.2.3 SEC of the crude mixture of Au₂₅ assemblies

a

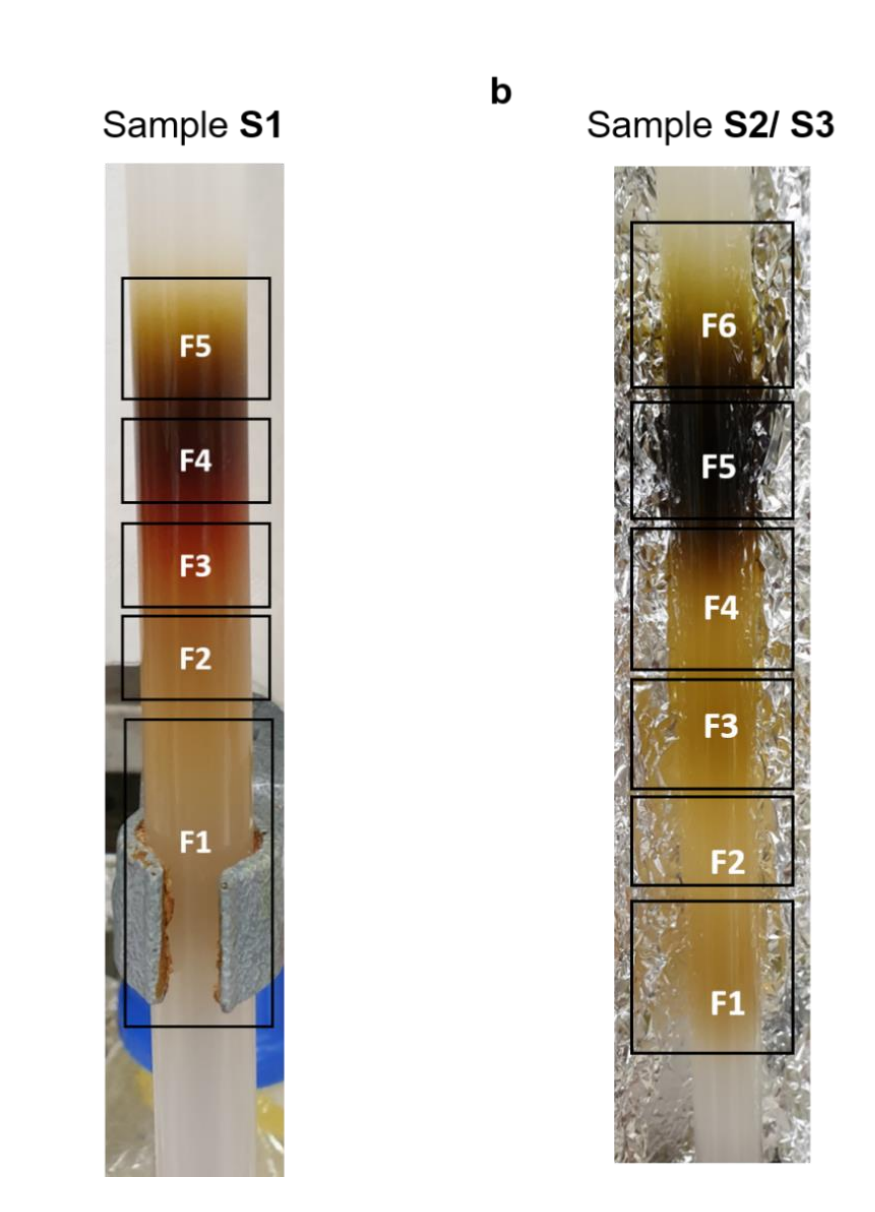


Figure A.4 Digital photograph of size-exclusion chromatography columns depicting separation of the mix of products after the ligand-exchange reaction during which the Au₂₅ assemblies were formed (a) SEC column for the S1 sample; (b) SEC column for optimized reaction producing the S2 and S3 samples.

A.2.4 MALDI-TOF-MS

Table A.8 Calculated MALDI m/z (for z = 1, 2) values of the symmetric and non-symmetric Au₂₅ dimers connected with a DTE linker.

species	notation	<i>M</i> ⁺ m/z	M^{2+} m/z
		calculated	calculated
$Au_{25}(2PET)_{17}$ -oDTE- $Au_{25}(2PET)_{17}$	0-0	14981.85	7490.93
SYMMETRICA	L DIMERS		
$Au_{25}(2PET)_{15}(oDTE^2)-oDTE-Au_{25}(2PET)_{15}(oDTE^2)$	1–1	15381.81	7690.90
$Au_{25}(2PET)_{13}(oDTE^2)_2 - oDTE - Au_{25}(2PET)_{13}(oDTE^2)_2$	2–2	15781.76	7890.88
$Au_{25}(2PET)_{II}(oDTE^2)_3 - oDTE - Au_{25}(2PET)_{II}(oDTE^2)_3$	3–3	16181.71	8090.85
NON-SYMMETRI	CAL DIMERS		
$Au_{25}(2PET)_{17}$ - $oDTE$ - $Au_{25}(2PET)_{15}(oDTE^2)$	0–1	15181.83	7590.91
$Au_{25}(2PET)_{17}$ - $oDTEAu_{25}(2PET)_{13}(oDTE^2)_2$	0–2	15381.81	7690.90
$Au_{25}(2PET)_{17}$ - $oDTE$ - $Au_{25}(2PET)_{11}(oDTE^2)_3$	0–3	15581.78	7790.89
$Au_{25}(2PET)_{15}(oDTE^2)-oDTE-Au_{25}(2PET)_{13}(oDTE^2)_2$	1–2	15581.78	7790.89
$Au_{25}(2PET)_{I5}(oDTE^2)-oDTE-Au_{25}(2PET)_{II}(oDTE^2)_3$	1–3	15781.76	7890.88
$Au_{25}(2PET)_{13}(oDTE^2)_2 - oDTE - Au_{25}(2PET)_{11}(oDTE^2)_3$	2–3	15981.73	7990.87
0: Au ₂₅ (2PET) ₁₇ ; 1: Au ₂₅ (2PET) ₁₅ (oDTE ²); 2: Au ₂₅ (2PE	$(ET)_{13}(oDTE^2)_2;$	3: Au ₂₅ (2PET) ₁₁ (c	$ODTE^2$)3

A.3 Actinometry

In order to determine the photoswitching quantum yields of the unknown samples, the photoirradiation setup was tested by measuring a system with known quantum yield. Here, the actinometric system that deemed suitable for validation with spectroscopic detection was the o-nitrobenzaldehyde \rightarrow o-nitrosobenzoic acid photoisomerization (see **Scheme A.1**).^{5,6}

Scheme A.1 Photochemical transformation of o-nitrobenzaldehyde to o-nitrosobenzoic acid under UV light irradiation.

o-nitrobenzaldehyde is a commonly used actinometer with the quantum yield of ~ 0.5 reported over its 300–410 nm absorption spectral region.⁷

The electronic absorption spectrum of the o-nitrobenzaldehyde (reactant) is depicted in **Figure A.5** (black line for 0 s). The measurements were performed with 340 nm light irradiation of 1 mL of 1.33×10^{-4} M solution of o-nitrobenzaldehyde in acetonitrile for ~ 35 min until the photostationary state (PSS) was reached. During the photoirradiation the decrease in the absorption band at 40,000 cm⁻¹ (250 nm) with concomitant increase of two bands at 35,220 cm⁻¹ (284 nm) and 32,474 cm⁻¹ (308 nm) was evident.

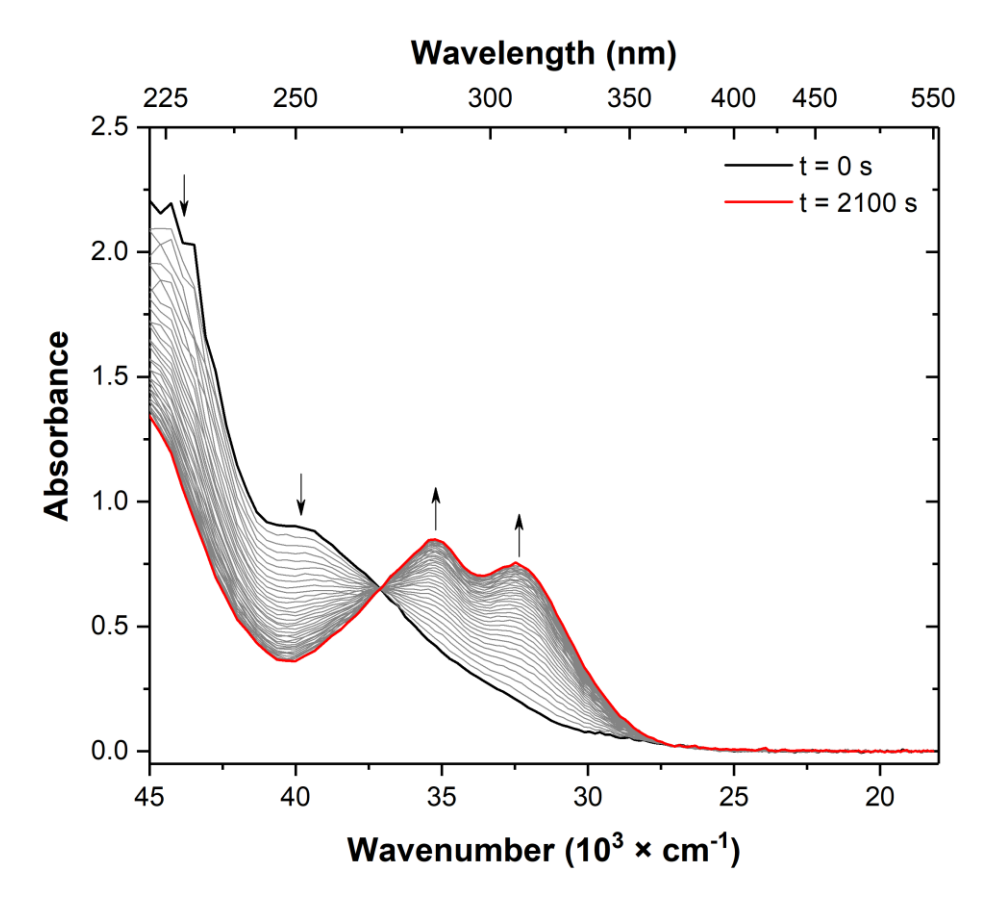


Figure A.5 Temporal evolution of electronic absorption spectra of o-nitrobenzaldehyde upon irradiation with 340 nm light. Spectra acquired in acetonitrile at 298 K.

Clear isosbestic point at 37,090 cm⁻¹ (270 nm) was observed. However, closer inspection revealed that after \sim 10 min the isosbestic point started to shift (see **Figure A.6**). This behaviour is attributed to the degradation of the formed *o*-nitrosobenzoic acid product as it undergoes further transformation to a byproduct after the photon absorption, a phenomenon that has also been reported by others.^{8,9}

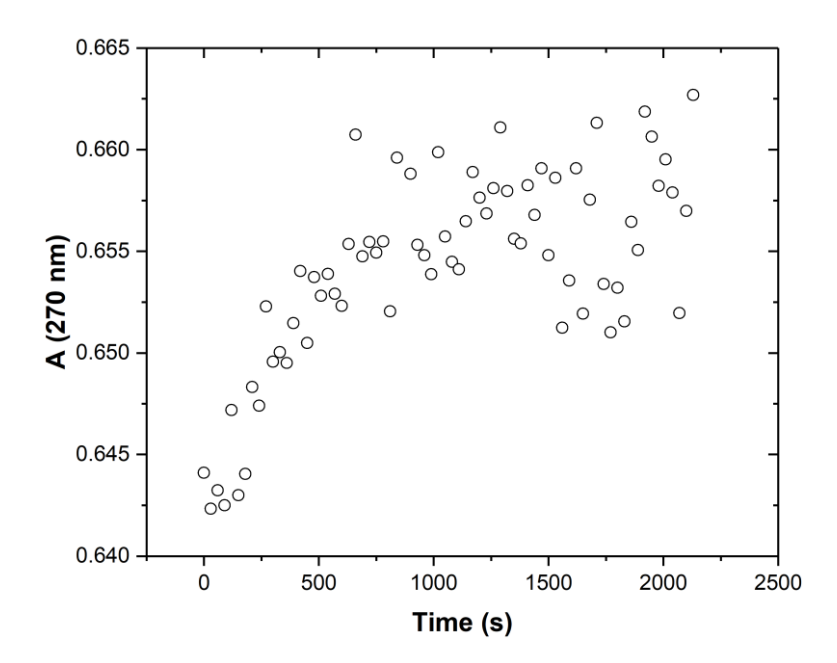


Figure A.6 Change in the position of the isosbestic point at 270 nm as a function of time. Due to the shift in the position of isosbestic point only the data points of the first 10 min of the experiment were used for the calculations of the quantum yields.

Monitoring the isosbestic point is important for determination of the spectra of the individual components participating in the photoreaction. Specifically, the invariance of the isosbestic point position allows assumption of the simple reaction reactant \rightarrow product that is occurring. As soon as that position starts to shift the reactant-to-product model fails, because the obtained product undergoes the follow-up reaction. This scenario is observed in the case of o-nitrobenzaldehyde after 10 min of the irradiation experiment (see **Figure A.6**).

Determination of the basis spectra of the species that participate in the photoreaction is crucial for the calculation of the photoreaction quantum yield. The spectrum of the pure o-nitrosobenzaldehyde is the first spectrum recorded during the time-scan experiment (black trace in **Figure A.5**), given that the photoreaction is not excessively fast. Additionally, the spectrum of o-nitrobenzaldehyde was acquired without the 340 nm irradiation, and these two spectra matched perfectly (data not shown here). The spectrum of the product (i.e., o-nitrosobenzoic acid) was obtained by taking the spectrum acquired after 10 min of the reaction and subtracting from it the spectrum corresponding to the o-nitrobenzaldehyde that was still left in the reaction mixture (scaled by factor k), according to **Equation A.1**:

$$S_{o-nitrosobenzoic\ acid}(\lambda) = \frac{A(\lambda, 10\ min) - kS_{o-nitrobenzaldehyde}}{1 - k}$$
 A.1

The resulting spectrum was compared to the spectrum of the o-nitrosobenzoic acid obtained by Stadler et al. who investigated the same photoreaction but under 385 nm LED irradition. Under these conditions, no formation of by-product from the o-nitrosobenzoic acid irradiation was demonstrated. Moreover, full

conversion of the starting *o*-nitrobenzaldehyde was shown. This allowed extraction of the spectrum of the by-product that was forming during the photoreaction.

With the established basis spectra of the species of interest, the concentration of each species, c_i , at each time point was obtained by decomposing every spectrum of the illumination experiment, $A(t_i, \lambda)$, into these basis spectra by solving the linear system of equations (**Equation A.2**):

$$A(t_i, \lambda) = \left(\epsilon_1(\lambda) \dots \epsilon_m(\lambda)\right) \begin{pmatrix} c_1(t_i) \\ \vdots \\ c_m(t_i) \end{pmatrix}$$
 A.2

These concentration dependences are then simulated/fitted (until reasonable residuals are obtained) using the approach described by Volfova et al. Briefly, it consists of solving the system of ordinary differential equations for the individual concentrations (**Equation A.3**), which contain a time-dependent pump-term (i.e., number of photons absorbed at each time step by the reactant), that corrects for the inner-filter effect due to absorption of species other than the reactant (here, *o*-nitrobenzaldehyde).

$$\frac{dc(t)}{dt} = K(t)c(t)$$
 A.3

where $\mathbf{c}(t)$ is the (time-dependent) concentration vector and $\mathbf{K}(t)$ is the (time-dependent) Kirchhoff-matrix, the off-diagonal elements of which are given by **Equation A.4**:

$$K_{ji} = \frac{\Phi_{ji}}{VN_A} \int \frac{\varepsilon_i(\lambda)d}{A(t,\lambda)} \left(1 - 10^{A(t,\lambda)}\right) f(\lambda) \frac{P(t)\lambda}{hc} d\lambda$$
 A.4

and the diagonal elements, K_{ii} , are given by **Equation A.5**

$$K_{ii} = -\sum_{i \neq i} K_{ji}$$
 A.5

Here, Φ_{ji} is the quantum yield associated with the reaction from c_i to c_j and $\varepsilon_i(\lambda)$ and d are the extinction coefficient spectrum of species i and the optical pathlength, respectively. V is the sample volume (in cm³), N_A – the Avogadro number, $A(t,\lambda)$ is the total sample absorbance, $f(\lambda)$ is the spectrum of the irradiation light source (see **Figure 3.1**) and P(t) is (time-dependent) power. h and c are the Planck constant and the speed of light, respectively.

In the simplest case, e.g., for *o*-nitrobenzaldehyde (assuming no follow-up reactions are taking place), **K** is given by **Equation A.6**:

$$K = \begin{pmatrix} -K_{21} & 0 \\ K_{21} & 0 \end{pmatrix}$$
 A.6

With the known basis spectra of the species involved in the photoreaction (red traces in **Figure A.7**), the only optimization parameters are the quantum yields, Φ_{ji} , and the initial conditions, i.e., $\mathbf{c}(0)$.

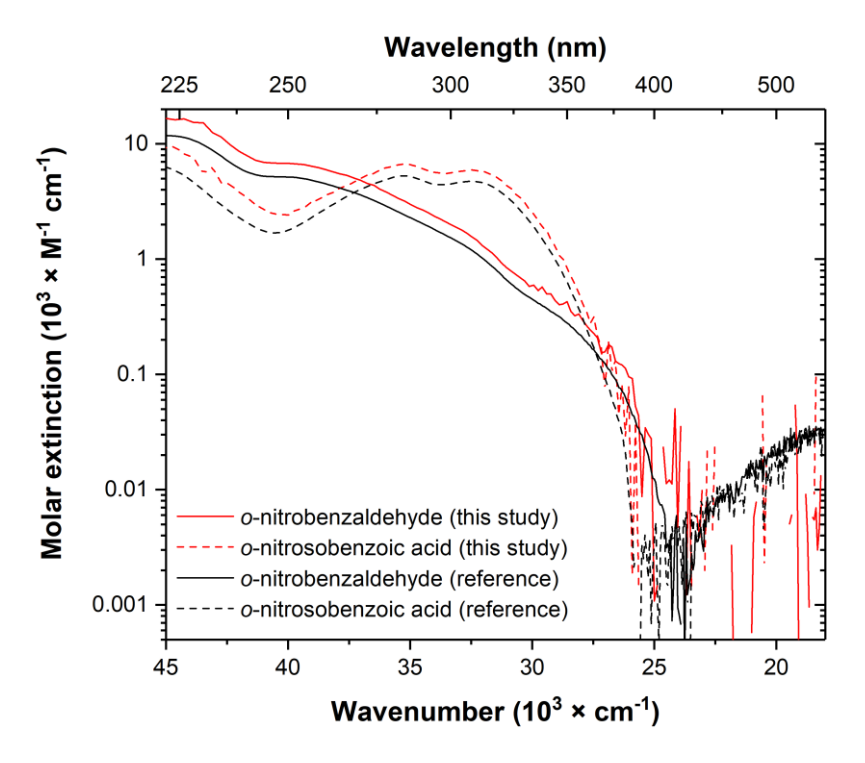


Figure A.7 UV-vis absorption spectra of the two species involved in the photoreaction ($\lambda_{irr} = 340$ nm): o-nitrobenzaldehyde (solid lines) and o-nitrosobenzoic acid (dashed lines). The spectra obtained in this study (red traces) were juxtaposed with the spectra reported by Stadler et al.¹⁰ performing the irradiation at 385 nm.

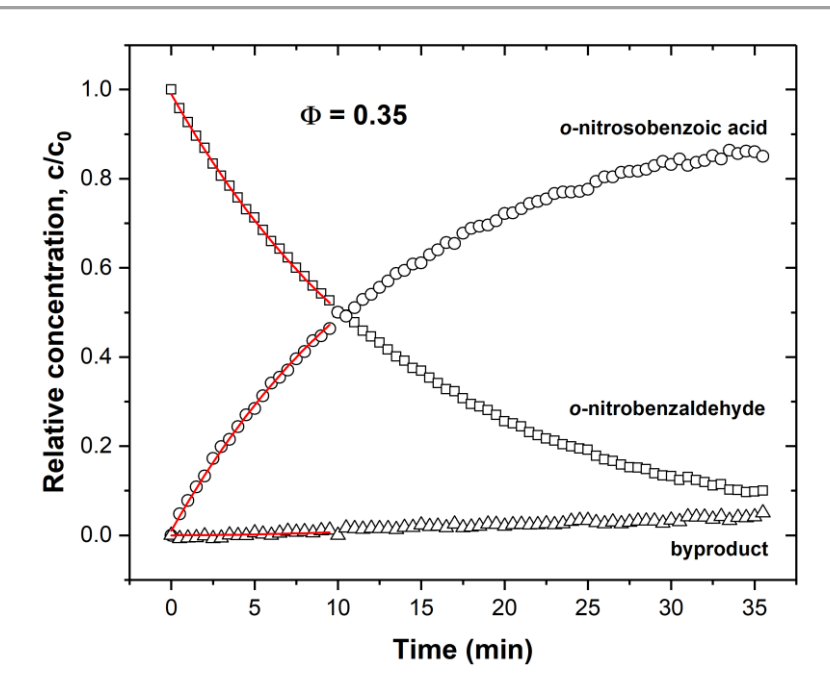


Figure A.8 Time evolution of the concentrations during the photoirradiation experiment of o-nitrobenzaldehyde in acetonitrile after illumination with 340 nm light.

The two most recent publications that reporting on the quantum yield of o-nitrobenzaldehyde photoreaction, using an identical approach that was employed in this study, have obtained similar values of Φ : 0.43 ± 0.02^{10} and 0.41, which is quite surprising given that the data analysis used by the two groups was different. More specifically, Stadler at al. analysed only the initial slope after the sample was excited at 385 nm. On the other hand, Volfova et al. performed similar analysis to the one presented in this study and their sample was also excited at 340 nm.

Interestingly, however, there are very large uncertainties found for the excitation coefficient, ε , of o-nitrobenzaldehyde (**Table A.9**).

Table A.9 Molar extinction of o-nitrobenzaldehyde obtained from different studies.

	Ref [¹⁰]	Ref [9]	Ref [11]	this study
ε (225 nm)/ M^{-1} cm ⁻¹	11 800	15 200	14 300	16 600

Even though there is almost a 40 % spread in the value of molar extinction, the reported quantum yield values are almost the same. This requires further investigation that was outside of the scope of this thesis.

The quantum yield value for o-nitrobenzaldehyde photoreaction excited at 340 nm obtained in this study was 0.35 ± 0.005 .

A.4 Photoswitching of the isolated Au₂₅ assemblies

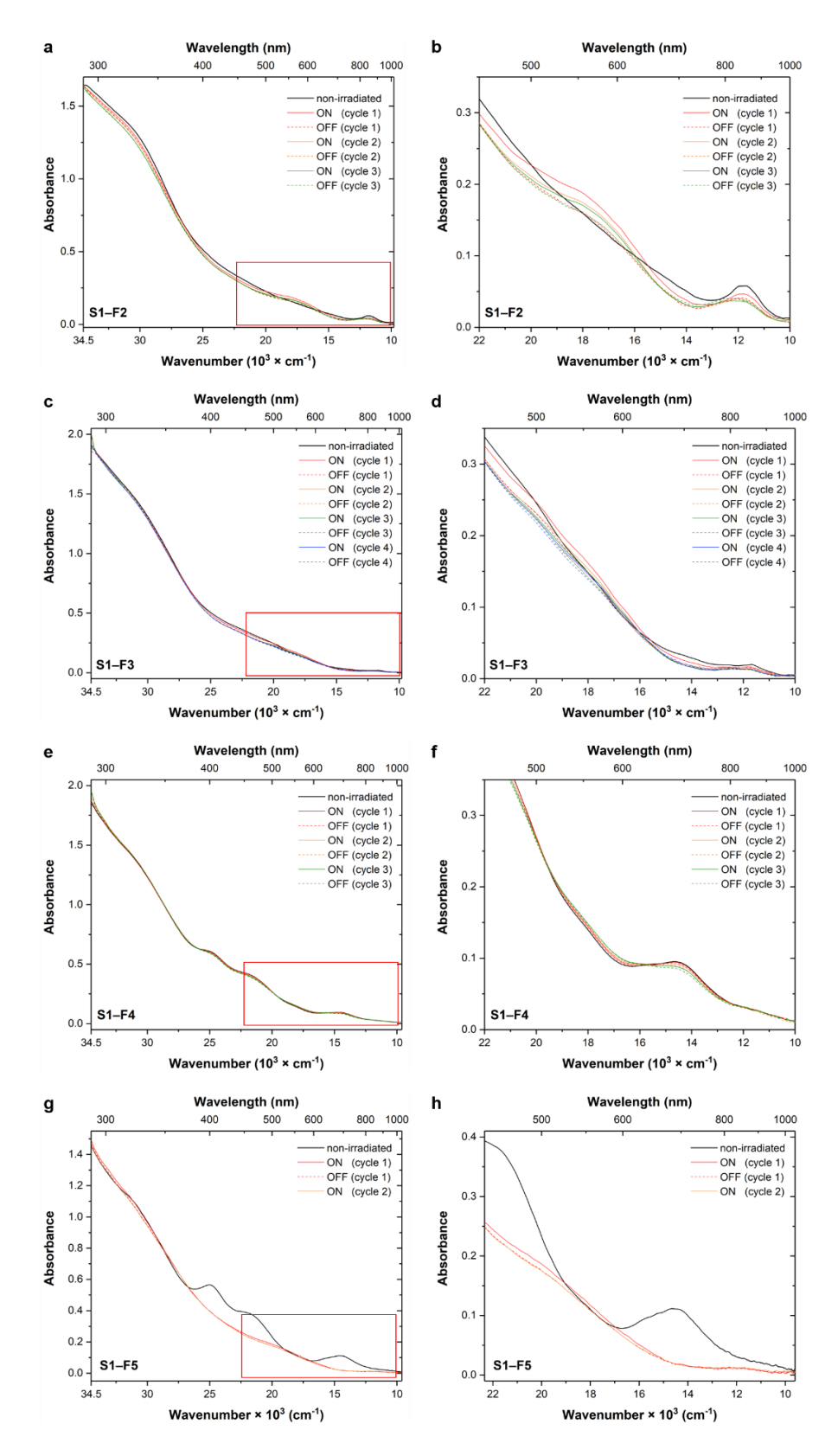


Figure A.9 UV-vis-NIR spectra of different size fractions of the **S1** sample exposed to photoirradiation. The spectra of the non-irradiated sample are shown as black traces. The irradiation with UV light produced ON samples (solid lines), and visible light—OFF samples (dashed lines). Spectra acquired in toluene at 298 K.

A.5 Stability of $[Au_{25}(2PET)_{18}]^0$ nanoclusters upon light irradiation

Electronic absorption spectra of $[Au_{25}(2PET)_{18}]^0$ ($c = 2.26 \times 10^{-5}$ M) cluster solution in toluene monitored with constant irradiation with 340 nm light (1.24 mW) for 17 h.

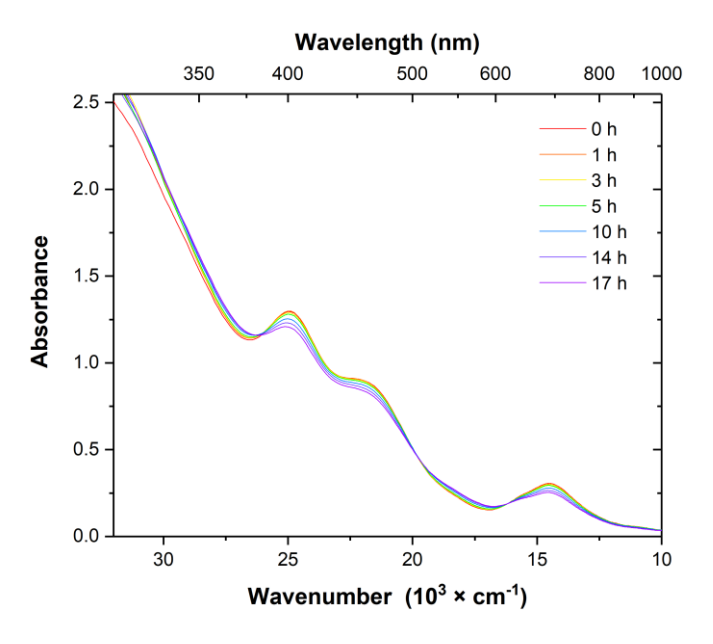


Figure A.10 Temporal changes in the UV-vis-NIR spectra of $[Au_{25}(2PET)_{18}]^0$ in toluene $(2.26 \times 10^{-5} \text{ M})$ during irradiation with UV light.

Electronic absorption spectra of $[Au_{25}(2PET)_{18}]^0$ ($c = 5 \times 10^{-6}$ M) cluster solution in toluene monitored with constant irradiation with 532 nm light (23.7 mW) for 14 h.

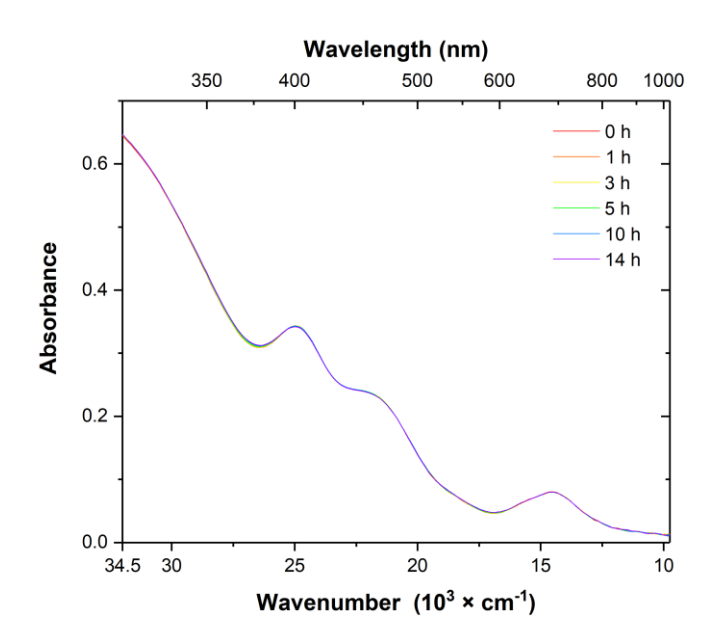


Figure A.11 Temporal changes in the UV-vis-NIR spectra of $[Au_{25}(2PET)_{18}]^0$ in toluene $(6.05 \times 10^{-6} \text{ M})$ during irradiation with visible (532 nm) light.

A.6 Photoluminescence of free DTE(SH) linker

The photoluminescence spectrum of the **DTH(SH)** linker were recorded after the UV illumination of the o-DTE isomer yielding the closed-ring product.

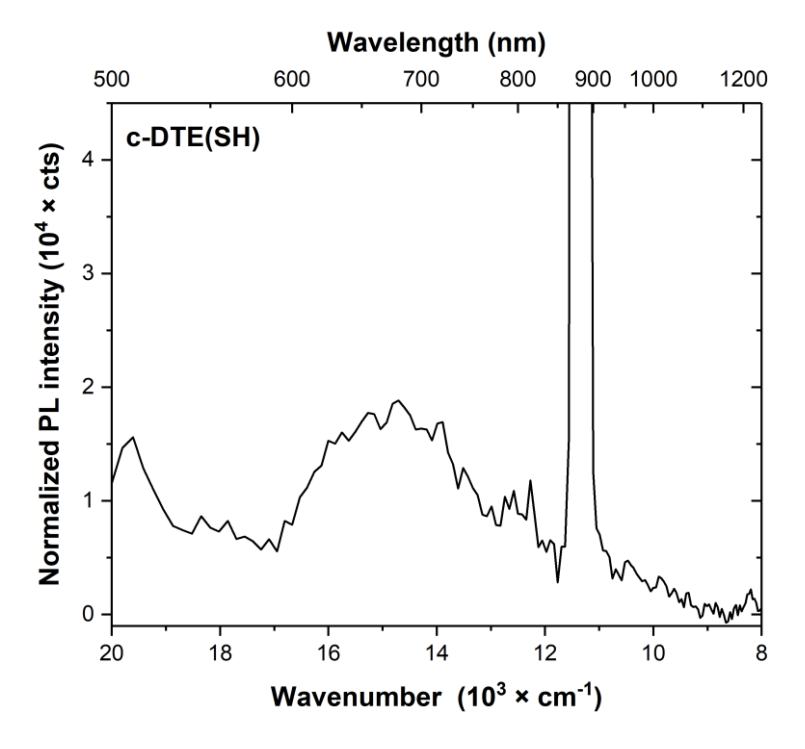


Figure A.12 Steady-state photoluminescence spectrum of c-DTE(SH) linker in toluene solution excited at 440 nm. The intense signal around 11,300 cm $^{-1}$ originated from the second order diffraction.

A.7 HR-TEM study of photoirradiated small Au₂₅ assemblies

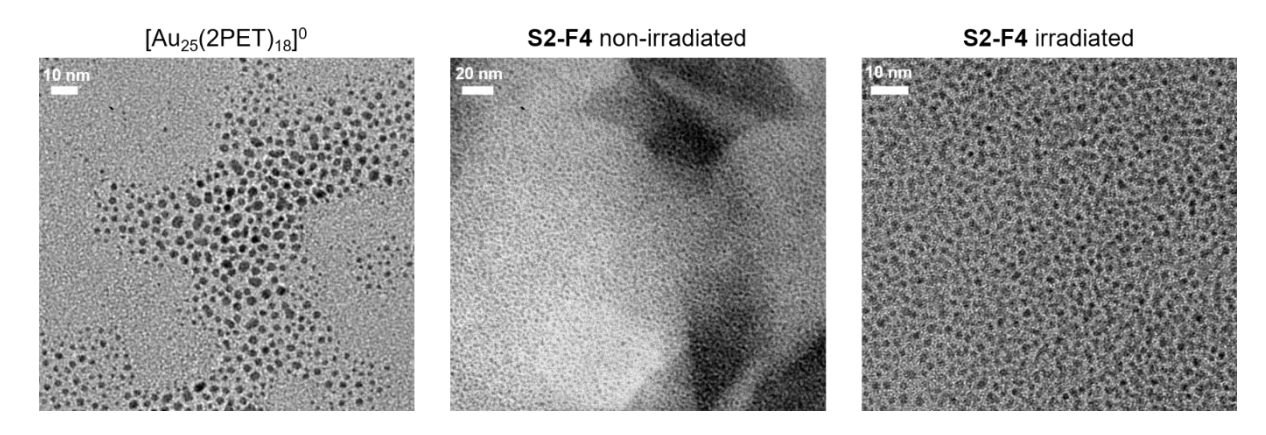


Figure A.13 HRTEM images of pure [Au₂₅(2PET)₁₈]⁰ and the **S2-F4** sample in two irradiation states. The irradiated sample was exposed to two ON/OFF cycles. Samples were prepared by drop-casting the solution of analyte and air-drying for several hours.

A.8 Characterization of the S3 sample containing mixture of monomers and dimers

A.8.1 MALDI-TOF-MS

MALDI-MS analysis of the starting **S3** sample showed the distinctive fragmentation pattern of the $Au_{25}(SR)_{18}$ cluster with the loss of four Au–SR units (**Figure A.14**). Additionally, the peaks were observed corresponding to the $Au_{25}(SR)_{18}$ species with 2PET ligands exchanged for dithiol **o-DTE** molecules, anchored through a bidentate mode, yielding Au_{25} clusters with (i) one dithiol molecule $(Au_{25}(2PET)_{16}(\mathbf{o-DTE^2}), m/z = 7591 \text{ Da})$ or (ii) two **o-DTE** $(Au_{25}(2PET)_{12}(\mathbf{o-DTE^2})_2, m/z = 7791 \text{ Da})$ in their ligand shell.

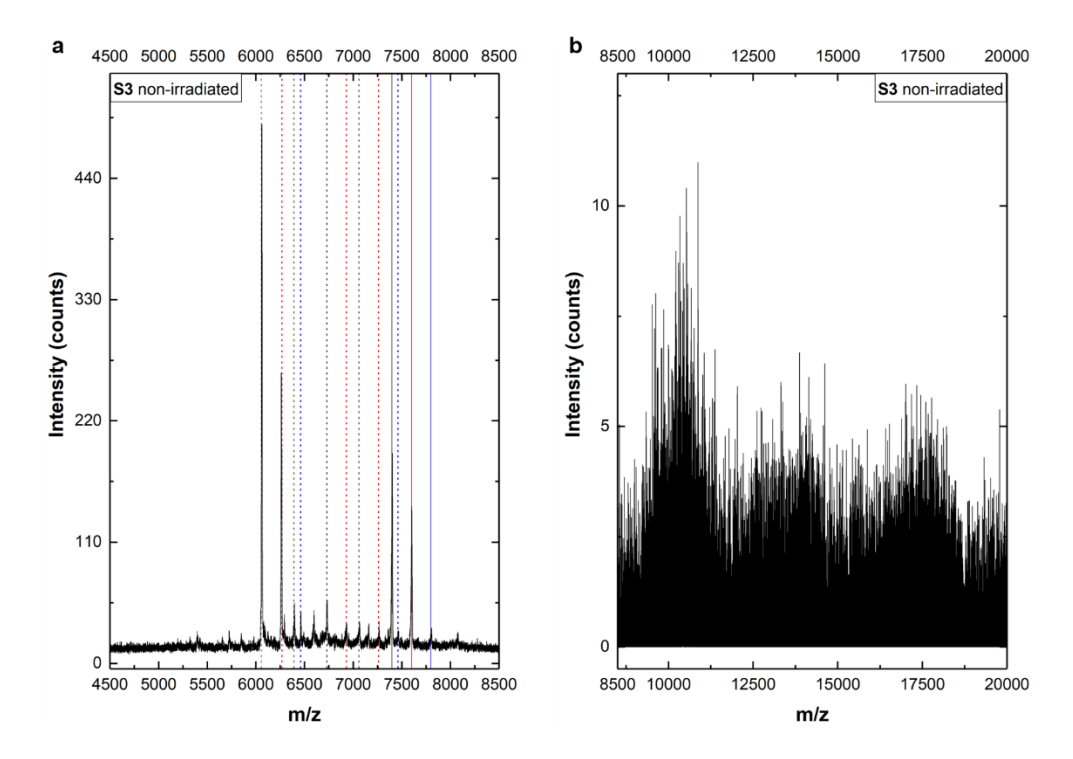


Figure A.14 MALDI mass spectrum of S3 non-irradiated sample acquired in linear positive mode at 20% laser fluence. The solid lines denote the monoisotopic mass peaks of $Au_{25}(2PET)_{18}$, in grey; $Au_{25}(2PET)_{16}(o-DTE^2)$, in red; and $Au_{25}(2PET)_{14}(o-DTE^2)_2$, in blue. Corresponding mass fragments are indicated with dotted lines.

A.8.2 ¹H NMR spectroscopy

The ¹H NMR spectrum of the **S3** sample, depicted in **Figure A.15**, showed no difference between the pure $[Au_{25}(SR)_{18}]^0$ cluster and the mixture of monomers and dimers in the **S3** sample, suggesting that either the monomers were the dominant fraction in the **S3** sample, or that the dimeric structures were undistinguishable from monomers since the protons in the Au_{25} clusters greatly outnumbered these in

the **o-DTE** linker. For the simplest dimer, $Au_{25}(2PET)_{17}$ -oDTE- $Au_{25}(2PET)_{17}$, the ratio of protons H_{Au25} : $H_{oDTE} = 306:24$, making these species difficult to detect.

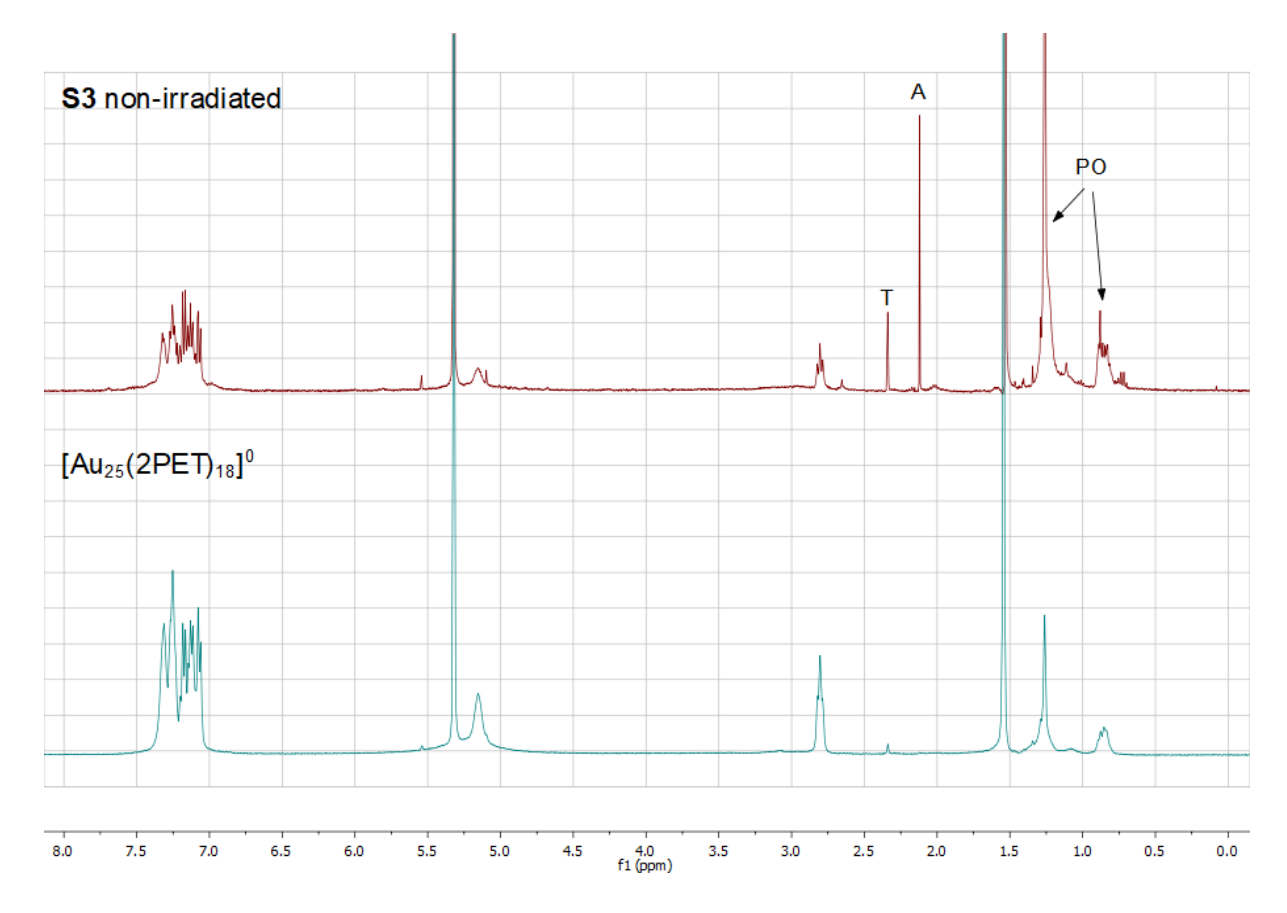


Figure A.15 ¹H NMR spectra of [Au₂₅(2PET)₁₈]⁰ and the S3-non-irradiated sample acquired in CH₂Cl₂-d₂ at 298 K. A– signals from acetone, T– toluene, and PO– signals from pump oil. Assignment of the residual signals was made according to the data published by Fulmer at al.³

A.8.3 UV-vis-NIR spectroscopy

Figure A.16 depicts the optical absorption spectra of the S3 sample after various irradiation events. The normalized spectra (at 25,000 cm⁻¹; 400 nm) of both non-irradiated S3 and pure [Au₂₅(2PET)₁₈]⁰ depicted in Figure A.16-a showed similarities in the visible part of the spectrum, the evident difference being the stronger absorption of the S3 sample at the frequencies below 25,000 cm⁻¹ which was ascribed to the strong absorption of the o-DTE photoligand in this spectral region. The irradiation experiments were carried out with the experimental set-up described in Section 3.3. The S3 sample was prepared by combining the almost identical (in terms of their absorption spectra) products isolated from several batches (synthesized under identical conditions) and dissolving them in toluene. The as-obtained solution was split into two portions (1:2, vol/vol), the smallest of which was kept intact, called hereafter as "S3 non-irradiated". The second portion was divided into 15 aliquots of 100 μL. Each aliquot was diluted to 1200 μL (c ≈ 0.2 mg/mL) and subsequently exposed to UV irradiation under constant stirring for about 1 h (~98 % conversion from open- to closed-ring form according to the fitting of the data, not

shown here). After irradiation, the toluene solvent was removed under reduced pressure. This procedure was repeated for all remaining aliquots. Next, the UV-irradiated sample was dissolved in toluene and again divided into two portions (1:1, vol/vol). The first part was reserved for SAXS measurements ("S3 UV-irradiated") and the second portion was exposed to visible light irradiation by dissolving the "S3 UV-irradiated" in toluene (0.2 mg/mL per aliquot) and irradiating under constant stirring for about 12 h (98 % conversion from closed- to open-ring DTE isomer) to obtain "S3 vis-irradiated" sample. The electronic absorption spectra of photoirradiated samples still possessed the characteristic bands of $[Au_{25}(2PET)_{18}]^0$ species (Figure A.16-b), indicating the electronic structure of clusters in the S3 sample was largely preserved. Noticeable differences could be found in the 16,667–20,000 cm⁻¹ (500–600 nm) and > 31,000 cm⁻¹ (< 322 nm) regions, as expected, where the **c-DTE** photoligand absorbs, indicating that the photoreaction has occurred.

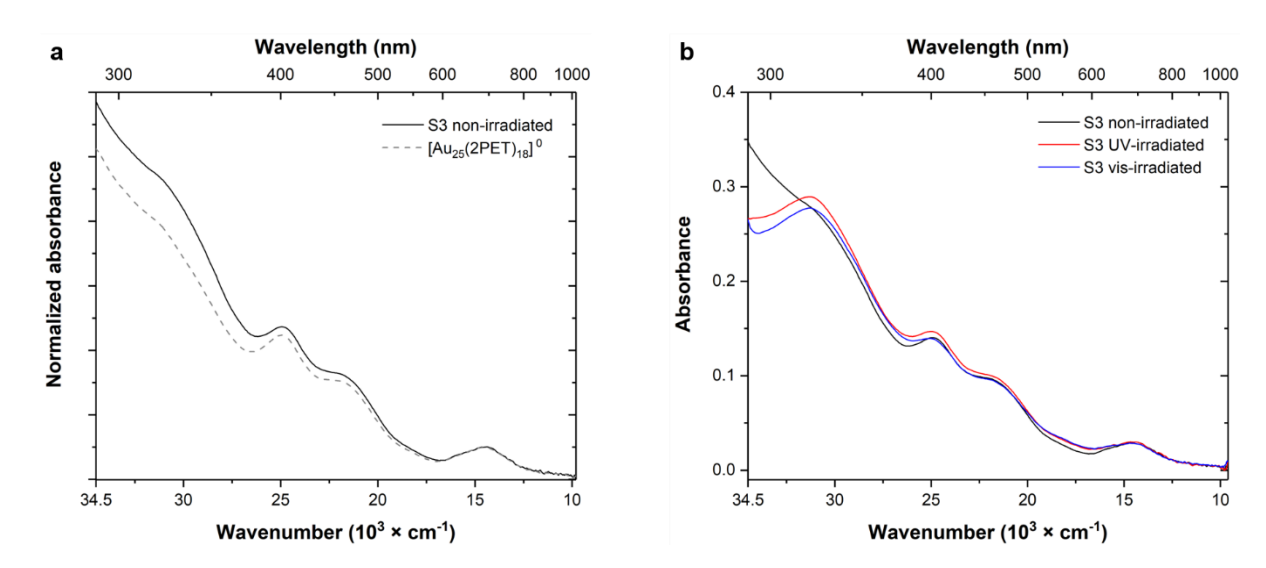


Figure A.16 UV-vis-NIR spectra of (a) non-irradiated S3 sample (solid line) showing the large resemblance of the electronic structure to monomeric $[Au_{25}(2PET)_{18}]^0$; (b) S3 sample in different irradiation states—non-irradiated (black), UV-irradiated (red) and vis-irradiated (blue).

A.8.4 Steady-state photoluminescence

The photoluminescence properties of the S3 sample after the photoswitching was investigated with steady-state photoluminescence spectroscopy in solution. Comparably to the S2-F4 sample, a significant rise in the PL emission intensity, accompanied by a red-shift in emission signal, is observed for the S3 vis-irradiated sample (Figure A.17-a, b).

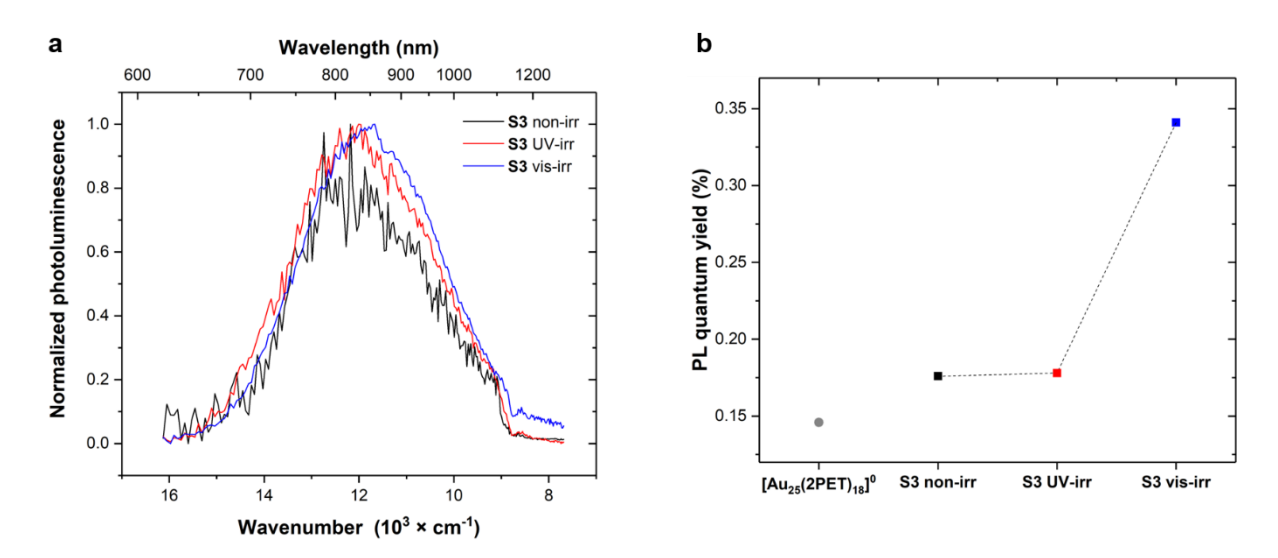


Figure A.17 Steady-state photoluminescence spectra of the S3 sample before and after UV and visible light irradiation. (a) Normalized spectra depicting red shift of the emission peak maximum after visible light irradiation experiment; (b) Evolution of a PL quantum yield of S3 sample with light irradiation. Samples were measured in toluene at 293 K, excitation wavelength—440 nm lambda excitation, bandpass slits 3 nm, right angle geometry.

A.8.5 SAXS

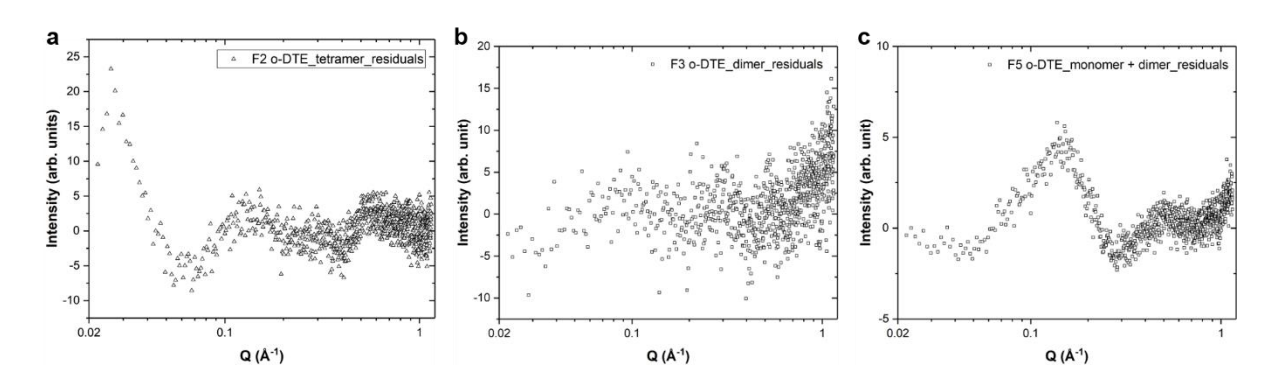


Figure A.18 Residuals from SAXS data fitting of fraction linked with open-form isomer of DTE photoligand using (a, b) pearlnecklace and (c) mixed 'sphere +pearl-necklace' model.

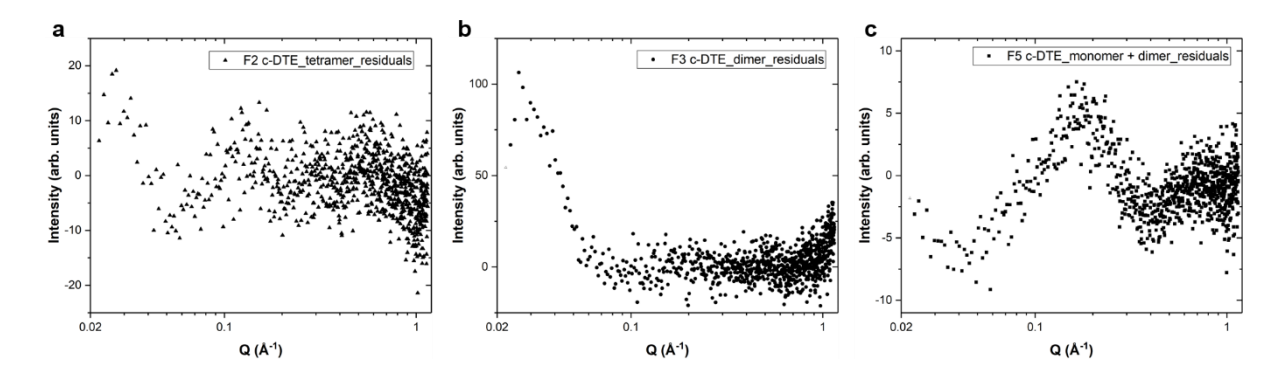


Figure A.19 Residuals from SAXS data fitting of fraction linked with closed-form isomer of DTE photoligand using (**a**, **b**) pearlnecklace and (**c**) mixed 'sphere +pearl-necklace' model.

A.8.6 DOSY NMR

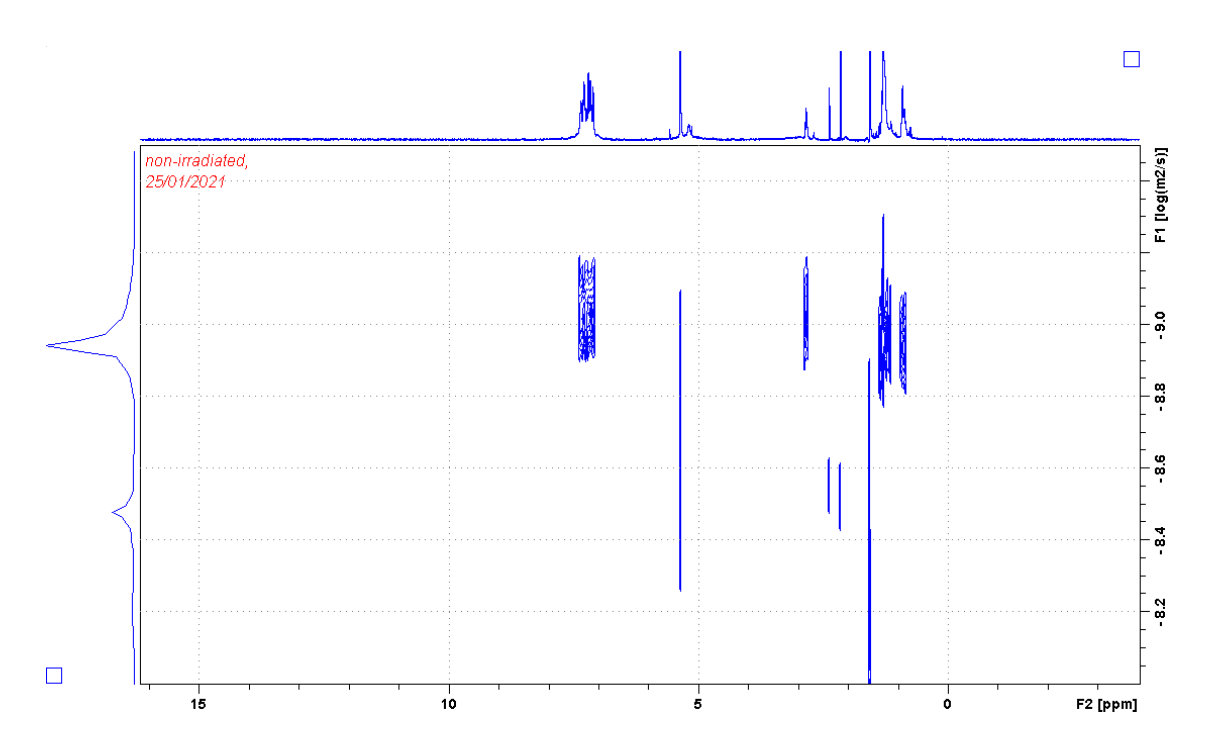


Figure A.20 DOSY NMR spectrum of the non-irradiated S3 sample containing mixture of monomers and dimers. Spectrum acquired in CH_2Cl_2 - d_2 .

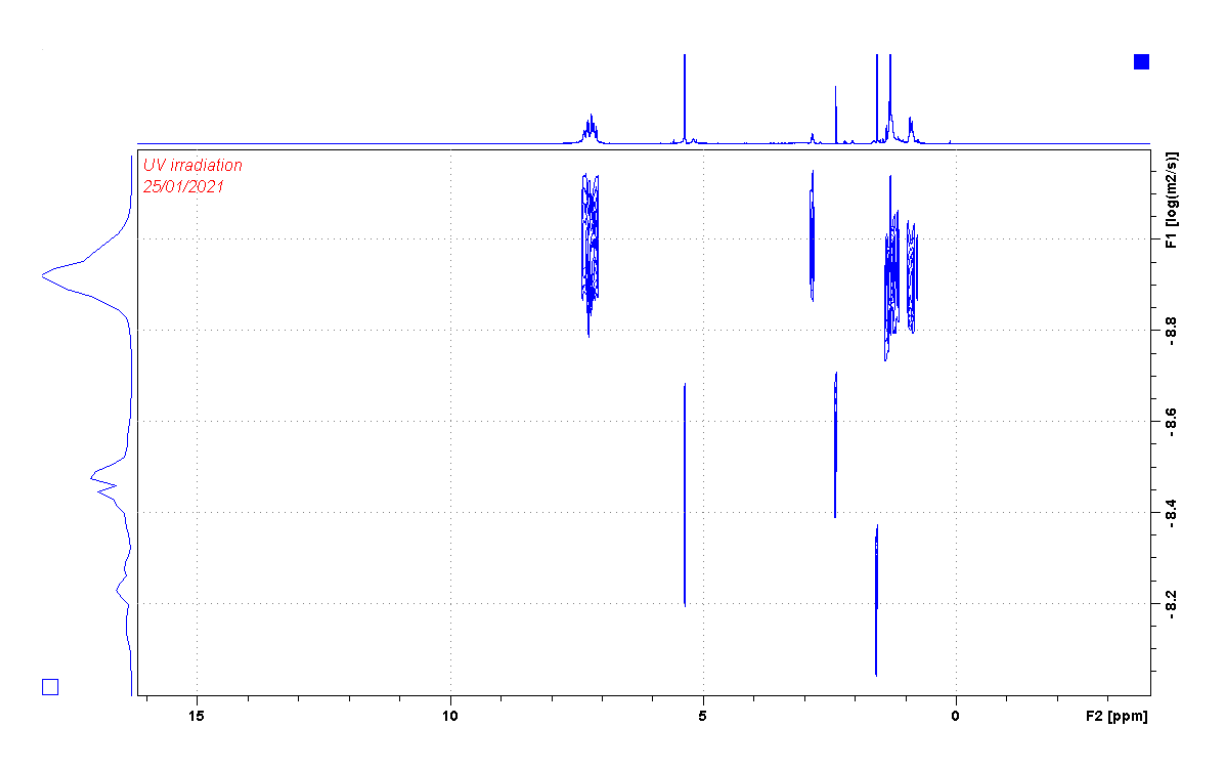


Figure A.21 DOSY NMR spectrum of the UV-irradiated S3 sample. Spectrum acquired in CH₂Cl₂-d₂.

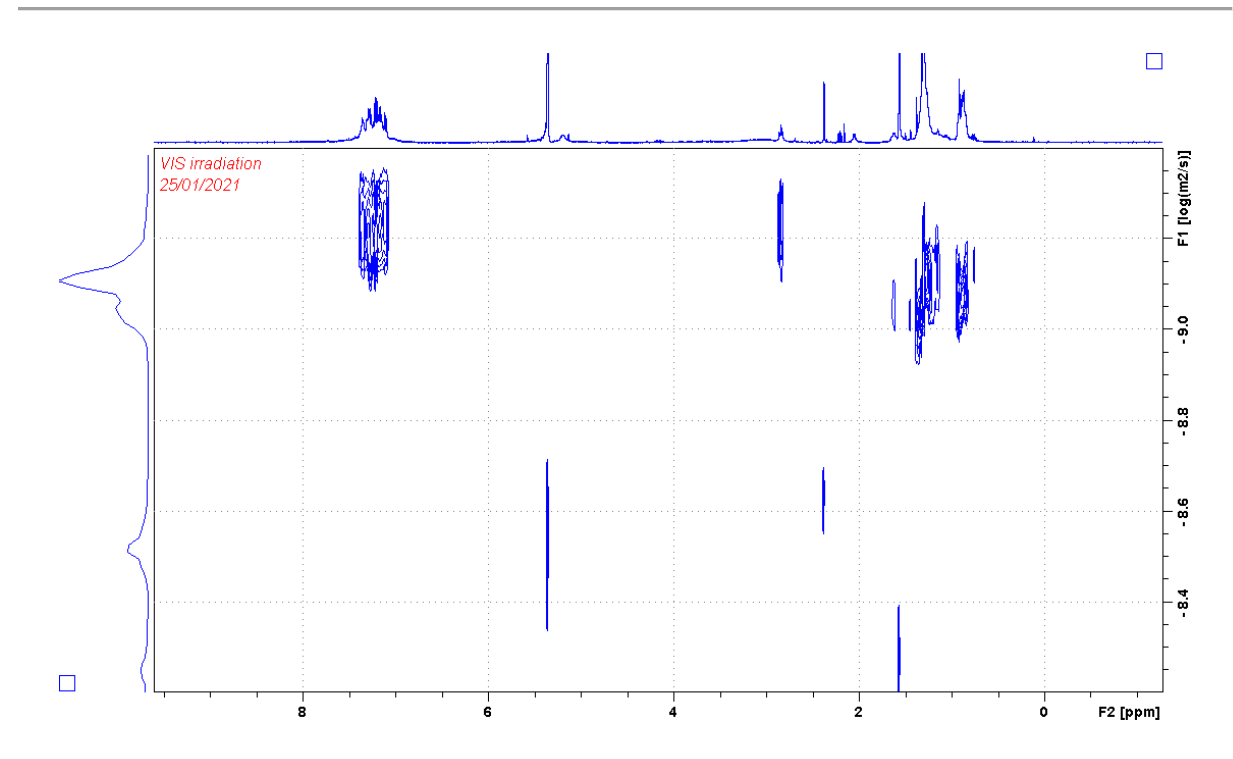


Figure A.22 DOSY NMR spectrum of the S3 sample irradiated with 532 nm light. Spectrum acquired in CH₂Cl₂-d₂.

A.9 References

- 1. Pinault, T.; Chérioux, F.; Therrien, B.; Süss-Fink, G., An Iterative Strategy for the Synthesis of Oligothiophenes by Catalytic Cross-Coupling Reactions. *Heteroatom Chemistry* **2004**, *15* (2), 121-126.
- 2. Lucas, Linda N.; Jong, Jaap J. D. d.; Esch, Jan H. v.; Kellogg, Richard M.; Feringa, Ben L., Syntheses of Dithienylcyclopentene Optical Molecular Switches. *European Journal of Organic Chemistry* **2003**, 2003 (1), 155-166.
- 3. Fulmer, G. R.; Miller, A. J. M.; Sherden, N. H.; Gottlieb, H. E.; Nudelman, A.; Stoltz, B. M.; Bercaw, J. E.; Goldberg, K. I., NMR Chemical Shifts of Trace Impurities: Common Laboratory Solvents, Organics, and Gases in Deuterated Solvents Relevant to the Organometallic Chemist. *Organometallics* **2010**, *29* (9), 2176-2179.
- 4. Venzo, A.; Antonello, S.; Gascón, J. A.; Guryanov, I.; Leapman, R. D.; Perera, N. V.; Sousa, A.; Zamuner, M.; Zanella, A.; Maran, F., Effect of the Charge State (z = -1, 0, +1) on the Nuclear Magnetic Resonance of Monodisperse Au₂₅[S(CH₂)₂Ph]₁₈^z Clusters. *Analytical Chemistry* **2011**, 83 (16), 6355-6362.
- 5. Kuhn, H. J.; Braslavsky, S. E.; Schmidt, R., Chemical Actinometry (IUPAC Technical Report). *Pure and Applied Chemistry* **2004**, *76* (12), 2105-2146.
- 6. Leighton, P. A.; Lucy, F. A., The Photoisomerization of the o-Nitrobenzaldehydes I. Photochemical Results. *The Journal of Chemical Physics* **1934**, *2* (11), 756-759.
- 7. Willett, K. L.; Hites, R. A., Chemical Actinometry: Using o-Nitrobenzaldehyde to Measure Lamp Intensity in Photochemical Experiments. *Journal of Chemical Education* **2000**, *77* (7), 900.

- 8. Ji, Y.; DiRocco, D. A.; Hong, C. M.; Wismer, M. K.; Reibarkh, M., Facile Quantum Yield Determination via NMR Actinometry. *Organic Letters* **2018**, *20* (8), 2156-2159.
- 9. Volfova, H.; Hu, Q.; Riedle, E., Determination of Reaction Quantum Yields: LED Based Setup with Better 5 % Precision. *EPA Newsletter* **2019**, 51-69.
- 10. Stadler, E.; Eibel, A.; Fast, D.; Freißmuth, H.; Holly, C.; Wiech, M.; Moszner, N.; Gescheidt, G., A Versatile Method for the Determination of Photochemical Quantum Yields via Online UV-Vis Spectroscopy. *Photochemical & Photobiological Sciences* **2018**, *17* (5), 660-669.
- 11. Leyva, V.; Corral, I.; Schmierer, T.; Gilch, P.; González, L., A Comparative Analysis of the UV/Vis Absorption Spectra of Nitrobenzaldehydes. *Physical Chemistry Chemical Physics* **2011**, *13* (10), 4269-4278.

Appendix B

A DFT study of [Au₂₅(SMe)₁₇]–DTE–[Au₂₅(SMe)₁₇], a model of the [Au₂₅(2PET)₁₇]–DTE–[Au₂₅(2PET)₁₇] dimer

B.1 Objectives

The $[Au_{25}(2PET)_{18}]$ clusters were connected in a ligand substitution reaction using a dithiolatefunctionalized dithienylethene (DTE) which in their antiparallel conformation can undergo a photocyclization. For two clusters, the reaction reads:

$$2 [Au_{25}(2PET)_{18}] + DTE^{(2-)} \rightarrow 2 2PET^{(-)} + [Au_{25}(2PET)_{17}] - DTE - [Au_{25}(2PET)_{17}]$$

The photocyclizable ligand can attach to so-called 'in' and 'out' staple positions, which will be referred to by the 'i' and 'o' letters in the following.

Actually, species with different sizes, hence with different degree of linking, have been isolated. Their absorption spectra differ from the one of the $[Au_{25}(2PET)_{18}]$ cluster. Insights into the origin of this difference could be gained from the computational studies of the Au_{25} polymers.

To proceed, only Au_{25} dimers are considered. More precisely, the model dimers obtained by replacing the $2PET^{(-)}$ ligand by $SMe^{(-)}$ are considered: $[Au_{25}(SMe)_{17}]$ –DTE– $[Au_{25}(SMe)_{17}]$. There exist three regioisomoers, denoted **DTE_ii**, **DTE_oi** and **DTE_oo**, for which the photocyclizable ligand can be in the open ('o') or closed formed ('c'). There are thus a total of 6 isomers to characterize: namely, oDTE xy and cDTE xy with (x,y) in ('i', 'o')².

B.2 Computational details

The geometries of the clusters have been optimized within density functional theory^{1, 2} using the dispersion-corrected PBE-D3 functional^{3, 4} and the hybrid Gaussian and planewave (GPW) method⁵ as implemented in the CP2K/QUICKSTEP program.⁶ The core electrons of the atoms were described with Goedecker–Teter–Hutter pseudopotentials,⁷⁻⁹ while their valence states were described with the Gaussian-type MOLOPT DZVP-MOLOPT-SR-GTH basis set of double-zeta polarized quality from the CP2K package.¹⁰ The electron density was expanded in a planewave basis set using a planewave cutoff of 300 Ry and a relative density cutoff of 40 Ry was employed. The ability of the GFN-xTB semiempirical tight-binding method¹¹ to describe the investigated clusters was also examined.

For the characterization of the clusters in the high-spin (HS) triplet state, the calculations have been performed within the restricted open-shell Kohn-Sham (ROKS) scheme. Test calculations have shown that ROKS and unrestricted Kohn-Sham (UKS) calculations give identical results for this type of clusters in the triplet state. For characterizing the clusters in the low-spin (LS) open-shell singlet state, the calculations have been performed using the LS ROKS scheme implemented in CP2K. ¹²

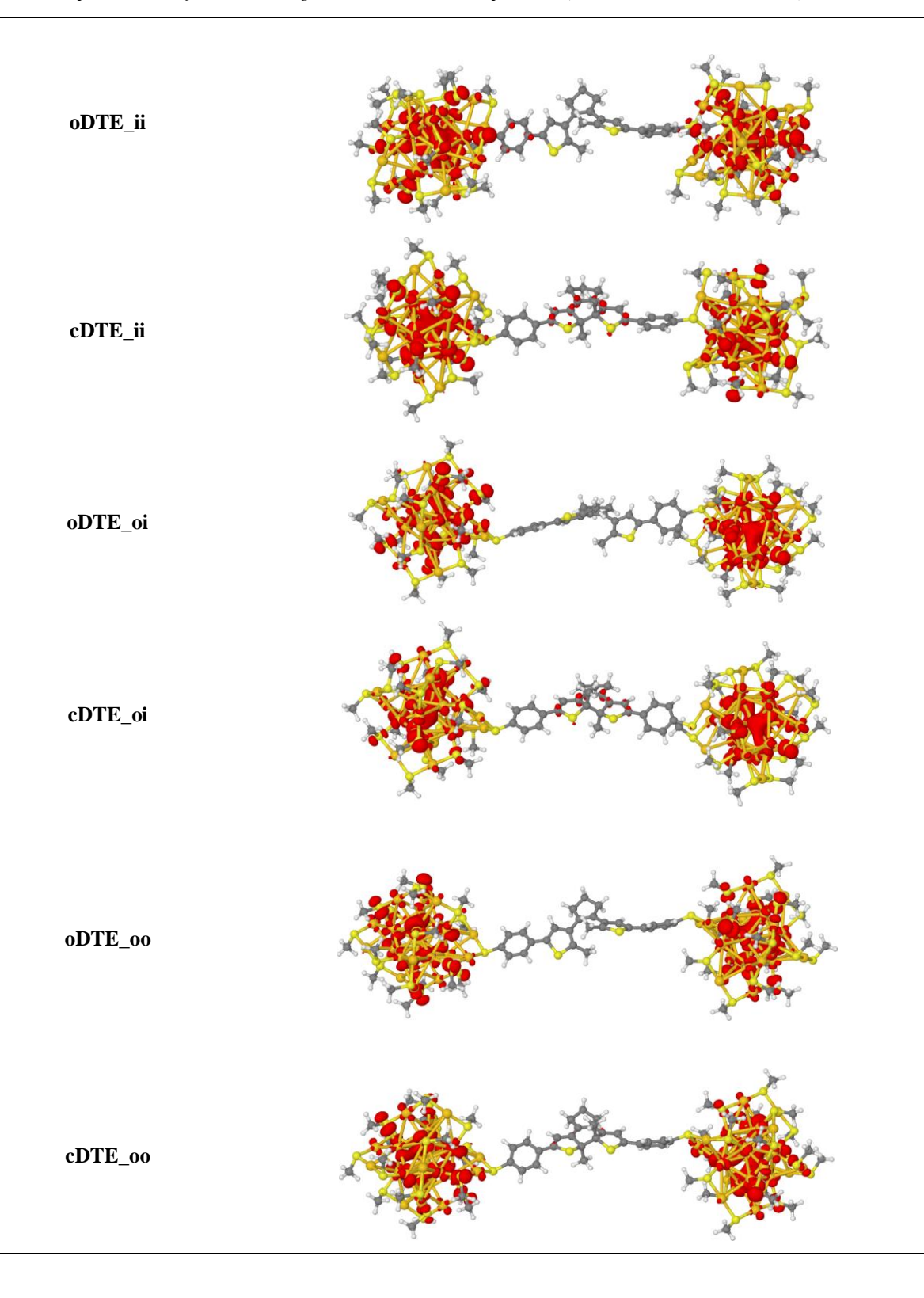
The optimizations have been performed using initial geometries constructed from the X-ray crystal structures of $[Au_{25}(2PET)_{18}]^0$ reported by Zhu et al.¹³ and the **o-DTE(SH)** ligand measured in-house.

B.3 Results and (brief) discussion

B.3.1 Electronic structures

The neutral [$Au_{25}(2PET)_{18}$] cluster and its [$Au_{25}(SMe)_{18}$] model is a radical. In the DTE-bridged dimer, the question which then arises is to know if, in the triplet state, the electronic spin density is delocalized over the whole dimeric system. **Table B.1** shows the calculated spin densities for the closed and open forms of all isomers in the triplet states. In all cases, the spin density remains localised on the Au_{25} clusters. That is, the Au_{25} dimers are (open-shell) diradicals, and for this reason, they have to be treated in the singlet state as open-shell singlet diradical systems.

Table B.1 Spin densities of the DTE-bridged Au₂₅ dimers in the triplet state (ROKS PBE-D3/DZVP results).



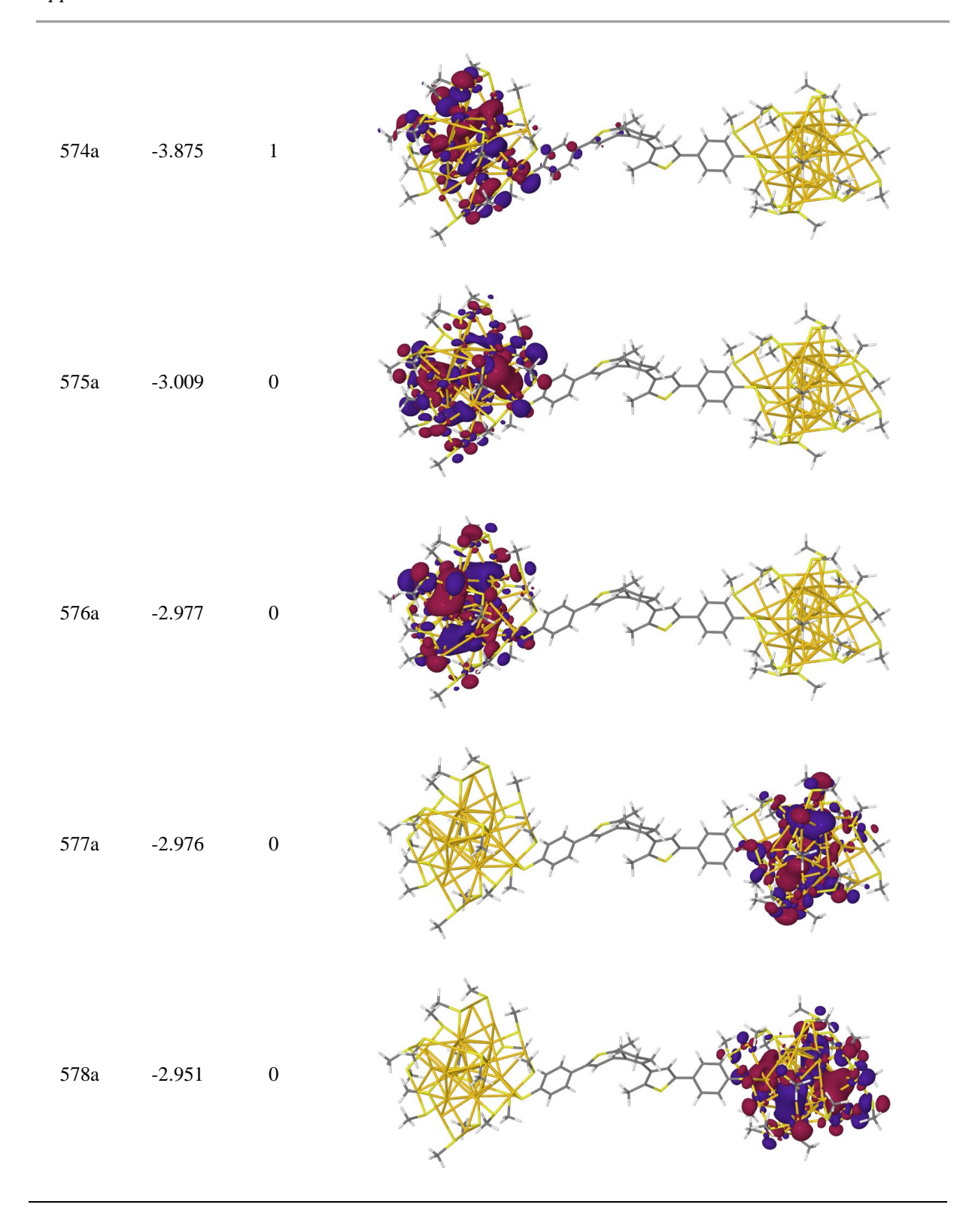
The localization of the spin density on the Au₂₅ clusters indicates that, with the DTE linker in either form, the clusters tend to retain their physico-chemical identity. This can be confirmed by inspecting the frontier molecular orbitals (MOs) of the dimers. The frontier MOs are plotted in Table **B.2** for the **oDTE_ii** isomer, which is predicted to be the most stable isomer (see **Section B.3.3**) and wherein the

Au₂₅ clusters are chemically equivalent. The considered MOs (565a-578a) are all localized on either cluster, with the exception of the MOs 567a and 568a, which are localized on the **oDTE** bridge. The four doubly-occupied and nearly-degenerate 569a-572a as well as the two singly-occupied and nearly degenerate 573a and 574a MOs can be identified to the P super atom molecular orbitals (SAMOs) of the individual clusters. That is, there is a set of three P SAMOs per Au₂₅ cluster, and in each set, there are two doubly-occupied and nearly-degenerate SAMOs lying ~0.3 eV below a singly-occupied P SAMO. Such a splitting of the three P SAMOs located on each cluster can be ascribed to Jahn-Teller distortions undergone by each Au₂₅ cluster. The considered MOs 156a and 568a, which are localized on either expenses and some singly-occupied and nearly-degenerate SAMOs per Au₂₅ cluster, and in each set, there are two doubly-occupied and nearly-degenerate SAMOs lying ~0.3 eV below a singly-occupied P SAMO. Such a splitting of the three P SAMOs located on each cluster can be ascribed to Jahn-Teller distortions undergone by each Au₂₅ cluster.

Table B.2 Frontier molecular orbitals of the **oDTE_ii** Au₂₅ dimer in the triplet state with their indices, energies, and occupations numbers (ROKS PBE-D3/DZVP results).

Index	ε/eV	occ.	Molecular orbital
565a	-4.872	2	
566a	-4.844	2	
567a	-4.733	2	

568a	-4.607	2	
569a	-4.221	2	
570a	-4.216	2	
571a	-4.211	2	
572a	-4.201	2	
573a	-3.888	1	



B.3.2 Structural properties

Figure B.1 shows the optimised geometry of the oDTE_ii cluster in the triplet state and the atom labelling used.

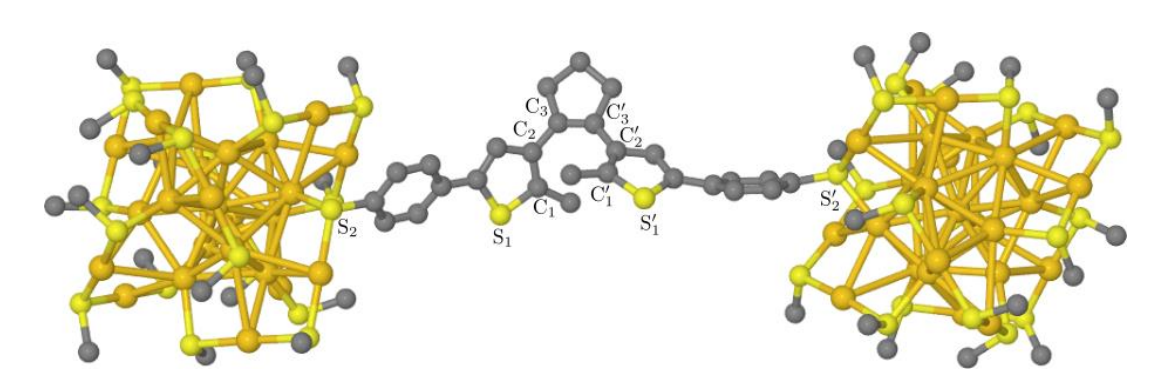


Figure B.1 Optimised geometry of **oDTE_ii** in the triplet state with the atom labelling used; H atoms are hidden for the sake of clarity (PBE-D3/DZVP results).

The following parameters have been selected to characterize the geometries of the clusters: namely, the dihedral angle C_2 - C_3 - C_3 '- C_2 ' and the interatomic distances C_1 - C_1 ', S_2 - S_1 , S_1 - S_1 ', S_1 '- S_2 ' and S_2 - S_2 '. Their values are reported in **Table B.3** for the clusters in the LS and HS states.

Table B.3 Selected angle (deg) and distances (Å) characterizing the optimized structures of the clusters in the triplet (T) and singlet (S) states (see Figure B.1 for the atom labelling used).

		C2-C3-C3'-C2'	C1-C1'	S ₂ -S ₁	S ₁ -S ₁ '	S ₁ '-S ₂ '	S ₂ -S ₂ '
oDTE_ii	T	-6.1	3.558	7.170	5.863	7.270	18.522
	S	-6.6	3.570	7.155	5.898	7.272	18.535
cDTE_ii	T	-9.3	1.545	7.166	3.740	7.196	18.015
	S	-9.2	1.546	7.168	3.745	7.204	18.028
oDTE_oi	T	11.4	3.663	7.213	6.377	7.274	19.638
	S	10.3	3.665	7.208	6.371	7.280	19.645
cDTE_oi	T	10.2	1.547	7.124	3.707	7.189	17.883
	S	10.6	1.545	7.120	3.691	7.182	17.850
oDTE_oo	T	-12.3	3.645	7.007	6.446	7.229	19.755
	S	-12.2	3.651	7.012	6.460	7.231	19.746
cDTE_oo	T	-8.9	1.549	7.248	3.804	7.379	18.263
_	S	-9.7	1.549	7.257	3.777	7.359	18.233

Inspection of **Table B.3** shows that the structures of a given cluster in the singlet and triplet states are quite similar. Ongoing from the open to the closed form, the C₂-C₃-C₃'-C₂' dihedral angle does not

significantly change for the **DTE_oi** isomers while its magnitude decreases by ~3 deg for the **DTE_oo** isomer and increases by ~3 deg for the **DTE_ii** isomer. For all isomers, the formation of the C_1 - C_1 ' bond translates into a ~2.0 Å decrease of the C_1 - C_1 ' distance, while the S_2 - S_1 and S_1 '- S_2 ' distances exhibit minor changes of $ca \pm 0.2$ Å, at most. In all cases, the formation of the C_1 - C_1 ' bond is also accompanied by a 2.2~2.7 Å decrease of the S_1 - S_1 ' distance, by a ~0.5 Å decrease of the S_2 - S_2 ' distance for the **DTE_ii** and **DTE_oo** isomers, and by a ~1.7 Å decrease of the S_2 - S_2 ' distance for the **DTE_oi** isomer.

B.3.3 Energetics

Table B.4 gives for all isomers: the triplet-singlet energy difference: $\Delta E_{ST} = E(T) - E(S)$; the energy difference between the open and closed form in either state: $\Delta E_1 = E(closed) - E(open)$; and the relative energies ΔE_2 of the studied isomers with respect to the most stable one.

Table B.4 Calculated values of the triplet-singlet energy difference ΔE_{ST} , of the energy difference ΔE_1 between the closed and the open forms, and the relative energy ΔE_2 of studied isomers (energies in cm⁻¹, PBE-D3/DZVP results).

	ΔE_{ST}	$\Delta E_1(T)$	$\Delta E_2(T)$	$\Delta E_1(S)$	$\Delta E_2(S)$
oDTE_ii	-140	_ 5165	0	5151	0
cDTE_ii	-127	_ 5105	5165	. 3131	5151
oDTE_oi	-151	_ 5775	2216	6109	2227
cDTE_oi	-486	_ 3773	7991	010)	8337
oDTE_oo	-201	100	2682		2742
cDTE_oo	-57	_ 4936	7618	4792	7535

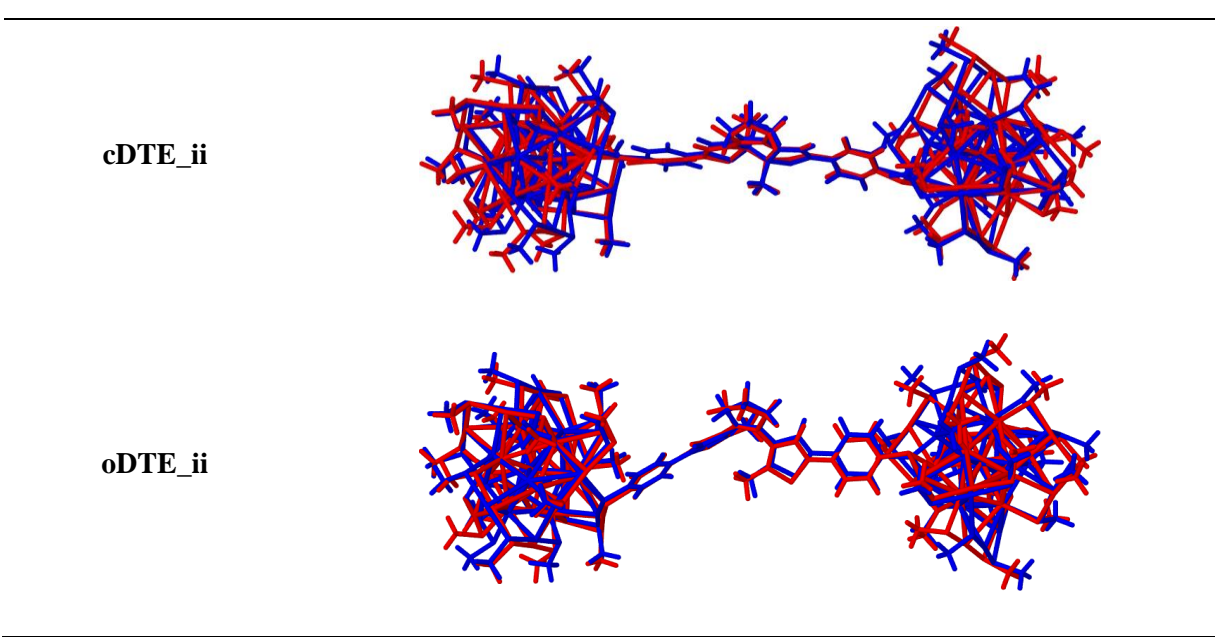
The triplet and singlet states are found to be nearly degenerate for all isomers in the open or closed form, with the triplet lying slightly lower in energy (Hund rule). For each isomer, the open form is found to be the most stable one; furthermore, the energy difference depends on the staple positions occupied by the DTE ligands. The most stable isomer is **oDTE_ii**.

B.3.4 Performance of the GFN-xTB method

The GFN-xTB and PBE-D3/DZVP methods have been used to optimize the geometries of the **oDTE_ii** and **cDTE_ii** isomers in the triplet state (UKS calculations). The GFN-xTB and PBE-D3/DZVP

geometries obtained with both methods are very close (**Table B.5**) with root-mean-square deviations (RMSDs) of atomic positions of 0.81 Å and 0.78 Å for the open and closed forms, respectively.

Table B.5 Comparison of the optimized GFN-xTB (blue) and PBE-D3/DZVP (red) geometries of cDTE_ii and oDTE_ii in the triplet state (UKS calculations).



With both methods, the open form is found to be the most stable form, with an energy difference ΔE_1 of 5336 cm⁻¹ and 2098 cm⁻¹ for the PBE-D3/DZVP and GFN-xTB methods, respectively.

B.4 Concluding remarks

The DFT study of the DTE-bridged Au₂₅ dimer ([Au₂₅(2PET)₁₇]–DTE–[Au₂₅(2PET)₁₇]) indicates that this dimer is a diradical wherein the radical Au₂₅ cluster tends to retain its physico-chemical identity. For each of the 3 regioisomers which have been considered in the open or in the closed form, the triplet and the open-shell singlet state are found to be quasi-degenerate, with the triplet state lying slightly lower in energy; furthermore, the structure of the dimer undergoes minor changes on passing from the triplet to the singlet state. The **oDTE_ii** regioisomer is predicted to be the most stable one. The inspection of its frontier MOs indicates that its highest-occupied MOs correspond to the *P* SAMOs of the Au₂₅ cluster¹⁶ whose splitting reflects the Jahn-Teller distortions of the Au₂₅ cluster.¹⁵

The semiempirical GFN-xTB method has been used for the determination of the geometries of **oDTE_ii** and **cDTE_ii** in the triplet state: these geometries are in a very satisfactory agreement with those

similarly determined at the PBE/DZVP level. This suggests that the GFN-xTB method offers an efficient means for determining the structures of Au clusters and derivatives.

Although the GFN-xTB and PBE/DZVP methods both predict the **DTE_ii** regioisomer to be most stable in the open form, they give very different results for their energy difference (5336 cm⁻¹ and 2098 cm⁻¹ for the PBE-D3/DZVP and GFN-xTB methods, respectively). Quoting Bannwarth et al. dealing with the GFN2-xTB method:¹⁷

"As for the predecessor [GFN-xTB], properties around energetic minima, such as geometries, vibrational frequencies, and noncovalent interactions, are the target quantities. Already in our work for the GFN-xTB scheme, we have identified that the preference for geometries (instead of covalent bond energies) in the fit procedure resulted in systematically overestimated covalent bond energies. We have not deviated from this strategy, as covalent bond energies are not of primary interest for this method, and furthermore, the errors are very systematic as in GFN-xTB. This way, the errors will be less random and more useful, once the systematic errors have been removed— (see ref. [18]) for such a correction scheme which in combination with GFN-xTB outperforms any other semiempirical method of comparable complexity."

Consequently, regarding the determination of the energetics of Au clusters and derivatives with the GFN-xTB method, additional benchmarking is required. In absence of such a benchmark study, the computationally cheapest and most reliable approach involving the GFN-xTB consist in a determination of the systems structures at the GFN-xTB level followed by single-point DFT calculations.

The electronic absorption spectrum of the dimers has not been investigated in the present study. Still, from the inspection of the frontier MOs of the **oDTE_ii** isomer (Table **B.2**), it is clear that in addition to cluster-centred and DTE-centred transitions, DTE \leftrightarrow Au₂₅ charge transfer transitions are to be expected. Thus, for **oDTE_ii**, the 568a \rightarrow Na (N = 573–578) MO \rightarrow MO transitions depict low-lying DTE \rightarrow Au₂₅ charge transfer transitions.

B.5 References

- 1. Hohenberg, P.; Kohn, W., Inhomogeneous Electron Gas. *Physical Review* **1964**, *136* (3B), B864-B871.
- 2. Kohn, W.; Sham, L. J., Self-Consistent Equations Including Exchange and Correlation Effects. *Physical Review* **1965**, *140* (4A), A1133-A1138.
- 3. Perdew, J. P.; Burke, K.; Ernzerhof, M., Generalized Gradient Approximation Made Simple. *Physical Review Letters* **1996**, 77 (18), 3865-3868.
- 4. Grimme, S.; Antony, J.; Ehrlich, S.; Krieg, H., A Consistent and Accurate Ab Initio Parametrization of Density Functional Dispersion Correction (DFT-D) for the 94 Elements H-Pu. *The Journal of Chemical Physics* **2010**, *132* (15), 154104.

- 5. Lippert, B. G.; Parrinello, J. H.; Michele, A Hybrid Gaussian and Plane Wave Density Functional Scheme. *Molecular Physics* **1997**, *92* (3), 477-488.
- VandeVondele, J.; Krack, M.; Mohamed, F.; Parrinello, M.; Chassaing, T.; Hutter, J., Quickstep: Fast and Accurate Density Functional Calculations Using a Mixed Gaussian and Plane Waves Approach. *Computer Physics Communications* 2005, 167 (2), 103-128.
- 7. Goedecker, S.; Teter, M.; Hutter, J., Separable Dual-Space Gaussian Pseudopotentials. *Physical Review B* **1996**, *54* (3), 1703-1710.
- 8. Hartwigsen, C.; Goedecker, S.; Hutter, J., Relativistic Separable Dual-Space Gaussian Pseudopotentials from H to Rn. *Physical Review B* **1998**, *58* (7), 3641-3662.
- 9. Krack, M., Pseudopotentials for H to Kr Optimized for Gradient-Corrected Exchange-Correlation Functionals. *Theoretical Chemistry Accounts* **2005**, *114* (1), 145-152.
- 10. VandeVondele, J.; Hutter, J., Gaussian Basis Sets for Accurate Calculations on Molecular Systems in Gas and Condensed Phases. *The Journal of Chemical Physics* **2007**, *127* (11), 114105.
- 11. Grimme, S.; Bannwarth, C.; Shushkov, P., A Robust and Accurate Tight-Binding Quantum Chemical Method for Structures, Vibrational Frequencies, and Noncovalent Interactions of Large Molecular Systems Parametrized for All spd-Block Elements (Z = 1–86). *Journal of Chemical Theory and Computation* **2017**, *13* (5), 1989-2009.
- 12. Frank, I.; Hutter, J.; Marx, D.; Parrinello, M., Molecular Dynamics in Low-Spin Excited States. *The Journal of Chemical Physics* **1998**, *108* (10), 4060-4069.
- 13. Zhu, M. Z.; Eckenhoff, W. T.; Pintauer, T.; Jin, R., Conversion of Anionic [Au₂₅(SCH₂CH₂Ph)₁₈]⁻ Cluster to Charge Neutral Cluster via Air Oxidation. *The Journal of Physical Chemistry C* **2008**, *112* (37), 14221-14224.
- 14. Chen, Y.; Wang, J.; Liu, C.; Li, Z.; Li, G., Kinetically Controlled Synthesis of Au₁₀₂(SPh)₄₄ Nanoclusters and Catalytic Application. *Nanoscale* **2016**, *8* (19), 10059-10065.
- 15. Tofanelli, M. A.; Salorinne, K.; Ni, T. W.; Malola, S.; Newell, B.; Phillips, B.; Häkkinen, H.; Ackerson, C. J., Jahn–Teller Effects in Au₂₅(SR)₁₈. *Chemical Science* **2016**, *7* (3), 1882-1890.
- Dong, R.; Chen, X.; Zhao, H.; Wang, X.; Shu, H.; Ding, Z.; Wei, L., Towards Ultra Small Noble Metal Nanoparticles: Testing Jellium Model for Ligand Protected Copper and Silver M₁₃ Core Nanoparticles. *Physical Chemistry Chemical Physics* 2011, 13 (8), 3274-3280.
- 17. Bannwarth, C.; Ehlert, S.; Grimme, S., GFN2-xTB—An Accurate and Broadly Parametrized Self-Consistent Tight-Binding Quantum Chemical Method with Multipole Electrostatics and Density-Dependent Dispersion Contributions. *Journal of Chemical Theory and Computation* **2019**, *15* (3), 1652-1671.
- 18. Kromann, J.; Welford, A.; Christensen, A.; Jensen, J., Random versus Systematic Errors in Reaction Enthalpies Computed Using Semiempirical and Minimal Basis Set Methods. *ACS Omega* **2018**, *3*(4), 4372–4377